Contributions to an electromagnetic and microfluidic microsystem for immunological detection using magnetic nanoparticles

Benjamin Garlan

Sorbonne Université

Ecole Doctorale Science Mécanique Acoustique Electronique et Robotique
Laboratoire d'Electronique et Electromagnétisme (L2E)

Contributions to an electromagnetic and microfluidic microsystem for immunological detection using magnetic nanoparticles

Par Benjamin GARLAN

Thèse de Doctorat en Electronique Biomédical

Soutenance prévue le 17.12.2019
Devant le jury composé de :

Mme Nadine MILLOT	Professeur, Université de Bourgogne, Laboratoire Carnot	Rapporteure
Mme Anne-Laure DEMAN	Maître de Conférences, HDR, Université Claude Bernard, Institut des nanotechnologies de Lyon	Rapporteure
M. Hans-Joachim KRAUSE	Professeur, Forschungszentrum Jülich, Institute of Bioelectronics, Germany	Examinateur
M. Stéphane HOLE	Professeur, Sorbonne Université, ESPCI, laboratoire LPEM	Examinateur
M. Jean-Michel SIAUGUE	Maître de Conférences, Sorbonne Université, laboratoire PHENIX	Invité
M. Vincent HUMBLOT	Chargé de Recherche CNRS, Université Franche Comté, Institut FEMTO-ST	Invité
M. Kieu NGO	Maître de Conférences, HDR, Sorbonne Université, laboratoire LISE	Co-encadrant
M. Hamid KOKABI	Professeur, Sorbonne Université, laboratoire L2E	Directeur de thèse

Acknowledgments

Je tiens d'abord à remercier Hamid Kokabi de m'avoir permis d'effectuer ce doctorat et pour son encadrement. Je remercie également Kieu Ngo et Guillaume Perry pour leur aide, leurs conseils et leurs disponibilités au cours de ces trois ans. Travailler avec Amine Rabehi lors de la première moitié de mon doctorat fut à la fois un plaisir mais aussi très enrichissant. Je remercie les stagiaires Owen Barrigar, Benjamin Lomuto, Quentin Fornasiero et Suzanne Wong pour leur motivation et leur aide.

Je remercie Damien Bricault du LISE pour son aide sur l'impression 3D des moules. Sophie Neveu, Jean-Michel Siaugue et Emilie Secret du laboratoire PHENIX pour leur travail sur la synthétisation des nanoparticules magnétiques et pour nos discussions. Je remercie également Souhir Boujday et Vincent Humblot du LRS pour leur précieuse aide sur la fonctionnalisation de surface. Je remercie également Antoine Miche, Yacine Mazouzi et Alexis Loiseau du même laboratoire pour leurs aides respectives.

Je remercie Chloé et Yves du L2E d'être toujours disponibles et pour leur gentillesse, mais aussi tous les autres membres du L2E qui rendent le travail dans ce laboratoire très agréable.

Je voudrais dire un grand merci aux autres doctorants du L2E avec qui j'ai forgé quelques souvenirs impérissables et qui sont devenus aux furs et à mesures des années bien plus que de simples collègues. Je voudrais citer Kévin, Laurent, Joanna, Mounir, Lydia, Mondiaye, Mathieu, Qiang, Rudy, Soroush, Tuan Anh, Oussama, Michael, Tianyu, Solofo. Je n'oublie pas les doctorants d'autres laboratoires que j'ai également côtoyés notamment via Doc'up.

Je voudrais également remercier mes amis de Paris, de Bretagne et d'ailleurs. Ils me permettent de faire face sereinement aux difficultés rencontrées. Qu'ils habitent dans la rue d'en face ou à l'autre bout du monde, je sais que je peux compter sur eux pour me remonter le moral.

Enfin je voudrais remercier ma famille. Notamment mon frère, ma sœur et mes parents qui m'ont soutenus, encouragés et aidés depuis toujours.

Je dédie cette thèse à mes grands-mères.

Contents

Glossary

Abbreviation	Description
APTES	(3-AminoPropyl)TriEthoxySilane
ATR	Attenuated Total Reflection
BSA	Bovin Serum Albumin
CCD Camera	Charged Coupled Device Camera
COC	CycloOlefinCopolymer
CRP	C-Reactive Proteins
DNA	DeoxyriboNucleic Acid
ELISA	Enzyme-Linked ImmunoSorbent Assay
EVD	Ebola Virus Disease
FTIR	Fourier Transform InfraRed spectroscopy
GMR	Giant MagnetoResistor effect sensors
GOPTS	(3-GlycidylOxyPropyl)TrimethoxySilane
HDT	Heat Distortion Temperature
HRP	HorseRadish Peroxidase
LOC	Lab-On-a-Chip
LOD	Limit Of Detection
MNP	Magnetic NanoParticles
MEMS	MicroElectroMechanical Systems
PBS	Phosphate Buffered Saline
PCB	Printed Circuit Board
PDMS	PolyDiMethylSiloxane
PMMA	PolyMethylMetAcrylate
POC	Point Of Care
PVA	PolyVinyl Alcohol
QCM	Quartz Crystal Microbalance
SNR	Signal to Noise Ratio
SPR	Surface Plasmon Resonance
SQUID	Superconducting QUantum Interference Device
T_g	Glass transition temperature
TEM	Transmission Electron Microscopy
TESU	11-TriEthoxySilyl Undecanal 90%
TMR	Tunneling MagnetoResistance effect sensors
WHO	World Health Organization
XPS	X-ray Photoelectron Spectroscopy

General introduction

The ever increasing number of traveling people leads to fast spreading of diseases worldwide and enhanced danger of epidemic or even pandemic diseases. A rapid and sensitive low-cost system for pathogen detection is urgently needed to contain these hazards among others like bioterrorism or facilitate environment protection. Many approaches have been tried towards development of a lab-on-a-chip (LOC) system that is able to perform cost-effective and reliable immunoassays. Lab-on-a-chip systems are based on microfluidics technologies and allow miniaturizing processes that normally require laboratory facilities to be performed.

This thesis describes an innovative magnetic detection system prototype that should lead to a fully integrated, portable, easy to use, affordable and reliable pathogen detection device. This in vitro diagnosis device uses the mixing frequency detection technique to detect the presence of magnetic nanoparticles (MNP) used as a marker in a microfluidic channel. The detection of these MNP reveals the absence or presence and concentration of the considered pathogen in the biological sample (blood, urine, saliva, etc.)

In this manuscript, first an overview of microfluidic and lab-on-a-chip technologies is presented. The principle of the magnetic detection system prototype is then described along with its electrical and microfluidic parts in the second chapter. The first results to miniaturize the electronic instrumentation are also described in this chapter. The results using different microfluidic structures and two different types of MNP to enhance performance of the device and the limit of detection (LOD) are described in the third chapter. Finally the functionalizations of MNP and the surface of microfluidic sample holder reservoirs which are needed to perform immunoassays are described.

Chapter 1. Microfluidic structures for lab-on-a-chip (LOC) immunoassays

1.1 Introduction

An immunoassay is a test or a technique that aims to detect a biological entity based on its capacity to act as an antigen. Recently, an effort has been made by the scientific community to make pathogen sensing devices portable by integrating and miniaturizing as much as possible the components required to make the tests. These portable pathogen sensing devices are also called lab-on-a-chip (LOC) for immunoassays. A lab-on-a-chip is a device that fulfills several laboratory functions on a small platform which usually isn't bigger than a few square centimeters. Smaller portable devices have many advantages if we compare them to benchtop versions. First, they allow the devices to be used outside the laboratories, directly in the field for in vitro diagnosis. This is particularly useful when the test has to give results quickly but also if there are no laboratories directly available near the location of the test.

To illustrate how a LOC would be of high utility, we can take the example of the Ebola virus disease (EVD) outbreak which started in December 2013 (Figure 1). According to the World Health Organization (WHO), the epidemic started in Guinea then spread to Liberia and Sierra Leone. Some cases were also observed in Nigeria. But Africa is not the only continent which was hit by Ebola. The United States, Italy, the United Kingdom and Spain had some citizens contaminated by the virus. Thankfully the virus did not manage to spread in these countries and the number of cases in Africa started decreasing in 2015 and the 26 March 2016, WHO terminated the Public Health Emergency of International Concern (PHEIC) status. But the outbreak killed 11,323 people according to the WHO and could have been a catastrophic worldwide pandemic. "Efforts to contain the outbreak are encumbered by weak laboratory and surveillance systems. Health experts are uncertain about how many EVD cases exist and where they are occurring, particularly in Liberia where roughly 20% of EVD cases have been confirmed through laboratory diagnosis. Limited laboratory capacity has resulted in extensive diagnosis backlogs, further calling into question the number of EVD cases and hindering efforts to contain the outbreak" [1]. With widely used portable pathogen sensing devices, this problem could be effectively tackled by facilitating diagnosis to contain epidemics as soon and as much as possible.

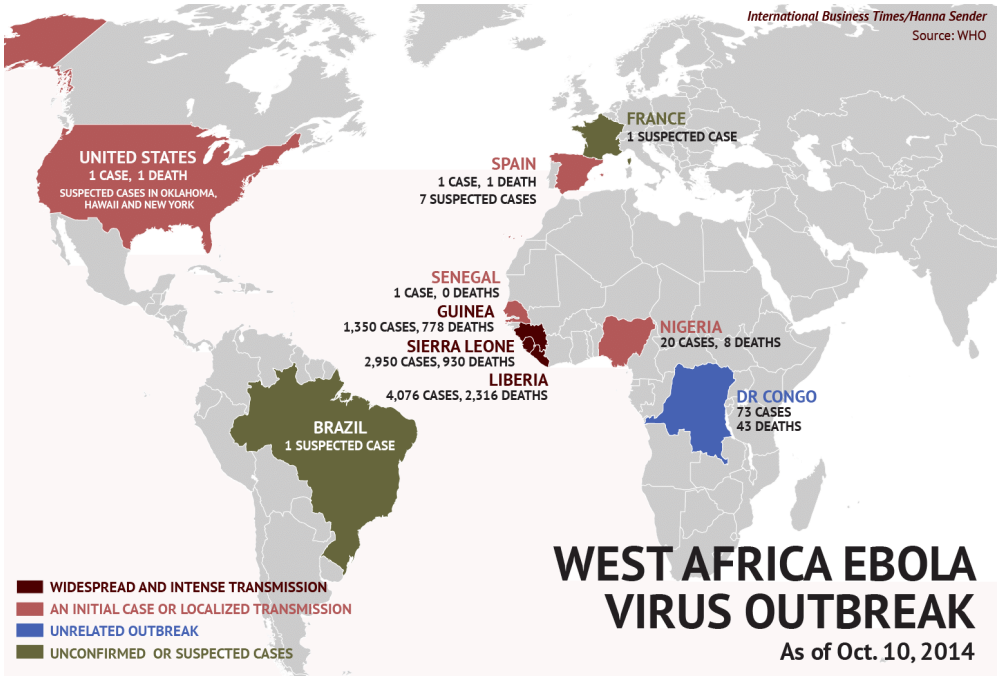

Figure 1: Map of the spreading of the Ebola virus in 2014, source WHO

Immunoassays with LOC have other potential applications like the detection of biological threats to counter bioterrorism [2]. But the design and fabrication of a LOC for immunoassays is often challenging because it involves interdisciplinary knowledge from fluid handling to detection schemes (microfabrication, microelectronics, microfluidics, chemistry, material science and biology). A particular field called microfluidics is usually extremely important for a LOC design and is growing in interest in the scientific community as well.

We will first present the principle of microfluidics and how it differs with more classical fluid mechanics. We will also show why it is important to carefully select the material and processing technique used for the creation of microfluidic channels and why this choice should be made early in a project development. Finally an overview of existing immunoassays techniques will be presented at the end of this first chapter.

1.2 Introduction to microfluidics

The matter is classified as solids, liquids and gases. Liquids and gases are both considered as fluids. Fluid has the ability to flow in any direction. The difference between a gas and a liquid is that a liquid will take the shape of the container that contains that liquid and the gas will occupy all the space possible. The shear force acting on any fluid due to the continuous relative motion between the fluid particles pushes the particles to move. And when the fluid particles are not able to resist the shear force the fluid particles tend to move over each other and create a fluid flow.

Microfluidics is a field which describes the behavior of a liquid or a gas in a very small volume (10^{-9} to 10^{-18} liter) and how to create and control the flow of that fluid using channels with dimensions of tens to hundreds of micrometers [2]. The microfluidics technologies benefited from the microfabrication progress made by the microelectronics field and is a good candidate for tackling the increasing demand of efficient, automated, sensitive and fast analytical systems [3].

In this chapter we will only consider incompressible (volume constant with pressure variations) Newtonian fluids, which have a linear relation between strain rate and deformation (figure 2). The proportionality constant between the two is the viscosity:

$$\tau = \mu \frac{du}{dy} \quad (1.1)$$

With:

- τ the shear stress applied by the fluid in Pa or $kg.m^{-1}.s^{-2}$
- μ the dynamic viscosity of the fluid ($kg.m^{-1}.s^{-1}$ or Pa.s)
- du/dy the sheer rate in s^{-1}

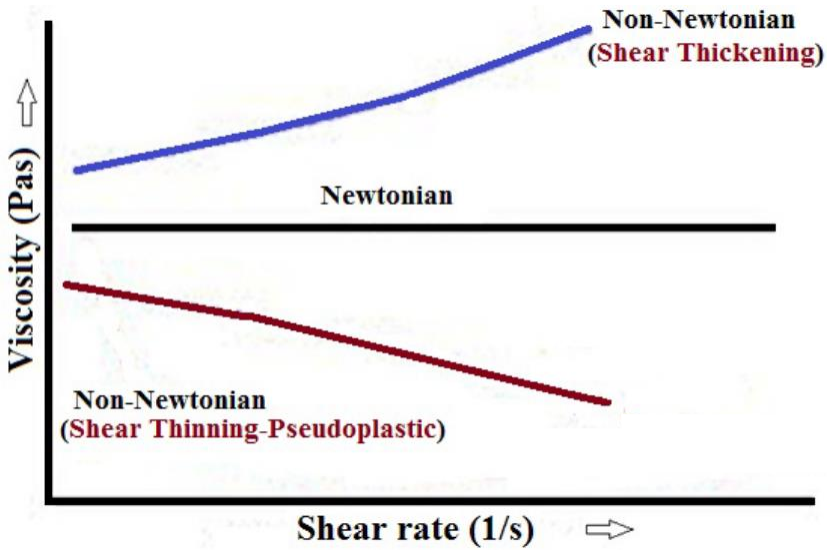

Figure 2: Typical rheogram of Newtonian and non-Newtonian fluids. [4]

1.2.1 Reynolds number and laminar flow

In small volumes, some physics phenomenon that are preponderant in the macroscopic scale become negligible and some physics phenomenon that are negligible at the macroscopic scale become critical in microfluidics. Thus, the capillarity phenomenon is extremely important when designing a microfluidic channel and, on the contrary, the gravity becomes a negligible force. Therefore, to describe the microfluidic world, dimensionless numbers are often used. The Reynolds number, introduced in 1883 by Osborne Reynolds [5], describes how a fluid behaves by balancing the inertial forces and the viscosity forces that are applied to it.

$$Re = \frac{\rho V H}{\mu} = \frac{V H}{\nu} \quad (1.2)$$

With:

- ρ the density of the fluid (kg.m^{-3})
- V the speed of the liquid (m.s^{-1})
- H the characteristic dimension of the microfluidic channel (m)
- ν the cinematic viscosity of the fluid (m^2.s^{-1})
- μ the dynamic viscosity of the fluid (kg.m^{-1}.s^{-1} or Pa.s)

The Reynolds number is dimensionless:

$$Re = \frac{F_{inertia}}{F_{viscous}} = \frac{\frac{kg}{m^3} \times \frac{m}{s} \times m}{\frac{kg}{m \times s} \times s} = dimensionless \quad (1.3)$$

The link between the cinematic and the kinetic viscosity is expressed as:

$$\nu = \frac{\mu}{\rho} \quad (1.4)$$

If the Reynolds number is low it means that the viscous force is preponderant, if it is high the inertial force is stronger than the viscous force. This can determine if a fluid is going to have different flow behaviors for a given channel layout. For an increasing Reynolds number, a Stokes flow is observed then a laminar flow, a transitory flow and a turbulent flow behavior for high Reynolds numbers. The Reynolds number increases when the velocity, the characteristic dimension or the density increase or if the viscosity decreases.

The Stokes flow is observed when the Reynolds number of a Newtonian fluid in a system is lower than 1. In that case, the inertial force due to the speed of the fluid is negligible and the viscous force and the pressure are balancing each other. It's the usual observed flow because in microfluidic channels the characteristic length L is very small (between tens of micrometers and hundreds of micrometers). The velocity of the fluid at the direct proximity of the walls of the channel is considered equal to 0, it is the no slip condition at the boundary layer. With a Stokes flow, the velocity depends of the position $\vec{r}$ considered on the radius of the system where $\vec{r}$=0 is the center of the tube and r_{max} is the boundary of the channel where the velocity is null. By simplifying the Navier Stokes, we can describe the Stokes flow with:

$$\overrightarrow{\Delta v} = \frac{\nabla p - \rho \vec{f}}{\mu} \quad (1.5)$$

With:

- $\vec{v}(\vec{r})$ the velocity of the fluid in the channel
- p($\vec{r}$) the pressure in the channel
- $\vec{f}$ an applied body force
- Δ the Laplace operator and ∇ is a gradient

When Reynolds number is higher than 1 but lower than 2300 for a pipe shaped channel, the flow is laminar which means that the viscosity begin to be less important and has an impact only close to the walls of the system at the boundary layers. In the middle of the channel the flow is laminar with well-defined line of flow; the fluid can be considered perfect which means that the viscosity has no impact on its behavior. In a laminar and Stokes flow regime the fluids don't mix. A straight pipe shaped channel is the ideal case for a laminar regime flow in a microchannel.

It is possible to calculate the flow rate with a laminar flow in a cylindrical channel with the Poiseuille equation:

$$Q = \frac{\pi P R^4}{8\mu L} \quad (1.6)$$

With:

- Q the volumetric flow rate ($m^3.s^{-1}$)
- P is the pressure difference between the exit and the entrance of the pipe channel in Pa or $kg.s^{-1}.s^{-}$
- R is the radius of the pipe (m)
- μ is the dynamic viscosity of the fluid ($kg.m^{-1}.s^{-1}$ or Pa.s)
- L is the length of the pipe (m)

An analogy can be made between the Poiseuille equation and Ohm's law that can be useful to represent and calculate the flow in complex microfluidic systems. The pressure difference between the exit and the entrance of the pipe channel is the product of the flow and its fluidic resistance that depends on its dimensions and on the viscosity of the fluid (figure 3 [6]).

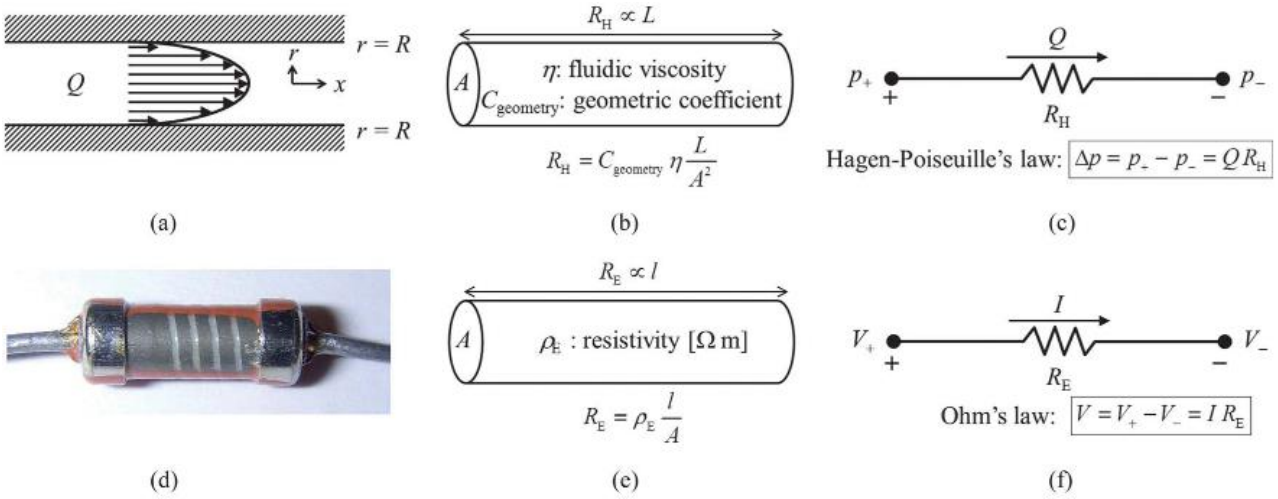

Figure 3: a) Poiseuille flow in a circular channel, (b) the hydraulic resistance of the circular channel ($C_{geometry} = 8\pi$ for the circular channel), (c) equivalent circuit symbol of a fluidic resistor for the hydraulic resistance and Poiseuille's law analogous to a resistor for the electric resistance and Ohm's law, (d) a partially resistor, (e) an electric resistance, and (f) circuit symbol of the resistor for the electric resistance and Ohm's law [6].

In a pipe if the Reynolds number is between 2000 and 3000 the flow is at a transitional regime which means that some instability can be observed on the flow lines. With a Reynolds number higher than 3000, the flow is no longer laminar and becomes a turbulent flow. At this regime, the lines of flow are not parallel anymore and the flow becomes chaotic. This regime usually doesn't appear in a simple microfluidic channel but it is possible to observe it with specific microchannels designs, like creating some cavities on the floor of a

channel [7]. Indeed in this later case a turbulent flow can appear at lower Reynolds number. Creating a turbulent flow can be interesting to mix a liquid in microfluidic channel (figure 4).

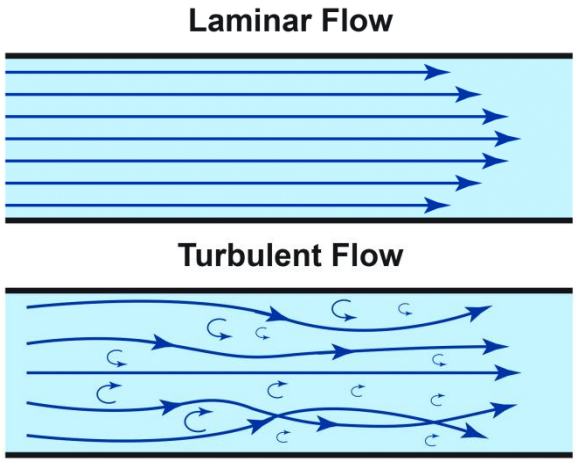

Figure 4: Laminar flow is a distribution of velocity, with the fastest moving fluid at the center www.automation.com.

1.2.2 Péclet number and diffusion

As introduced in the previous section (1.2.1), a fluid in a microfluidic channel is usually flowing in a laminar regime where the fluids do not mix. For example, it is possible to put in contact the same fluid from two different sources in a single microfluidic channel, they will not easily mix [8].

The Péclet number for mass transfer describes the ratio between the transfer of particles by convection and the transfer of particles via the diffusion.

$$Pe = \frac{H.V}{D} = Re.Sc \quad (1.7)$$

With:

- H is the characteristic dimension of the microfluidic channel (m)
- V is the flow velocity
- D is the mass diffusion coefficient
- Re is the Reynolds number
- Sc is the Schmidt number $Sc = \frac{\mu}{\rho D}$ (μ the dynamic viscosity and ρ the density)

$$Re = \frac{Convection\ transfert\ rate}{Viscous\ diffusion\ rate} \; ; \; Sc = \frac{Viscous\ diffusion\ rate}{Mass\ diffusion\ rate}$$

$$Pe = \frac{Convection\ transfert\ rate}{Mass\ diffusion\ rate}$$

In a classical microfluidic channel the Péclet number is low because since the Reynolds number is usually under 1, the diffusion transfer rate is the major way for the particles to travel inside the fluid or between different fluids. Obviously, it explains why the mixing of different liquids is difficult in classical pipe shaped microfluidic channel whereas it is easy to increase the convection in macroscopic flow by inducing a turbulent regime. To increase this Péclet number several strategies can be implemented in microfluidic system like adding scratches on the channel floor [7] or adding pillars in the channel. Making a lot of turns in channel is also effective to create some convection.

1.3 Different materials for microfluidics devices

1.3.1 Commonly used material: PDMS, advantages and drawbacks

Polydimethylsiloxane or PDMS is a silicone polymer (or polysiloxane), which means that it contains several times the linkage -Si-O-Si-. It is a group of inorganic macromolecules of silicon of different chemical properties, weight and sizes. PDMS is transparent, non-toxic, biocompatible [9] and cheap. Thanks to the strong covalent Si-O bond, it has a decent thermal stability (stable at up to 200°C), chemical resistance and has some inertness against chemical attack [10]. It is a widely used material in a lot of different applications including lubricating, caulking, as an antifoaming agent for food. PDMS is also present in some shampoos to make the hair shiny and slippery. This material has been the focus of an increasing number of studies since the end of the 90s thanks to the spreading of the PDMS lithography technique which allows an easy way to create microchannels [11] even if the first microfluidic channel had been realized before [12].

In lab-on-a-chip devices the PDMS is used as an elastomer, a polymer with a low Young modulus which means that it is easily deformed when a mild strain is applied on the material (figure 5). PDMS is composed of the monomer $[SiO(CH_3)_2]$ repeating several times to form the chemical $CH_3[Si(CH_3)_2O]_nSi(CH_3)_3$ with n the variable number of monomers bonded together to form a molecule of PDMS. The polymerization consists of mixing a cross linker to the liquid monomer then pouring it in a mold before curing it [13]. One can tune the properties of the solidified PDMS by changing the ratio between the PDMS and the curing agent. If the percentage of cross linker in the mixture is increased, the PDMS will be harder and less elastic which is useful to create very small microfluidic channels without collapsing them and to increase the soft lithography resolution [14]. The common ratio between the monomer and the cross linker is 10 to 1. The PDMS obtained can then be sealed with glass or any other material that can be activated via O_2 plasma activation. You can also seal a PDMS channel with another PDMS part.

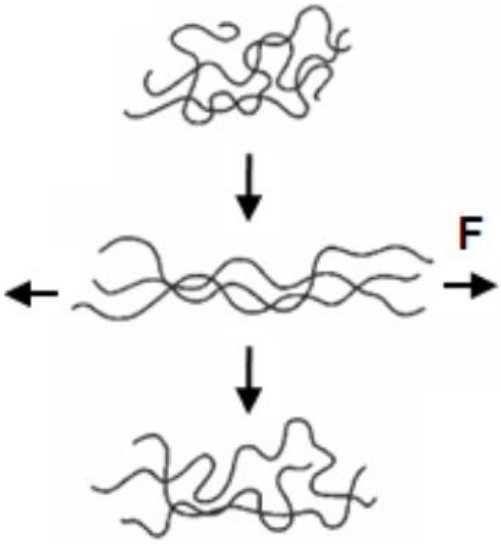

Figure 5: Performance of an elastomer under loading force and after its removal: plastic deformation of an uncrosslinked elastomer. [15]

PDMS can be processed in normal condition, is quite cost-effective and is permeable to gas which can be useful for cell culture inside the material [16]. Permeability can also be used to create a flow. One can indeed, create a microchannel without an exit but the evaporation of the liquid in the channel will create a suction that can create a flow in the channel. To do that, the microfluidic channel can be put under vacuum during 15 to 30 minutes. When the channel is brought back to air the PDMS will reabsorb the ambient air and create the passive pumping (figure 6 [17]).

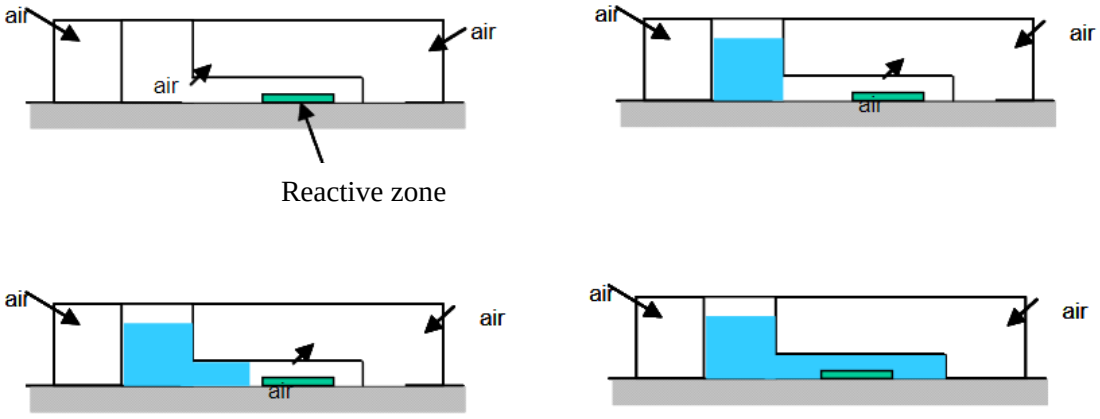

Figure 6: Effect of the passive pumping allowing the introduction of a sample inside a microfluidic device without any active parts. (1) Closed system with the reactive zone where we want to bring a liquid sample. (2) Sample insertion. (3) Sample aspiration. (4) Reaction. [17]

The fact than the mixture before the curing is liquid makes it very easy to cast on a lot of different molds which can be used to create structures that are smaller than 1 µm. By combining several PDMS parts, it is possible to create complex 3D microfluidic structures [18]. The transparency of the PDMS can be useful for several applications like colorimetric measures [19] and is very practical feature for directly assessing the phenomena that are occurring in the system.

It is easy to integrate valves in a PDMS channel to generate the flow. There different techniques to create these valves. For example, it is possible to sandwich a PDMS channel with PMMA fluidic channel that are used as pneumatic valves (figure 7 [20]).

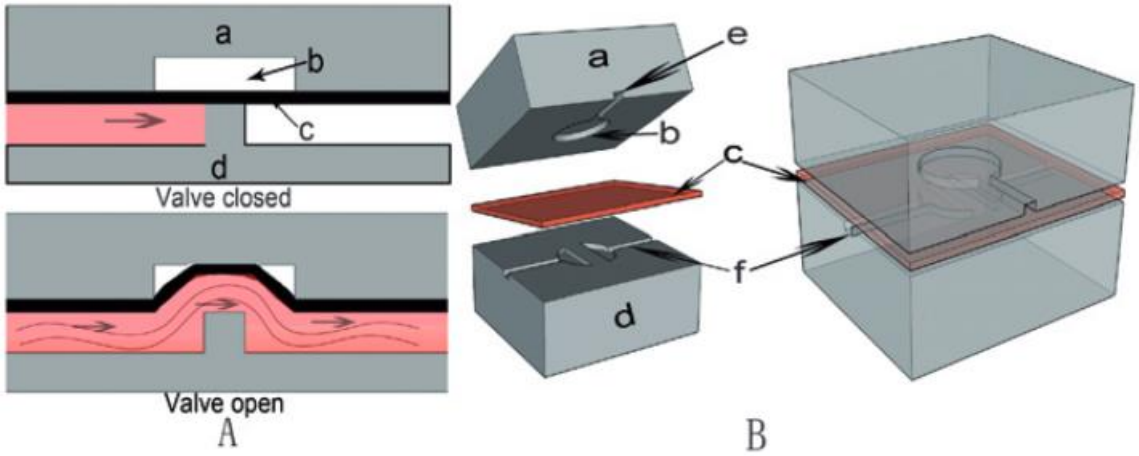

Figure 7: Cross-sectional views of a three-layer monolithic PMMA/PDMS membrane valve (A) and exploded and assembled illustrations of a single PMMA/PDMS membrane valve (B). a: PMMA pneumatic wafer; b: displacement chamber; c: PDMS membrane; d: PMMA fluidic wafer; e: pneumatic channel; f: fluidic channel [20];

PDMS is hydrophobic but the surface of the material can be altered to have a hydrophilic behavior for a limited duration thanks to different techniques like plasma treatment (see section 4.2.1) [21]. When PDMS is hydrophobic, it is easy to create volume-controlled droplet in the microfluidic channel [22]. Polydimethylsiloxane is not dissolved in most solvents, it is resistant to most acid and bases, only some strong acids and amines are not compatible with PDMS. For crossed linked polymers that do not dissolve, solubility is measured with the swelling of the polymer which can be problematic especially with organic solvents like diisopropylamine, triethylamine, pentane and andxylenes. To assess the effect of a solvent on the PDMS we can use different parameters that are linked to each other. The first one is the solubility parameter δ (or Hildebrand number) which is the square root of the cohesive energy value $c = -\frac{U}{V}$ where U is the molar internal energy (cal/mol) and V is the molar volume (cm^3/mol). Two entities with similar δ numbers will be soluble, for polymers it means that some swelling will occur. The second number S allows to directly quantifying the swelling. It is equal to $\frac{D}{D_0}$ where D_0 is the length of the PDMS sample before the contact with the solvent and D is the length of the PDMS sample in the solvent [23].

solvent	δ^a	S^b
perfluorotributylamine	5.6	1.00
perfluorodecalin	6.6	1.00
pentane	7.1	1.44
poly(dimethylsiloxane)	7.3	∞
diisopropylamine	7.3	2.13
hexanes	7.3	1.35
n-heptane	7.4	1.34
triethylamine	7.5	1.58
ether	7.5	1.38
cyclohexane	8.2	1.33
trichloroethylene	9.2	1.34
dimethoxyethane (DME)	8.8	1.32
xylenes	8.9	1.41
toluene	8.9	1.31
ethyl acetate	9.0	1.18
benzene	9.2	1.28
chloroform	9.2	1.39
2-butanone	9.3	1.21
tetrahydrofuran (THF)	9.3	1.38
dimethyl carbonate	9.5	1.03
chlorobenzene	9.5	1.22
methylene chloride	9.9	1.22
acetone	9.9	1.06
dioxane	10.0	1.16
pyridine	10.6	1.06
N-methylpyrrolidone (NMP)	11.1	1.03
tert-butyl alcohol	10.6	1.21
acetonitrile	11.9	1.01
1-propanol	11.9	1.09
phenol	12.0	1.01
dimethylformamide (DMF)	12.1	1.02
nitromethane	12.6	1.00
ethyl alcohol	12.7	1.04
dimethyl sulfoxide (DMSO)	13.0	1.00
propylene carbonate	13.3	1.01
methanol	14.5	1.02
ethylene glycol	14.6	1.00
glycerol	21.1	1.00
water	23.4	1.00

Table 1: [a] δ in units of $cal^{1/2}\,cm^{-3/2}$. [b] S denotes the swelling ratio that was measured experimentally; S) D/D0, where D is the length of PDMS in the solvent and D0 is the length of the dry PDMS [23].

As it is shown in table 1, water and some commonly used organic solvents like acetone have no or very little effect on the PDMS and can be used in microfluidic channels of this polymer without problems. However most organic solvents induce a swelling in PDMS, which is a drawback of this material.

Other drawbacks of the PDMS in comparison with other materials used for microfluidics are:

- It can't be easily mass produced with industrialization processes. Classic PDMS is not compatible with the two major methods for high throughput microfluidic device creation techniques: injection molding and hot embossing (see section 1.3.2.B.).

- The flow in the microfluidic channel as a function of the pressure difference between the entrance and the exit of the PDMS channel is not linear after a certain pressure (figure 8). This is due to deformation of the PDMS channel that changes the fluidic resistance of the tube.

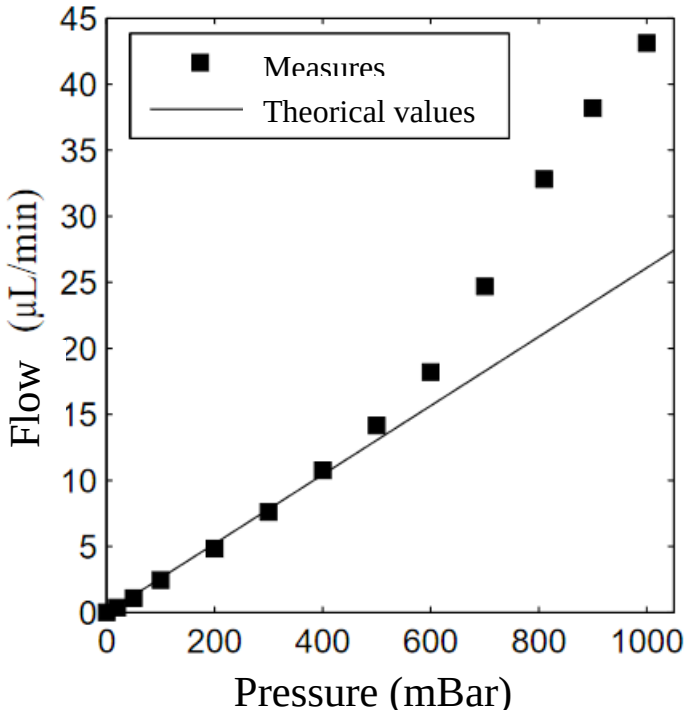

Figure 8: Measurement of the flow for different pressure differences between the entrance and the exit of a microfluidic channel [17].

- The PDMS channel can collapse for low aspect ratio (the ratio between width and height) [24]. This phenomenon was observed during my PhD studies and will be illustrated later in this manuscript (see section 3.4).

- The transparency of PDMS is not as perfect as glass, it shows a small amount of fluorescence.

- There is an adsorption problem with PDMS channels; they tend to suck up small, hydrophobic molecules from suspensions. After this adsorption the molecules cannot be washed away with water or detergent. This pH-dependent phenomenon could have an important effect on the outcome of drug screening tests [22].

- As said before, PDMS is hydrophobic but can be treated to have a hydrophilic surface. But these treatments are limited in time as PDMS revert back to hydrophobicity when it is exposed to air. Uncontrolled adsorption of proteins can begin to occur at that point [22].

- PDMS is not the best suited material for cells culture; it doesn't show very good cell viability because of a non-perfect cell adhesion on its surface and because of the leaching phenomenon: Some remaining uncrosslinked polymer chains can stick to the cells membrane [25]. And since water evaporate through PDMS, osmolality changes over time in cells culture [22]. However, this intrinsic drawback is not an issue for this PhD project.

To summarize PDMS is a very practical material to use for prototyping but it has also several drawbacks that have to be considered when creating a microfluidic device. Since there are actually a lot of different possible materials to select for creating microfluidic channels with different advantages and drawbacks for each one of them, PDMS shouldn't be the automatic answer. Sometimes it is a default choice when it is actually not the best-suited material for the targeted application.

1.3.2 Criteria for the right material – technology combination selection

For choosing a microfluidic material, several factors have to be taken into account. The material has to match with the manufacturing process which can utilize different technologies. The properties of the device and the process to obtain it have to be defined. For example, PDMS should not be used if the aimed production output per year exceeds a few thousands devices per year since this material is not compatible with high output technologies like hot embossing or injection molding. Furthermore the work environment is also important on the chosen process. Consequently, three main elements have to be considered, the material itself, the manufacturing process and the environmental context.

1.3.2.A Material properties

The wide variety of materials available with a broad range of mechanical, optical, chemical and electronic properties make the choice of the right material a difficult task but it also means that an optimal material exists for almost every given application.

- First the mechanical properties of the material should be considered, a stretchable material can be utilized for wearable devices [26] or create stretchable antennas for frequency tuning [27]. On the other hand a harder material with a higher Young modulus can withstand higher strains with lower deformations which are useful for high pressure procedures [14]. A material has also thermal properties that have to be considered. The thermal conductivity can be very important if the microfluidic device utilizes entities that are very sensible to high temperatures like cells or antibodies. The thermostability is also essential, especially for a device that works at high temperatures.

- The optical properties can also be important for the choice of the material if an optical signal has to be measured directly in the microfluidic reservoir (see section 1.4.2.A). Electrical properties should also be considered, especially if an electronic or a magnetic signal has to be measured in the device (see sections 1.4.2.B and 1.4.2.C).

- The chemical resistance has also to be compatible with the fluid that flows in the microfluidic channel. For example, acetone deteriorates PMMA channel but doesn’t affect a COC channel. The chemical activity is also important, especially if a surface treatment is necessary for the microfluidic device to fulfill its purpose.

- As mentioned in section 1.3.1 permeability to gas has to be considered and can be used to create a flow.

- Finally the cost of the material has to be considered for prototyping.

There is a wide choice of materials for the realization of microfluidic devices with different properties, advantages and drawbacks. Here is a non-exhaustive list:

Non polymers: Paper, Silicon, Glass,…

Polymers: Poly(Dimethyl)siloxane (PDMS), Cycloolefincopolymer (COC), Polycarbonate (PC), Polyester (PE), Poly ether ether ketone (PEEK), Polyehtylene terephthalate (PET), Polyimide (PI), Polymethylmetacrylate (PMMA), Polystyrene (PS), Polypropylene (PP), Polyvinyl Chloride (PVC), Thermoset Polyester (TPE),…

- Paper is very cheap, biocompatible, easy to fabricate and has interesting mechanical properties for microfluidic devices comprising flexibility, lightness and low thickness. It has also a high surface to volume ratio which is useful for increasing the number of entities that can be immobilized in the channel. Capillarity is easy on paper, so a passive flow can be implemented in a paper microfluidic system [30]. But it is also a fragile material that doesn't withstand high pressures so the throughput volume of a paper microfluidic device can't exceed a few µl per second. The fragility of paper makes these systems also very sensible to the harshness of the environment. Finally the fabricating process of paper microfluidic channels is not very well controlled which implies a certain inaccuracy on the result of the operation [31]. Fabrication techniques for paper are cutting, ink-jet etching or wax dipping.

- Silicon was one of the first materials used to create microfluidic channels [32]. It permits to create high precision microchannel, it has a good chemical and mechanical stability and also have a good conductivity that can lead to various applications. However, this material is not optically transparent and it requires a cleanroom to be processed with a real expertise in microfabrication. It is now widely replaced by polymers for most microfluidics applications.

- Glass, which was also used early to create microfluidic devices [32], is a versatile material in term of resistance to harsh conditions and precision of the resulted device. As silicon, glass is indeed resistant to a lot of solvents and high pressure strains. The main drawback of glass devices is the cost of their fabrication [33]. However a recent work on a combination of silicon and glass for making a cheap disposable device has been achieved [34]. As silicon, glass has been progressively replaced by polymers for microfluidics channels fabrication in the recent years.

- The polymers are widely used because they are usually cheap, robust with various properties (table 3). For example, different polymers do not react in the same way when put in contact with different chemicals as shown on table 2 for PDMS, PC, PE, PS and PVC. They can be used for prototyping but can also be compatible with large scale production. They don't always require cleanroom facilities like silicon. Most polymers can be separated in two categories: Thermoplastics and thermosets (PDMS is an elastomer; it is cured like thermoset polymers but shows elastic behavior) [35].

- Thermoplastics soften and become moldable when the temperature is higher than a certain point called “glass transition temperature”. This process is reversible; the material regains its initial properties and hardens when cooled off. Thermoplastics are compatible with hot embossing and injection molding process. Thermoplastics include: COC, PC, PE, PEEK, PET, PMMA, PS, PP, PVC,… These thermoplastics are characterized by three temperatures. The glass transition temperature T_g above which the once rigid polymer softens. The heat distortion temperature (HDT) is the temperature from which the material doesn’t keep a structural resistance and fall apart when a mechanical strain is applied. Finally the decomposition temperature (TD) is the temperature from which the polymer chains break apart and the material is denaturized. Typically, thermoplastics have a wide gap between T_g and TD which create a large process window where the material is soft enough to change its shape [36].

Table 2: A list of thermoplastic polymers that have been used for micro molding [37].

Acronym	Full name	Temperature stability [°C]	Properties	Structure
COC	Cyclo-olefine copolymer	140	High transparency	Amorphous
PMMA	Polymethylmethacrylate	80	High transparency	Amorphous
PC	Polycarbonate	130	High transparency	Amorphous
PS	Polystyrene	80	Transparent	Amorphous
POM	Polyoxymethylene	90	Low friction	Semi crystalline
PFA	Perfluoralkoxy copolymer	260	High chemical resistivity	Semi crystalline
PVC	Polyvinlchloride	60	Cheap	Amorphous
PP	Polypropylene	110	Mechanical properties	Semi crystalline
PET	Polyethylene terephtalate	110	Transparent, low friction	Amorphous/Semi crystalline
PEEK	Polyetheretherketone	250	High temperature resistivity	Semi crystalline
PA	Polyamide	80–120	Good mechanical properties	Semi crystalline
PSU	Polysulfone	150	Chemical and temperature resistivity	Amorphous
PVDF	Polyvinylidenefluoride	150	Chemically inert, piezo-electric	Semi crystalline

- Thermosetting polymers are irreversibly hardened by curing from a liquid state. After this curing step these polymers can’t be reshaped, they can’t be melt when heated and decompose at high temperature. Thermosetting polymers are not compatible with hot embossing and injection molding techniques. TPE, PI and SU8 are thermosetting polymers.

Table 3: Chemical resistance of common polymer substrate [38].

	Methyl-methacrylate	Poly-carbonate	Poly-ester (styrene alkyd)	Poly-styrene	Poly-vinylchloride	Silicones
Mineral Acids						
Weak	Good	Excellent	Good	Excellent	Excellent	Fair–good
Strong	Fair–poor	Fair	Poor	Excellent	Good–excellent	Poor–good
Oxidizing Acids	Attacked	–	Poor	Poor	Fair–good	–
Bases, weak	Good	Poor	Good	Excellent	Excellent	Fair
Bases, strong	Poor	Poor	Poor	Excellent	Good	Poor
Alcohols	–	Poor	Good	Excellent	Excellent	Poor
Ketones	Dissolves	Poor	Poor	Dissolves	Poor	Poor
Esters	Dissolves	Poor	Good	Poor	Poor	–
Hydrocarbons						
Aliphatic	Good	Poor	Good	Poor	Excellent	Fair–good
Aromatic	Softens	Poor	Poor–fair	Dissolves	Poor	Poor
Oils, Vegetable, animal, mineral	Good	Poor	Good	Excellent–poor	Excellent	Good

1.3.2.B Manufacturing processes

After choosing the right material for the microfluidic device, a manufacturing process must be selected in a wide range of possibilities. Different techniques change the cost of the operation, the time taken by the creation of one microchannel, the resolution of the microchannel and if it possible to integrate objects in it like electrodes. The process to create polymer microfluidic device can be separated in three main categories: create a master mold, directly fabricate the microfluidic channel with or without a photomask (figure 9 [36]).

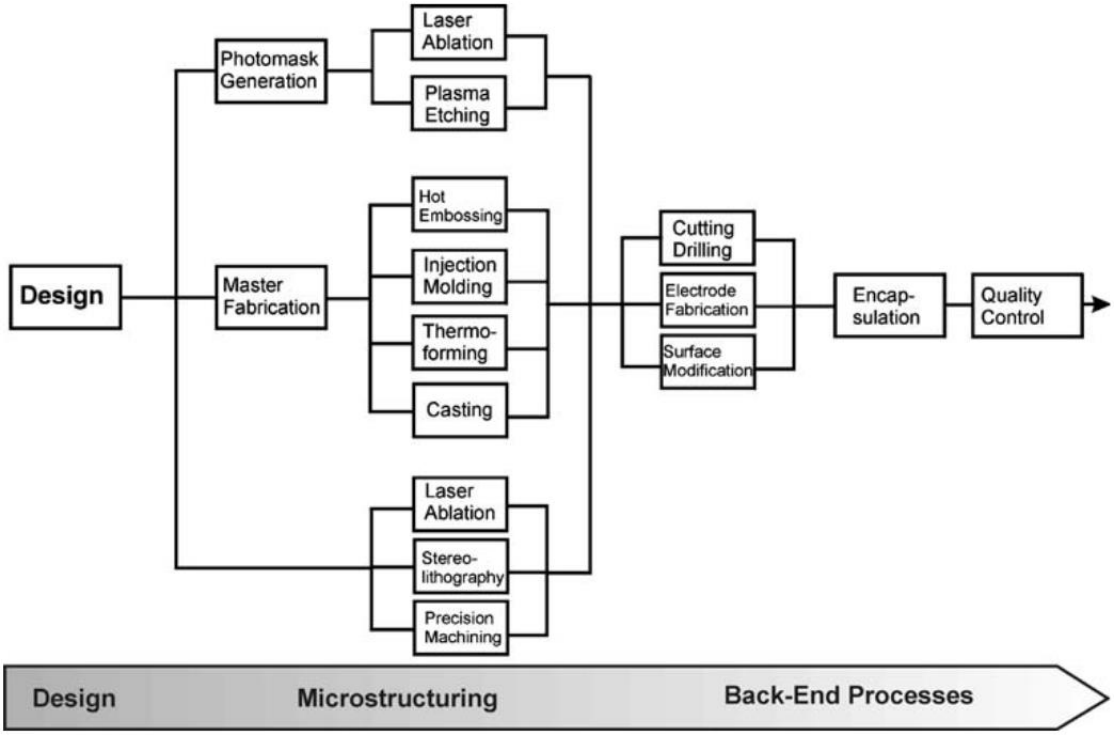

Figure 9: Process diagram of polymer microfabrication technologies [36].

The use of a photomask, a plate with opaque and transparent parts, to create a pattern is called photolithography (figure 10). The transparent parts of the photomask, which is place on top of the material where the microchannel is aimed to be formed, allow the light to pass. A photomask can be made of chrome or sometimes transparent and black plastic sheets.

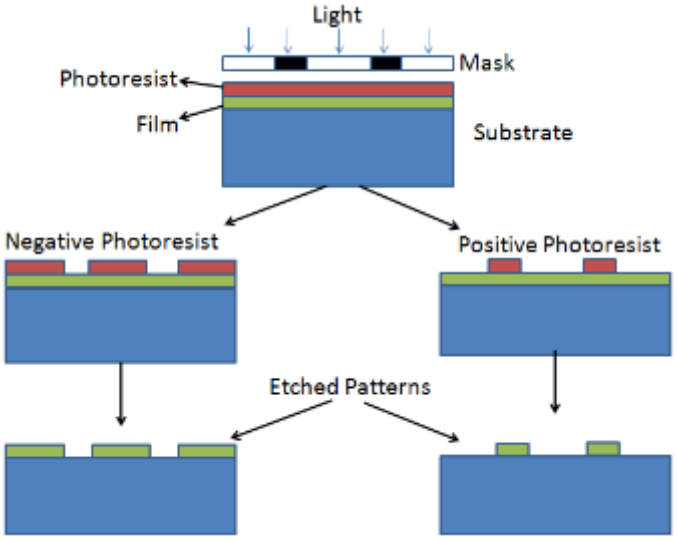

Figure 10: Photolithography principle using light sensitive photoresists [39].

To etch the pattern on the material, you can use plasma etching after protecting some parts using a positive or a negative photoresist (figure 11) or directly use a laser ablation. Negative photoresist is deteriorated by light whereas positive photoresist is solidified by it.

It is possible to etch a thermoset polymer like polyimide by applying on it a plasma composed of different gas. Plasma is a highly energetic state of the mater composed of chemically aggressive particles that react preferentially with organic materials. A metallic photomask should be placed on top of the material so that only the targeted areas are etched by the plasma. On figure 11, it is shown how it is possible to create channels with 50 µm polyimide foils coated with 5 µm copper. The copper is etched chemically on the areas that will form the microchannel after a photolithography step (the photoresist left is protecting the copper from the etching on the other parts of device). The plasma etching is then applied to carve the PI where it is no longer protected by copper. Through holes can be fabricated since both sides of the device are exposed to the plasma. Copper electrodes can be created by etching the rest of the copper except two discs that are then electroplated with gold. The channel is finally sealed by lamination with a PET/PE polymer which is heated at 135°C during 1 s [40].

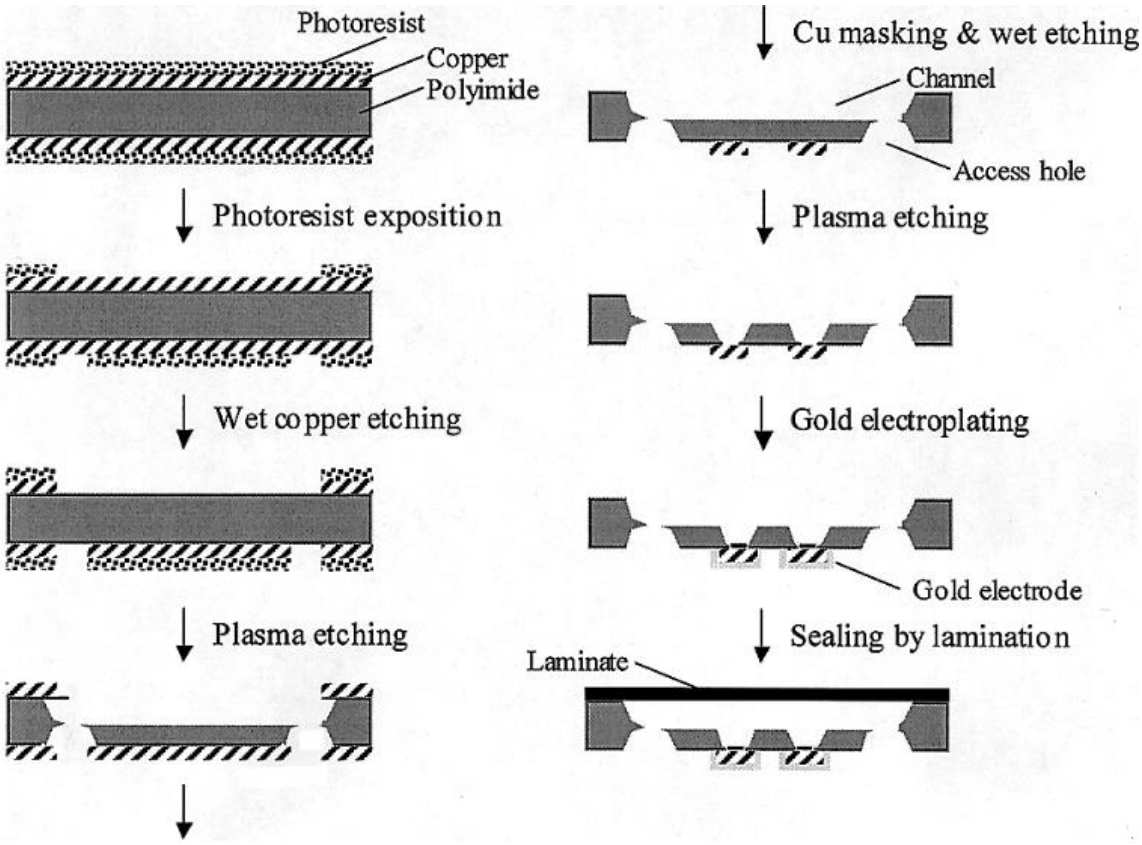

Figure 11: Schematic of the entire fabrication process of plasma-etched microchips with integrated gold/copper microelectrodes, sealed by lamination of a polymer film [40].

The plasma etching technique requires several steps and a cleanroom but it is possible to do a few samples at a time, which increases the throughput.

A laser can be used to carve the material where the photomask is transparent by evaporating the material with a high-energy focused beam. Laser ablation is also possible without photomask if the laser has a controlled trajectory on *x* and *y* and not a broad sweeping. This technique is quite rapid, can create complex 3D geometries on the sample and is well suited for rapid fabrication of small to medium throughput. UV lasers are especially effective for polymers. [41][42]. Laser ablation is well suited for thermoset polymers like PI, one of the reason is the fact that thermoset polymers are not compatible with hot embossing and injection molding because their glass transition temperatures (T_g) are usually too close to their decomposition temperatures (TD) [43][44]. However the laser ablation changes the surface chemistry and charge of the surface which can lead to variations of performances especially on electroosmotic flows [45]. The open microfluidic channel is then sealed with a substrate.

It is also possible to create a microfluidic structure by precisely focusing two high density laser light beams on a photoresist resin which solidify when exposed to light. The photoresist crosslink only if it is exposed by the two light beams, so it possible for one laser beam to penetrate the resin without inducing a solidification. Therefore, complex 3D structures can be created by moving the point created by the intersection of the two lasers. The photoresist is placed on a platform that can move on the *z* direction while the point of focus of the beams moves on the *x* and *y* axis. The process is simple and precise but it has a very low throughput and the choice of material is quite limited [46][47].

It is also possible to directly carve the material with precision machining techniques on polymers because of their rather high softness. The realized microchannel is directly the result of a CAD (computer aided-design) file but the process is actually long, from a few hours up to a few days and even if it is precise (down to about 30µm), it creates a notable roughness on the surface of the material [48][36].

For the other four techniques that can be used to create a microfluidic channel a master mold, that has the inverse pattern to the desired microfluidic channel, has to be created first before the replication fabrication can be performed. The master mold has to be as precisely fabricated as possible since the resulting microchannel formed from it (substrate) can only be as good as this master structure. The roughness of the master mold should be as limited as possible. The chemistry between the master mold and the substrate has to be carefully chosen and no undercut in the master structure itself can be allowed so that the separation between the master structure and the substrate can be possible [36]. Table 4 shows the common fabrication methods for the master structure. One of the more common techniques is to fabricate in a cleanroom a master structure with SU8 photoresist patterned by photolithography [49]. SU8 is a negative photoresist, which means that it is cross-linked when exposed to UV light; the resist not exposed is washed away. One drawback of this technique is that the formed master mold has a limited lifetime (number of time it can be used) after which it deteriorates.

Table 4: Overview on main master fabrication methods [36].

Microfabrication technology	Choice of geometry	Minimum feature size	Height	Total surface area	Aspect ratio	Lifetime	Cost	Commercial availability
Wet silicon etching	–	+	0	++	–	+	+	++
Dry silicon etching	+	++	+	++	+	–	0	+
Photoresist	+	++	+	++	++	–	+	0
Polymer casting (elastomer)	+	++	0	++	–	–	++	–
Optical lithography & electroforming	+	++	+	++	0	+	0	0
Laser ablation & electroforming	++	+	+	–	+	+	–	–
LIGA	+	++	++	–	++	+	–	–
(Ultra) precision micromachining	+	0	+	+	0	++	–	–
μ-EDM	–	0	+	–	+	++	–	–

Microthermoforming is the less used of the four replication techniques. A polymer foil is placed above the master mold and is heated to temperature T_e that should be close to the future temperature of the molding step T_m but should not be higher than the glass transition temperature T_g of the polymer. A vacuum is created at the same time in the chamber which is divided in two parts. One part above the polymer foil which is clamped at its ends and a second part between the master mold and the foil. The aim of the next step is to heat up the foil so that the temperature exceeds T_g and reach T_m. Then a pressure difference between the two parts is applied by pressurizing the space above the foil. After a certain time, the pressure is increased a second time so the molding can be as precise as possible. Finally the chamber is cooled and vented to atmospheric pressure so that the substrate can be retrieved (Figure 12 [50])[51]. The advantage of this technique is the simplicity of the approach. However the replication accuracy is not as good as the other techniques and some pattern errors can occur if the experiments parameters are not fine-tuned. A microfluidic channel is created in about half an hour which is rather quick but not if it is compared to the hot embossing and injection molding techniques.

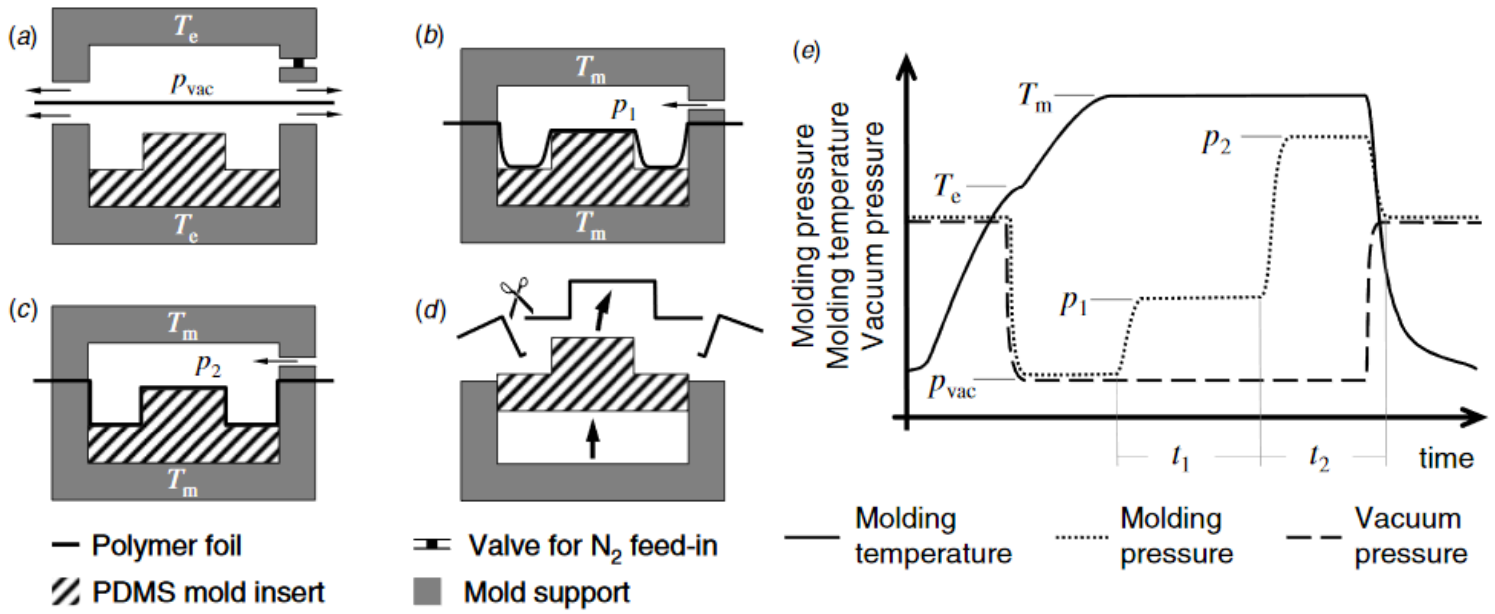

Figure 12: Process flow of microthermoforming. *(a)* Assembly in the process chamber, evacuation and heating. *(b)* Foil pre-stretching by pressurizing the space above the foil at pressure p_1 and molding temperature T_m. *(c)* Molding at pressure p_2. *(d)* Detachment and trimming after cooling and venting. *(e)* Schematic process chart [50]

Hot embossing (figure 13) is a well-known and widely used technique for the last 20 years in industry and academics [52][36][53]. Hot embossing allows low cost and flexible fabrication of polymeric microsystem with high aspect ratio. The process is rather simple and compatible with a lot of different materials especially thermoplastics.

1. The first step of the hot embossing process is the insertion of the polymer substrate (foil, wafer, bulk piece,…) in the system.

2. The master and the substrate are then heated higher than the glass transition temperature T_g of the substrate in vacuum.

3. The master mold is then pressed against the substrate with a force that depends on the design and the two materials of the master and the substrate.

4. The chamber is cooled down just under the T_g of the substrate and two pieces are separated.

5. Finally, the substrate is retrieved from the system.

The vacuum is critical for the substrate to be perfectly molded by the master mold otherwise air will be trapped between the two structures and the features on the substrate will be deteriorated. Moreover the temperature has to be homogenous in the chamber, the master has to have a good surface quality and a chemical compatibility is required between the master structure and the substrate to prevent sticking.

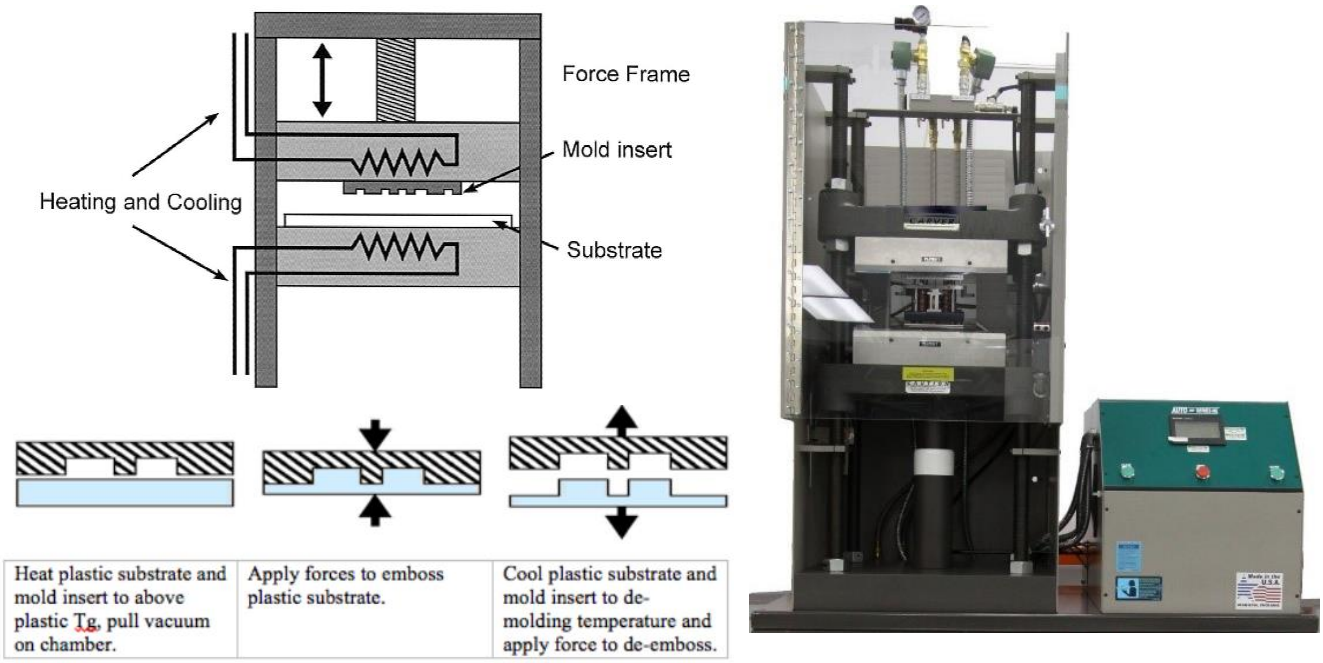

Figure 13: *(a)* Schematic drawing of the hot embossing equipment. [53] *(b)* SIMTech Microfluidics Foundry (SMF) hot embossing machine "Hot press". *(c)* Process summary of hot embossing (MNX – MEMS and Nanotechnology exchange).

In comparison with other technologies, the cost of hot embossing is very low for precise substrates with good aspect ratio. The combination of cost advantages with good performance makes hot embossing a very widely used technique for producing systems for medical applications. Furthermore, the internal stress applied to the material is rather low because no phase transitions occur during the process, this allows to avoid warpage in the material that can affect the optical properties of the system. Finally, hot embossing is even capable of doing nano-imprint lithography, microstructures that measure less than 100 nm [54] (down to approximately 50 nm [55]). There is an even faster way to create microfluidic devices with the same principle with the roll-to-roll hot embossing (figure 14). The substrate is a foil that is heated between hot plates and then pressed between two rollers; one of them has the master structure on its surface so that the features are replicated on the foil. This technique increase the throughput in comparison to normal hot embossing but it is less precise in the replication of the master mold patterns [56].

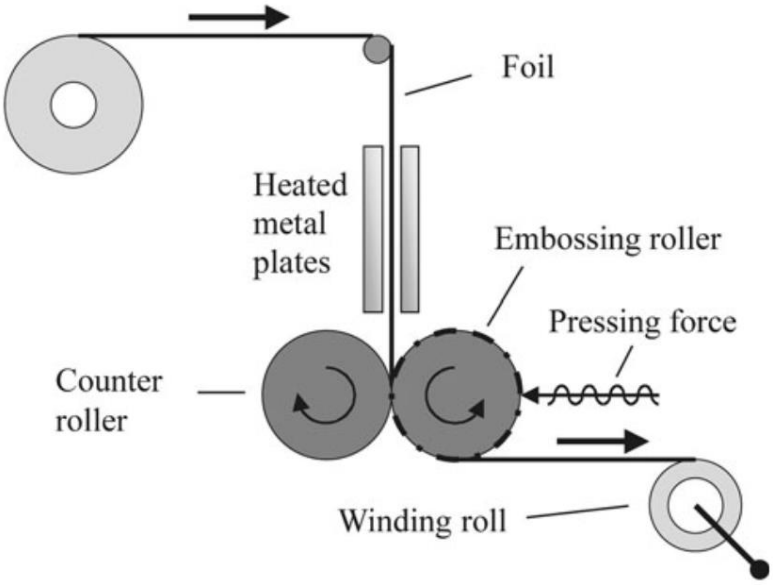

Figure 14: Principle of the roll-to-rool embossing process [56]

Injection molding is most widespread technique in the macroscopic world for polymer replications [36]. It can be adapted for the microstructure systems (figure 15) and is a very fast technique to replicate microfluidic devices. The master structure is composed of two pieces called mold inserts that are heated above the glass transition temperature and vacuumed so no air bubbles is stuck in the system. The polymer substrate is also heated so it can be viscous and inserted between the two mold inserts. The whole system is then cooled off below the glass transition temperature so the substrate hardens which is called the variotherm process. Finally the polymer is demolded. This technique has the advantage to create three dimensional structures to integrate directly fluidics interconnects in the substrate or through-holes. The major disadvantages of injection molding are the complexity of the process and the high cost of the equipment which explain the fact that this technique is not widely used in the academics. Furthermore the master molding tool has to be in a material that can withstand high mechanical strains and temperatures. Micro-injection molding is compatible with silicon, glass and a lot of different polymers [56][57][58][59].

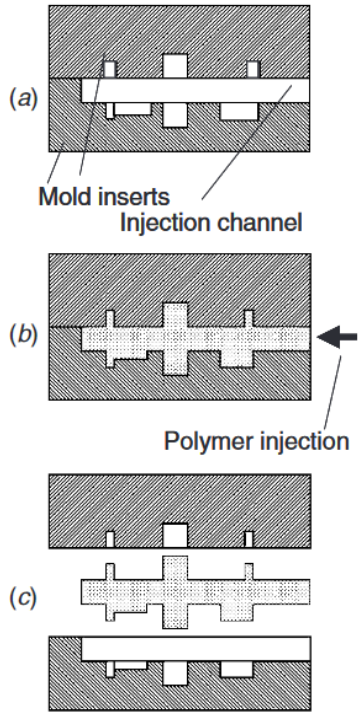

Figure 15: Principal process steps of micro injection molding: *(a)* the molding tool is closed, evacuated, and heated above the glass transition temperature of the polymer; *(b)* the polymer is injected into the tool, and *(c)* tool and polymer are cooled down and the polymer is demolded [58].

Another technique related to injection molding and hot embossing for microfluidics is the injection compression molding technique which is based on the CD (Compact Disc) process industry and produce what is known as "centrifugal microfluidics" as the flow is created by the rotation of the disk (figure 16)[60][61]. This technique is especially useful when handling biological sample because the movement is independent from the liquid properties like pH, viscosity or conductivity. Moreover the creation of the flow doesn't need a pump and is actuated solely with a motor which induce the rotation of the disc. This rotation applies a centrifugal force F_ω on the liquid that has to follow the microchannel (Figure 16). Cells can be separated from their surrounding medium because they are denser and subjected to a more powerful centrifugal force. This sedimentation technique can be used to separate the cells and the plasma of a blood sample [61]. Labs on a CD have other applications like cell lysis or cell culture [62]. Finally, it should be mentioned that CD process is the fastest way to create a microfluidic structure.

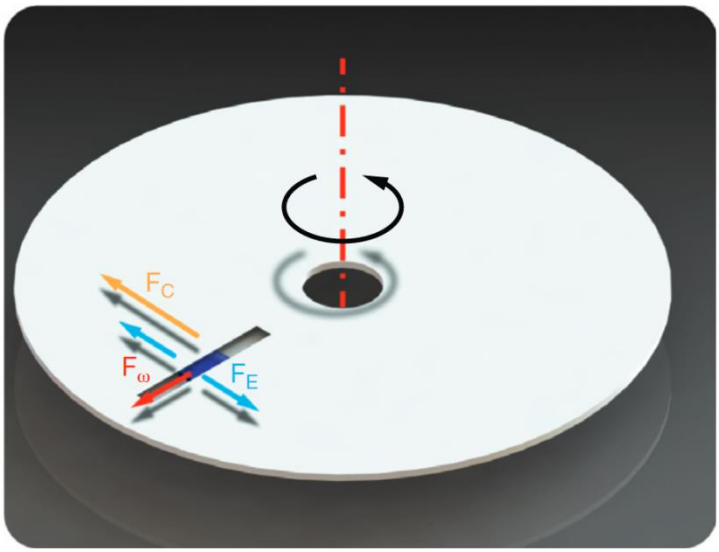

Figure 16: Forces acting on a liquid plug in a channel of rotating disc. F_c = Coriolis force, F_E = Euler force and F_ω = centrifugal force [61].

Finally, soft lithography, or casting, of elastomer is the most widely used technique and the most subjected to publications [63]. There are several advantages to this technique that can explain its popularity. It is cheap, simple to process, the elastomers have good material properties with interesting surface chemistries, and have a good replication accuracy [36]. It is usually used with the PDMS elastomer which is optically transparent, chemically inert and is an electric insulating material. The classical PDMS process follows these steps:

- The liquid PDMS is mixed with the cross linker with a ratio of 10 to 1. The stiffness of the cured material can be raised by increasing the cross linker part in the mix.

- This mixture is poured on the master structure.

- The system is then cured at 65°C during 2 hours.

- The PDMS substrate is demolded from the master mold and through holes are punched for the entrance and the exit of microfluidic channel.

- To create the microfluidic channel, the substrate is sealed to another material. PDMS can be activated with plasma O_2 so its surface is activated with oxygen and can then stick to a number of surfaces including glass or other polymers substrate.

However, other materials can also be used like polyurethane methacrylate (PUMA [64]) Norland optical adhesive (NOA [65]) which is a commercial photocurable polymer, or thermoset polyester (TPE [66]). These materials have a stronger stiffness than PDMS (~100 to 1000 times harder) (Figure 17 [67]). These polymers are cured by either temperature like PDMS or UV light.

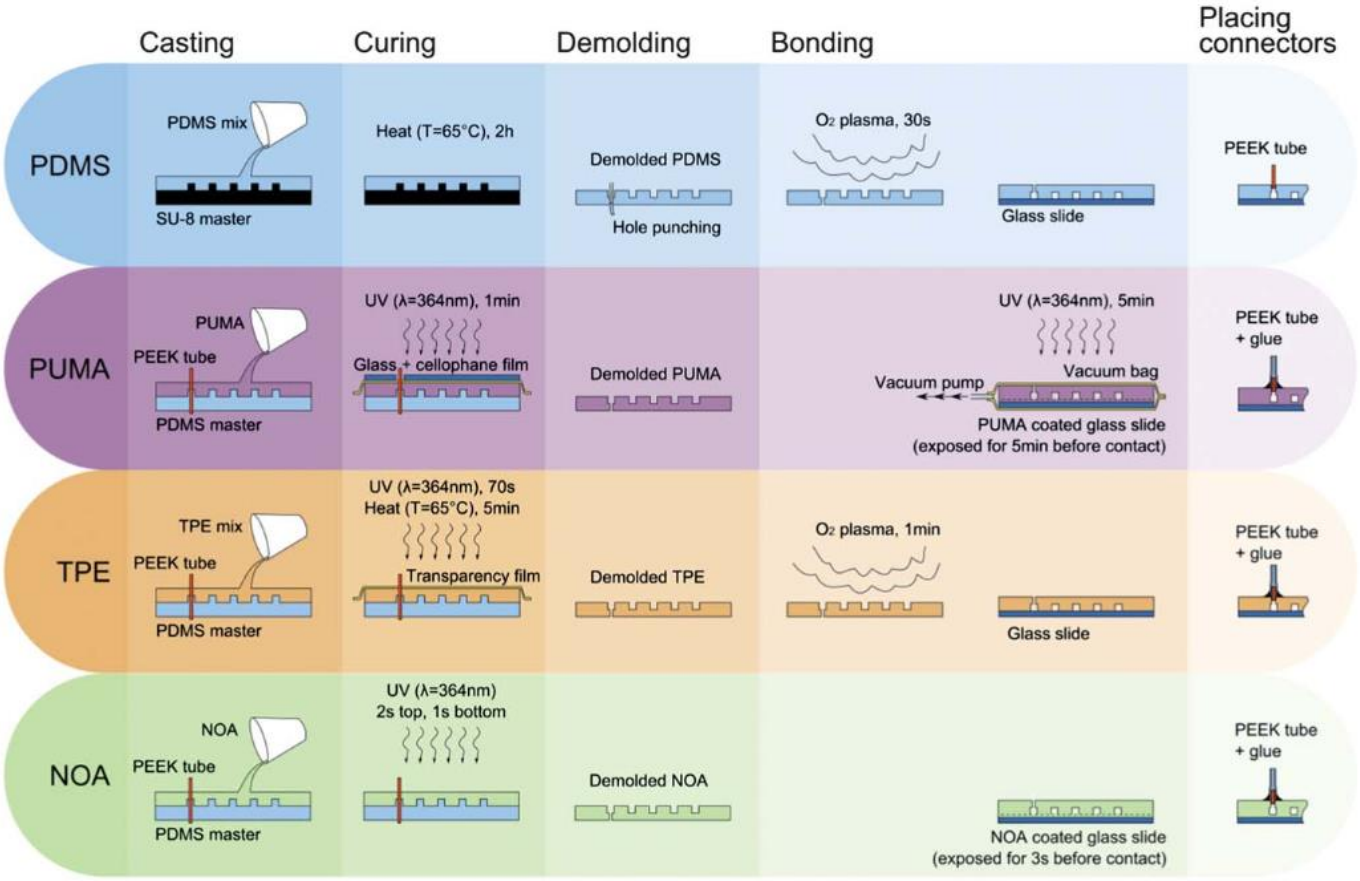

Figure 17: Protocols for fabrication of PDMS, PUMA, TPE and NOA chips. (i) PDMS microfluidic devices were fabricated using standard replica molding processes with a cross linker to polymer ratio of 1:10. As PUMA, NOA and TPE adhere to SU8 and make demolding impossible, a PDMS master mold with the same polarity as the silicon master was produced as indicated by Kuo et al. [64] (ii) The PUMA chips were prepared as previously described by Kuo et al., [68] (iii) TPE devices were fabricated following the protocol published by Fiorini et al., [66] (iv) NOA chips were made using a protocol adapted from Bartolo et al. [65] [67].

The advantages and disadvantages of a PDMS device are presented in the section 1.3.1. The casting technique is perfect for prototyping but is not compatible with industrialization because of its very low throughput.

Table 5: Comparison of the different molding technologies [36].

Process	Process and equipment setup	Equipment/ infrastructure requirements	Tooling requirements	Cycle time	Geometrical flexibility	Equipment availability	Production automation	Process availability
Casting	Simple (hours)	Very low	Very low(<2 k$)	Long (min–hours)	High	No special needs	Not existing	Yes
Hot embossing	Medium (hours–days)	Low (some water & 10 kW elec.)	Low (mold insert, 2–15 k$)	Medium (min)	Medium (2D)	Various suppliers	Medium	Limited
Injection molding	Difficult (days)	High (water & 20 kW elec., material drying & feed)	High (closed cavity mold, 20–150 k$)	Short (sec–min)	High (3D)	Various suppliers	High	Partly yes
CD process	Difficult (days)	High (water & 20 kW elec., material drying & feed)	High (closed cavity mold, 10–100 k$)	Very short (sec)	Limited	Medium	Very high	Yes

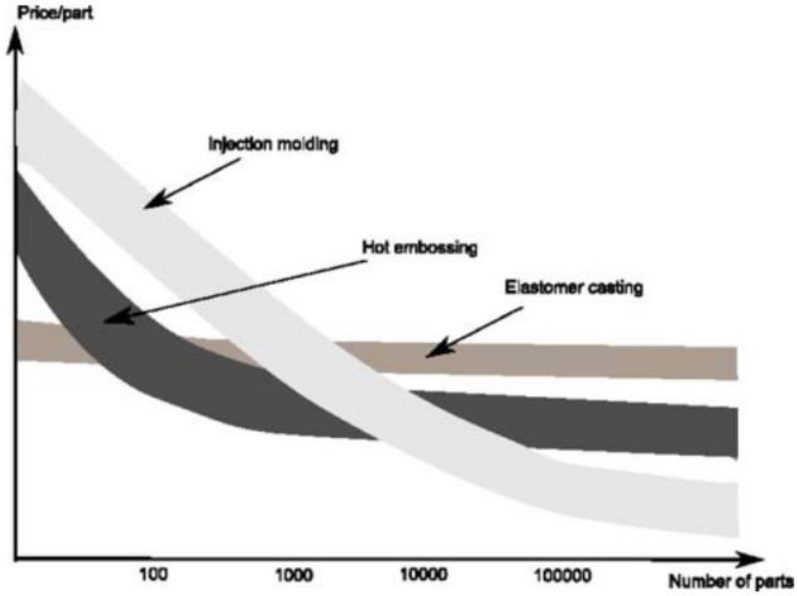

Figure 18: Economy of scale consideration for the polymer replication process (adapted from lecture notes of Prof. R. Zengerle, IMTEK, University of Freiburg) [36].

To summarize, the choice for the polymer replication technique should focus on the number of microstructure to be produced. CD process and injection molding require a larger initial investment for the setup than elastomer casting. If the aim of the process is to create a prototype for a proof of concept, soft lithography is the most obvious candidate but if the goal is to create a commercialized product, other replications techniques should be considered because of the economy of scale (figure 18). Hot embossing requires less costly equipment than injection molding but is more difficult to setup than soft lithography. For microfluidics to truly invest the market as widely commercialized products, the technologies developed should try to get away from elastomer casting and the automatic use of PDMS. The different molding technologies utilizing master structure is summarized in Table 5.

After the creation of microstructures, other steps, called back-end process, are sometimes required to create a functional microfluidic channel adapted to a precise application. For example, after a hot embossing creating microstructure on its surface, a substrate has to be closed by another material to form a microfluidic channel. Additional features can also be added like electrodes or surface modifications.

- Encapsulation is the step where the microstructure is sealed to create a closed microfluidic channel. Several techniques exist to make this encapsulation:
    - Adhesion is simplest technique that works with some polymer and especially with elastomer like PDMS. If the surface of the substrate and the sealing material are perfectly, a simple mechanical contact can be sufficient to seal the microchannel if no mechanical force or high pressure is applied on the channel. As mentioned above, plasma activation can be extremely effective to strengthen this sealing [63].
    - If two thermoplastic polymers are heated above their glass transition temperature and then pressed against each other, they can be bonded together. The process has to be carefully controlled as the

microstructures can be deteriorated when the temperature is above T_g [69].

- Ultrasound or laser can be used to apply energy on the interface between two polymers that are consequently sealed together [70][71].

- Two structures can be bound together by a third material that plays the role of an adhesive [72]. For example, PDMS can be used to stick two PMMA structures together [73]. The material used as adhesive should be viscous so it doesn't enter and clog the channel. The activation of the adhesive can be made by evaporation, heating, pressure (lamination) or irradiation by UV light.

- An alternative to the adhesive technique is to put a thin film of solvent at the interface between the structures to be bonded. Consequently, the materials should dissolve and solidify again after the evaporation of the solvent. The solvent should be applied carefully as it can damage the microstructures and can also present health risks [74].

- Cutting and dicing: A microstructure has to be separated from the rest of the substrate. Several techniques can be used to separate them like with a CO_2 laser or a wafer saw.

- Electrodes can be added to the microstructure with a number of different fabrication techniques that are sometimes inspired by microelectronics such as lift-off lithography technic or metal evaporation technique. With electrodes in a microstructure, it becomes possible to manipulate fluids or biological entities with dielectrophoresis [75].

- The surface chemistry of polymers can be largely modified to suit various applications. The surface chemistry can be modified as well as the hydrophilicity (with plasma treatment for example [76]) or the geometrical patterning of the surface. Thus, surface modifications can, for example, allow the binding of biomolecules on a polymer surface [77] (see chapter 4).

As we saw, there is a large choice of processes to obtain a microfluidic channel for a specific application. The choice of material for the application is directly linked to this process but the environmental context has also some importance.

1.3.2.C Environmental context

The third factor that has to be considered for the choice of the material-process combination is the environmental context.

The first thing to consider is the budget available for the microfluidics project. As said before, the materials and processes have different costs. PDMS casting costs a lot less than COC injection molding but the throughput and the properties of the device are different.

The second thing is the availability of equipment and facilities. For example, some processes like photolithography require a cleanroom to be performed with expensive machines (mask aligner, spin coater, reactive-ion etch …).

Most processes require knowledge and a practical formation. Sometimes, several batches have to be produced before a process is totally mastered.

Finally, the time allocated to the project is a factor to be reckoned with. Short projects should focus on soft lithography or process that do not require a master structure fabrication whereas long projects can take more time to elaborate and master techniques like hot embossing or injection molding.

Consequently, it is advised for the academics to work together and create collaborations and trainings so that microfluidics projects can be developed as much as possible and not be limited by the means and the resources of a particular laboratory. It is also important to consider collaborations between academics and industrialization actors as they can bring an expertise on high throughput process techniques and big equipment resources.

1.3.3 Comparison and summary

To summarize, the fabrication of a microfluidic is basically composed of a material and a process that have to be compatible to each other. This choice shouldn't be automatically PDMS with casting and should depend on the application, the resources and time available.

To make this difficult choice easier, table 6 and 7 present and compare the characteristics of different groups of materials.

Table 6: Comparison of materials for microstructuring [36].

	Silicon	Glass	Technical thermoplastics (e.g. PMMA, PC, PEEK)	Thermoset polymers	Elastomers
Microfabrication	Easy–medium	Easy–medium	Easy	Medium	Easy
Structuring processes	Wet and dry etching	Wet etching, photostructuring	Injection molding, hot embossing, thermoforming, laser ablation	Casting, lithography, etching	Casting
Possible geometries	Limited, 2D	Limited, 2D	Many, 2D, 3D	Mostly 2D, 3D possible	Mostly 2D, 3 D possible
Assembly	Easy	Medium	Easy	Medium	Easy
Interconnections	Difficult	Difficult	Easy	Easy	Easy–medium
Mechanical stability	High	High	Low–medium	High	Very low
Temperature stability	High	High	Low–medium	Medium	Low
Acid stability	High	High	High	High	High
Alkaline stability	Limited	High	High	High	High
Organic solvent stability	High	Medium–high	Low–medium	Medium–high	Low
Optical transparency	No	High	Mostly high	Partly	High
Material price	Medium	Medium–high	Low–medium	Medium	Low

Table 7: Rough guide to properties of construction materials used in microfluidic processing [31].

		Glass	Polymer	Ceramic	Silicon	Paper
Material Properties	Optical properties	+++	+	--	--	--
	Chemical Inertness	++	+/-	+++	-	--
	Surface properties	++	+/-	--	++	--
	Thermal stability	++	+	+++	++	--
	Biocompatibility	++	++	--	++	?
	Hydrophility	+++	-	?	?	--
User Advantages	Shelf life	+	-	+++	++	-
	Reproducibility	++	+/-	?	+++	-
Application Specific	Porosity (absorption)	+++	-	?	+++	-
Functionalization	Integration of Electrodes	++	+	--	+++	--
	Coating	+	+/-	--	+++	-
	Built-in Electronics	+	--	--	+++	--
Manufacturing	3D structuring	--	++	+++	---	--
	Price	-	++	--	--	+++
	Industrial infrastructure	+	++	+	+++	---
	Set up cost	+	--	--	-	+++

The desired number of devices per year, the resistance of the system, the accuracy of the result and the flow that a device can sustain are parameters that help deciding which material to choose with figure 19 and 20. Figure 21 and 22 can then help deciding which fabrication process that one can use by comparing the same characteristics [31].

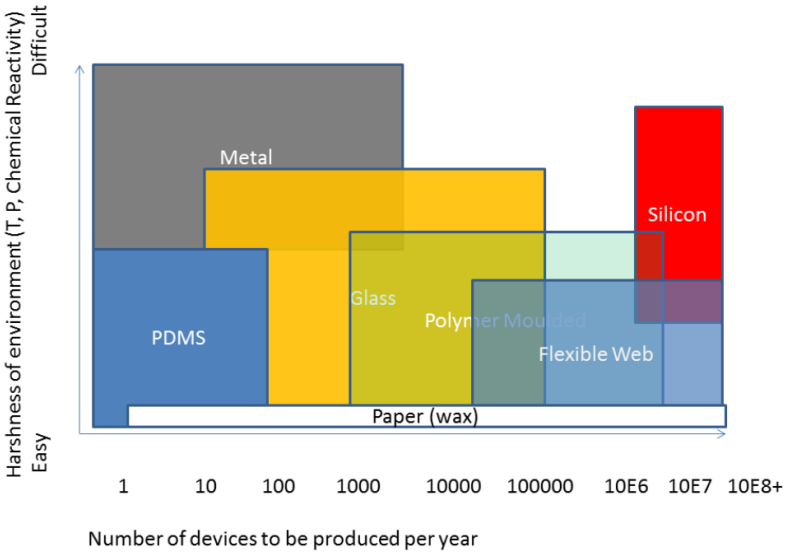

Figure 19: Material selection decision support chart 1 [31].

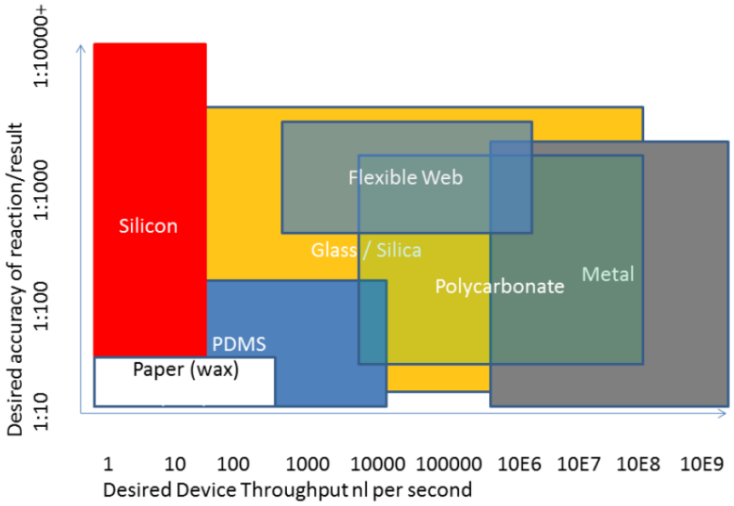

Figure 20: Material selection decision support chart 2 [31].

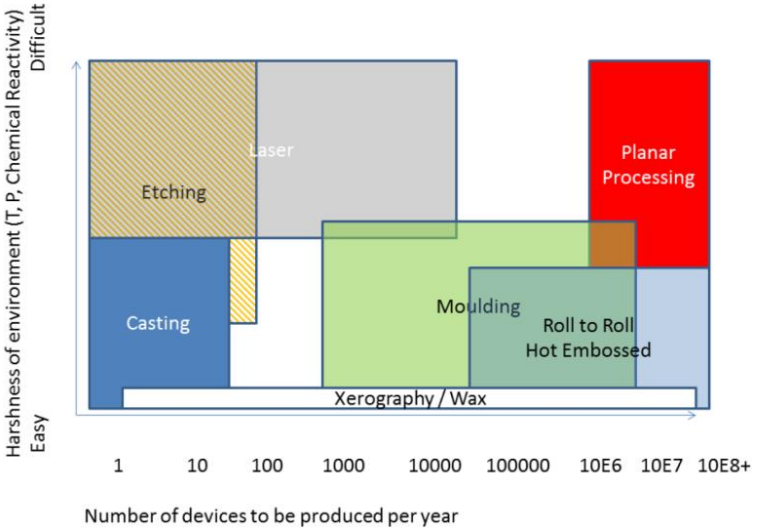

Figure 21: Material selection decision support chart 3 [31].

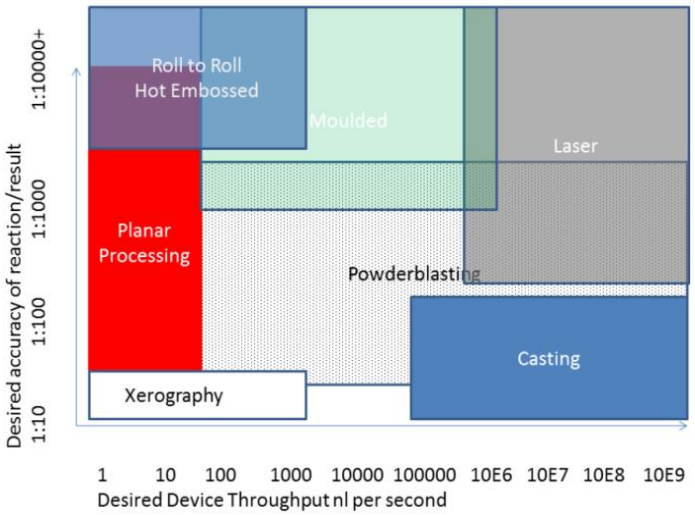

Figure 22: Material selection decision support chart 4 [31].

There are a lot of possibilities to choose from the thermoplastic polymers group with different characteristics. Table 2 in section 1.3.2 presented some of them than can withstand molding [58].

Other useful tables to choose the material can be freely found on the "Design for Microfluidic Device Manufacture Guidelines" edited by Henne van Heeren and Peter Hewkin [31].

As mentioned, the choice of the fabrication process with a specific material for microfluidics is difficult because of the huge amount of possible combinations. But it implies that for a particular application, there is an optimal material-process combo that has all the properties required. An effort should be made to discover and use this optimal combination instead of going right to PDMS casting in every case.

1.4 Lab-on-a-chip (LOC) immunoassays technologies

Immunoassays, the detection of a pathogen using antibodies as analytical reagent, are used in numerous applications: medicine, protection of the environment, agriculture, national defense for example. A pathogen is a substance that causes diseases, a micro-organism like a virus, a bacterium, a fungus, etc.

A lab-on-a-chip (LOC) is an integrated device that can carry out measurements with extremely small sample fluid volumes. The LOC pathogen sensing system for immunoassays should be sensitive with a low limit of detection (LOD), cost effective, size selective, simple to use and with a large dynamic range. Having a low cost and very sensitive detection system is rather challenging.

The miniaturization of immunoassays with LOC has a lot of advantages including small requirements for reagents and solvents, low cost, portability, low power consumption, versatility in design, and potential for parallel operation and for integration with other miniaturized devices.

A typical immunoassay uses the sandwich configuration where two antibodies are used (figure 23). The first antibody is bound to the system; the antigen (green circle in the figure) will chemically bind to its active paratopes. Then a second antibody with a label that the device can detect (yellow small circle), binds to the antigen. If the antigen is absent from the sample, the labeled secondary antibody is washed away from the device and the test is negative

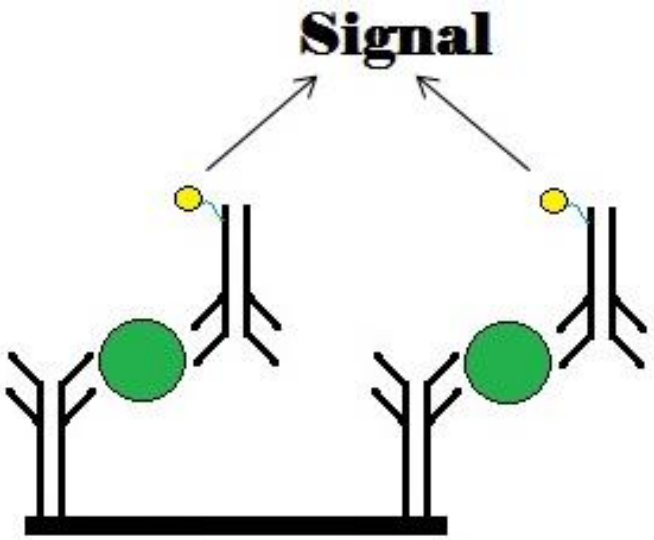

Figure 23: Sandwich immunoassay: antigen (analyte) in green, antibody (black) and label (yellow) [78].

1.4.1 Biosensors, principle and applications

Biosensors convert a biological signal into an electrical response that can be measured and analyzed. The biosensors can be used for pathogen sensing.

Bisoensors are composed of three distinct parts (figure 24):

- A biorecognition site that is composed of biomolecules which bond specifically to the targeted analyte that has to be detected. These biomolecules called bioreceptors can be antibodies, peptides, cells, nucleic acids (DNA and RNA),…

- Then the biotransducer part converts the biological response that comes from the biorecognition part into a measurable signal. It can be a photo detector, electrodes, coils,…

- Finally, the electronic system is responsible of the treatment and conditioning of the signal so it can be intelligible for the user of the biosensor.

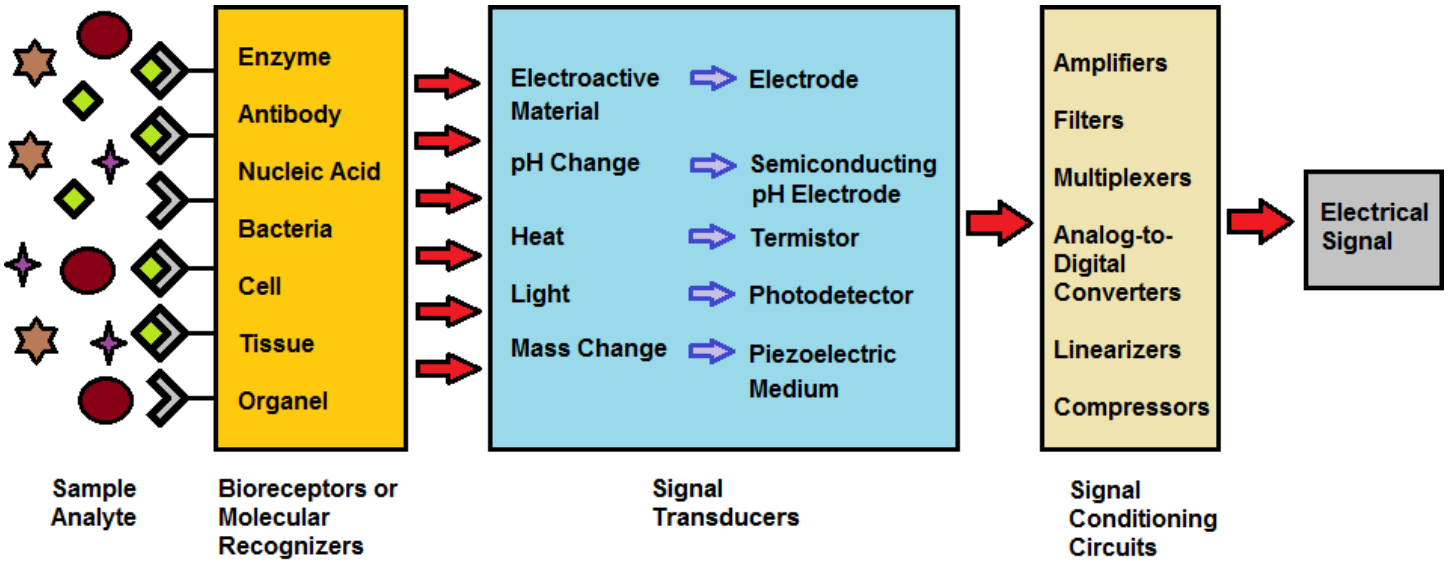

Figure 24: Most common types of bioreceptors, biotransducers and signal processing circuits [79].

Biosensors use the sensitivity and specificity of bioreceptors which make them very interesting for immunoassay, especially if they are highly specific, reusable and independent of environmental parameters like pH and temperatures. However, the fabrication of biosensor can be tricky since it requires interdisciplinary knowledge like chemistry, biology and engineering [80].

Biosensors have a lot of different applications like food monitoring or plant biology. This work is focused on the pathogen sensing use of biosensors for point of care (POC) applications.

1.4.1.A Biorecognition site

A widely used receptor is the antibody. An antibody is a Y-shaped protein normally produced by the immune system to bind to pathogens to neutralize them. There are a lot of different antibodies with distinct variable paratope, also called antigen-binding site, on the end of Y shape that will bind to a specific region of an antigen. Therefore an antibody is specialized to bond with a specific antigen which allows system using antibodies as bioreceptor to have low false positive, good precision and specificity. However antibodies are expensive and once it is stuck to its antigen, it is very difficult to separate them again so the detection can only be done once without changing the biorecognition site.

Another bioreceptor that can be used on biorecognition site is enzymes. The enzymes are protein catalysts than can be found in the body accelerating chemical reactions by transforming substrates molecules into products molecules. This process can be used by observing the changes in a sample caused by an increase of the products concentration or a decrease of the substrate concentration or by the chemical reaction itself. This result signal can be a release or uptake of gases like oxygen, a light emission, heat release, etc. This implies that the biotransducer is directly dependent to the kind of signal that has to be detected [81]. However, enzymes as bioreceptors have drawbacks. They are expensive because they are difficult to produce, isolate and purify [82]. Moreover the results are often unstable for the same measurements and change at different temperatures and pH. Finally, chemicals present in the sample can interfere with the measurements [83]. Some techniques exist to minimize these issues, therefore enzymes are widely used in a large variety of applications.

It is also possible to use deoxyribonucleic acid (DNA) as bioreceptor. DNA is usually composed of two chains that bind to each other to form a double helix thanks to a complementarity that creates hydrogen bonds between the chains. So the strategy to use DNA as a bioreceptor is to bind one chain on the biorecognition so the completing chain will bind to it [84]. Since it is the gene that is directly detected, these DNA detection systems are usually more precise than the antibody detection based ones.

1.4.1.B Biotransducer

Biotranducers transform the biological signal into an electrical signal and can be sorted in four groups of methods: optical, electrochemical, mechanical and magnetic.

1.4.1.B.a Optical methods

In optical biosensors, a light beam is created and sent across the sample or reflected on it. The measurement is made possible by the change of the properties of the light (color, intensity, etc.) after it went through the analyte. These methods of detection are often rapid, cheap, simple and sensitive. They are also often suited to work with microfluidic chips. However, optical methods are difficult to integrate in small lab-on-a-chip devices as coupling light into microsystems typically requires accurate alignment components [85] and there are often background interferences. Nevertheless, some devices with optical method biosensors are already on the market [86].

Fluorescent biosensors usually work by using fluorochrome molecules that are previously bonded on secondary antibodies. The analyte binds to the primary antibody to form a “sandwich” immunoassay. A light is emitted by a light-emitting diode (LED) source that excites the fluorochrome which reemits some fluorescent light that a CCD camera can detect. The intensity of the fluorescence is function of the quantity of the analyte present in the sample tested. This method can detect various diseases by detecting protein markers [87]. Fluorescent techniques are very precise but expensive with long incubation times and complex processes [88].

Colorimetric biosensors are the other widely used optical sensors. They rely on the analysis of the sample color to determine the quantity of analyte in it. They are widely used for diagnostics because of their simplicity, as the changing of color can sometimes be even noticeable by the naked eye. One common technique that relies on a colorimetric signal is the lateral flow assay method (LFA) which is used for pregnancy tests [89][90]. This system relies on the capillarity force to make the sample (urine in the case of pregnancy test) moves across the device, from the sample pad to the reaction area. During this movement, the sample passes the conjugate pad where it sweeps away colored antibodies. If the analyte is in the sample, a sandwich configuration forms on the test line creating a colored line that can be observed. Else, there is no color binding on the test line. Either way a sandwich forms on the control line with two antibodies even without any analyte. If there is no color on the control line, it means that something went wrong during the process (figure 25). Therefore, in case of pregnancy test, if both lines appear, it means that the person controlled is pregnant.

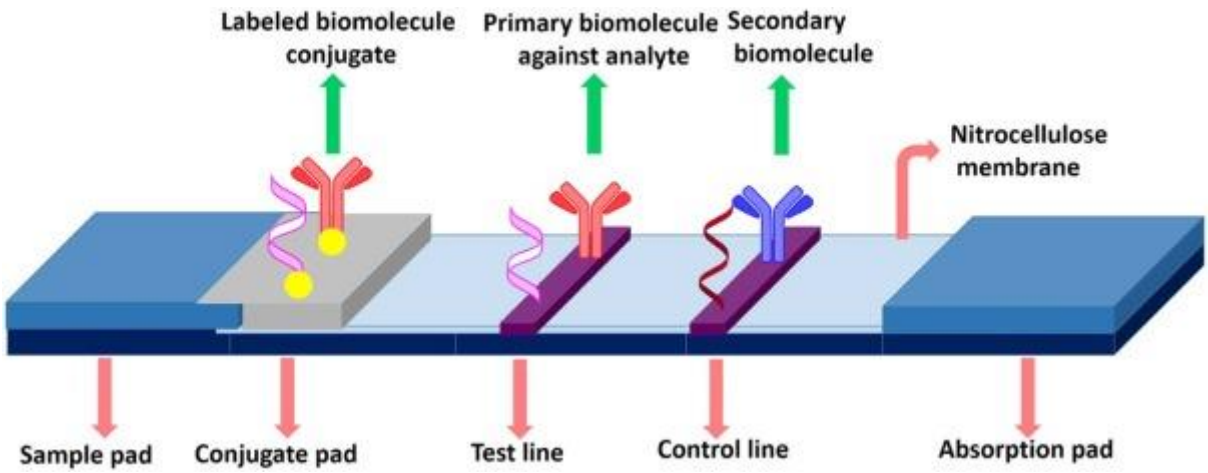

Figure 25: Lateral flow assay method [88].

Living organism bioluminescence can also be used to produce a biosignal. Some enzymes catalyze the reaction of cells creating this luminescence [90]. Chemiluminscence can also be used; it is an emission of light than happens during a chemical reaction [91]. These techniques do not require a light source but are limited to specific applications.

Finally the surface plasmon resonance (SPR) method measures the reflection angle of a light beam on metal film. If the analyte is grafted on the other face of the film, the angle of reflexion changes because of the creation of an evanescent wave [92]. SPR has a good sensitivity, is reliable and fast but is, on the other hand, expensive.

1.4.1.B.b Electrochemical methods

The conductivity of an aqueous solution depends on the ions that it contains. This can be used to create different methods of biosensing by applying an electrical current that passes through the solution. Each electrochemical biosensor is based on a different measurable electrical parameter: voltage, current, impedance and conductivity. Most of these techniques rely on enzymes that release electroactive products in presence of the analyte to be detected.

The potentiometric based sensors use two electrodes to measure a voltage. One electrode is a membrane and is the working electrode which changes its electric potentiel depending on the concentration of ions in the sample. A second electrode is the reference one. The potential is measured between the two electrodes and the obtained value is directly correlated to the concentration of analyte in the sample. This method, also called voltammetry, has a low detection limit and good signal-to-noise ratio [93][94].

The amperometric sensors work by applying a specific potential to the electrode and the current is measured as a function of time [3]. The amperometric methods are the most widely used because they are very simple, easy to fabricate, cheap and robust. But they are also susceptible to give false positive results because of non-specific binding of molecules and they are sensitive to pH changes in the sample solution [95].

As the analyte binds to the biosensor the conductivity of the sample changes on electrode surface. This change may be expressed in terms of impedance for impedance based sensors. The benefit of this method is that only one electrode is necessary as the reference electrode is no longer needed. This make the fabrication of the sensor simpler and easier to integrate. But these impedance based methods need to improve their sensitivity,

reproducibility and speed of process. These methods need more improvements to be used in commercialized immunoassays devices.

Finally the conductometric sensors measure the conductivity of a zone that contains charged entities at different frequencies. These methods can be coupled with electrophoresis so that a flow and the measurement of the analyte can be applied to the charged sample; therefore the system has two pairs of electrodes, one pair of sensing electrodes for the detection of analyte and one pair of feed electrodes to create the electrophoresis flow [96]. Other than the advantage of getting rid of the reference electrode, conductometric methods also have the advantages to use little power to work. However, they need difficult experimental conditions to work properly and are therefore not widely used.

1.4.1.B.c Mechanical methods

The aim of mechanical biotransducers is to detect the mass of the analyte or the frequency change of resonance of a rigid biorecognition site where the analyte (sometimes directly the pathogen to detect) binds [97].

A quartz crystal microbalance (QCM) is composed of piezoelectric quartz crystal where the biofunctionnalization takes place (figure 26). The piezoelectric crystal is oscillating at a precise frequency thanks to an applied electric current. The frequency of oscillation changes if particles are grafted to the surface of the crystal. In case of immunoassays it can be the pathogen that binds to an antibody. When the mass of analyte increases on the sensor, its oscillating frequency decreases proportionally. A washing step is needed to remove any molecules that are non-specifically bounded to the sensor.

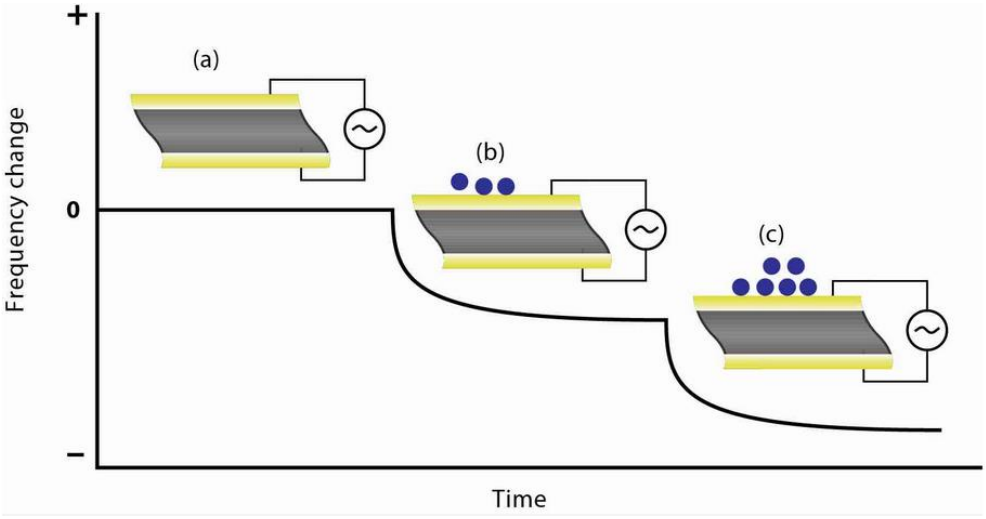

Figure 26: (a) The sensor is oscillating in free space and there is no change in the frequency of oscillation with time. (b) When particles begin to deposit onto the surface of the oscillator, the frequency of oscillation begins to decrease. (c) As more particles adsorb onto the oscillator, the frequency of oscillation decreases further [98].

This technique is very sensitive and can directly determine the amount of analyte but it is quite difficult to integrate because the sensor has to be totally dry at the moment of the measurement because it can affect the oscillating frequency. This renders this technique not suitable for portable lab-on-a-chip device.

Cantilevers, that are beams anchored at one end that can bend, can be used as biosensors. There two main pathogen sensing techniques involve cantilevers. One way is to implant antibodies on the surface of the cantilever that specifically bind to the aimed analyte (figure 27 [99]). The surface is then illuminated by a laser. The deflection of the light is measured; it indeed depends on the degree of bending of the cantilever which is directly related to the number of analyte in the sample [100].

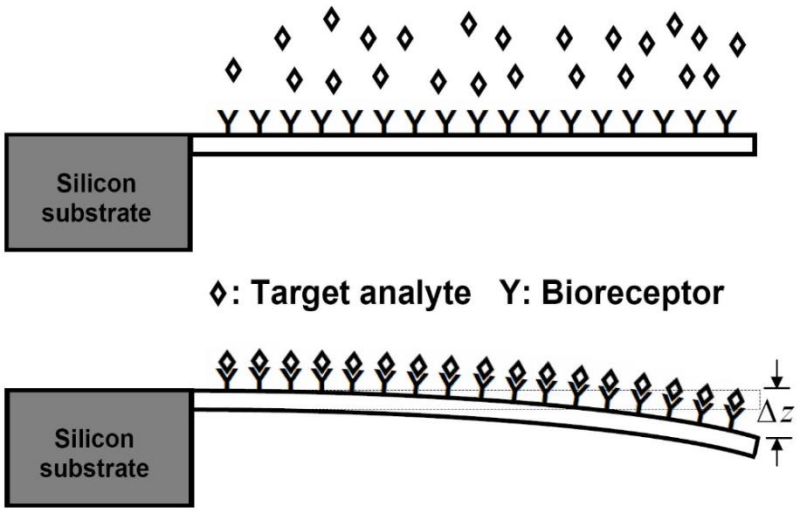

Figure 27: Working principle of a cantilever array biosensor. Cantilever is functionalized by depositing a bioreceptor layer (top); surface-stress induced deflection upon binding between target analyte and bioreceptor (bottom) [99].

Cantilevers can be integrated in portable lab-on-a-chip systems but it can suffer from parasite results during measurements and detection of multiple analytes are difficult with one device.

1.4.1.B.d Magnetic methods

Magnetic biosensors rely on the measurement of a magnetic field which is modified by the presence of the analyte in the tested sample. In LOC systems, magnetic beads are usually used that bind to analytes via antigen-antibody sandwich immunoassays [84]. The aim of the magnetic methods is to detect the magnetic nanoparticles (MNP) instead of directly the analyte.

One way to detect MNP is to monitor the change of magnetic permeability that is function of the change in inductance. The magnetic beads are inserted into a cylindrical coil changing the value of the relative permeability that changes the coil inductance.

The magnetic relaxation of the MNP can be detected and discriminated by several methods. For example, AC susceptometers use the Brownian relaxation tie to determine the size of the magnetic beads. The magnetorelaxometry method uses the Néel relaxation and determines if magnetic nanoparticle is bound to analytes or not [101].

When an external magnetic field is applied, charge carriers in a current-carrying conductor are pushed to one side of the conductor by the transverse force of this magnetic field due to the Hall effect. The charge buildup at the sides of the conductor generates a measurable electric field (or Hall voltage) with a direction perpendicular to both the applied

magnetic field and the current. The measurement of this voltage is the basic principle of the Hall effect magnetic sensors.

The electrical resistance of a material can change when a magnetic field is applied to it [102]. This phenomenon is used for two sorts of magnetoresistance based sensors: giant magnetoresistor sensors (GMR) and tunneling magnetoresistance sensors (TMR).

Diagnostic magnetic resonance methods (DMR) use the effects of the magnetic resonance of the magnetic nanoparticles (MNP) on their surroundings to detect them. MNP are used as proximity sensors to accelerate the relaxation rate of neighboring water molecules. If the magnetic beads are bound to a bioentity, it creates heterogeneities in the sample that can be measured and are directly related to the amount of analyte in it [103]

Finally, the frequency mixing technique can be used to detect MNP (see section 2.2.1)

Methods that use MNP have a lot of advantages in comparison to the optical, electrochemical and mechanical methods [104]:

- MNP have high contrast thanks to the fact that bioentities are not strongly magnetic.
- MNP can be functionalized by creating several binding sites on their surface, so that they can bind to several bioentities.
- Magnetic properties of MNP are stable for different pH or saline concentrations.
- They can be manipulated by magnetic field gradients and consequently can be sorted or can carry the bioentities that are binded to them [105].
- MNP are relatively cheap and can be made biocompatible for in vitro diagnosis experiments (it has to be evaluated case-by-case for in vivo processes [106].

These methods have also some disadvantages. The colloidal suspension can be difficult to stabilize as the MNP can agglomerate and change their magnetic relaxation. The magnetic nanoparticles can form nonspecific interactions with other entities than the aimed analyte.

1.4.2 Comparison table

The table 8 presents most of mentioned detection techniques with comparative comments concerning relative sensitivity, dynamic range, assay time, portability, simplicity and cost. It has to be noted that the mentioned notes are only there to get an idea about the “usual” performance of the corresponding technique and are not representative of the best possible results that could be found in literature. This comparison was made by Amine Rabehi [107] and adapt to make table 8.

Table 8: Comparison of important characteristics for different pathogen sensing methods. (97)

Method		Sensitivity	Dynamic Range	Assay time	Portability	Simplicity	Cost	Comments
Optical	Colorimetric	*	*	Rapid (minutes)	****	Very simple	$	Difficult for multiplexing. Must use preconcentration step for quantitative measurements
	Fluorescence	*****	***	Rapid to long (10 mins to > hour)	*	Complex	$$$	Very versatile (allows observing activity of target). Multiplexing possible. Extensive research is done to integrate the method
	Plasmonic	****	***	Relatively fast to slow (minutes-hours)	*	Complex	$$$	Multiplexing possible. Label free.
	Luminescence	***	***	Average time (> hour)	***	Simple	$$	Can be used to detect chemicals like heavy metals or for specific bacterial detection. Restricted detection to certain antigens.
Electrochemical	Amperometry	***	***	Relatively rapid (dozens mins)	****	Simple	$	Sensitive to environment (pH) possible nonspecific binding. Need for reference electrode.
	Voltammetry	***	**	Real time monitoring	***	Moderate	$/$$	Need of reference electrode, better performance when miniaturized
	Conductometry	**	**	Rapid (minutes)	****	Simple	$/$$	Good coupling with electrophoresis actuation. Low power consumption. Issue of low specificity and low SNR.
	Impedance based	**	NA	Moderate time	****	Moderate	$/$$	No need for reference electrode. Issues are nonspecific binding, reproducibility.

Method		Sensitivity	Dynamic Range	Assay time	Portability	Simplicity	Cost	Comments
Mechanical	Microcantiliver	***	NM	> 10 mins	***	Moderate	$$	Can be label free, can be coupled with optical detection. Issue with striction, multiplexing is very difficult.
	QCM	***	NM	> 10 mins	***	Simple	$$	Can be label free, low power consumption. Can be used to validate immunosensors fabrication steps. Difficult multiplexing and need of dry environment.
Magnetic	Relaxation based	** to ****	****	> 20 mins	**	Simple to complex	$/$$$$	Difficult to multiplex, not much integration attempts. Low background noise.
	Magnetoresistance based	****	***	minutes	****	Moderate to complex	$$/$$$	Possibility to multiplex. Extensive research for miniaturization. Requires clean room work. Issues with linearity.
	Hall effect sensors	****	****	minutes	****	Moderate	$/$$	Better when miniaturized, detection is localized. Compatible with CMOS technology
	Magnetic resonance	***	***	minutes	**	Moderate	$$	Volumetric testing possible. Issues with temperature drift. Needs high magnetic field.
	Frequency mixing technique	****	****	minutes	***	Simple	$/$$	Can be optimized for qualitative and quantitative multiassay, compatible with miniaturization technologies but not yet miniaturized. Possibility to multiplex.

Notes:

1. General reviews that study specifically one or many aspects of optical microfluidic sensors are given whenever possible.
2. References include examples and review articles that discuss methods characteristics.

1.5 Conclusions

In this chapter, we presented how microfluidic structures can be made for lab-on-a-chip immunoassays and what kinds of sensors are suited to be integrated in them.

Thanks to the progress in microfluidics design and fabricating techniques, LOC immunoassays are being developed for numerous applications like point-of-care diagnostics or bioterrorism protection. The huge choice of materials and manufacturing processes to create microfluidic channels for theses LOC is a great opportunity to have an optimal combination for a particular microfluidic chip.

Although the first material chosen for the microfluidic structure has been PDMS, PMMA and COC were then preferred to be compatible with an eventual industrialization and commercialization.

We also presented the different possible detection methods for most lab-on-a-chip devices with their advantages and drawbacks. One has to keep in mind that for an optimal biosensing method, the choice of the material and the choice of the manufacturing process for microfluidic structure are interdependent.

The miniaturized magnetic detection system, on which this PhD thesis is focused on, relies on the frequency mixing technique because of its sensitivity, rapidity of analysis, cost-effectiveness and its possibility of integration and miniaturization.

Chapter 2. Electromagnetic miniaturized detection device of magnetic nanoparticles in a microfluidic channel

2.1 Introduction

A magnetic detection prototype has been designed to detect superparamagnetic nanoparticles (SPN). The project began in a previous PhD thesis [107]. The experiment setup is composed of two main parts:

1. An electronic part that is responsible to generate the excitation magnetic field and to detect and process the response signal. The magnetic detection uses the frequency mixing method and planar coils. Efforts have been made to miniaturize these electronic elements that create and retrieve the magnetic fields.

2. A microfluidic part where the SPN circulate and the immunoassay sandwich is formed. The microfluidic microchannels have been first created with SU-8 master molds before this technique was replaced by a 3D printing technique. PDMS have been used for microfluidic channels but then COC and PMMA have been considered to replace the elastomer.

The magnetic detection uses the frequency mixing method [108] and planar coils [109]. The general aim of the project is to create a rapid, cost-effective, easy to use and sensitive portable immunoassay device (figure 28).

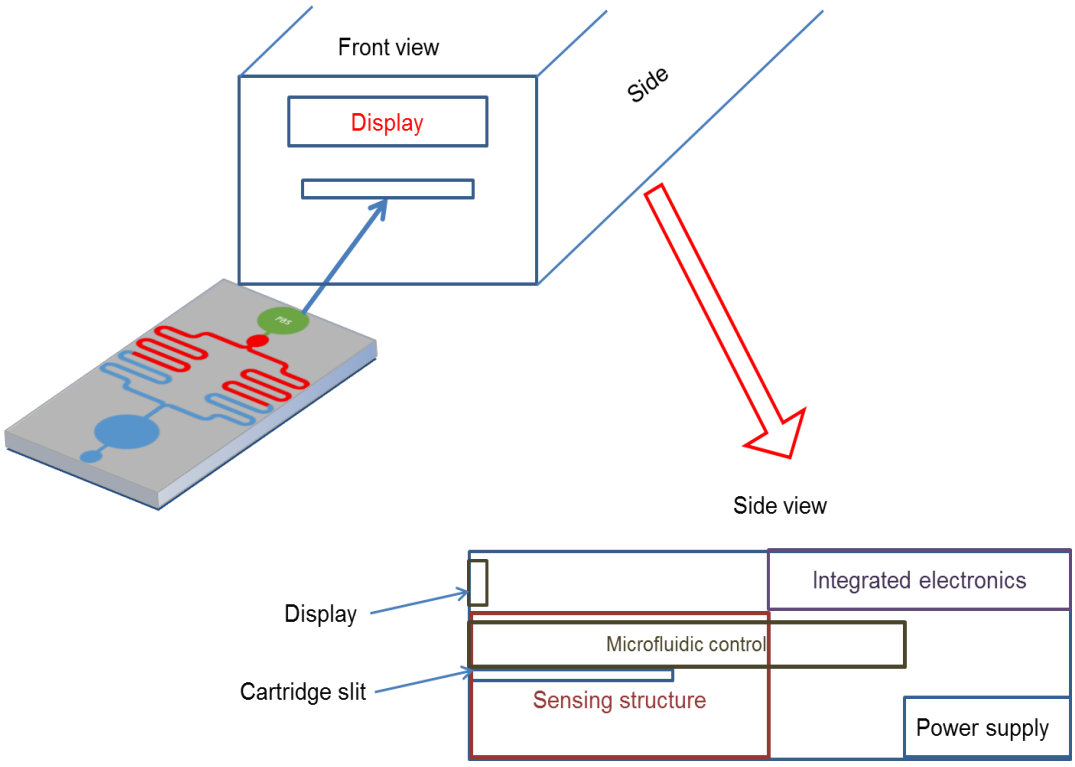

Figure 28: Schematic of the envisaged portable pathogen detection device.

2.2 Magnetic detection of nanoparticles

As presented in the section 1.4, the magnetic detection of nanoparticles can be used for LOC immunoassays.

The frequency mixing detection technique is a very promising technique for the detection and is suited to be integrated in a lab-on-a-chip immunoassay device as it has been proven to be very sensitive and reliable [108].

2.2.1 Frequency mixing technique

2.2.1.A Principle

The frequency mixing detection technique is used to detect superparamagnetic nanoparticles (SPN) [109]. When a magnetic particle is small enough (a few tens of nanometers), it shows superparamagnetic properties; it means that has a parametric behavior with higher susceptibility than classical ferromagnetic materials. Moreover, its magnetization curve is nonlinear, does not have a hysteresis and has a saturation effect (figure 29). Having a paramagnetic behavior means that the material does not show any magnetization in normal conditions but if a magnetic field is applied to it; it acquires a magnetization oriented in the same direction than the magnetic field because of a high statistical alignment of magnetic moments. Unlike ferromagnetic materials which present a hysteresis in their magnetization curves (a narrow hysteresis for "soft" ferromagnetic materials and a wide hysteresis for "hard" ferromagnetic material which means that they stay magnetized for a longer period of time), paramagnetic materials lose their magnetization when the external magnetic field is no longer applied. With superparamagnetic nanoparticles (SPN), it is the whole particle that is magnetically oriented by the externally applied magnetic field and not some random atoms as it happens in a classical paramagnetic material. The magnetization curve of SPN is directly related to their size [110]. The volume magnetization field M is the quantity of magnetic moment and is expressed in ampers per meter (A/m), it can be also expressed in emu per gram (1 emu/g = 1 $A.m^2.kg^{-1}$) for mass magnetization. The magnetic field strength H is also expressed in A/m or in oersted (1 $Oe = \frac{1000}{4\pi}$ A/m). The magnetization curve M = f (H) is the magnetization M as a function of the magnetic field strength H [111]. The magnetization curve is nonlinear as it saturates for higher H at a certain M value because the molecules of the material begin to lose their ability to increase their magnetic moment by the current in the field windings, so the magnetic strength curve begins to flatten out with increased current flow.

The magnetization curve of superparamagnetic nanoparticles usually follows a Langevin function [107]:

$$M(\mu_0 H) = M_s L\left(\frac{\mu_0 H m}{k_B T}\right) \quad (2.1)$$

Where:

- M_s is the saturation magnetization and $M_s = nm$ (n is the density of particles in the sample and m is the individual magnetic moment of each particle)
- L is the Langevin function $L(x) = \frac{1}{\tanh(x)} - \frac{1}{x}$

- k_B is the Boltzmann constant
- T is the temperature

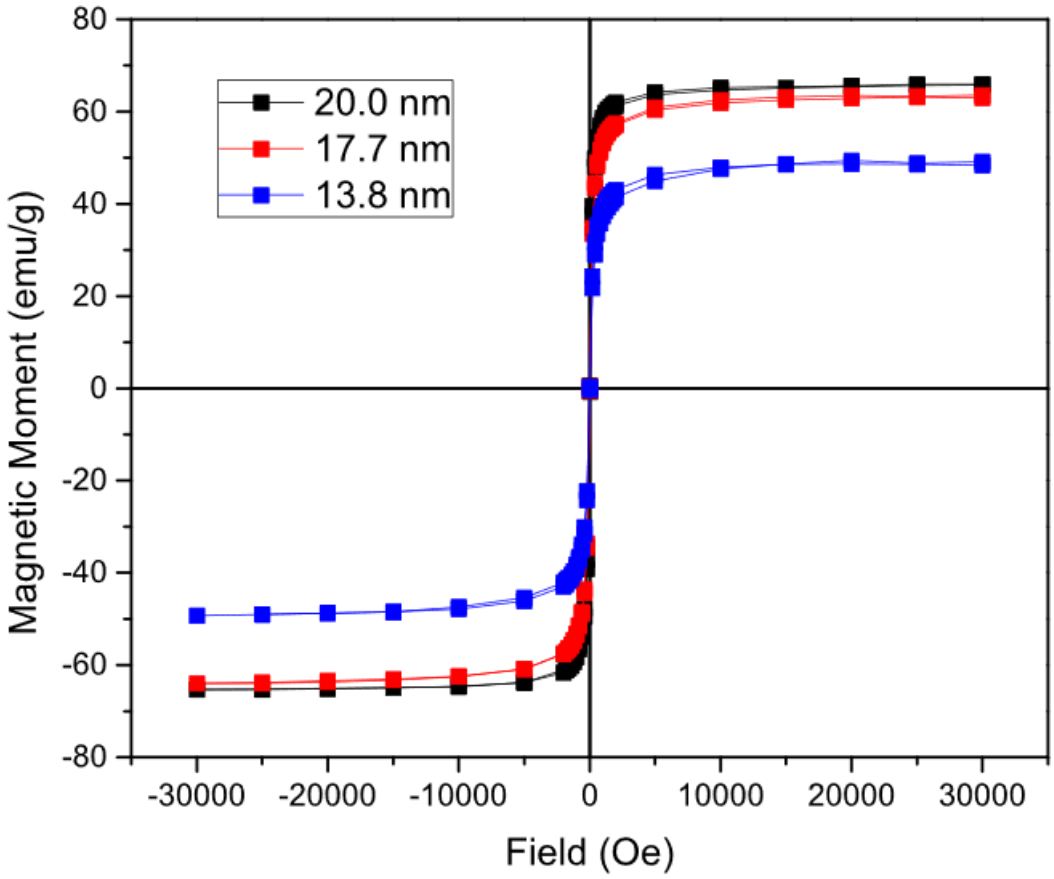

Figure 29: Magnetization of the nanoparticles coated with n-octylamine showing a slight hysteresis curve but with no coercivity or magnetic remanence. A significant increase in saturation magnetization is observed directly proportional to the size of the iron oxide nanoparticle [110].

The mixing frequency detection technique uses the nonlinearity of the magnetization curve of the SPN as a novel way to detect them [112]. The principle is to apply two magnetic fields of different frequencies f_1 (high frequency) and f_2 (low frequency) for magnetic excitations and then detect the response signal at a frequency representing a linear combination mf_1+nf_2 where m and n are entire variables (figure 30). The existence of this frequency is directly linked to the nonlinearity of the magnetization curve of the SPN [113] as the low frequency is used for the SPN to reach the nonlinear magnetization area while the high frequency signal probes this nonlinearity. Normal coils can be used to create the excitation signals but also to detect the response signal. To summary, if the superparamagnetic nanoparticles are present in the tested sample, the response signal has mixed terms, if there is no SPN in the sample, only the two fundamental frequencies f_1 and f_2 of the exciting magnetic fields appear in the response signal. The amplitude of the response signal is directly proportional to the number of nanoparticles in the sample. We usually use the frequency f_1+2f_2 to perform the measurement because the other mixed terms present a lower sensitivity for quantitative tests.

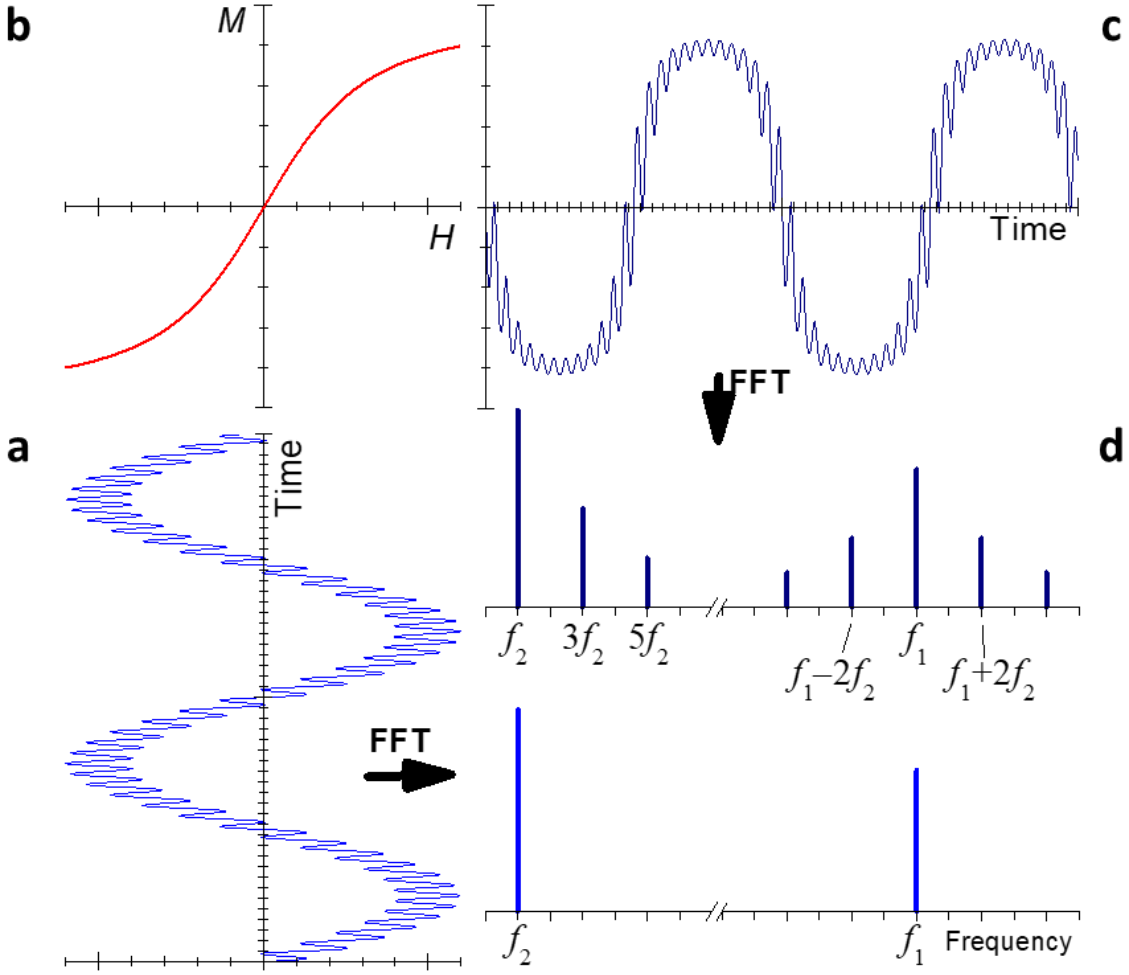

Figure 30: (a) The magnetic particles are exposed to a magnetic field consisting of two frequency components f_1 and f_2. The excitation frequency spectrum (b) exhibits two distinct lines at f_1 and f_2. Due to the nonlinear magnetization curve (c) of the superparamagnetic nanoparticles, the resulting time-dependent magnetization (d) of the particles saturates at higher fields, leading to higher harmonics and frequency mixing components in the Fourier-transformed response signal (e) [109].

The main advantage of magnetic immunoassay is its high selectivity, rapid quantification is also possible in native matrices, which is quite difficult for optical methods assays due to variations of the optical properties of the medium (turbid fluid,…) [109]. The frequency mixing is also sensitive, has a high signal to noise response because of very low biological noises and is relatively easy to implement. Furthermore, as the relaxation time of SPN is function of their size and composition, this can be used to discriminate different nanoparticles and the different bioentities that can be binded to them, allowing achieving multiplex detection [114]. However a drawback that has to be kept in mind is that no ferromagnetic or ferrimagnetic materials should be used next or in the mixing frequency detection device since this method is very sensitive to magnetic environment. For example, iron cored coils should not be used in order to enhance the magnetic field amplitude.

2.2.1.B Experimental device developed in the previous work

With a non-miniaturized device, studied and developed (figure 31) at Forschungszentrum (Institute of Bioelectronics) at Jülich in Germany, Hans Joachim Krause et al. developed a transportable magnetic reader device that uses the mixing frequency magnetic detection method for immunoassays. C-reactive proteins (CRP) detection in different liquids such as PBS buffer, human saliva, urine and blood serum was tested [115].

Immunoassays using frequency mixing techniques has also been used to detect the bacteria Francisella tularensis [116] and the bacteria Yersinia pestis [117]. The system is integrated and is able to create the excitation magnetic fields and detect the response signal [108].

The device is composed of a measurement head and readout electronics along with a display screen. The measurement head is composed of coaxial cylindrical excitation and pick-up coils. The excitation coils are composed of two coaxial solenoid coils (red and blue) that generate the low frequency and high frequency magnetic fields (f_1 and f_2). The detection coils which are doubled (yellow) detect the resulting magnetization. In order to enhance the signal to noise ratio, the resulting signal is the difference between the upper and lower detection coils as the upper coil measures the response at the sample while the lower coil is the reference coil with no sample in the middle of it. If no sample is put in the upper pick-up coil and if the lower coil is exactly similar to the upper one, the detected signal is equivalent to the noise level. This balancing (or gradiometry) technique helps to reduce the external interfering signals that induce noises and this method is suitable for relatively low operating frequencies [118]. Furthermore, the balancing configuration also prevents saturation of the first stage preamplifier. The sample holder is a commercially available ABICAP® column (AntiBody Immuno Column for Analytical Purpose). Finally, the system is shielded with aluminum shielding.

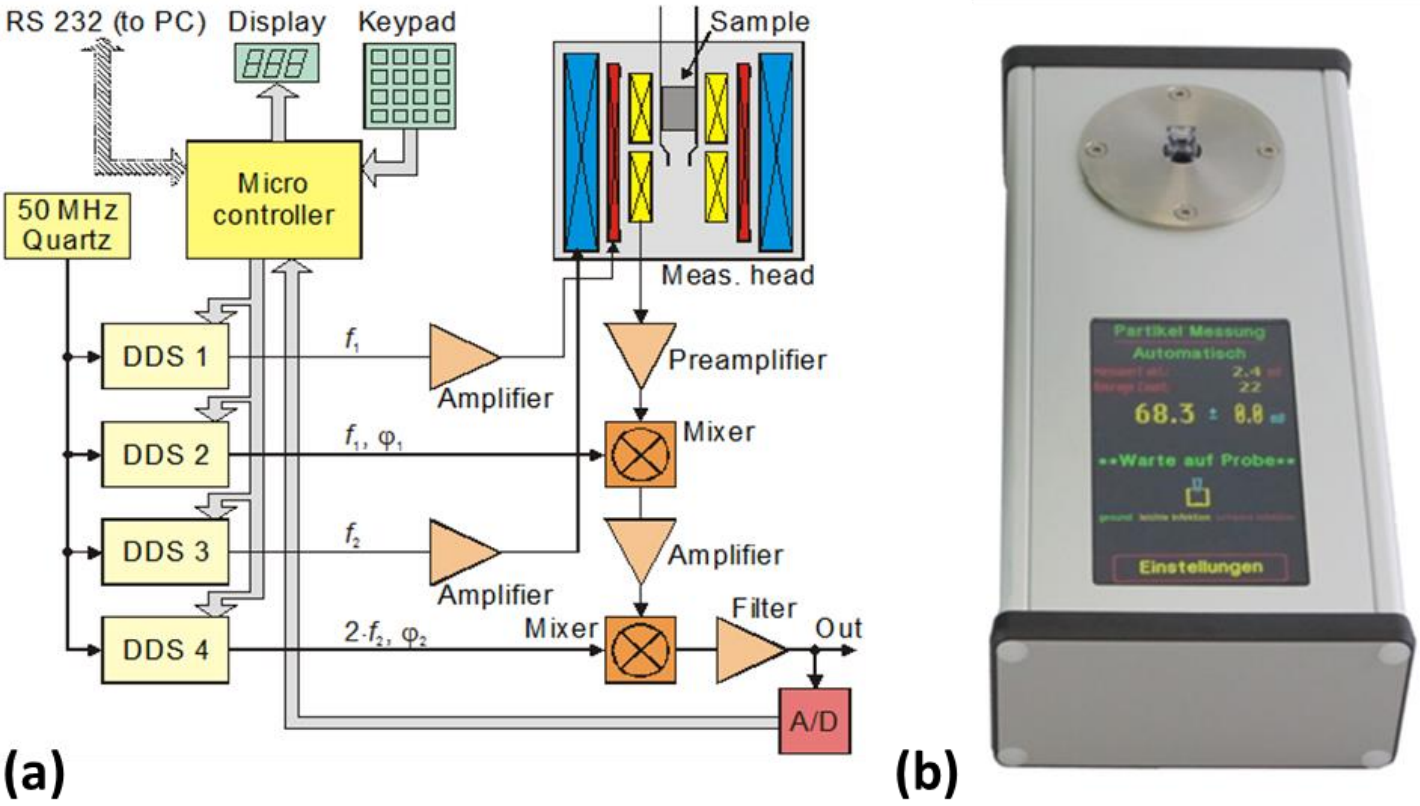

Figure 31: Schematics of the measurement electronics (a) and a photo of the device by the bioelectronics laboratory in Juelich, Germany.

A keypad allows the user to tune the two magnetic fields frequencies f_1 and f_2. Two signals at these frequencies are generated by direct digital synthesizers (DDS), amplified to the proper strength and then applied to two sets of coils to generate the two excitation magnetic fields. The signal response is picked up by the detection coils and then pre-amplified, demodulated by f_1, amplified again and finally demodulated by $2f_2$. The demodulated signal is filtered to enhance the response and finally converted into a digital signal by an analog-to-digital converter so it can be displayed on the screen of the device (figure 32).

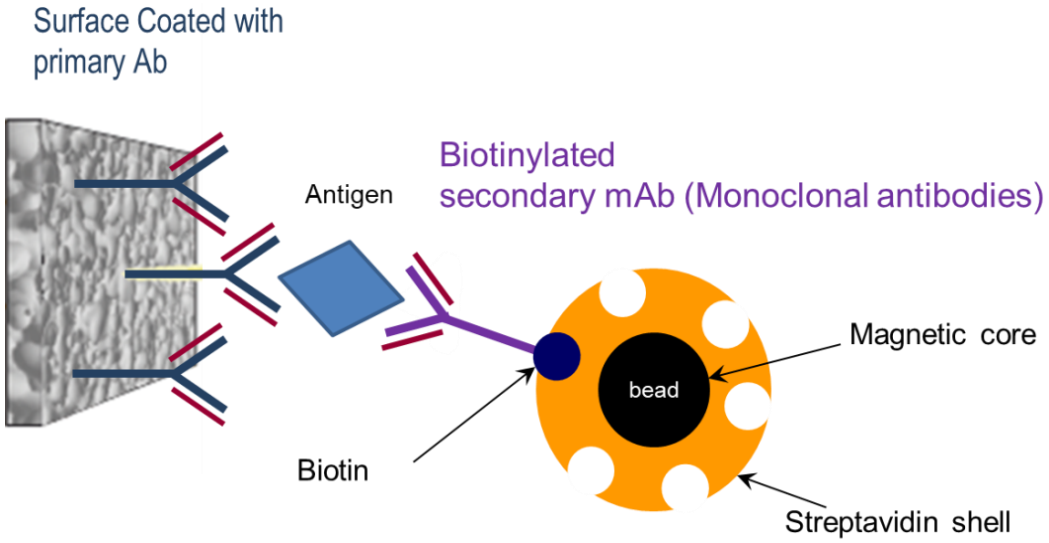

Figure 32: Magnetic detection immunoassay sandwich configuration

The pathogen sensing technique relies on the antibody-antigen interaction in sandwich configuration. As seen on the figure 32, primary antibodies (Ab) are bounded to the sample holder surface. In the mentioned device these antibodies are bonded to polyethylene ABICAP column filters. The antigens to be detected bind to these antibodies. Then superparamagnetic nanoparticles coated with streptavidin that hold biotinylated secondary antibodies target the antigen as well. This sandwich antigen-antibody configuration allows trapping the superparamagnetic nanoparticles in the system where the magnetic fields are applied.

Table 9 details the different steps that we have considered for magnetic detection immunoassays with a sandwich configuration. First the sample is injected into the device, if the sample is contaminated by the antigen it binds to the primary antibodies that are present in the system. Then, a second set of biotinylated antibodies is put in so they can also bind to the antigens. After that, magnetic nanoparticles coated with streptavidin are injected too so they can form a bioaffinity bonding with the secondary antibodies. Biotin and streptavidin have indeed a very high affinity and bind together almost instantly. After the sample injection step and after the secondary antibodies injection step, the system has to be washed by injecting phosphate-buffer saline (PBS) to remove any entities nonspecifically bounded to the surface of the system. Finally the magnetic measurement can be done for detecting the presence of the antigen in the sample.

The frequency mixing method with before-mentioned device shows a better sensitivity than the classically used enzyme-linked immunosorbent assay (ELISA) as it has a lower detection limit (6 ng/mL against 105 ng/mL for the ELISA method to detect grapevine fanleaf

virus). The ABICAP sample holder contains a volume of about 0.4 mL and the test takes about half an hour including the injection and washing steps [114].

The main objective of our project is to miniaturize the existing device, notably by using microfluidic channels, because of the following advantages:

- The test would take only a few minutes thanks to shorter reaction times.
- A LOC uses less sample and reagents because it only requires very small volumes
- A better sensitivity can be achieved by reducing the distance between the coils and the sample which lead to better magnetic excitation and detection efficiency.
- A smaller device decreases the energy consumption needed for the system which implies using smaller battery and improving the portability of the device.
- Parallel sample reservoirs could be integrated in one device which could lead to the development of multipathogens parallel testing by using different nanoparticles for different pathogens.

Table 9: Processes steps for magnetic immunoassays using magnetic nanoparticles in microfluidic reservoir.

Biological test steps	Explanatory illustration	Electronics
1. Injection of biological sample (blood, urine or saliva)		Micropump activation and control via embedded electronics
2. Incubation process (antigens react with primary antibodies immobilized on micro-fluidic channel)	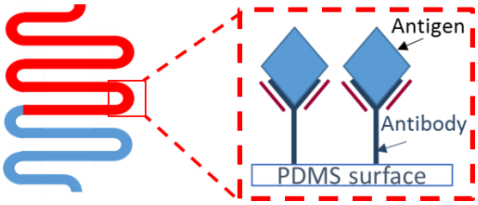	
3. Injection of biotinylated secondary antibodies	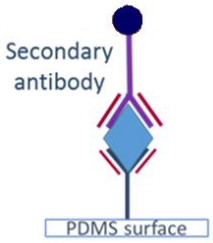	
4. Injection of magnetic nanoparticles (MNP) coated with streptavidin	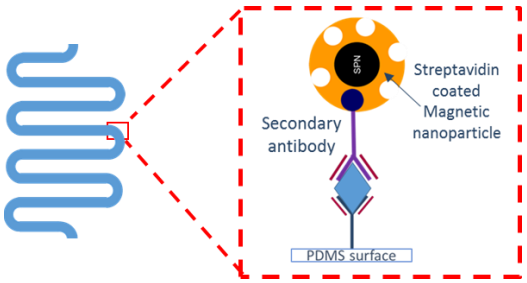	
5. Injection of PBS to remove non-specific absorbed nanoparticles. Measurement and quantification of antigen concentration through MNP detection	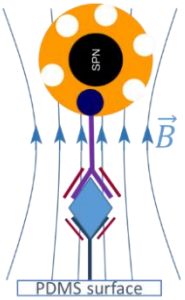	Electronic activation of the detection structure including excitation and detection coils using a microcontroller
6. End of test, display of results and cleaning or disposal of the microfluidic sample holder		1. Signal processing using a microcontroller and display of the result. 2. Micropump activation to clean microfluidics channel or prepare for sample holder ejection.

2.2.2 Developed electromagnetic and microfluidic instrumentation

We developed a miniaturized superparamagnetic nanoparticles detection device prototype that uses planar printed circuit board (PCB) coils and microfluidic channels. An experimental setup has been set up to generate the excitation signals, to receive and process the response signal and to create a flow in microfluidic channels. The aim is to realize a rapid, easy and cost-effective, portable pathogen detection device.

2.2.2.A Multilayer planar PCB Coils

Planar coils allow a system to be smaller than with normal spiral cylindrical coils. A PCB/microfluidic prototype has been developed in our laboratory. The structure is composed of 3 copper coils as all used materials have to be purely nonmagnetic. Two coils emit the electromagnetic field, one for low frequency and the other for high frequency, the third one is the detection coil. These coils are contained in two PCB structures (100×40×1.55 mm^3) surrounding the serpentine like microfluidic channel (12×12 mm^2) which can contain 14 µL of magnetic nanoparticles suspension. The coils are composed of four layers each; the tracks are 100 µm wide with an inter-distance of 100 µm. Each layer of track has a thickness of 35 µm. The emitting coils have a radius of 13 mm (60 turns per layer) and the detection coil has a radius of 10 mm (46 turns per layer). Because both the excitation and pick-up coils are made in the same PCB, we had to balance the above-mentioned criteria for proper magnetization and detection. The distance between the PCBs is 2.4 mm and the distance between the detection coil (lower PCB) and the microfluidic chamber is 1 mm. There are two sets of coils as one of them does the sample measurement and the other does a reference blank measurement. The result signal is the subtraction of these two measurements which leads to the removal of external noises. Air cored coils are used in many applications, including industrial, geophysical and biomedical applications [119]. The coils are arranged as presented on figure 33. Other prototypes were made using different order for the coils but the results obtained have been better with this configuration [107].

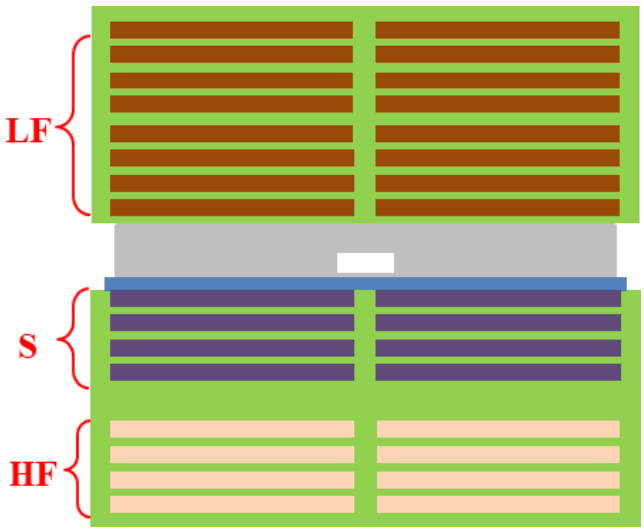

Figure 33: Schematic design of the PCB coils. LF are low frequency excitation coils, HF are the high frequency excitation coils and S are the sensing (or pick-up) coils. The grey (PDMS) and blue parts (glass) represent the microfluidic structure between the coils where the tested sample flows. This figure is only half of the PCBs as one half is for the sample measurement and the other half is for the reference needed for the reduction of external noises.

The figure 34 shows a top view of the magnetic detection prototype that has been used during this PhD project. The white plastic screws are used to have the best parallelism between the two PCBs so the gradiometry subtraction can be as precise as possible.

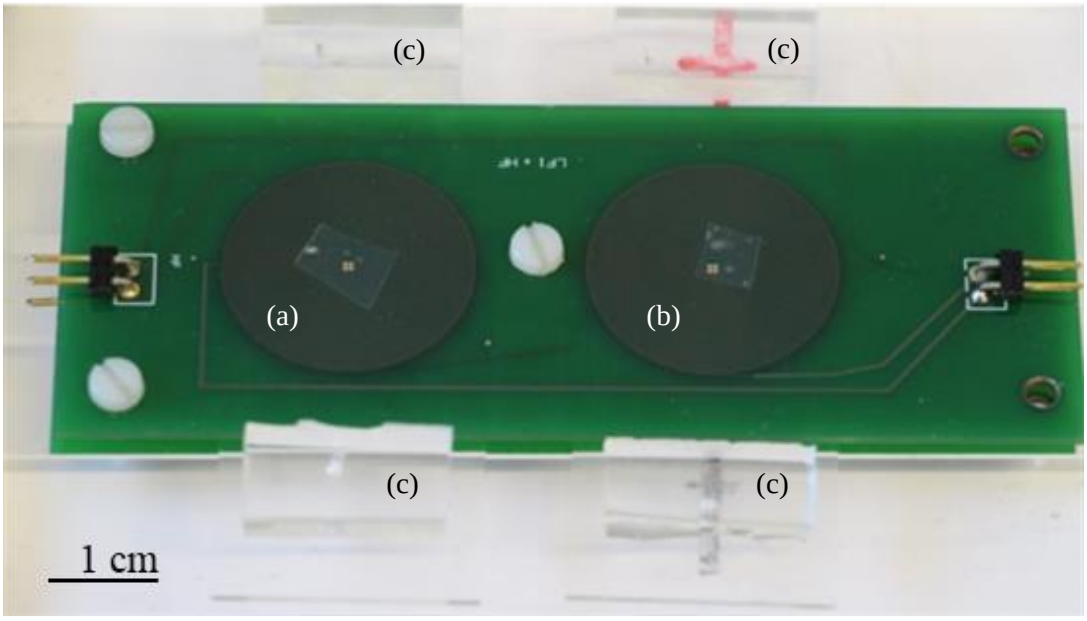

Figure 34: Detection structure is composed of two sets of PCB coils and the two microfluidic reservoirs between them for sample and reference. (a) is the sample set of coils. (b) is the reference set of coils and (c) are the microfluidic channels that are slid between the PCBs.

The pick-up coil's dimensions can be optimized by finding a compromise between sensitivity and minimum detectable magnetic moment. Figure 35 shows the best sensing characteristics that can be obtained by applying PCB restrictions on copper section, interlayer distances and minimal practical internal radius. For this particular chosen manufacturer, copper section is equal to 35 µm × 100 µm and inner radius is at a minimum of 800 µm. The calculation was done for a four-layer PCB coil. As seen on figure 35, if the outer radius is higher than 4 mm the minimum detectable magnetic moment increases more rapidly than the sensitivity so it is not advised to add more turns in the coils. Furthermore, it seems that the best compromise between sensitivity and minimum detectable magnetic moment for an outer radius is around 10 mm.

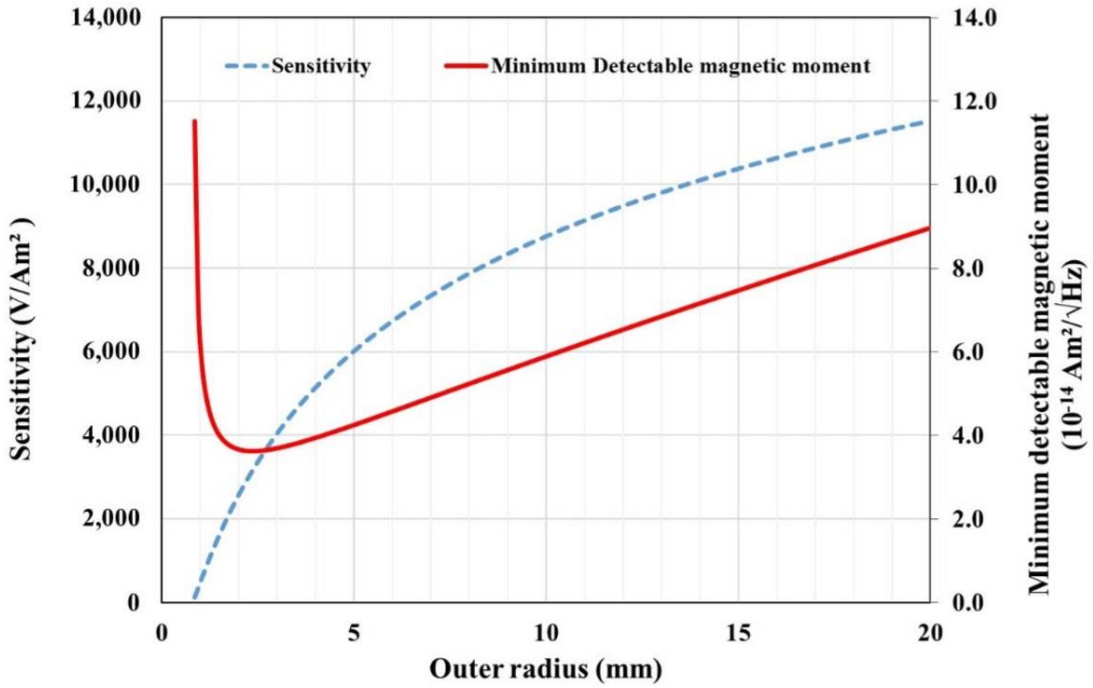

Figure 35: Pick-up coil optimization with sensitivity and minimum detectable moment versus coil outer radius. Internal radius fixed at 0.8 mm.

The dimensions we used for the PCB coils are presented in the table 10.

Table 10: Dimension of the coils

	layers	R_{in} (mm)	R_{out}(mm)	Turns/layer	Total number of turns
LF[1]	4	0.8	10	46	324
	4	3	10	35	
HF[2]	4	2.5	9	35	140
sensor	4	0.8	10	46	184
(1) Excitation coil with lower frequency bias (Low frequency (LF) coil))					
(2) Excitation coil with higher frequency bias (High frequency (HF) coil))					

The impedance of the coils and the magnetic field on the surface of the excitation and sensor coils were measured with an impedance analyzer and a Gaussmeter respectively. The magnetic field was measured as a DC voltage (3, 4 and 6 V) was applied in the coils. The results are presented in the table 11.

Table 11: Measured electronic parameters of different coils. The magnetic field is measured for different applied voltages.

	Resistance	Inductance (mH)	V=3 V	V=4V	V=6 V
HF	35 Ω	176	697 µT	890 µT	1.3 mT
Detection	44 Ω	265	708 µT	1.01 mT	1.45 mT
LF	90 Ω	950	581 µT	715 µT	1.11 mT

To make a magnetic measurement and detect SPN in the microfluidic structures, the excitation coils have to be supplied by two currents of frequencies f_1 and f_2. The result signal obtained by the detection coils has then to be amplified and demodulated so the response can be exploitable.

2.2.2.B Magnetic measurement experimental setup

The excitation coils provide the sinusoidal signals using two frequency generators for both low frequency (LF) and high frequency (HF) signals. The LF signal frequency range from few Hz to hundreds of Hz while the HF frequencies are between 10 kHz to 100 kHz. The high frequency signal is generated by a Stanford Research Systems ultra-low distortion generator DS360 and is able to emit a high enough power signal to directly provide the HF coil (figure 36). The high frequency is limited by the demodulating capacity of the Lock-in amplifiers and the response time of the nanoparticles. The low frequency signal is generated by a BK Precision 4087 low frequency generator and has to be amplified before supplying the LF coil.

Concerning the detection part, the detection coils transduce the magnetic field response to an electrical signal. This signal must then be demodulated to the aimed mixing term with two lock-in amplifiers that are used for the sequential demodulation. The synchronization of the demodulation frequency is performed by connecting the synchronization output of the frequency generators with the reference input of each lock-in amplifier (figure 36 and 38). The f_1+2f_2 signal is measured to determine if magnetic nanoparticles are present in the channel with f_1 the high frequency signal and f_2 the low frequency signal. The first lock-in amplifier, a Standford Research Systems SR830, demodulate the response signal by f_1 and amplifies it (usually by 500). The second lock-in, a Standford Research Systems SR530, demodulate by 2 times f_2 and display the resulting signal that is proportional to the amount of SPN in the device. The whole electronic setup can be piloted, and the measurement result showed, via a Labview software on an adjacent computer.

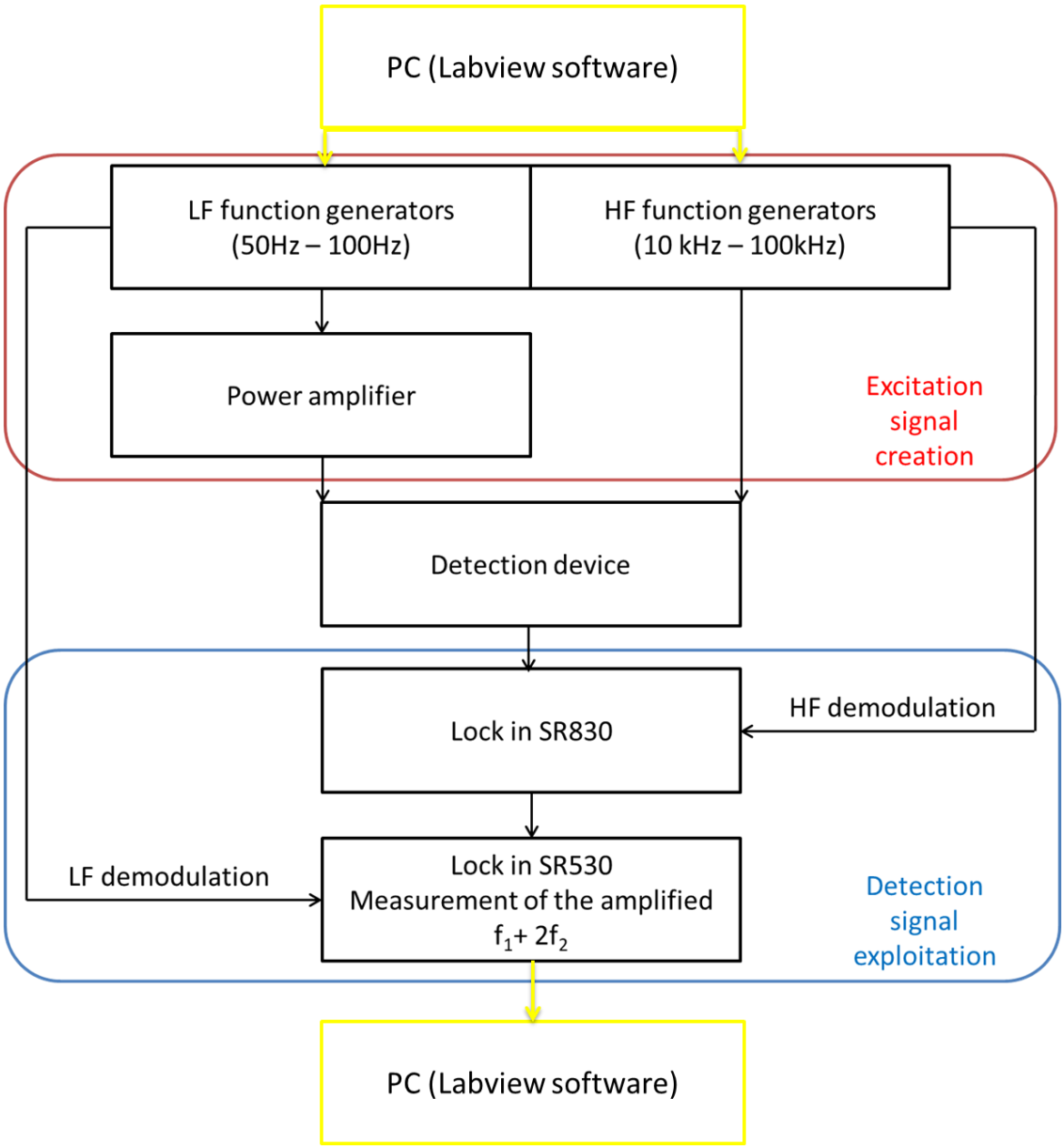

Figure 36: Block diagram of the electronic setup

To protect the magnetic nanoparticles detecting system from any electromagnetic interference, a Faraday cage was designed and realized (figure 37).

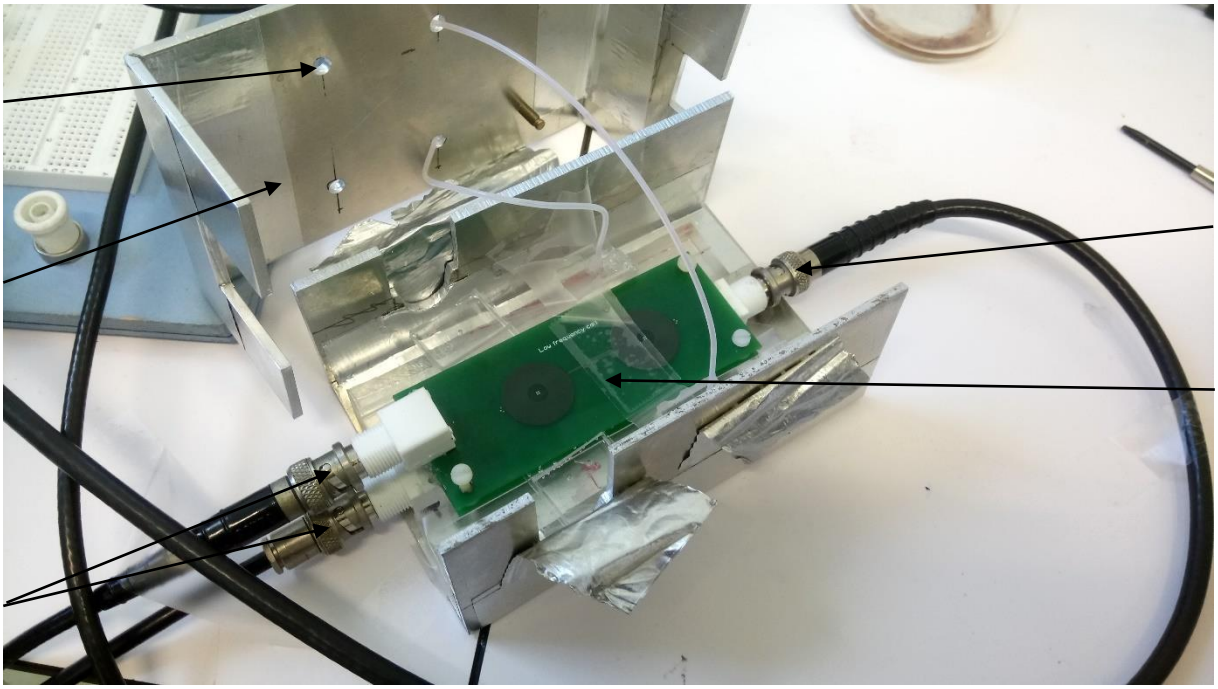

Figure 37: Opened Faraday cage

The Faraday cage slightly improves the signal detected but it is not very practical to do the measurements due to the plastic tubes necessary for the fluid flow in the microfluidic reservoir. These tubes tend to get out of the inlet and the outlet of the microfluidic channel when there are frictions between them and the cage when it is opened or closed. The Faraday cage has been redesigned and rebuilt to be more integrated and practical (figure 39). Holes for microfluidic tubes are not needed anymore as the microfluidic channels entrance and exit stay at the exterior of the cage.

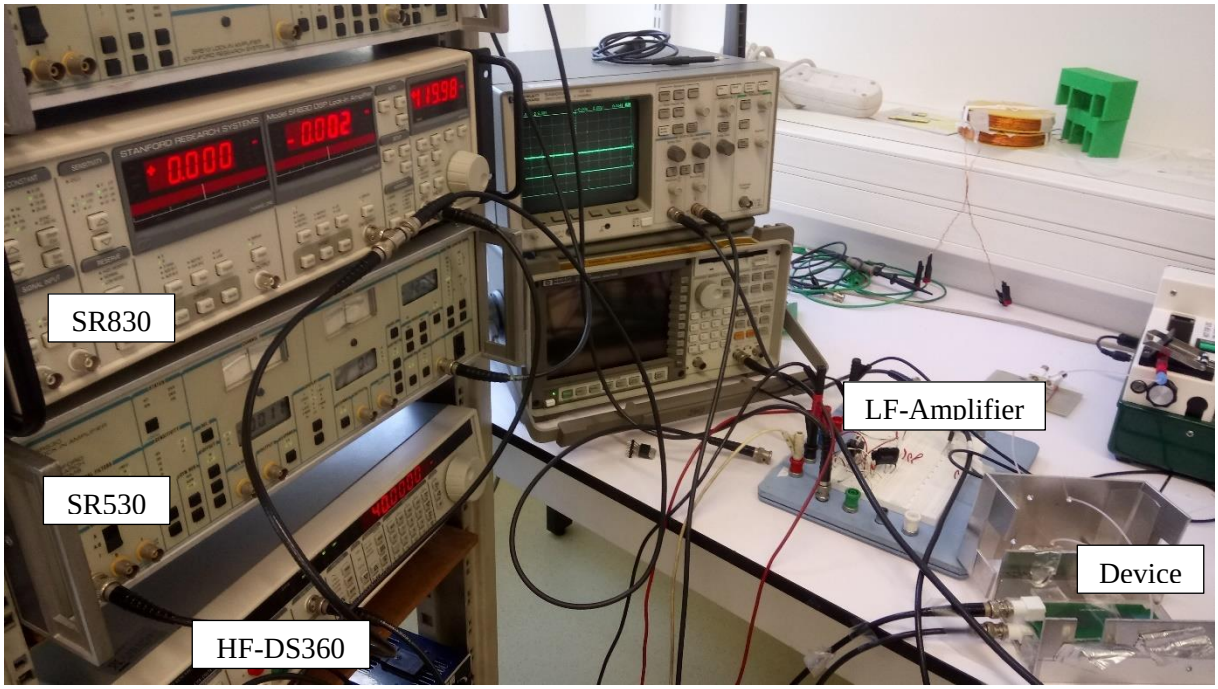

Figure 38: Photo of the major part of the electronic setup for the generation and the treatments of the excitation and detection signals

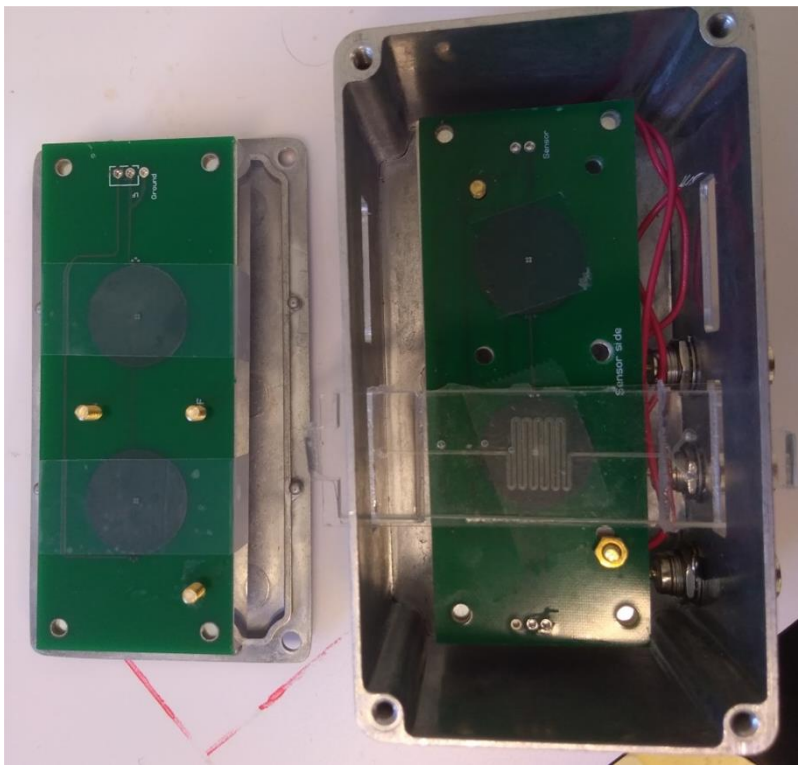

Figure 39: Opened new Faraday cage

2.2.2.C Miniaturization of electrical devices

Efforts have been made to miniaturize the electronic components of the experimental setup so that the device could be as compact and integrated as possible. A source of noise and a major component to miniaturize is the low frequency generator and the voltage amplifier needed to reach a sufficient power to generate the LF magnetic field. After testing the considered voltage amplifier (figure 40) on a Labdec board (figure 41), it has been realized on a PCB in the framework of a master student (M1) internship (Benjamin Lomuto, 2018) with my participation in his supervision. However, this circuit still required a generator to create the low frequency (LF) signal. An integrated circuit with a voltage-controlled oscillator (VCO) for generating the LF signal and a voltage amplifier was then designed and fabricated (figure 42).

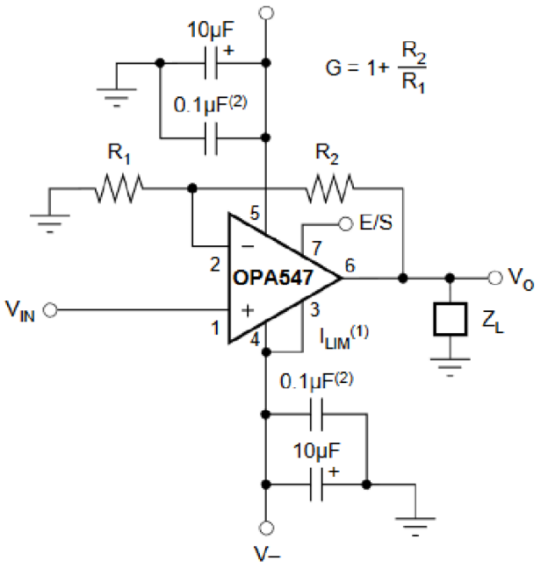

Figure 40: Schematic of the voltage amplification circuit

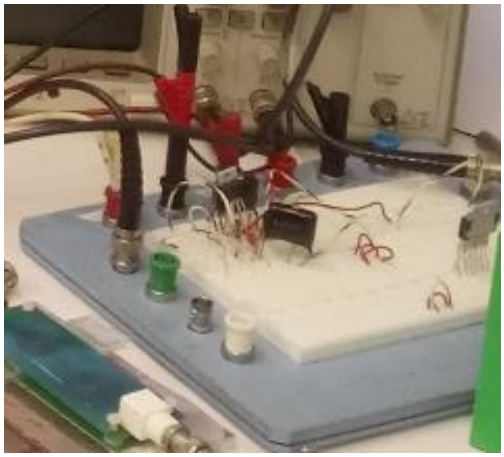

Figure 41: Voltage amplifier tested using a Labdec board.

Figure 42: First trails of miniaturization of low frequency electronic parts. (a) voltage amplifier, (b) is a low frequency generator using a VCO and (c) is the first version of a combined VCO and amplifier.

A more stable second version of a combined VCO and amplifier was then designed and fabricated (figure 43) during a master student (M2) internship (Quentin Fornasiero, 2019) with my participation in his supervision.

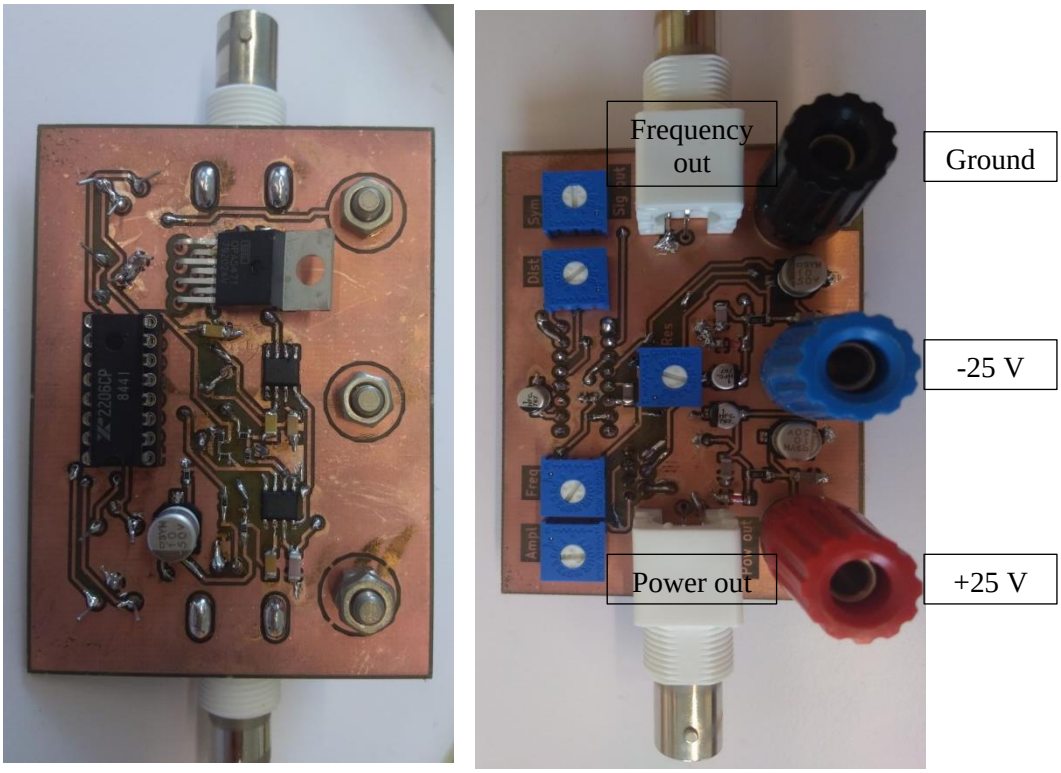

Figure 43: Second version of the VCO and amplifier for low frequency. The frequency out is used to tune the frequency and the power out to use as the low frequency intput signal.

The perspectives are to also miniaturize the high frequency generator and the lock-in amplifiers to obtain a fully integrated electronic measurement device.

2.2.2.D Pressure controlled flow inducing pump for microfluidic channels

The flow in the microfluidic channel is created by a Fluigent microfluidic pressure controlled pump (figure 45). Syringe pumps were previously used but their use is not completely adapted to microfluidic channel as they control the flow in the channel and not the pressure (figure 44). This can damage the channel if something clogs it and creates a pressure surge. On the other hand, pressure controlled pumps that we then purchased allows safer and more uniform way to create the flow in the microfluidic channel.

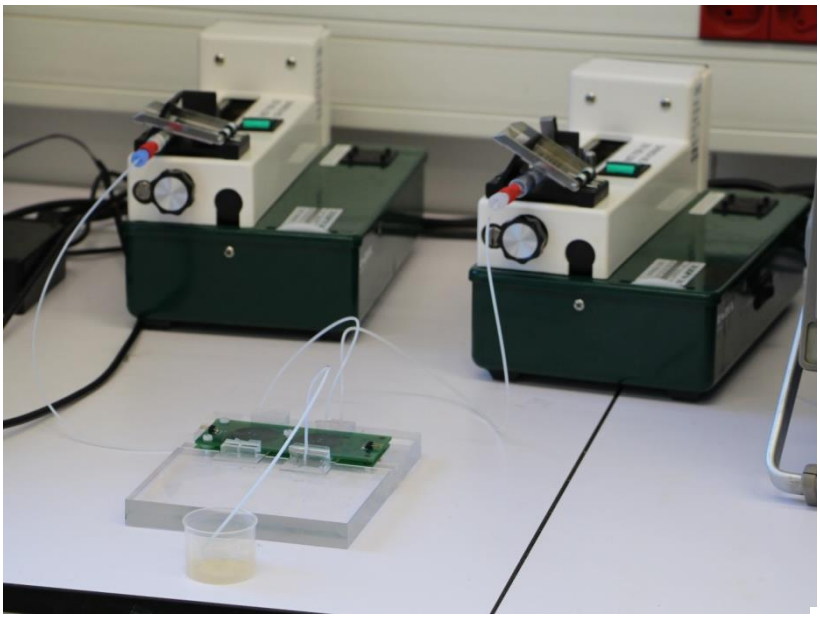

Figure 44: The two syringe pumps used previously to create the flow in the microfluidic channel

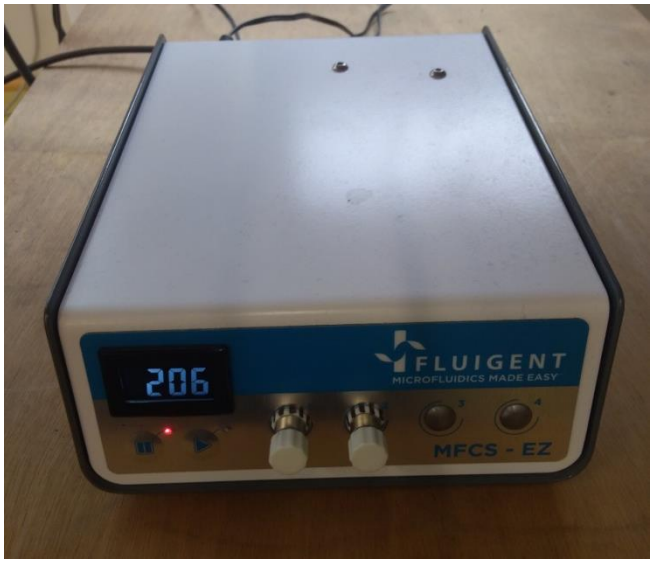

Figure 45: Fluigent pressure controlled pump

The Fluigent pressure pump (figure 45) is controlled by software where it is possible to apply a different pressure on each exits of the pump. The pump is linked to a tube containing the fluid to inject in the device with a plastic capillary. The pump creates an overpressure in the tube that induces the injection of the fluid in another capillary that goes to the microfluidic channel in the device (figure 46).

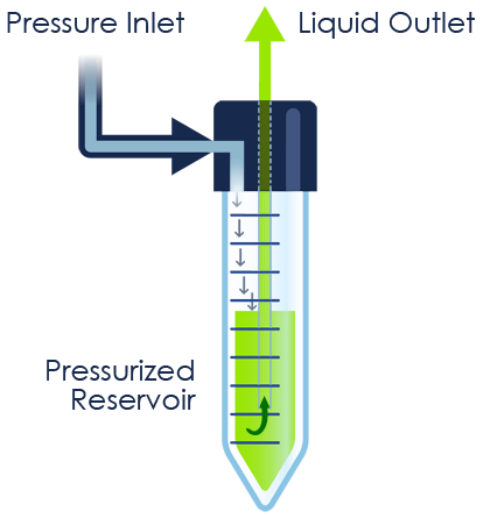

Figure 46: Principle of sample flow creation with Fluigent pump [118].

2.2 Microfluidic structures for immunoassays

The last part of the device to present is the microfluidic channel itself. This is where the magnetic nanoparticles are measured by the detection system. Polydimethylsiloxane (PDMS) has been used to create the microfluidic channel as it is a well suited material for prototyping (see section 1.3). Some works were then done with PMMA and COC. In the final device, the microfluidic channel should be prefunctionalized before the immunoassay and should be a single use disposable microfluidic chip. Cleanable and reusable microfluidic chips are also possible but that strategy is complicated, especially for medical purposes.

2.3.1 PDMS

2.3.1.A SU8 mold protocol

The chemical structure of PDMS is presented on figure 47. To create a PDMS microfluidic channel, a master mold has to be first made. Its microfluidic features are then replicated.

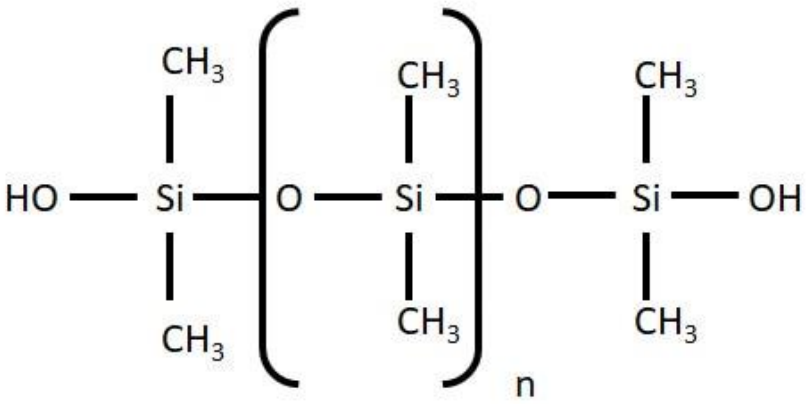

Figure 47: Chemical structure of Polydimethylsiloxane (PDMS) [119].

To create the master molds, the used photoresist was SU-8 for photolithography process. SU-8 is an epoxy-based negative photoresist which means that the portions that are exposed to light become insoluble to the resin developer and cross linked at the surface of the substrate. Our experiments were carried out in the cleanroom of the IPGG (Institut Pierre-Gilles de Gennes) in Paris. The SU-8 photoresist is spin coated on a silicon wafer. A mask aligner with a specially designed chrome mask is then used to irradiate ultraviolet light on the parts that need to be kept. The wafer is then put in the SU8 developer to remove all the resin that was not exposed to UV light. This photolithography technique is very precise and can create microfluidic master molds with features smaller than a micrometer. However it is rather expensive notably because it requires a cleanroom to be performed, complicated and the master mold deteriorates after a few uses because of some adherence between the photoresist resin and the PDMS when it is peeled off from it. Here is a step by step example for the photolithography of a SU-8 master mold generation (figure 48):

- Clean the silicon wafer with acetone then dry it with nitrogen gas and heat it at 120°C for 15 minutes to remove any stain on the surface of the wafer. Moreover the heating allows the photoresist resin the stick better to the surface of the wafer.

- The SU-8 is then spin-coated on the wafer usually in two steps. One with a low acceleration and maximum rotation speed and a second one with a high acceleration and rotation speed. These accelerations and maximum speeds have to be optimized to obtain the desired thickness layer of SU-8 on the wafer. This thickness also depends on the type of SU-8 used (several length of polymers exist). The photoresist is poured during the first slower rotation step for what is called a dynamic coating, this allows to obtain thickness of 50 µm and higher. For example, the first step can have an acceleration of 100 rpm/s up to 500 rpm and holds that speed for 30 seconds. The second step can ramp up to 2000 rpm at an acceleration of 300 rpm/s. With a SU-8 50 resin from Microchem, the thickness obtained on the wafer is about 50 µm.

- The wafer is then heated on a hot plate so the SU-8 is soft baked to remove the solvent from resin and solidify it. A progressive temperature baking can be applied to limit the stress on the resin and have a better evaporation. The wafer is heated for 5 minute at 65 °C and then 20 minutes at 95°C for a thickness of 50 µm. The wafer is let on the hotplate as it is cooling down so the return at room temperature is progressive.

- The specific chrome photomask, that let UV light passes through only where the microfluidic channel will be on the silicon wafer, is loaded in the mask aligner. The wafer is also loaded into the mask aligner beneath the photomask. UV light at 365 nm is then applied on the photoresist that is not protected by the mask. The photoactive component in the SU-8 will then activate the cross linkage of the resin making it not soluble in the SU-8 developer where the UV light exposure occurred. The time of exposure depends on the thickness of SU-8 but also on the power of the UV lamp. For a 50 µm thickness of SU-8 50, a UV light energy of about 200 mJ/cm^2 should be applied to the wafer using the mask aligner (110). The chrome mask used for photolithography is designed using the Clewin software and then fabricated by a commercial firm.

- The resin has to be then baked a second during the step called “post-exposure baking”. This step is necessary for the exposed photoresist resin to crosslink completely. Contrary to the soft bake step that to be performed on a hot plate; the post-exposure can be done either on a hot plate or in an oven. For a thickness of 50 µm with SU-8 50, the wafer can be baked at 65°C during 1 minute and then at 95°C during 5 minutes. The cooling has to be progressive exactly like the soft bake step.

- The development step aimed to remove the negative photoresist SU-8 from the areas of the wafer that were not exposed. The wafer is put in approximately 50 mL of developer solution and strong agitation is applied during the process. The development time depends on the thickness of photoresist to remove. For 50 µm thickness of SU-8 50 it is approximately 50 minutes as it depends on the agitation and the room temperature. The wafer is then rinsed with isopropanol. If some white spots remain on the wafer it means that the resin is underdeveloped and should be immersed again in the developer for a short time. After the rinsing the wafer has to be dried under a nitrogen gas stream.

- A last baking is applied to the wafer so the photoresist is mechanically strengthened. The temperature has to be progressively increased to 150°C and then cooled down gently (figure 48).

- The quality of the mold can be checked using a microscope for the XY dimensions and mechanical profiler for Z the dimensions.

Following these steps lead to the creation of a SU-8 master mold which can be used to create several PDMS microchannels. Some aluminum foil can be used to create a barrier on the edge of the wafer so it can contain liquid PDMS. The other steps to create PDMS microfluidic chips are detailed in section 2.3.1.C.

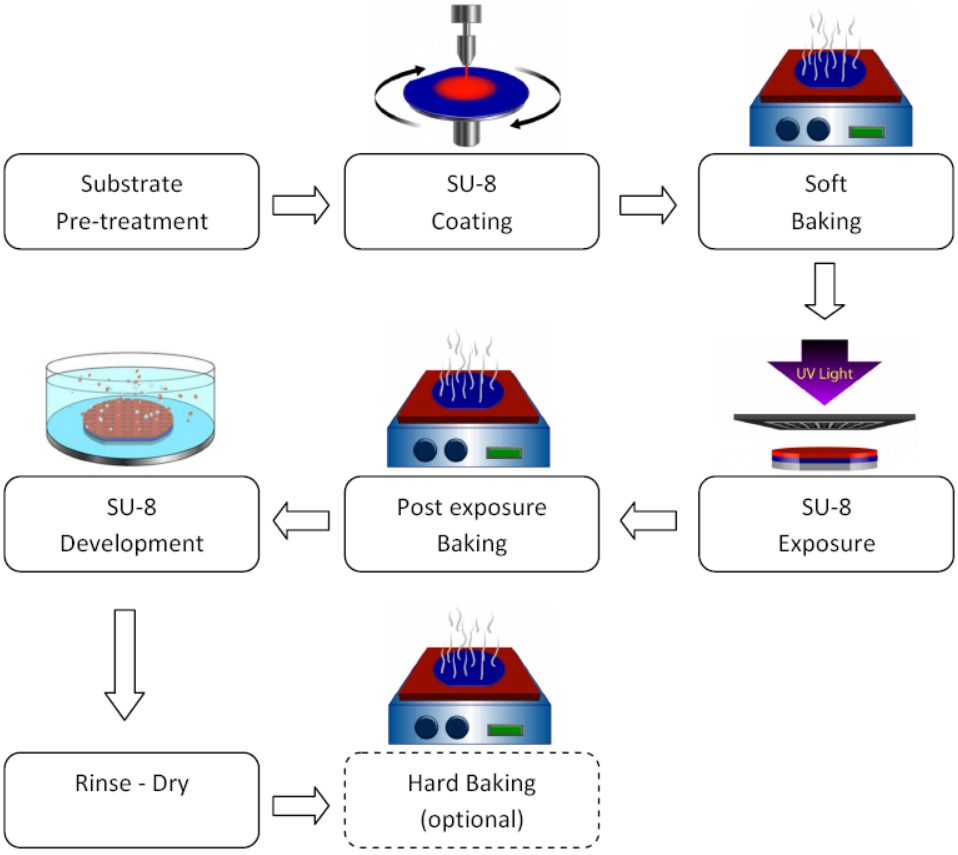

Figure 48: Photolithography steps for SU-8 photoresist [120]

Since the microfluidic channel structures needed for our project didn't require very small features (between 50 µm and 200 µm), a simpler and cheaper 3D printing technique has been used instead of the photolithography.

2.3.1.B 3D printed mold protocol

With the help of Damien Bricault and Kieu Ngo from the "Laboratoire Interfaces et Systèmes Electrochimiques" (LISE), another technique was used to create master molds using a Formlab 3D printer (figure 49). For this PhD project, the majority of the master molds that have been used were crafted using this process. This technique is faster, cheaper and simpler

but it only works for microfluidic structures that require a spatial resolution of 50 µm and coarser. For smaller features, the photolithography technique is more suited.

The desired mold is first designed on the free Openscad software. The ".scad" files have to be then converted into ".obj" or ".stl" files so that they can be transcribed by the printer into physical objects. The printer uses a low force stereolithography technique to print 3D objects. The principle is that a tank full of photoresist resin is exposed to high energy laser that solidify the resin on a precise spot (figure 50).

Figure 49: Formlab 2 3D printer (www.amazon.com)

Figure 50: An object forming from the resin tank

This printer allows the utilization of different photoresist resins and doesn't require a cleanroom to be operated. The figures 51 presents an openscad file and the resulting printed master mold obtained from the Formalab 2.

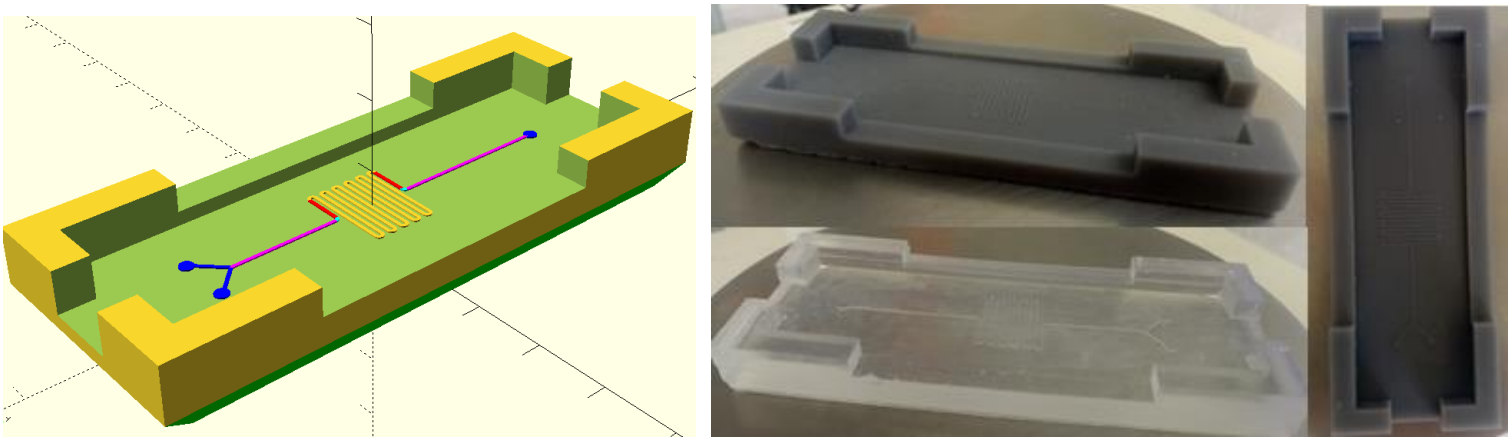

Figure 51: (Left) Openscad 3D drawing of a master mold. (Right) Master mold printed by Formalab 2 printer.

The thickness of the mold walls decreased in the middle part of the channel. A solid bloc of plastic is put on the master mold when PDMS is poured to create a thinning In fact it is very important that the PDMS be quite thin to place as close as possible the PCB planar coils to the microchannel in order to improve the detection sensitivity of magnetic nanoparticles. Nevertheless, high thickness is still needed at the extremities of the channel to connect the inlet/outlet tubing. See section 3.4 for details about the different microfluidic channels that were fabricated.

2.3.1.C PDMS casting

To create a channel, the liquid monomer and the curing agent (ratio 10:1) were poured on the master mold after degassing the mixture. It is then put in the oven at 80°C for one hour (figure 52). The now rigid polymer is peeled off from the mold. Holes are punched in the elastomer to create the inlet and the outlet of the channel. The PDMS is then exposed with a glass slide under plasma O_2 for one minute. The plasma will create hydroxyl functions (-OH), on both the PDMS and the glass slide, that will create covalent bonds when they are stick together. These steps are made in the cleanroom of INSP (Institut des NanoSciences de Paris) in Jussieu. Alternative materials can be used to replace the glass and seal the microfluidic channel, like another piece of PDMS for example.

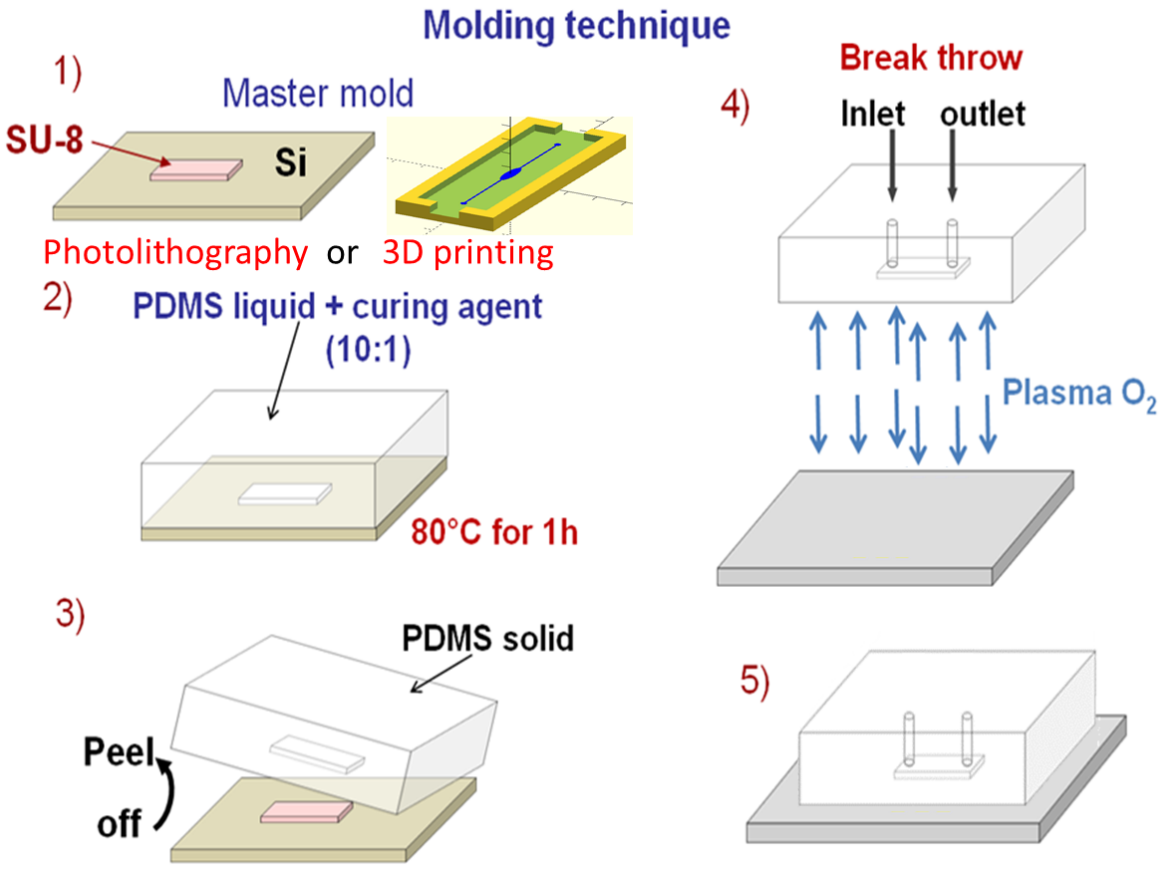

Figure 52: Molding technique for the creation of PDMS microfluidic channels.

The master mold can be cleaned and reused to create other replications of the microstructure.

2.3.2 Other utilized materials, PMMA and COC

As it has been mentioned in the section 1.3 the PDMS is not suited for industrialization as it is not compatible with hot embossing and injection molding. In comparison to PDMS, thermoplastics offer increased solvent resistance, higher rigidity and low cost of mass production.

2.3.2.A General characteristics

For our project, the material used for the microfluidic channels needs to have:

- Possibility of antibody bonding on the surface of the material
- Suitability for hot embossing and/or injection molding replication techniques

It is also better if the chosen material is:

- As thermally and chemically resistant as possible
- Strong under mechanical strains (with a high enough elastic modulus E)
- As cheap as possible

We selected poly(methyl methacrylate) (**PMMA**) and cyclic olefin copolymer (**COC**) as the two most interesting polymer materials to work with.

PMMA also called Plexiglas®, acrylic or acrylic glass is a transparent, light weighted and resistant thermoplastic material that is used for a number of applications and is fabricated from petroleum (figure 53). For example, it is used for motorcycle helmet visors, basketball boards, helicopter and aquarium windows, etc. [121]. It composed of carbon, hydrogen and oxygen atoms.

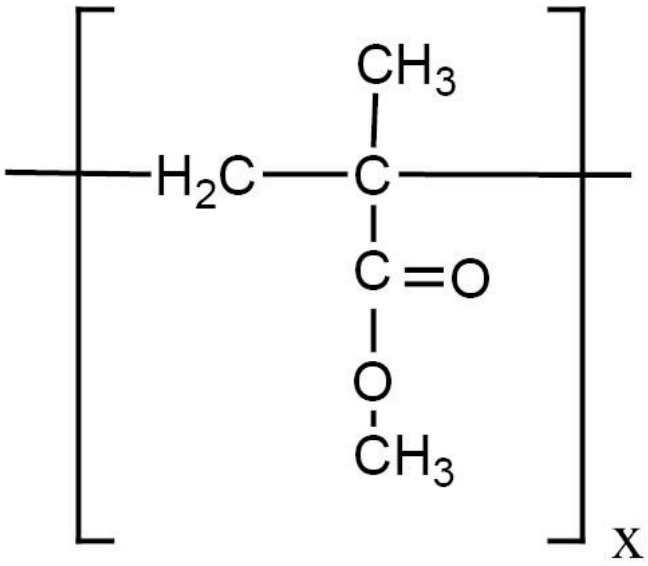

Figure 53: Chemical structure of PMMA. X denotes a repetition of its building units, called monomer [121]

It is biocompatible as it is already used for artificial teeth and intraocular lenses [123]. The latter application proves that this material is highly biocompatible as the interior of the eye is extremely sensitive with a lot of immune cells [124]. Moreover, antibodies have been graphed to a PMMA surface before [125] which is a crucial property for the creation of the immunoassay device in this project.

PMMA has good tensile strength, flexural strength, transparency and UV tolerance. It is also a cheap material, easy to clean and 100% recyclable. However heat, impact and chemical resistances are limited (table 12). The glass transition temperature (T_g) of PMMA is between 85°C and 165°C [126].

Table 12: PMMA chemical resistance against some solvents [127].

	Behavior		
Solvents	**Good**	**Limited**	**Poor**
Water	X		
Detergent	X		
Acetic Acid			X
Alcohol			X
Acetone			X
Toluene			X
Methanol			X
Hexane		X	
Heptane		X	

PMMA is suited for hot embossing and injection molding [127].

Finally PMMA is a widely used thermoplastic polymer for biomedical LOCs [129][130].

COC also called ethylene copolymer is a group of translucent thermoplastic copolymers that are the repetition of cyclic monomers like tetracyclododecene and a second monomer called ethene. COC materials are, in fact, copolymers because they are the product of the copolymerization of two different before-mentioned monomers. These rather new materials are used for packaging, cameras lens, touchscreens, etc. They are usually only composed of carbon and hydrogen atoms (figure 54).

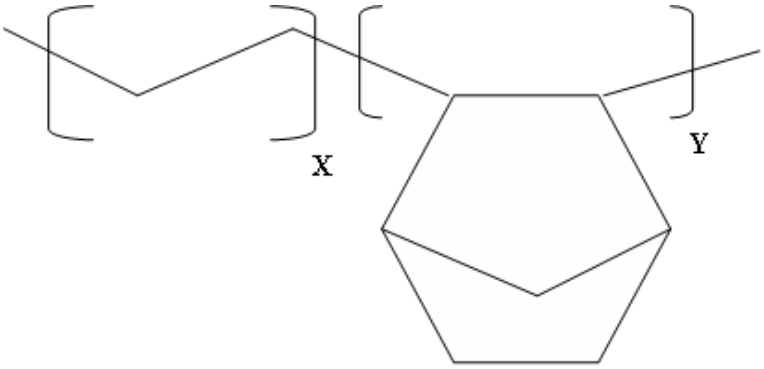

Figure 54: Chemical structure of COC with X and Y denoting a repetition of the building units, called monomers [131].

Like PMMA, cyclic olefin copolymer is biocompatible and antibodies have already been bounded to COC surfaces before [132][133].

COC materials have exceptional optical properties similar to glass with low dispersion and birefringence. They are also mechanically strong materials (with young modulus higher than PMMA[134]) with a good thermal resistance. They are a bit more expensive than PMMA but stay cheap none the less.

COC materials are very chemically resistant to a vast majority of solvents except some non-polar solvent like toluene (table 13). COC glass transition temperatures ranged from 80°C to 180°C [135].

Table 13: TOPAS COC chemical resistance against some solvents [135].

	Behavior		
Solvents	**Good**	**Limited**	**Poor**
Water	X		
Detergent	X		
Acetic Acid	X		
Alcohol	X		
Acetone	X		
Toluene			X
Methanol	X		
Hexane			X
Heptane			X

COC is also suited for hot embossing and injection molding [128].

They are upcoming materials for microfluidics and especially for biomedical LOCs [136][137][138].

Cyclic olefin polymers (COP) are polymers that are chemically close to COC and are also interesting for LOC applications [139].

Low water absorption of COC is beneficial to ensure that the dimensions of the structures do not change with the environmental conditions.

PMMA and COC can be used for prototyping by applying: (i) a temperature higher than the glass temperature T_g of the material and (ii) a pressure high enough to deform the substrate on the master mold and obtain a replication of microfluidic channel. However this prototyping is more difficult in comparison to the easier PDMS casting.

2.3.2.B Comparison table of PDMS, PMMA and COC

In table 14, we have summarized the most important properties of PDMS, PMMA and COC for comparison. PDMS begins to swell at about 300°C and deteriorates at about 500°C [140][141].

Tableau 14: Summary of advantaged and drawbacks for PDMS, PMMA and COC [142].

	Biocompatibility	Antibody bonding	Thermal resistance	Chemical resistance	Elastic modulus E	Optical transparency	Prototyping	Industrialization	Price
PDMS	+	++	+++	+	-	+++	+++	-	+++
PMMA	++	++	++	+	++	++	+	++	++
COC	++	++	++	+++	++	+++	+	++	+

The PDMS polymer has been used on this project for the prototype tests and trials of different microfluidic channels. However, some experiments have been done with COC and PMMA, especially on the biofunctionnalization, to anticipate a future industrialization of the LOC immunoassay device (see chapter 4).

2.4 Conclusions

The magnetic detection principle based on frequency mixing method has been described as well as the previous device that has been developed by the institute of bioelectronics in Juelich research center using this method. The portable device studied during my PhD at “Laboratoire d’Electronique et d’Electromagnétisme (L2E) aims to be miniaturized so it can be smaller, faster and more cost-effective using less sample and reagents, with higher sensitivity as the distance between the coils and the sample is lower, less energy consumption implying smaller battery and longer autonomy of the device and the possibility of multipathogens parallel testing.

The developed electronic setup has been presented with the planar PCB coils and the latter improvements for the low frequency generator.

Master molds for microfluidic channels have been made using SU-8 photoresist in a cleanroom and with Formlab II 3D printer. The technique to obtain PDMS microfluidic channels via elastomer casting has also been described.

Finally, a comparison has been made between PDMS, PMMA and COC to show what advantages and drawbacks each of these materials present. PDMS is the go-to material in term of prototyping but it is not suited for industrialization. COC shows interesting properties but it is still quite new in comparison to PMMA. The studies of biofunctionalization with these materials for immunoassays tests will be presented in chapter 4.

After presenting the magnetic detection miniaturized prototype device and the measurement experimental setup, the results of magnetic measurements are described in chapter 3.

Chapter 3. Enhancement of the detection limit: magnetic and microfluidic approaches

3.1 Introduction

The magnetic detection device has been tested with several different nanoparticles to determine which characteristics of the magnetic nanoparticles (MNP) are critical for their detection and to determine the best nanoparticle candidate to use in future sandwich immunoassays. The newest MNP have also been coated with silicon dioxide (or silica) for future biofunctionnalization.

Then several microfluidic channel layouts have been tested to optimize their geometrical properties. Three different microchannel geometries have been created: serpentine, spiral and pillar- based reservoirs. The latter was fabricated to improve the surface to volume ratio as it is a critical property for sandwich based immunoassays. Simulations and magnetic measurements are presented below.

Finally, a new approach with the application of an external static (DC) magnetic field, using Helmholtz coils and permanent magnets, was used to improve the limit of detection (LOD) of the device for the MNP.

All the mentioned MNP have been synthetized by our collaborators at PHENIX laboratory (Physicochimie des Electrolytes et Nanosystèmes Interfaciaux) from Sorbonne University by either Mrs. Sophie Neveu or Mrs. Emilie Secret.

3.2 Influence of MNP concentration

The limit of detection (LOD) in term of MNP concentration has been, firstly assessed. Indeed, it is a very important property to show the effectiveness and sensitivity of the frequency mixing technique as viable immunoassay method.

The magnetic nanoparticles used to determine the limit of detection of the device are iron oxides Fe_2O_3 nanoparticles (also called maghemite). These MNP referenced Magh-20nm have been synthetized and characterized (microstructure with TEM and magnetic properties) at PHENIX laboratory in Jussieu campus. Physical characterizations of these MNP show that: (i) the particles form flower-shaped structures of 20 nm in diameter (figure 55) and exhibit stability even for relatively large diameters and (ii) they display superparamagnetic behavior with no hysteresis and saturation in the magnetization curve (figure 56) [143]).

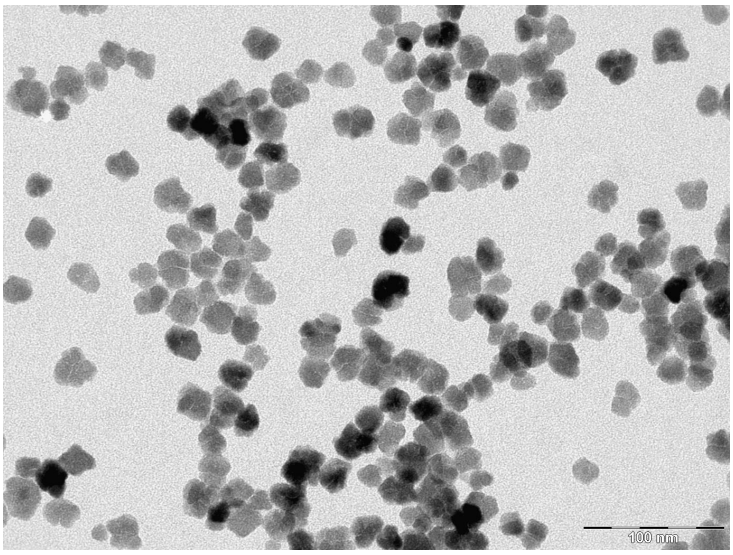

Figure 55: TEM image of 20 nm Magh-20nm iron oxides nanoparticles.

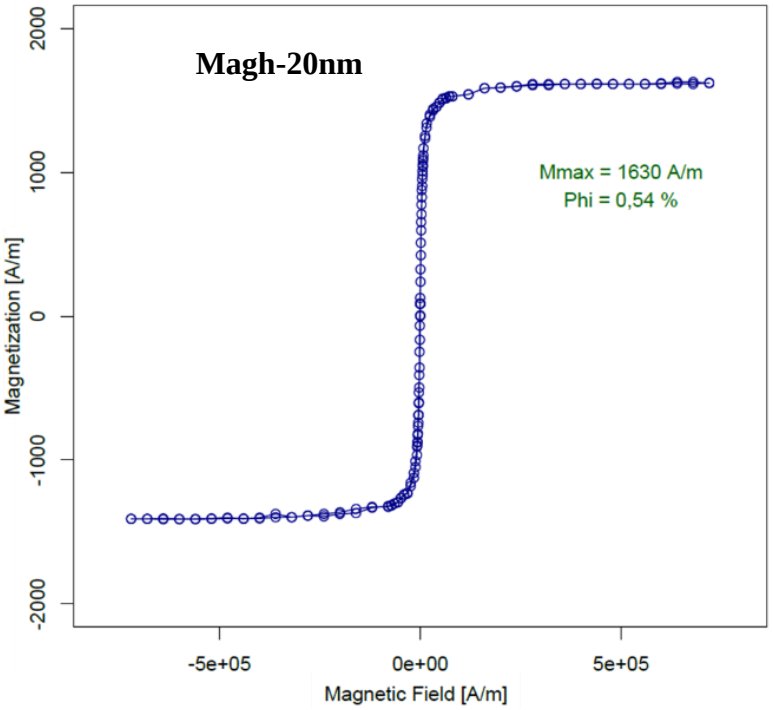

Figure 56: Magnetization curve of 20 nm diameter Magh-20nm maghemite (Fe_2O_3) from PHENIX laboratory.

These characterizations show the suitability of these MNP for the frequency mixing technique as described in section 2.2.1. The Magh-20nm nanoparticles were injected at different concentration in the microfluidic channel surrounded by the PCBs, the flow is stopped at the moment of the magnetic measurement. The distance between the two PCB is 1.5 mm. The detailed protocol for the complete test is in the appendix 1. The test was made using different MNP concentrations with the same PCBs and the same microfluidic channel design (serpentine shape, 12x12 mm, 200 µm height and 500 µm width) for each measurement. The low frequency in the LF coils was set to 65 Hz and fed by a signal of 48 Vpp (peak to peak after amplification) and the high frequency in HF coils was set to 40 kHz with a feeding voltage of 40 Vpp. The signal response is amplified by 500 during the demodulation by the high frequency by the first lock-in (figure 57). Thanks to this setup, the magnetic measurements were performed with various MNP concentrations from C_0 =

$0.254.10^{-3}$ mol/L (stock suspension which is equivalent to 14.23 g/L in term of iron mass concentration) to $C_0/1000 = 2.542x10^{-7}$ mol/L equivalent to 14.23 mg/L.

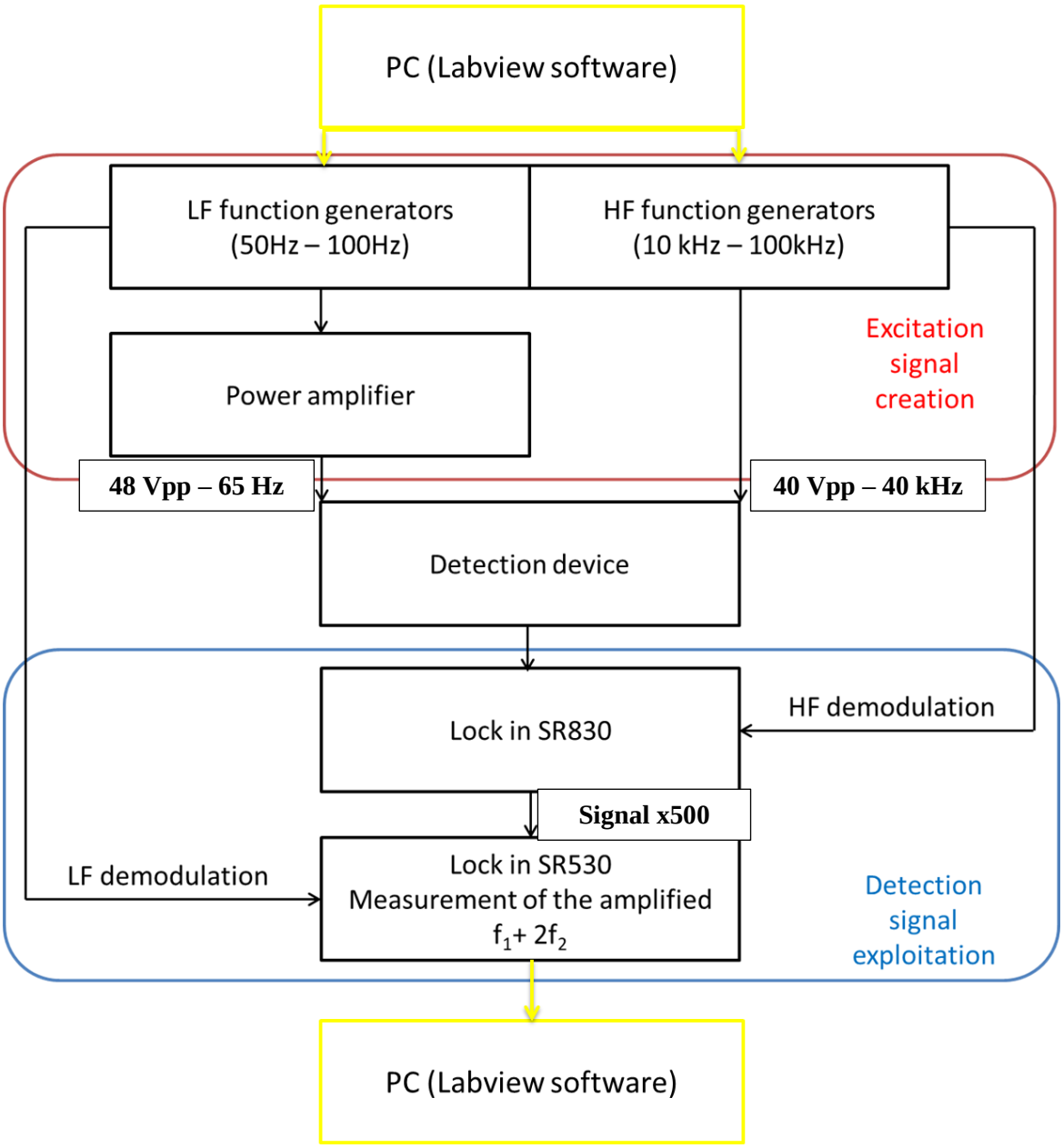

Figure 57: Electrical parameters used for the measurements.

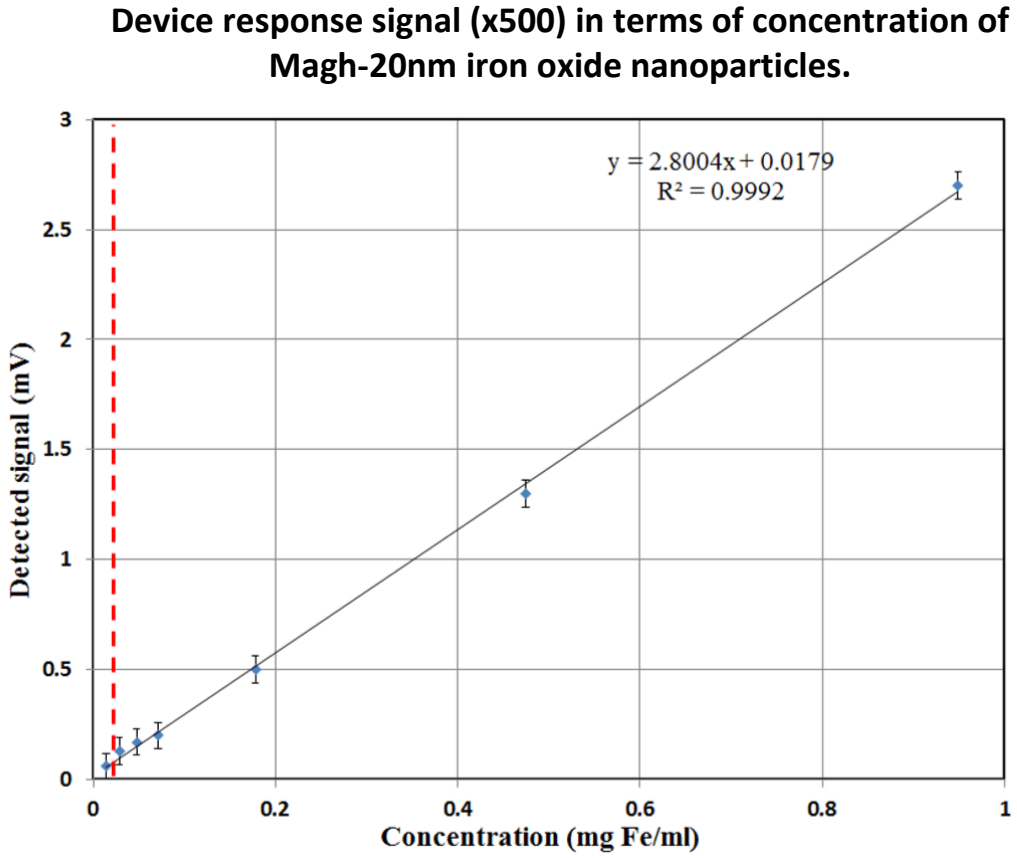

Figure 58: Magnetic response signal f_1+2f_2 as a function of the mass concentration of 20 nm iron oxide (Fe2O3) nanoparticles. The red dotted line indicates the limit of detection at about 0.015 mg/mL or 15 mg/L for these measurements.

The figure 58 clearly shows that the magnetic detection device has a very good linearity of detection as a function of the concentration of iron nanoparticles in the microfluidic channel (R^2=0.999). The reproducibility is also good as this test has been repeated several times with separations of a few days each time. The limit of detection was determined when the signal is no longer distinguished from the noise level of the system. The result is at about 15 µg/mL (15 ng/µL) which is a very promising result that validated the technique to detect MNP in a suspension as a function of its concentration. This limit of detection is roughly equivalent to detecting 0.2 µg of iron in a volume of 14 µL.

These results will be further improved by notably working on the mechanical stability of the system. The parallelism of the two PCB is indeed critical as a height difference between the two sides of PCB induce noises since the magnetic gradiometry technique is no longer well applied (see section 2.2.2). In that case a false response result is created by the difference of magnetic field between the two sets of coils (measurement and reference). To reduce this problem, the adjustment system for the horizontality of the two parallel PCBs has been improved.

The results presented above were all measured with Magh-20nm nanoparticles that were produced at PHENIX laboratory and provided in fairly big quantities for good reproducibility and repeatability results. The physical and chemical characteristics of MNP may have crucial influences on the detection sensitivity. Therefore different sorts of magnetic nanoparticles have been considered and the results are presented in the following section.

3.3 Study of different MNP

The device response has been characterized for several types of magnetic nanoparticles with different chemical compositions and sizes. Magnetization units are described in section 2.2.1 (page 45).

3.3.1 Influence of MNP properties on sensitivity

To improve the response of the device, the MNP characteristics have to be optimized.

The magnetic response of nanoparticles mainly depends on their sizes and chemical compositions. Several nanoparticles were tested with our detection device. The results of four different nanoparticle suspensions synthetized by the PHENIX laboratory (Mrs. Sophie Neveu) have been compared (figure 60, and table 15).

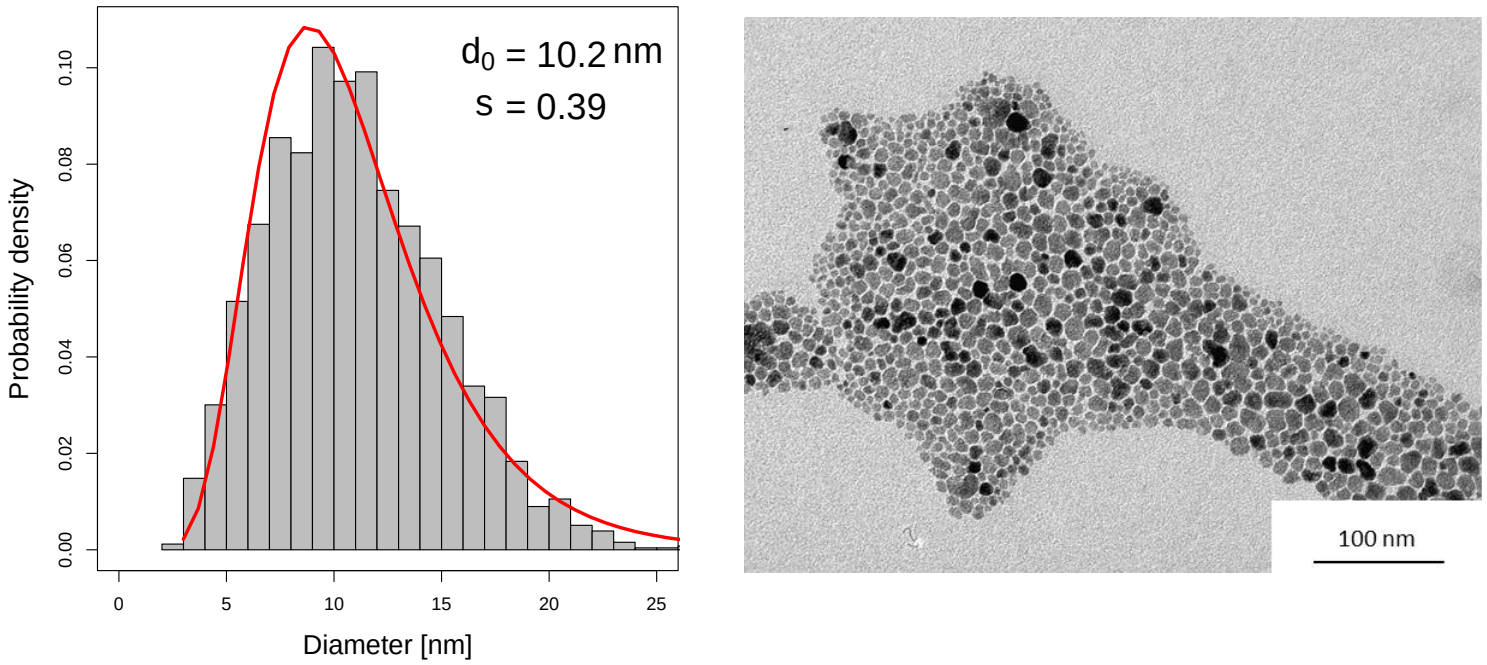

Figure 59: (Left) Particle size distribution (PSD) of the CoFe-20nm. The parameter d0 is the mass-median-diameter of the SPN (average particle diameter by mass) and σ is the standard deviation. (Right) TEM image of CoFe-20nm nanoparticles.

Table 15: Comparison table of different iron oxide and cobalt ferrite nanoparticles.

Nanoparticles references	Magh-20nm	CoFe-45nm	CoFe-10nm	CoFe-20nm
Composition	Fe_2O_3	$CoFe_2O_4$	$CoFe_2O_4$	$CoFe_2O_4$
Size (core)	20 nm	45 nm	10 nm	19 nm
Magnetic compound concentration (iron/cobalt) [mg/mL]	15/0	8/4	121/65	19/8
Initial concentration (C0) whole molecule [mg/mL]	21.16	14.66	262.55	31.66
Initial molar concentration (whole molecule) [mol/L]	0.13	0.062	1.12	0.14
Saturation magnetization (C0) [A/m]	1630	1012	20780	2790
Normalized Ms (saturation magnetization) (to reference 10 mg/mL) [A/m]	770.36	690.46	791.47	881.14
Normalized Ms (saturation magnetization) (to reference 10 mg/mL) [emu/g]	77	69	79	88

The saturation magnetization has been normalized at a concentration of 10 mg/mL to compare this value between the different MNP (table 15).

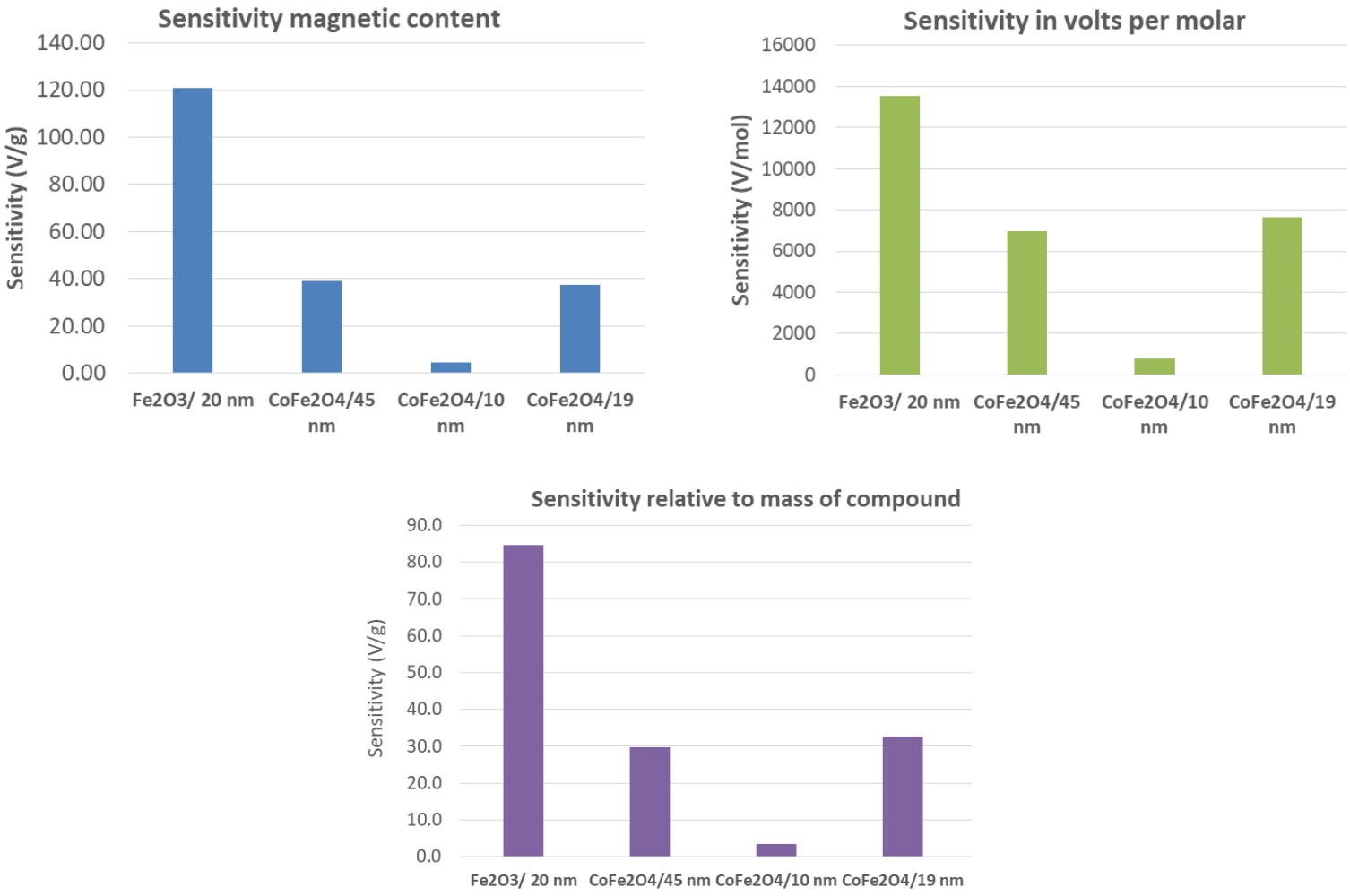

Figure 60: Sensitivity measurements for various nanoparticles.

We can firstly deduce from figure 60 that the performances of the smallest nanoparticles are lower than the bigger ones as the sensitivity from the particles with a diameter of 10 nm is very low even with normalization to the magnetic mass. That can be explained by the surface effect as the surface and the core of nanoparticle have different magnetic properties. If the nanoparticle is too small, the "effective radius" is also reduced and the magnetic response is not optimal [144]. We can also observe that this effect is no longer critical between the particles of 19 nm and 45 nm as the synthesis techniques of these two particles are different as CoFe-20nm was made using a hydrothermal process and CoFe-45nm was made using a polyol process (figure 61).

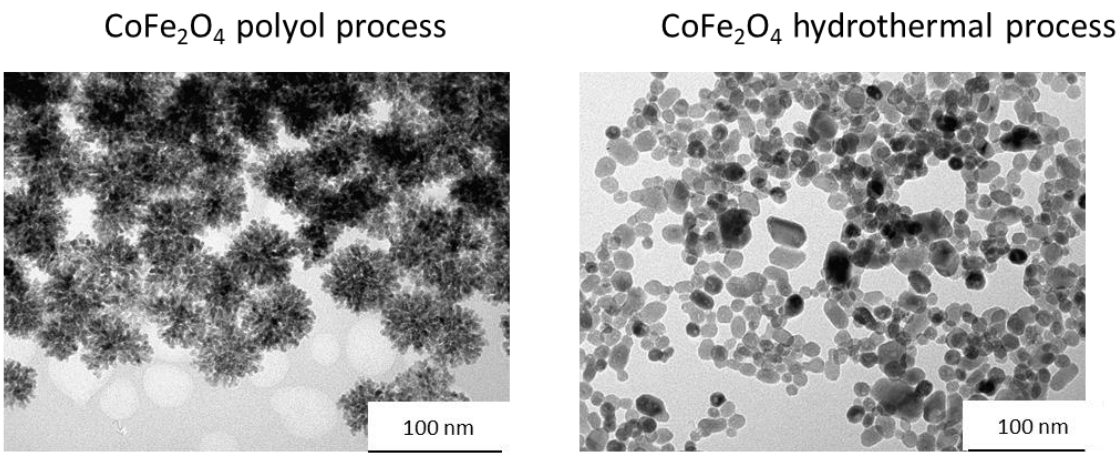

Figure 61: Transmission electron microscopy (TEM) pictures of the 50 and 19 nm cobalt ferrite nanoparticles realized through polyol and hydrothermal processes respectively.

If we compare the Magh-20nm composed with maghemite nanoparticles (Fe_2O_3) with CoFe-20nm that is composed of cobalt ferrite nanoparticles ($CoFe_2O_4$), we can observe that, for a similar core size (about 20 nm), the iron oxide nanoparticles give better magnetic responses. In fact, the cobalt ferrite nanoparticles are not perfectly superparamagnetic and exhibit some hysteresis on their magnetization curve and could explain that difference in the detection sensitivity (figure 62). This can be explained by the fact that the colloidal stability of the cobalt ferrite nanoparticles is weak [145]. This effect increases with the size of the nanoparticle and depends also on its morphology.

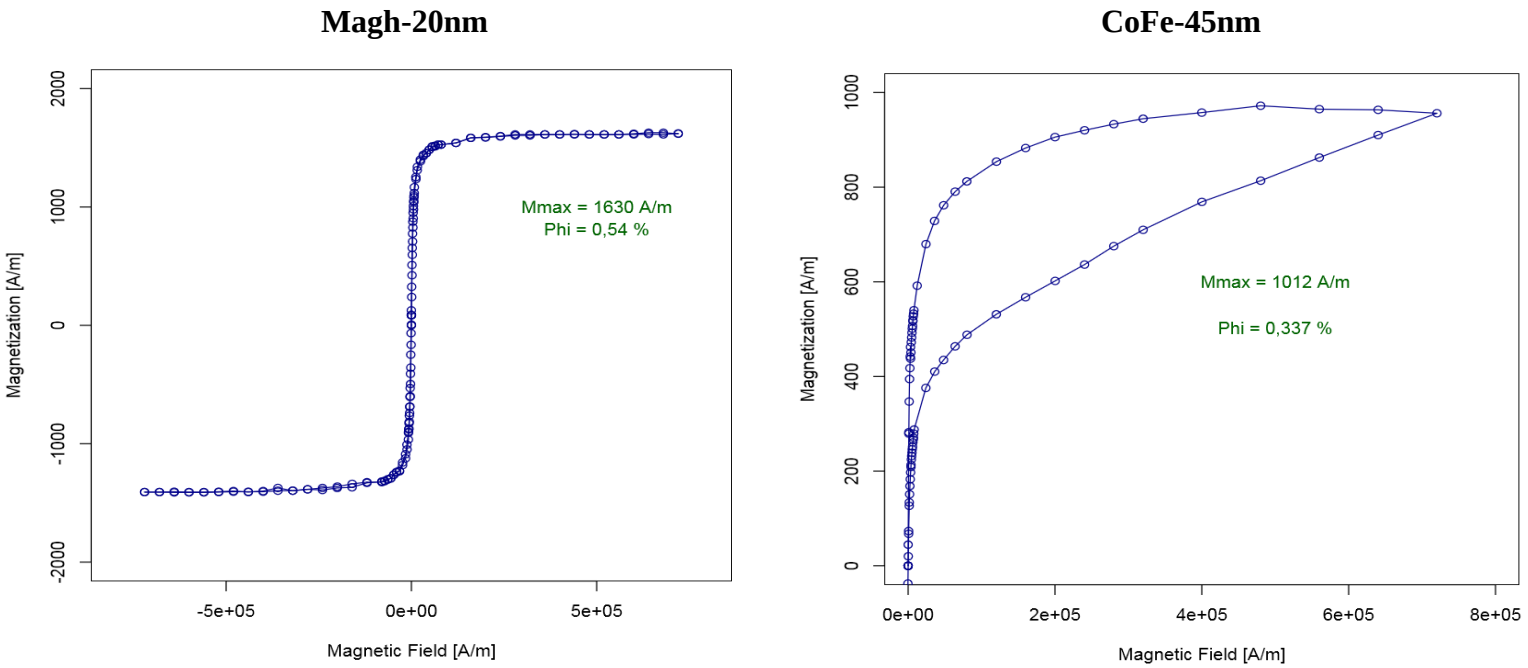

Figure 62: Magnetization curves for Magh-20nm (Fe_2O_3) and CoFe-45nm ($CoFe_2O_4$). Cobalt based nanoparticles exhibit some hysteresis effects. Measurements have been made using superconducting quantum interference device (SQUID) technique.

Magh-20nm MNP show good magnetic properties and constitute a good candidate for magnetic sensing. It has been the most broadly used MNP during the course of this PhD thesis, especially to determine the limit of detection of the device (see section 3.2).

3.3.2 Iron oxide nanoparticles

As the iron oxide nanoparticles gave the most promising results, new nanoparticles were made to improve the device response and prepare the formation of the sandwich immunoassays by binding antibodies on MNP (see section 4.3). These particles have been synthetized by Mrs. Emilie Secret at PHENIX laboratory.

3.3.2.A Nanoparticles synthesis and magnetization

The maghemite cores (Fe_2O_3) are produced by creation of both iron salts Fe (II) and Fe (III) in a basic suspension. The magnetite (Fe_3O_4) nanoparticles are oxidized to obtain a maximum of maghemite which present better magnetic stability in the air but less magnetic response (see section 3.3.2). A size sorting is then applied to only keep the biggest particles. The nanoparticles are citrated to make them stable at pH 7. Different parameters can be used during these steps to change the properties of the obtained MNP like the ratio of magnetite/maghemite or their sizes which are directly related as a bigger nanoparticle size implies a bigger magnetite core.

Figure 63 describes precisely these process steps.

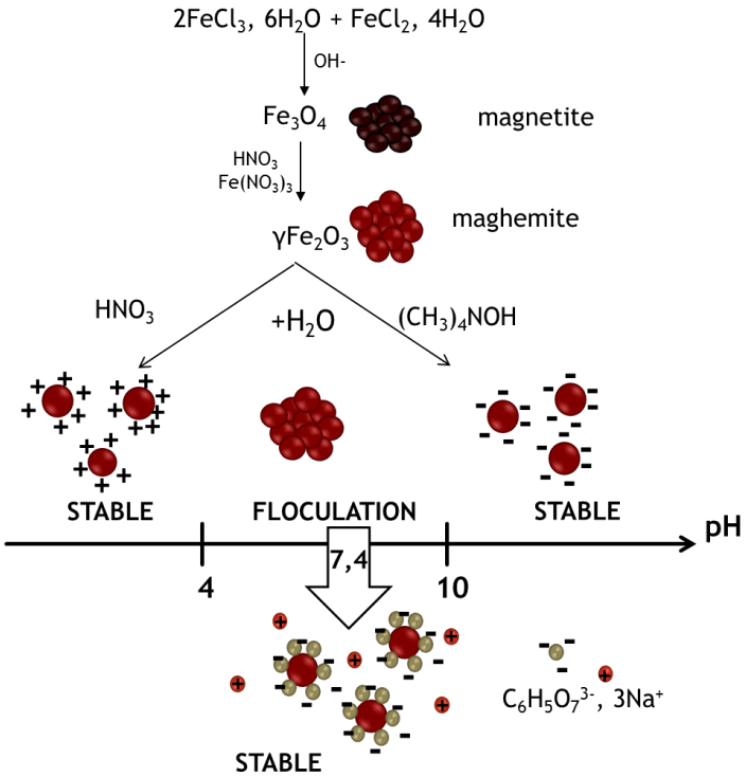

Figure 63: Coprecipitation of magnetic nanoparticles.

As we observed before in the case of the Magh-20nm suspension, the maghemite nanoparticles possess good properties for the magnetic detection device. Four different batches were made: FFRS2, FFRS3, FFRS4 and FFRS9. The different batches have different nanoparticles sizes and maghemite/magnetite ratio (degree of oxidation). The figure 64 shows the magnetization curves of these nanoparticles.

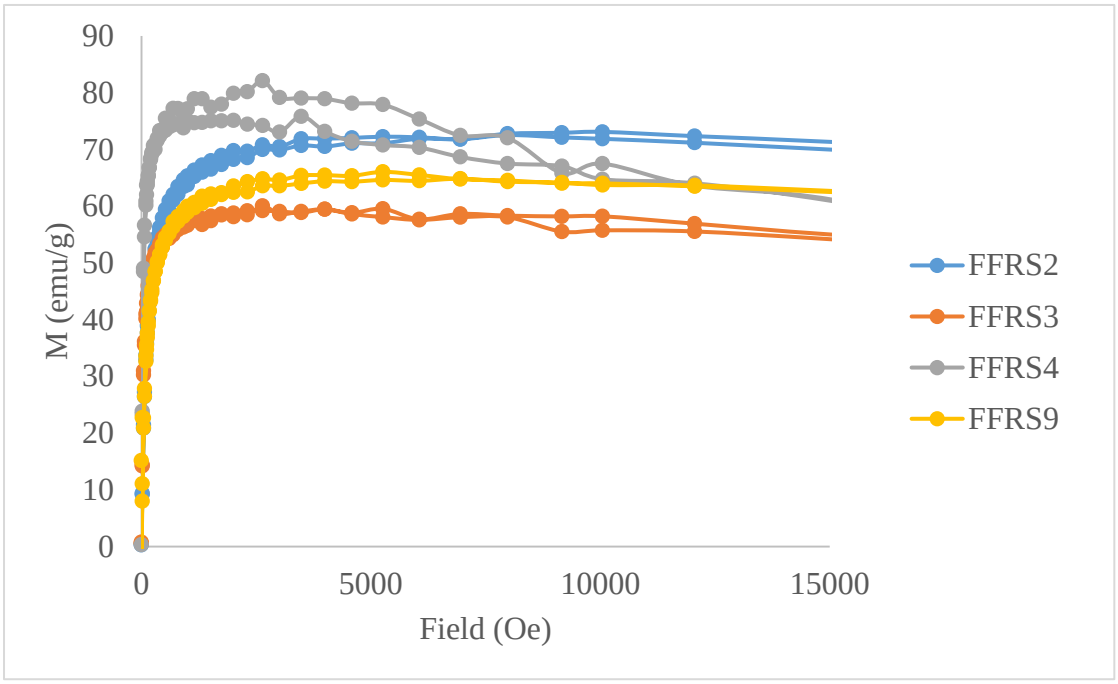

Figure 64: Magnetization curve of maghemite cores. Measurements have been made using SQUID technique.

3.3.2.B Magnetic measurements

We tested the response of these nanoparticles with the magnetic detection device for two different Fe concentrations (4.10^{-3} mol/L and 40.10^{-3} mol/L). FFRS4 shows the best results while FFRS2 had some aggregation problems that prevented a good detection measurement. When magnetic nanoparticles aggregate in macroscopic groups, they do not respond to magnetic excitation fields anymore. As we can observe on figure 66, some of these new nanoparticles show higher detection signals than the previously used Magh-20nm for the same concentration.

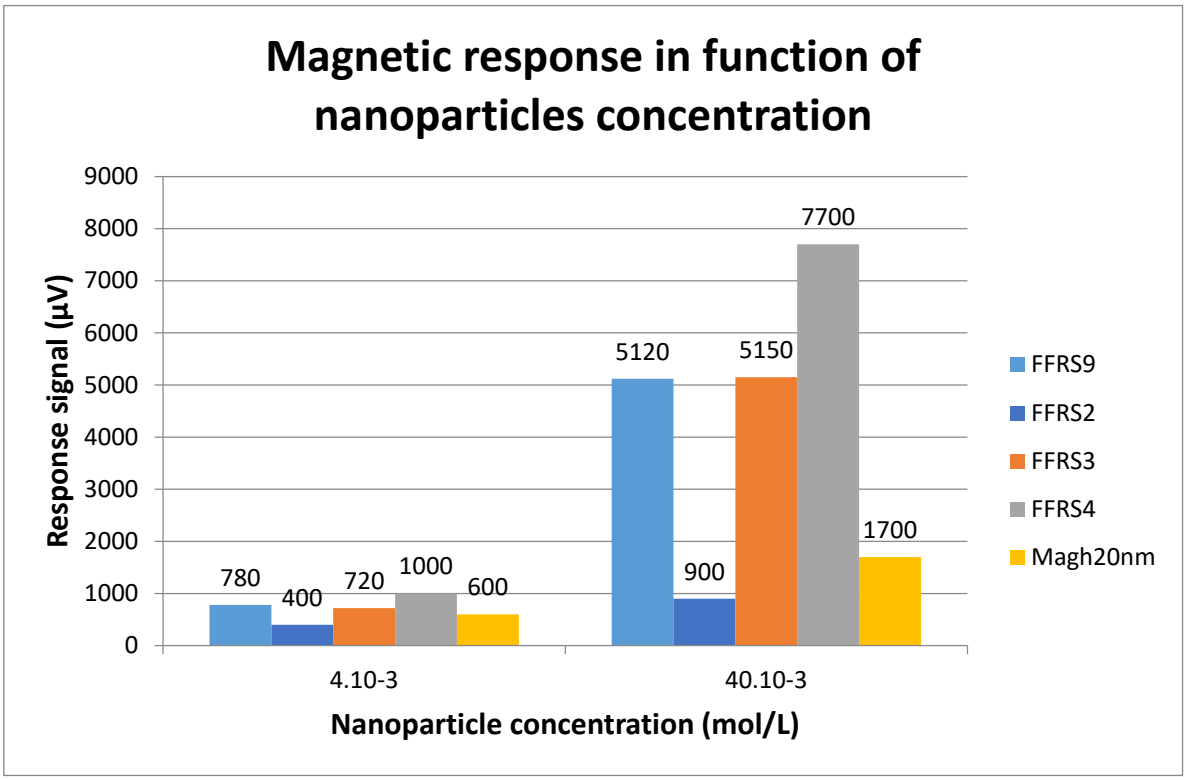

Figure 65: Magnetic response signals of different magnetic nanoparticles for two different concentrations.

We tried to determine which differences between the three new MNP batches are critical for the nanoparticles to show the best result in the magnetic sensing device. The magnetic signal response has been compared to the magnetization saturation, the magnetic susceptibility and the size (table 16 and figure 66).

Table 16: Magnetic properties of different batches of considered MNP.

Nanoparticles references	FFRS9	FFRS3	FFRS4
Composition	Fe_2O_3	Fe_2O_3	Fe_2O_3
Ms (emu/g)	65	60	80
Magnetic susceptibility	0.4428	0.6097	0.9634
Size (core)	8.8 nm	17.4 nm	20.4 nm

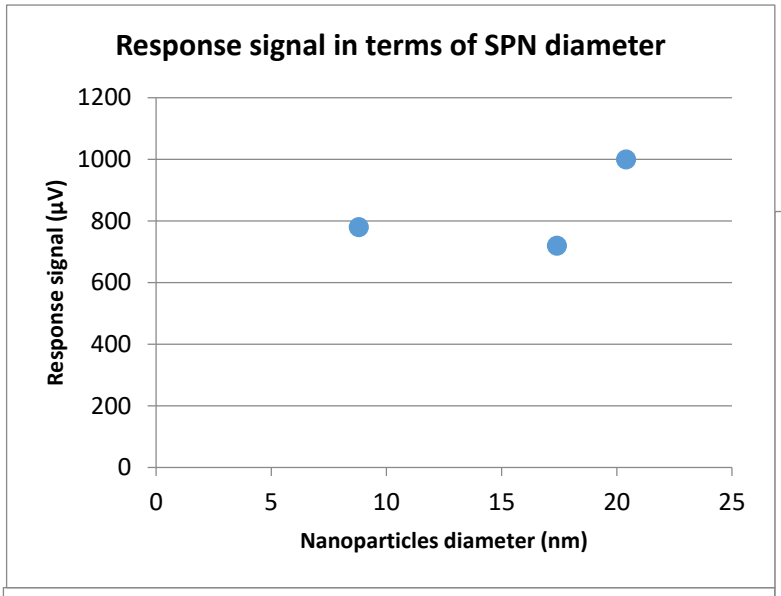

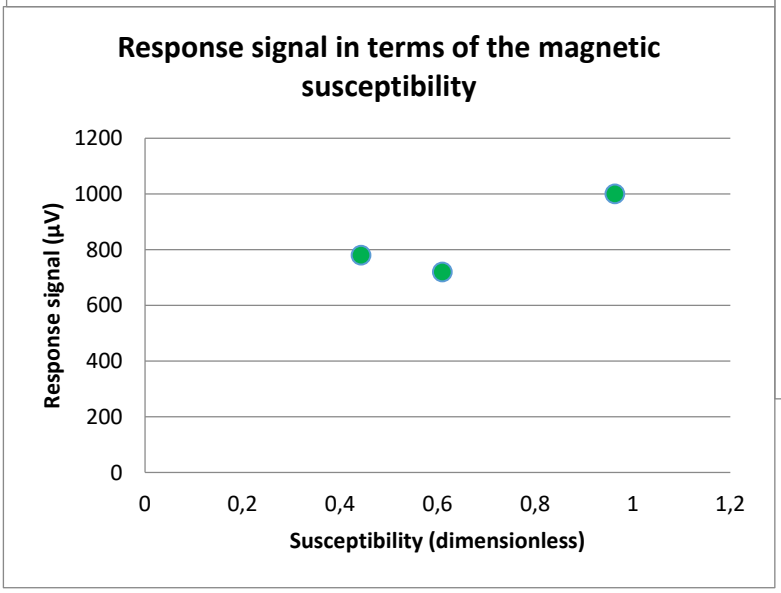

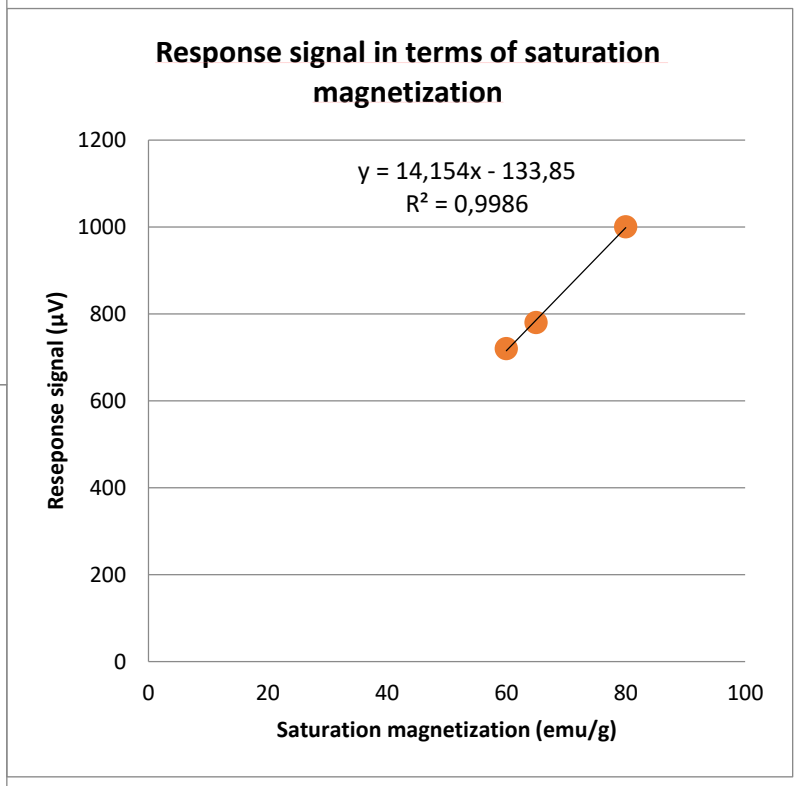

Figure 66: Response signal in function of different magnetic properties for FFRS9, FFRS3 and FFRS4.

As we can see on figure 66, only the response signal in terms of saturation magnetization has a good linearity. Therefore, we can hypothesize that the difference of performance between the nanoparticles is due to the saturation magnetization differences but further measurements have to be done to validate this hypothesis since several parameters change between two batches. Moreover the homogeneity and the maghemite/magnetite ratio are difficult to control and assess as they can change the response signal.

To summarize, superparamagnetic nanoparticles used for the magnetic detection device should be small enough to show a magnetic response, with a good saturation magnetization, synthesized with as much magnetite as possible and shouldn't be aggregated in the suspension thanks to a thick enough maghemite shell.

3.3.2.C Influence of the silicium shell coating on the output signal

Magnetic cores have been coated with a silica shell so that antibodies can be later bounded to them (see section 4.3). This silica has been synthetized using a Stöber process [147], condensing silica precursors in an alcohol media. In our case, the silica layer has been formed in two steps. First, tetrathylorthosilicate (TEOS) is condensed. Then, a thin layer of three different chemicals is cocondensed: TEOS, aminopropyltriethoxysilane (APTES) and [methoxy(polyethyleneoxy)6-9propyl]trimethoxysilane (PEG6-9-silane). The short PEG chains and the amino groups of the APTES allow the stabilization of the synthesized nanoparticles. The amino groups are critical to the future antibody binding by click chemistry that consists of the reaction between an alkyne and an azide. The PEG chains also prevent the formation of a protein corona around the nanoparticle that can interfere with the future antibody-antigen interactions and thus create false negatives [147].

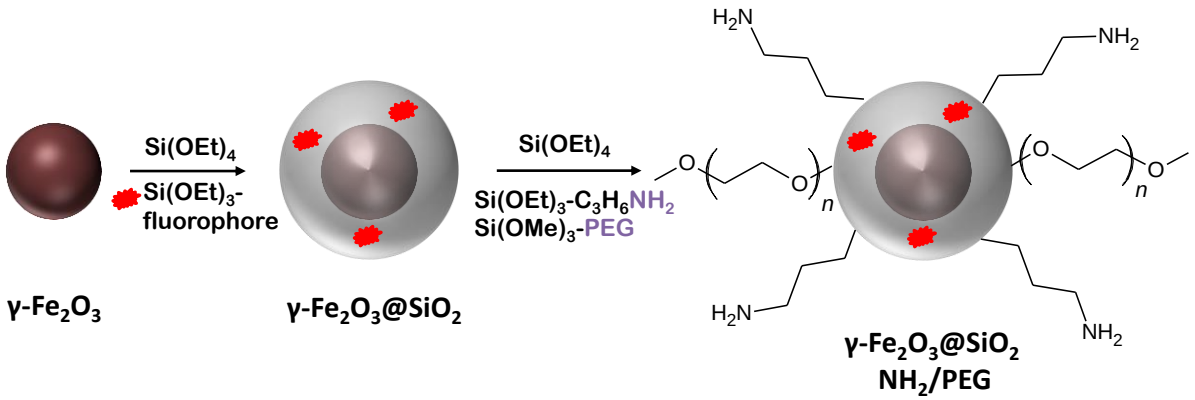

Figure 67: Coating process of magnetic core with silica

FFRS2, FFRS3, FFRS4 and FFRS9 superparamagnetic nanoparticles batches have been coated with silica using this process (figure 67 and 68), they have been respectively named 68, 111, 253 and 168. The coated nanoparticles were tested in the magnetic detection device to determine how the response signal is affected by this nanoparticles coating. A decrease of detection sensitivity performance in terms of concentration could be expected as the coating could affect the nanoparticles rotation.

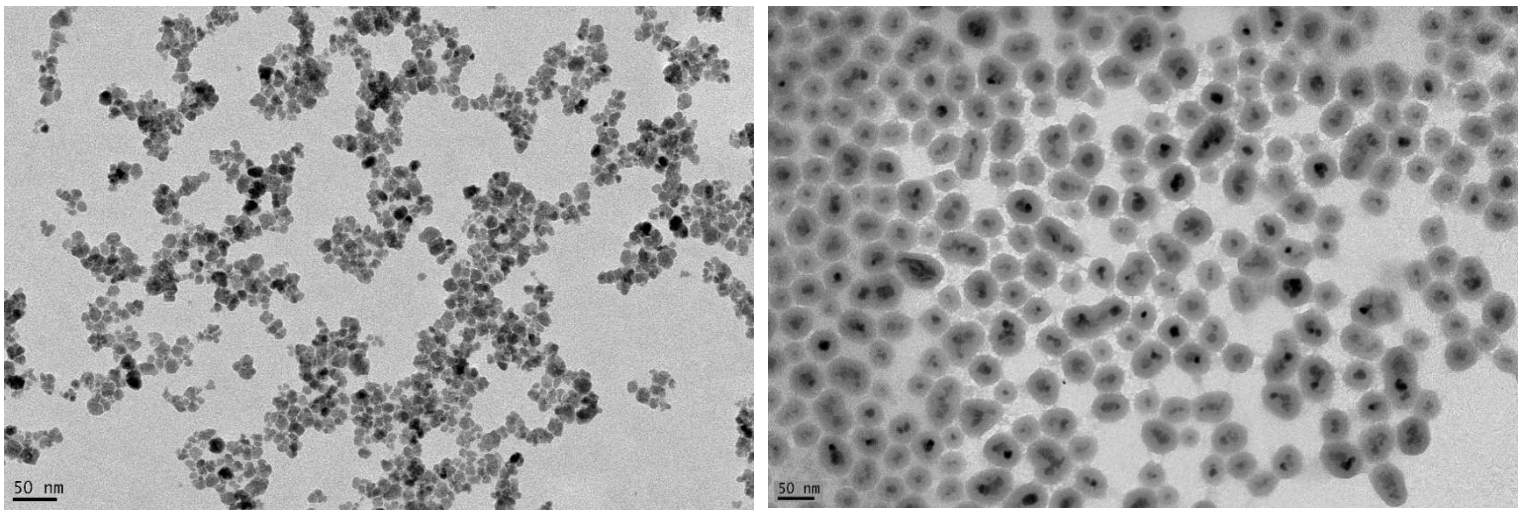

Figure 68: FFRS9 nanoparticles. (Left) Raw nanoparticles. (Right) Nanoparticles coated with silica.

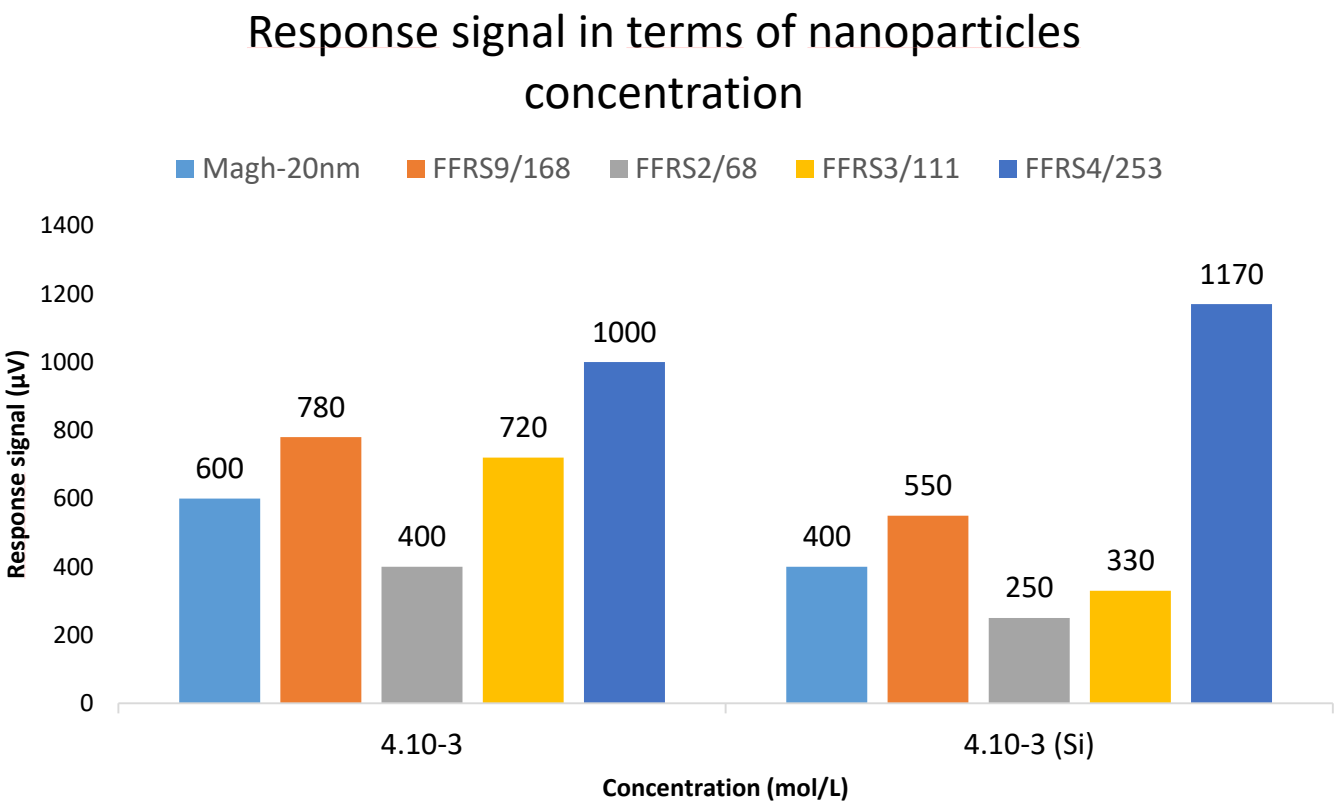

Figure 69: Response comparison of detection response signal between raw nanoparticles (left) and silica coated nanoparticles (right). The same sample of Magh-20nm was used both times, it was not coated.

For these measurements, no notable difference between the raw nanoparticles and the coated ones (figure 69). We notice a decrease between FFRS3 and 111 and an increase between FFRS4 and 253. It should be noted that the general signal response decrease between the two set of measurements, maybe because of mechanical instability, as we can see a difference between the two measurements of Magh-20nm while it is the same batch of particles in both cases. To summarize, it seems that the silica coating does not induce a critical decrease on the signal response (especially on FFRS4 which is still the best suited nanoparticle) as a general trend didn't appear but further measurements could be made to validate this hypothesis.

However there is still a difference between uncoated and silica core shells as the latter have a bigger diameter (between 40 and 60 nm, the raw nanoparticles are between 8 and 20 nm) which implies that for the same volume, the maximum concentration of nanoparticles possible is lower for silica coated beads. There is a nonmagnetic silica volume for the coated nanoparticles.

3.4 Different designed and realized microfluidic structures

After testing the effect of different nanoparticle characteristics on the response signal of the magnetic detection device, we investigated the effect of different shapes and dimensions for the microfluidic channels where the MNP circulate. The goal has been first to maximize the volume of the reservoir between the coils responsible of the magnetic fields emission and detection, but then the emphasis was refocused on improving the surface to volume ratio in order to increase the amount of nanoparticles trapped in the channel for immunoassays. The sandwich configuration indeed needs a bonding surface to be formed so a bigger surface to ratio allows to have more bonded MNP and therefore a higher detected signal.

Three different shapes were mainly used during my PhD project: serpentine shaped channels, spiral shaped channels and microchannels with pillars.

We made all the following channels both in our lab and in the INSP cleanroom in Sorbonne Université.

3.4.1 Serpentine shape

Before the serpentine like microfluidic channel, an oval shaped reservoir (figure 70) was used, but it tended to collapse in its middle after a few experiments, so a more stable serpentine form was designed and realized (figure 71). This serpentine shape does not critically decrease the volume of the reservoir and shows a very good mechanical stability.

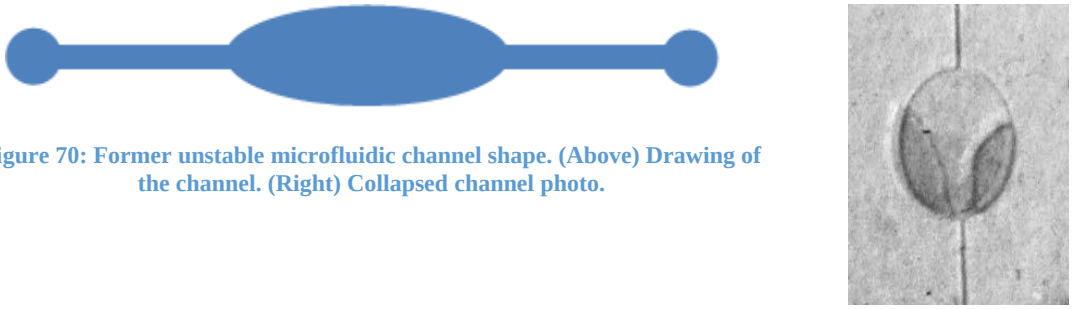

Figure 70: Former unstable microfluidic channel shape. (Above) Drawing of the channel. (Right) Collapsed channel photo.

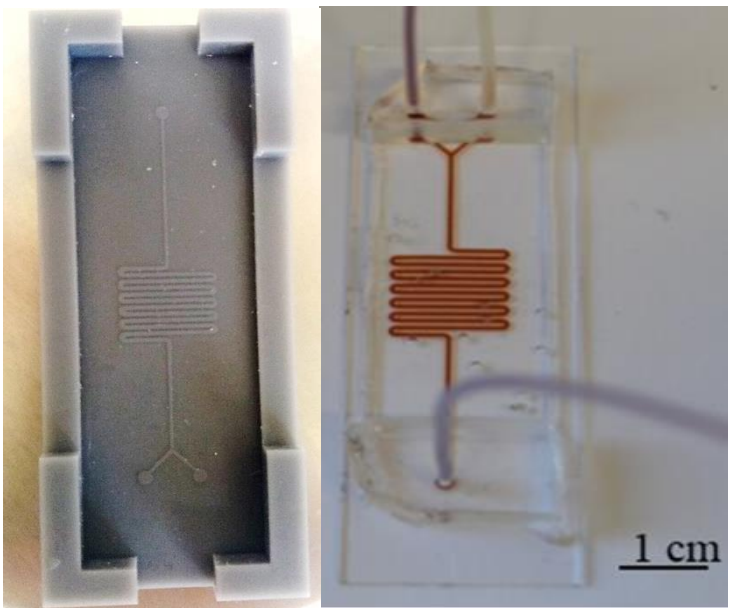

Figure 71: Serpentine microfluidic shape. On the left, a 3D printed master mold. On the right a PDMS serpentine microfluidic channel filled with magnetic iron oxide nanoparticles (orange color) and input/output plastic tubes.

Different geometrical parameters were tested for the serpentine 3D printed master mold to assess the signal responses of the device. The channel width is set at 500 µm for every mold but two different channel heights were tested: 100 µm and 200 µm. The serpentine reservoir part is either a 6x6 µm area or a 12x12 µm (like on figure 71). The space between the channels in the serpentine is set at 500 µm; lower values are indeed not enough to have separated channels as the fluid is passing through because of some irregularities created by the printing technique (figure 72).

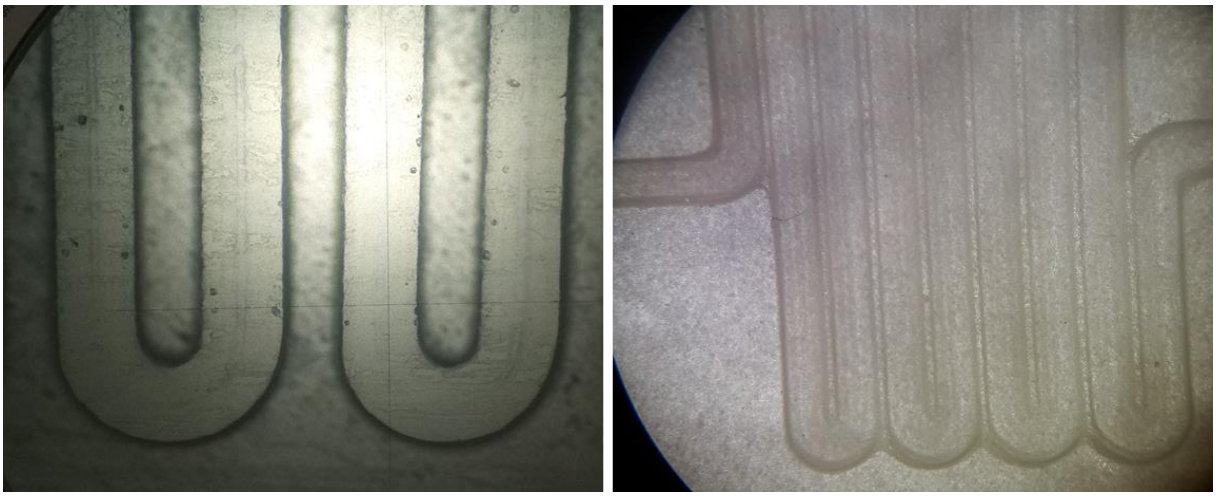

Figure 72: Photos of successful (left) and unsuccessful (right) printing parameters. The spacing between channels is 500 µm (left) and 100 µm (right). We can clearly see that there are some residues left in the spacing between channels.

Measurements were made with three different PDMS microfluidic channels created from these three different master molds. The experimental conditions are quite similar as described in section 3.2, the high frequency signal is set at 40 kHz and the low frequency at 65 Hz. The measurement is made for a high concentration of iron oxide nanoparticles (Magh-20nm) and with a response amplification of 200. The results are shown in table 17.

Table 17: Characterization measurements for different geometrical parameters of serpentine microchannels

Serpentine microfluidic reservoir		**Height between PCBs [mm]**	**Detected signal [mV]**
Dimension reservoir [mm*mm]	**Height channel [µm]**		
12*12	200	2.4	5.60
12*12	200	3.2	3.88
12*12	100	2.4	2.77
6*6	200	2.4	3.21

As we can observe in the above table, a change in the height of the channel will lead to a linear change in the signal response as the channel which is two times thinner lead to a result two times lower ($2 \times 2.77 \approx 5.60$). This result is quite logical because the number of nanoparticles that are responding in the detection zone of the reservoir (namely the serpentine) is directly correlated with the channel height.

We can also observe that reducing the big dimensions of the reservoir from 12x12 µm to 6x6 µm does not imply a linear change in the signal response. This change indeed implies a reduction of 4 times in the volume of the reservoir but the signal response ratio is way lower than 4 ($\text{ratio} = \frac{5.60}{3.21} = 1.74$). This can be explained by the decreasing excitation magnetic field magnitude when moving away from the vertical center point of the excitation coils. As a result, the MNP in the center of the microfluidic reservoir give a higher response than the MNP on the ends. Therefore, we could miniaturize the microfluidic part with limited consequences on the response signal but it also means that increasing the size of the reservoir is not effective to increase this signal.

Finally, we can see that the distance between the coils is critical as a decrease of 0.8 mm (from 3.2 to 2.4 mm for the height between PCBs) induces a reduction of 1.72 mV in the response signal. Therefore, to keep a good sensitivity of the device, the coils should be as close to each other as possible.

3.4.2 Optimization of the reservoir design

In the framework of the Master level internship of Mr. Owen Barrigar (from the university of Waterloo in Canada), that I participated to his supervision at L2E laboratory, COMSOL simulations have been realized considering the microfluidic and chemical engineering parameters.

3.4.2.A Spiral reservoir

The spiral geometry was conceived to localize the nanoparticles within the strongest magnetic field between the two PCB planar coils so that the channel aligns better with the electromagnetic coils. Assuming that the magnetic field generated by the coils is relatively uniform at their center, this shape aims to increase the efficiency of magnetic excitation and detection of the magnetic nanoparticles under the coils center in compare to the larger serpentine channel. Therefore it can provide a more sensitive response to the same amount of MNP in the device.

The mold has been made with a channel width of 500 µm and height of 200 µm (figure 73).

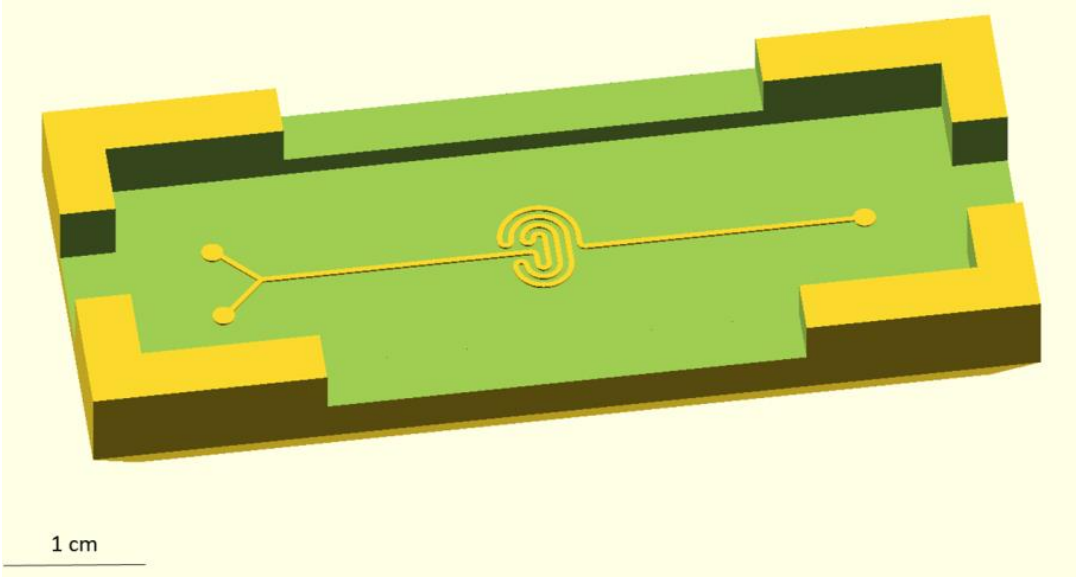

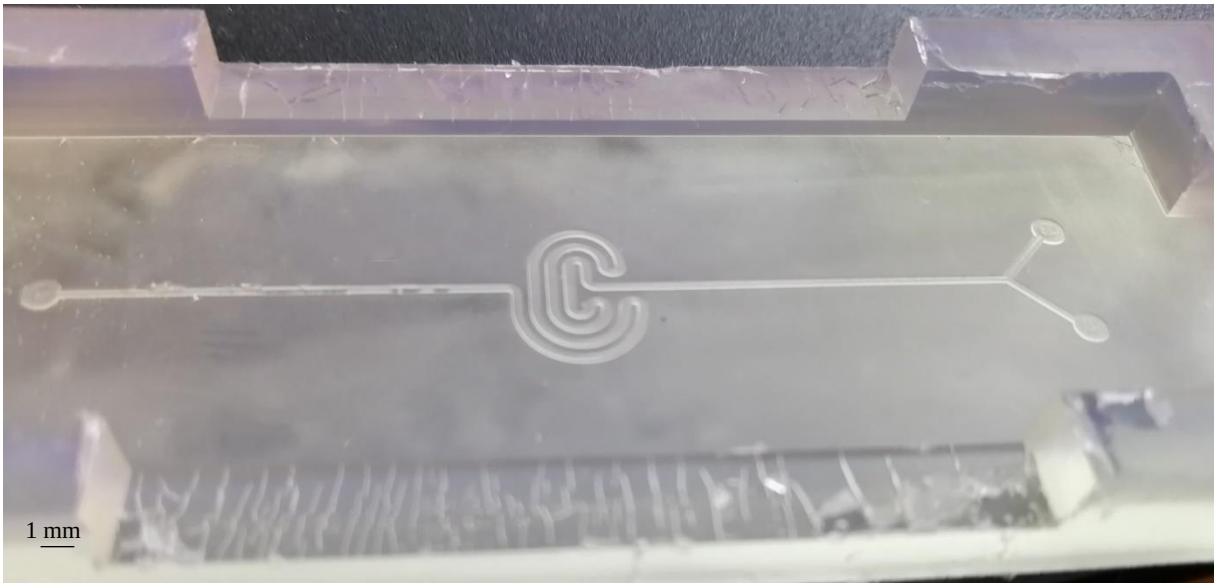

Figure 73: Spiral based reservoir. (Above) Openscad design. (Below) Photo of the realized spiral master mold.

3.4.3.A Pillar-based reservoirs

As described in section 2.2.1, the goal of the magnetic detection device is to create a sandwich immunoassay for the detection of pathogens. Therefore the nanoparticles will only be present on the surface of the microfluidic structure during a test and not in the rest of its volume. Consequently, an effort has been made to improve the surface to volume ratio in the microfluidic reservoir to maximize the amount of nanoparticle bounded to the surface. One way to do that is to create pillars in the reservoir. This approach can also decrease the amount of sample needed for a test and should induce some mixing of the suspension with the flow which can improve its homogeneity (figure 74).

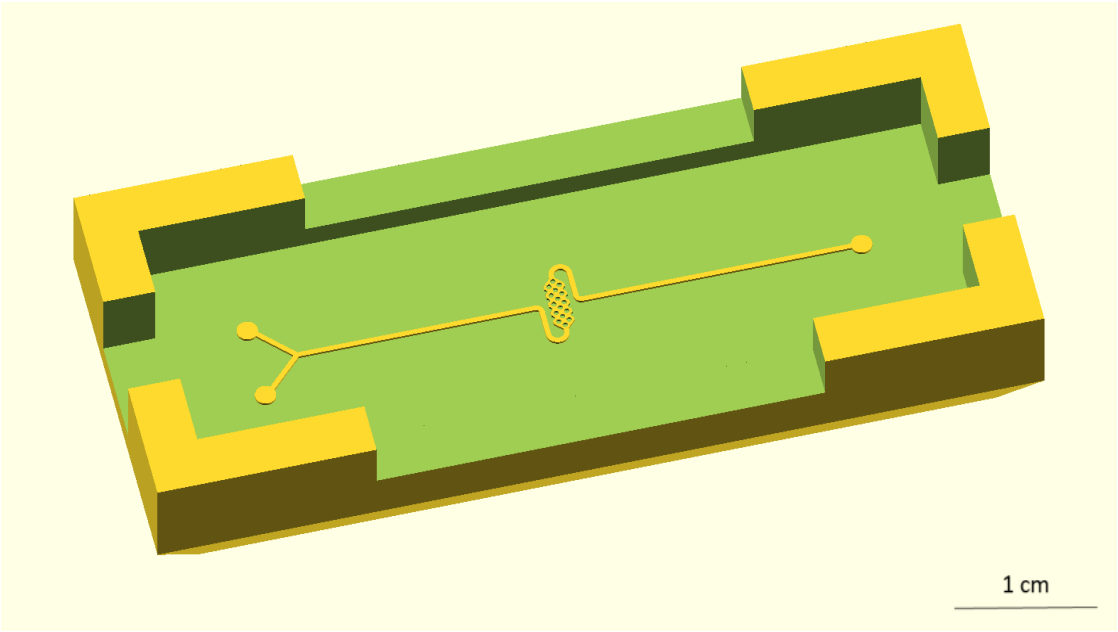

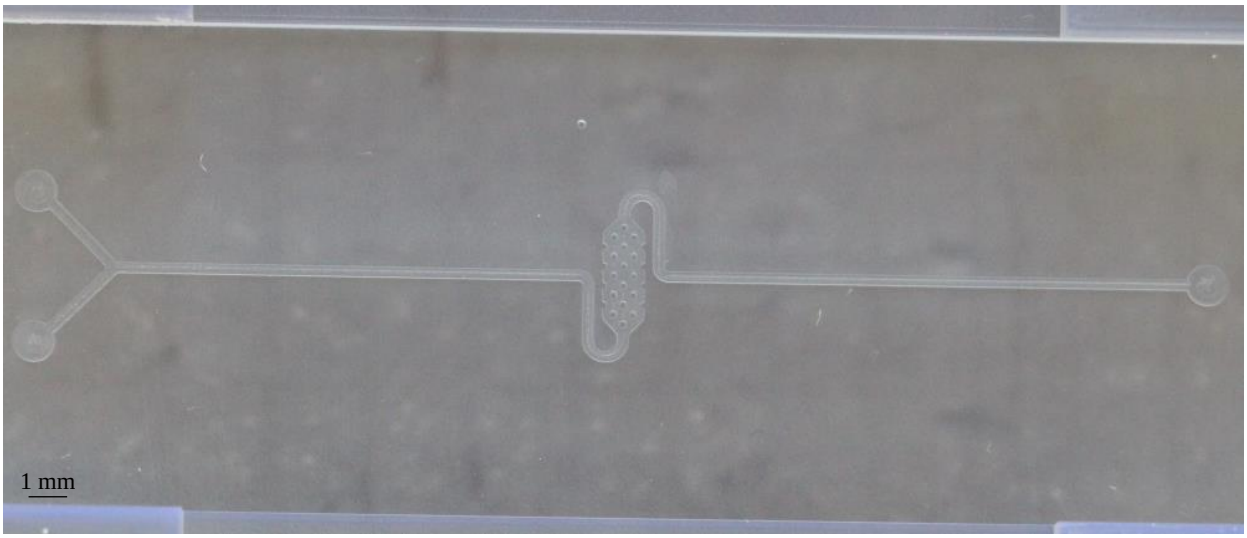

Figure 74: Pillar based reservoir. (Above) Openscad design. (Below) Photo of the realized pillar master mold.

Each pillar radius is 200 µm and the reservoir width that contains these pillars is 2 mm wide and 6 mm long. The surface to volume ratio for the serpentine and spiral reservoirs is equal to 9000:1 (9000 cm^2/cm^3) whereas the surface to volume ratio of the pillar-based reservoir is equal to 11500:1.

3.4.3 Simulations

COMSOL simulations have been achieved to address the fluid velocity profile (and potential dead volume), concentration profiles in fluid flow, surface concentrations and reaction kinetics in order to select the most adapted design. These simulations intend to compare the different designs and not necessarily to replicate their exact behavior, especially in terms of surface reaction kinetics. COMSOL 5.0 and 5.3 were used with parameters given in appendix 2. The Laminar Flow, Transport of Diluted Species, and Surface Reactions modules were used.

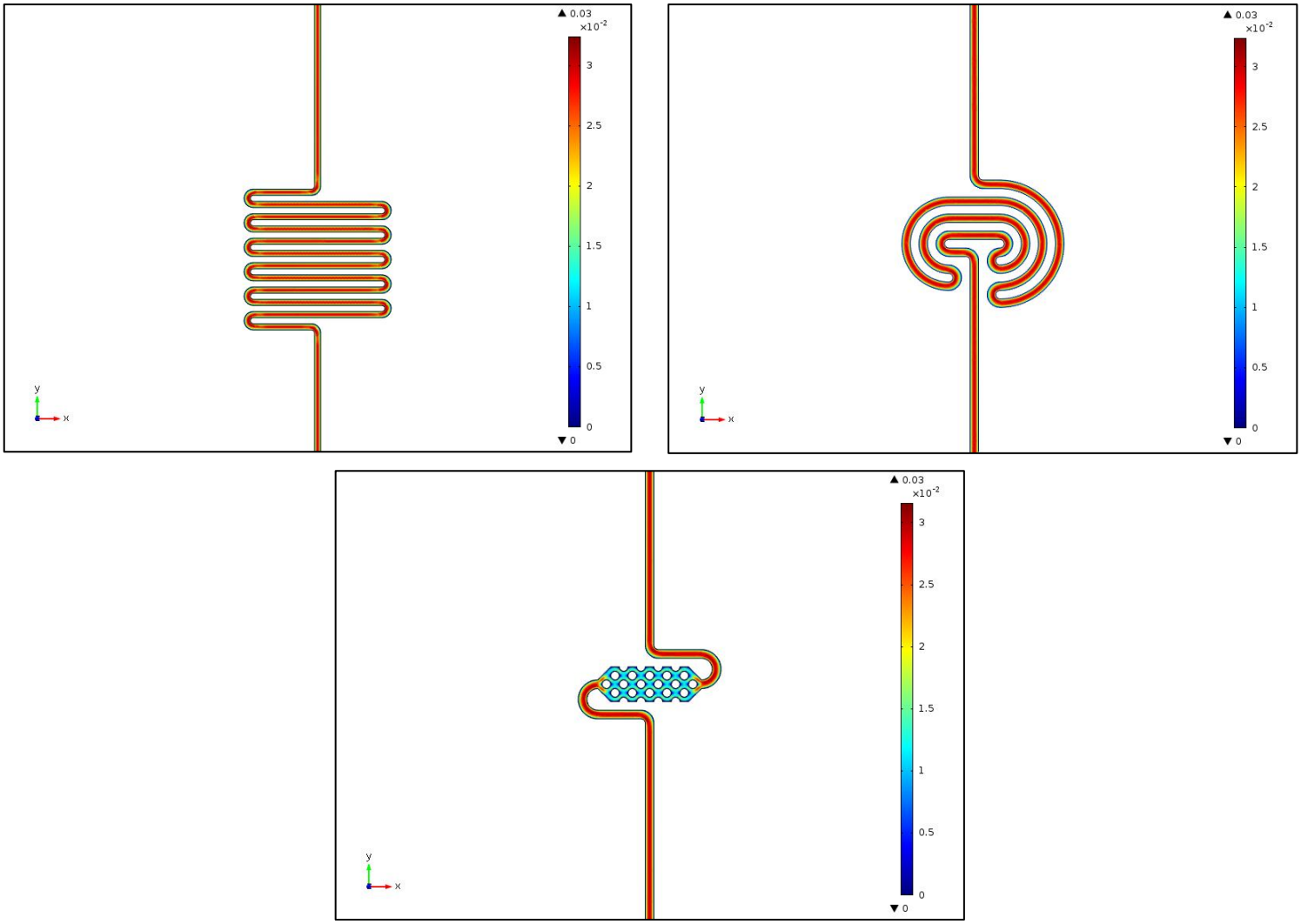

Figure 75: Simulated steady-state fluid velocity profile (m/s) in the serpentine reservoir. The inlet and outlet are located at the bottom and top of the image, respectively. Volumetric flow rate was 90 µl/min. (Top left) Serpentine reservoir. (Top right) Spiral reservoir. (Down) Pillar-based reservoir.

As we can see on the simulations observable on figure 75, the flow of the fluid in the channel is quite constant for the serpentine and spiral shapes whereas the flow of the fluid is decreased by half when it enters the reservoir containing the pillars. This can be explained by a higher fluidic resistivity due to the presence of pillars in this type of reservoir. This should not be a problem for the use of this microfluidic channel design; on the contrary, a slower flow rate could improve the antibody-antigen interactions on the central portion of the device. However, some dead volumes are visible on either side of the pillars and in the corners along the edges of the reservoir. This indicates that there could be a lack of homogeneity of the surface species in this reservoir over time, at least until saturation has been reached.

Antigen surface concentrations have been simulated for the three different reservoirs at different adsorption rates but the results are practically the same for every design.

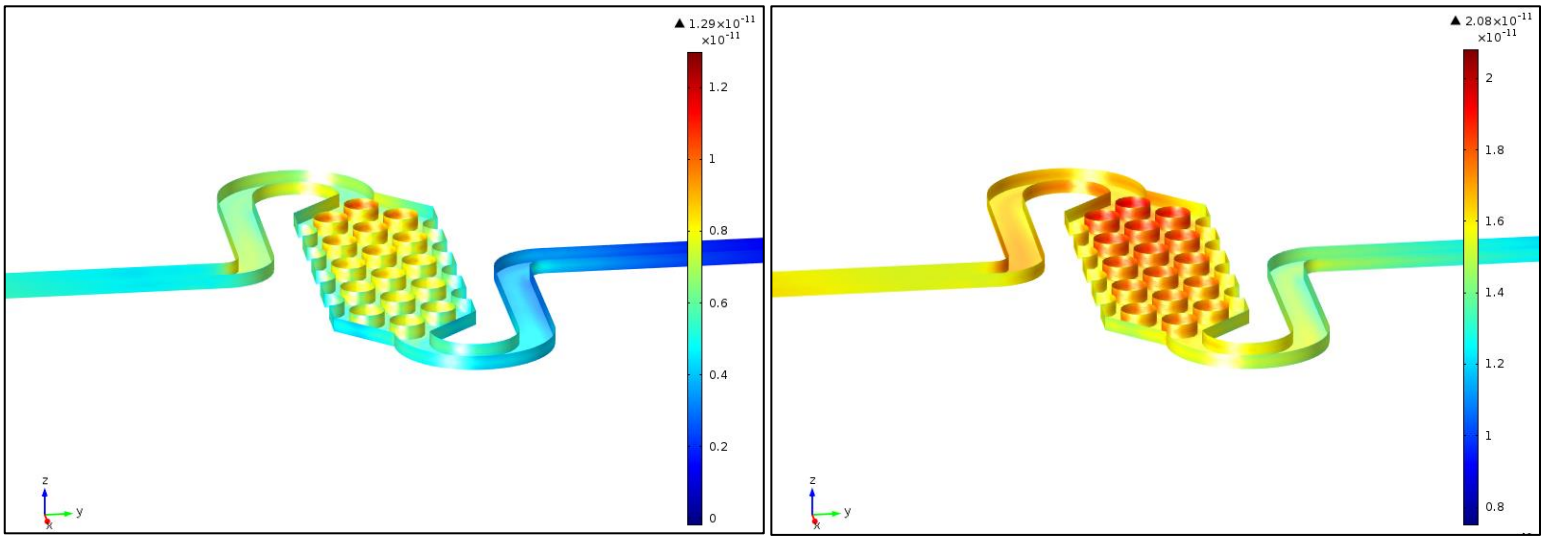

Figure 76: Pillar geometry analyte surface concentration after 5 seconds of flow (left) and 10 seconds of flow (right).

Figure 76 demonstrates the lack of homogeneity in terms of the immobilization of the analyte onto the surface, as predicted based on the velocity profile. The difference in surface concentrations of the pillars might present some difficulty in attempting to achieve high device sensitivity. This problem could be limited by optimizing the time of flow before the measurement.

3.4.5 Measurements and comparison

The three different channels were tested in the magnetic detection device with the same conditions and show results that appear in the table 18.

Table 18: Characteristics comparison between the three microfluidic designs

Geometry	Serpentine	Spiral	Pillar-based
Simulated pressure drop (Pa)	900	410	250
Surface to volume ratio (m^{-1})	9000	9000	15500
Reservoir volume (μL)	17.28	8.26	1.32
Results for a test with iron oxide nanoparticles suspension (mV)	3.8	2.8	1.5

The pressure drop of the spiral and pillar based designs is lower because they have shorter channels in comparison to the serpentine one. The pillar-based reservoir seems to show a very good response to volume ratio but, as we saw in section 3.4.1. The comparison with the serpentine channel is difficult because the particles close to the center of the channel show a higher response which means that the relation between the signal response and the reservoir volume is not linear. To reduce this phenomenon and allow a better comparison between the serpentine and the pillar-based channels, a bigger pillar based channel was fabricated that contains approximately the same sample volume (figure 77).

Figure 77: Photos of the small volume 1.32 µL pillar based reservoir (left) and the bigger one that can be compared to the serpentine reservoir (right) that can contain 17.3 µL.

The new pillar-based microchannel (figure 78) was tested and compared to a serpentine microchannel in the same experimental condition (iron oxide and a first lock-in amplification of 500 (table 19)):

Table 19: Serpentine and pillar-based reservoir comparison.

	Serpentine reservoir	Pillar-based reservoir
Volume (µL)	17.28	17.3
Response (mV)	12	7

The pillar-based response is lower than the previously used serpentine design microfluidic channel for a similar volume. Again this can be explained by the fact that pillars take some space in the middle of the reservoir that is critical to retrieve the maximum response.

The spiral microfluidic channel is interesting to use because it needs less sample and is more efficient than the serpentine shape reservoir. But in the end, the pillar-based reservoir is most interesting since the improvement of the surface to volume ratio is critical to bind as much superparamagnetic nanoparticles as possible in the system in the context of a sandwich immunoassay. Other techniques have been investigated to increase this ratio in the microfluidic device to further improve the magnetic response; they are presented in the following section.

3.4.6 Further work for surface/volume ratio improvements

Improving the surface to volume ratio is a way to improve the signal response of the magnetic detection device in the case of immunoassays but it also complicates the device fabrication. Several strategies should be tested to determine the advantages and drawbacks of each one and select the most suited one for our application.

A very precise 3D printer could be used to add even smaller pillars in the microfluidic channels to increase the surface. But this kind of printer is very expensive, and the mechanical stability of the pillars would have to be tested. SU8 method could also be used again with the drawbacks described in section 2.3.1.A. [148].

A porous material could also be inserted in the channels to greatly increase the usable surface. In that case, the use of syringe pump can be risky because with a constant flow rate the pressure could increase during the experiment and deteriorate the channel. The pressure controlled microfluidic pump that we purchased and installed recently on pur setup can prevent this problem and allow us to test this approach. Some works can be found in the literature regarding this strategy [149].

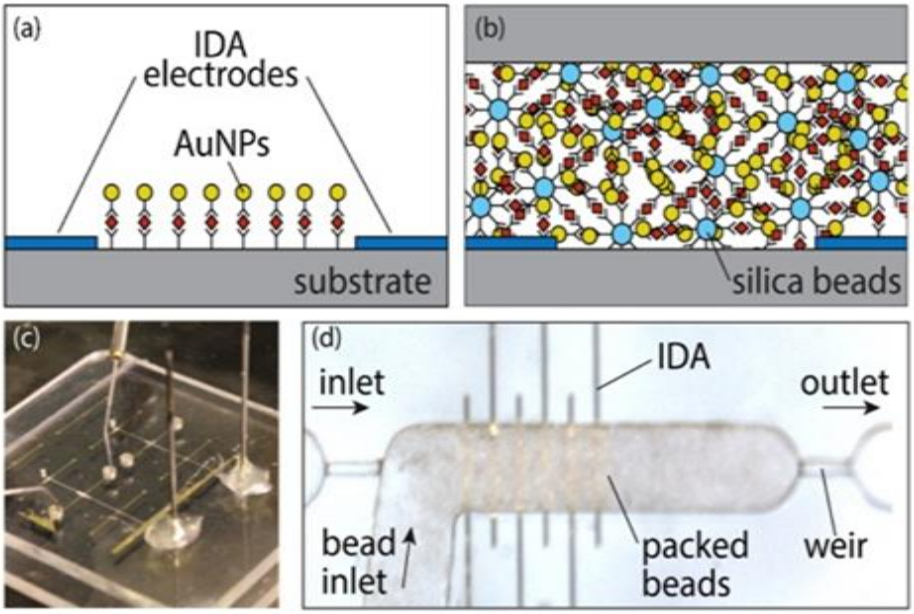

Figure 78: Idealized views of a (a) planar and (b) volumetric impedimetric immunosensor. (c) Fabricated thermoplastic device, and (d) magnified view of the detection zone including thin film gold interdigitated electrode array (IDA) and packed bed of functionalized silica beads in a 150 µm deep channel [150]

Another method consists of trapping silica beads, where the antibodies could also bind, inside the microfluidic channel (figure 78). With this method the sandwich configuration can be formed on the surface of the channel but also on the surface of the silica beads that would lead to an increased number of MNP trapped in the system in case of a positive response during an immunoassay. This strategy has been applied to improve immunosensors before [150]. Silica beads are nonmagnetic which make them compatible with our device. A drawback is that the way to trap silica beads in the channel could complicate the design of the microchannel and increase the cost of its fabrication.

3.5 Improving the limit of detection (LOD) using an external DC magnetic field

Until now all the measurements were made at the mixing frequency term f_1+2f_2 but the results could be improved by adding a static magnetic field (DC field) and measure the peak at f_1+f_2. This test has been made with the bigger transportable device developed at the institute of bioelectronics in Juelich research center described in the section 2.2.1 and illustrated in the figure 79 [109].

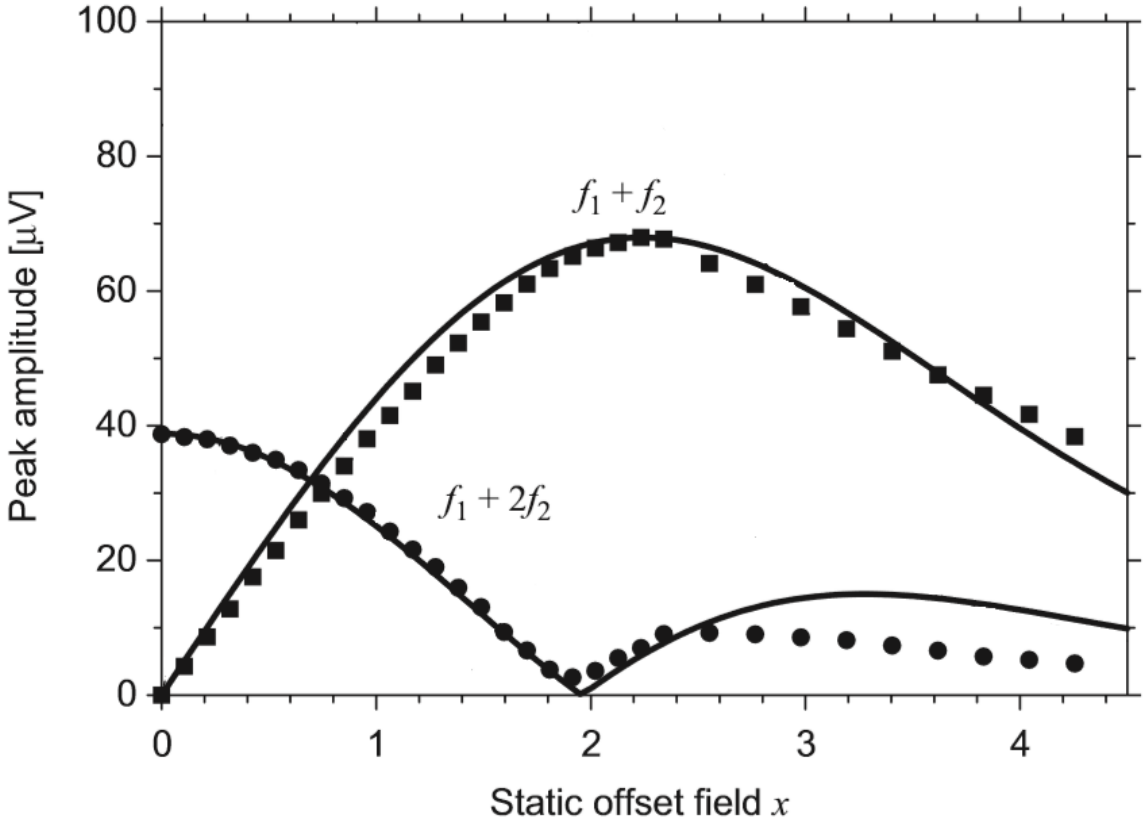

Figure 79: Measured frequency mixing amplitude of the components $f_1+ f_2$ (squares) and $f_1 +2f_2$ (circles) as a function of the dimensionless static magnetic offset field $x=\mu_0*H/B_0$, with B_0 = 1,9 mT, for an excitation amplitude $A_1=0.8*B_0$ at 49.38 kHz and a driver amplitude A_2 = $2.4*B_0$ at 61 Hz [109].

First, we assessed the response signal for f_1+2f_2 and for f_1+f_2 without adding any DC field and with different excitation voltages for f_1 (figure 80). The parameters are:

- f_1 = 40 kHz
- f_2 = 65 Hz with 48 Vpp
- Magh-20nm magnetic nanoparticles

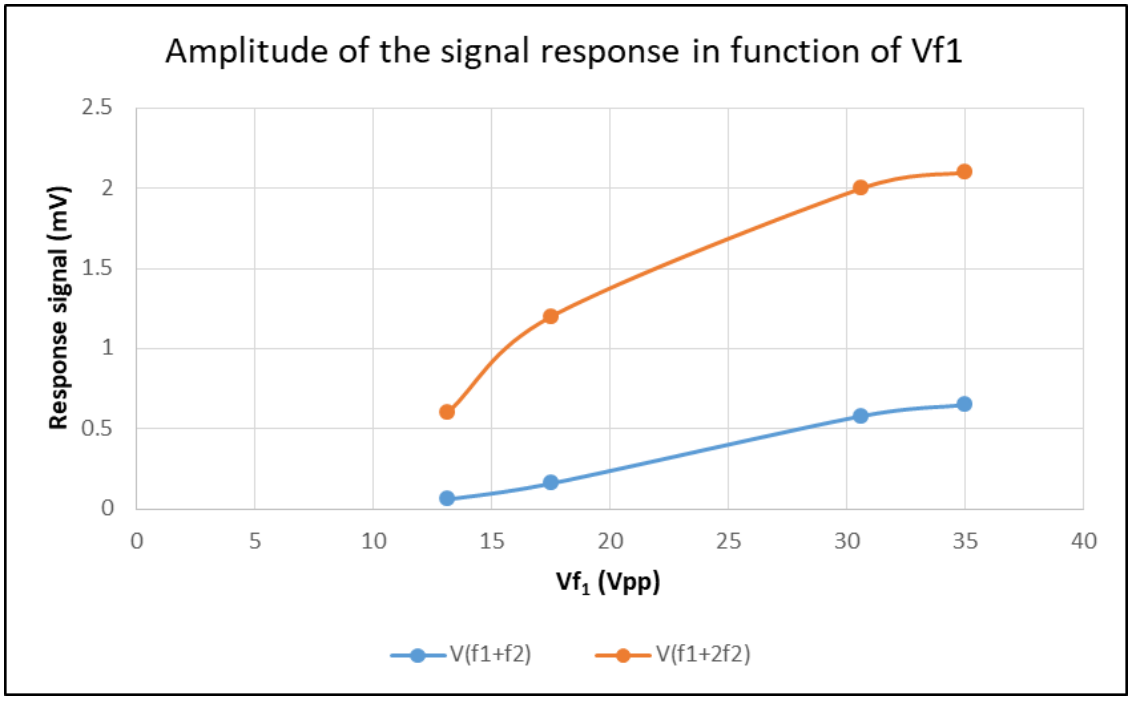

Figure 80: Amplitude of the response signal in mV for f_1+2f_2 and for f_1+f_2 without an external applied DC field.

As expected, without the static offset the response is better at f_1+2f_2. For the rest of the experiments the response will be measured at the maximum of Vf_1.

3.5.1 Measurement results using designed and realized Helmholtz coils

A DC field is now added by using Helmholtz coils which surround the device (figure 81) as they can produce a static magnetic field when an electrical current is applied to them [151]. These coils have been made by 3D printing for the plastic support then coiled with a copper wire around these parts. The two coils are placed above and below the magnetic detection device.

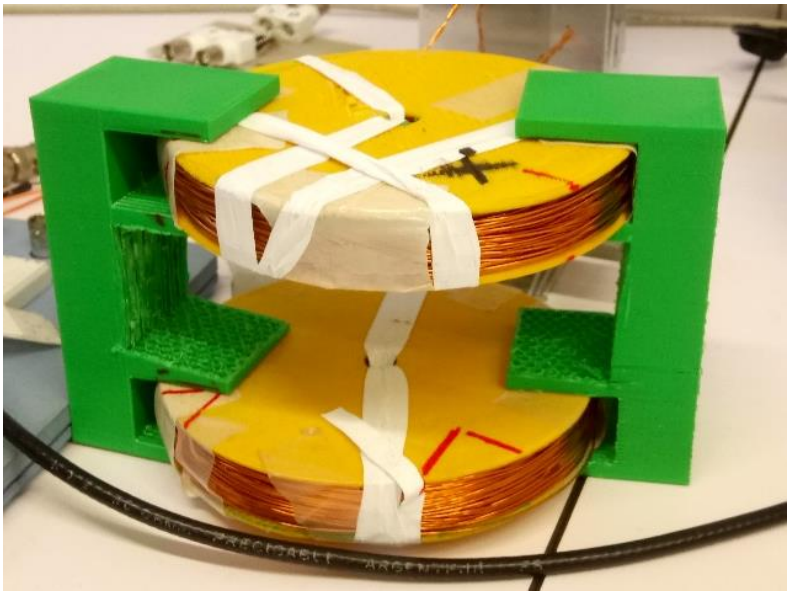

Figure 81: Helmholtz coils with 200 turns for each of the copper wire coils.

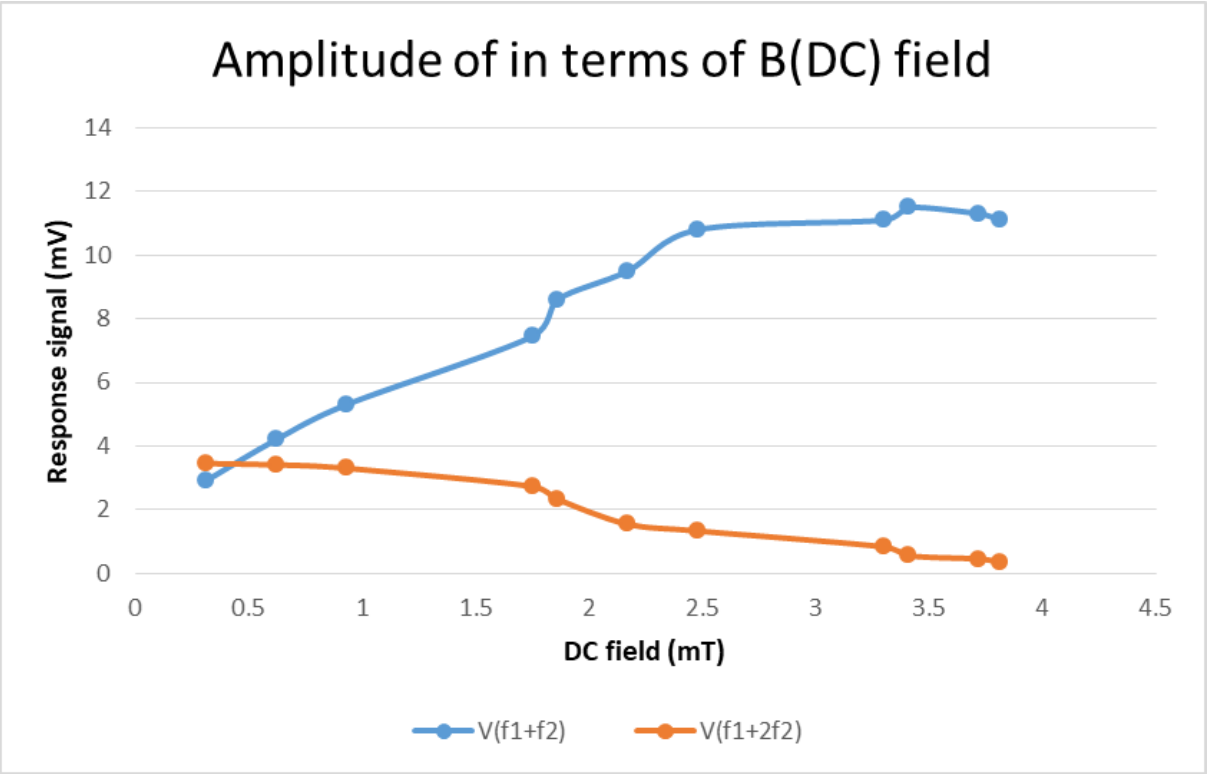

Figure 82: Amplitude of the response in mV for f_1+2f_2 and for f_1+f_2 with a DC field

It is clear that the response is better with f_1+f_2 when a DC field is applied with the Helmholtz coils (figure 82). But this strategy has been too impractical and cumbersome, as Helmholtz coils are relatively is big and need power supply, in comparison to the permanent magnets that are presented in the next section.

3.5.2 Measurement results using adapted permanent magnets

We then used permanent magnets to create the static magnetic field. They are much smaller than Helmholtz coils and do not require any electrical current to generate a magnetic field.

The permanent magnets were placed at different distances from the device to vary the strength of the DC field applied on the nanoparticles (figure 83). The DC magnetic field was measured using a gaussmeter.

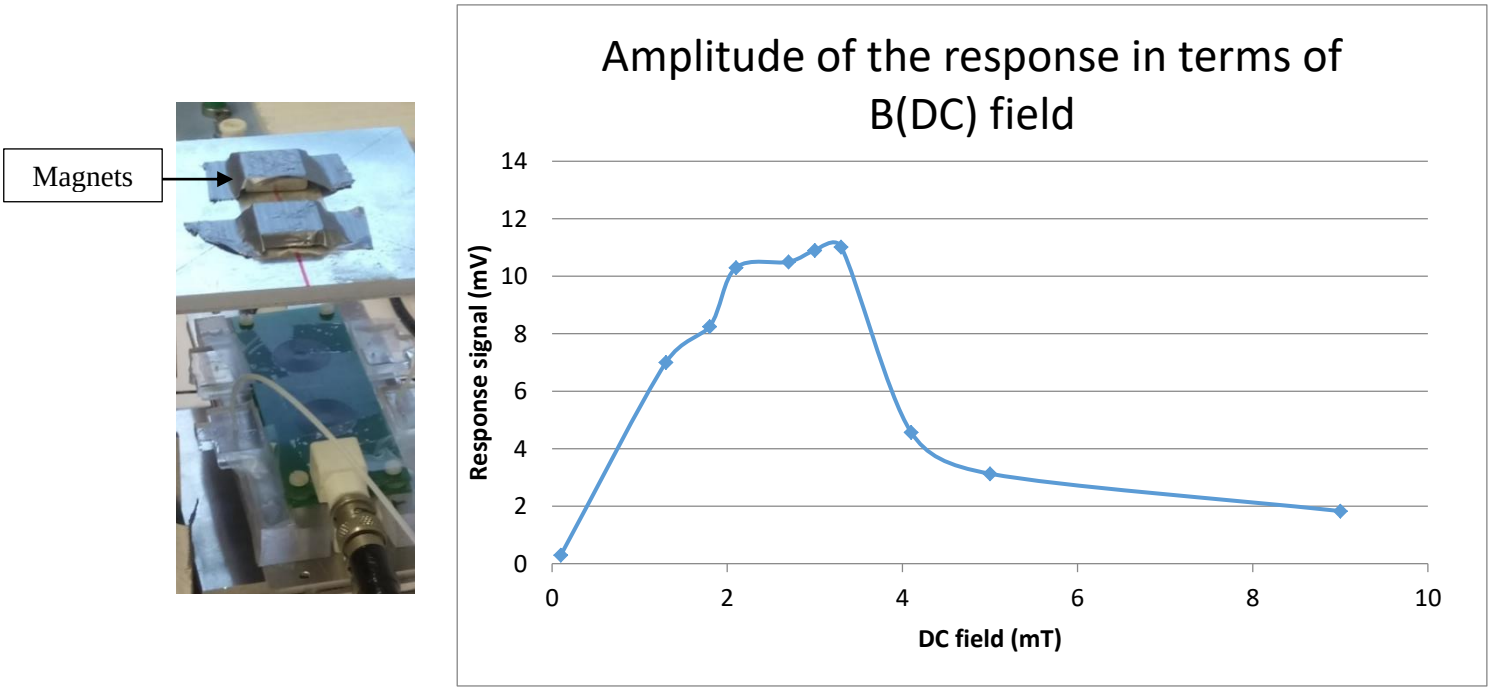

Figure 83: (Left) Permanent magnets above the system. (Right) Amplitude of the response signal as a function of the applied DC field using the permanent magnets.

The maximum response signal for f_1+f_2, that we obtain for a static field of around 3 mT at the sample reservoir microchannel, is approximately 5 times higher than the response signal for f_1+2f_2 without DC field and almost 20 times better than f_1+f_2 without DC field, having for all measurements the same concentration of iron oxide nanoparticles. We also observe that if the DC field is too strong the response from the nanoparticles becomes less measurable which is in agreement with the result by Krause *et al.* (figure 79 [109]). The increase in the amplitude response with permanent magnets is interesting because it can improve the limit of detection, but it can also allow us to diminish the amplitude of the excitation signal of f_1 and get the same result than before. This is very interesting if we want to decrease drastically the energy consumption of the system.

3.6 Conclusions

The optimization of magnetic nanoparticles sizes, physical and chemical properties have been considered using various experimental conditions in order to enhance the sensitivity of our magnetic detection device. The effect of microfluidic microchannel geometries, forms and especially the surface to volume ratios have been also investigated to improve the sensitivity and bonding surface area for biofunctionalization purpose.

However, at this time the device has only been tested with nanoparticles suspensions where they are in suspension in a volume. The device has not been tested yet in immunoassays conditions, namely in a sandwich configuration where MNP will be only present on the surface of the microchannel and not in the whole volume.

The next chapter presents the preliminary results to create this sandwich configuration necessary to perform pathogen sensing immunoassays. In the final IVD (In-Vito Diagnosis), and hopefully optimized point of care (POC) magnetic immunoassay device, these sandwich configuration antibody-antigen interactions should take place in a single use microfluidic chip that can be inserted in the magnetic detection device.

Chapter 4. Surface and nanoparticle functionalizations for immunoassay

4.1 Introduction

In this chapter, the work to bind antibodies on the microfluidic materials and on nanoparticles is presented. PDMS, COC and PMMA have been selected for the microfluidic channel materials and therefore been functionalized with antibodies. We have been doing this functionalization with the help of the LRS laboratory while the PHENIX laboratory has been working on the nanoparticles functionalization (figure 84).

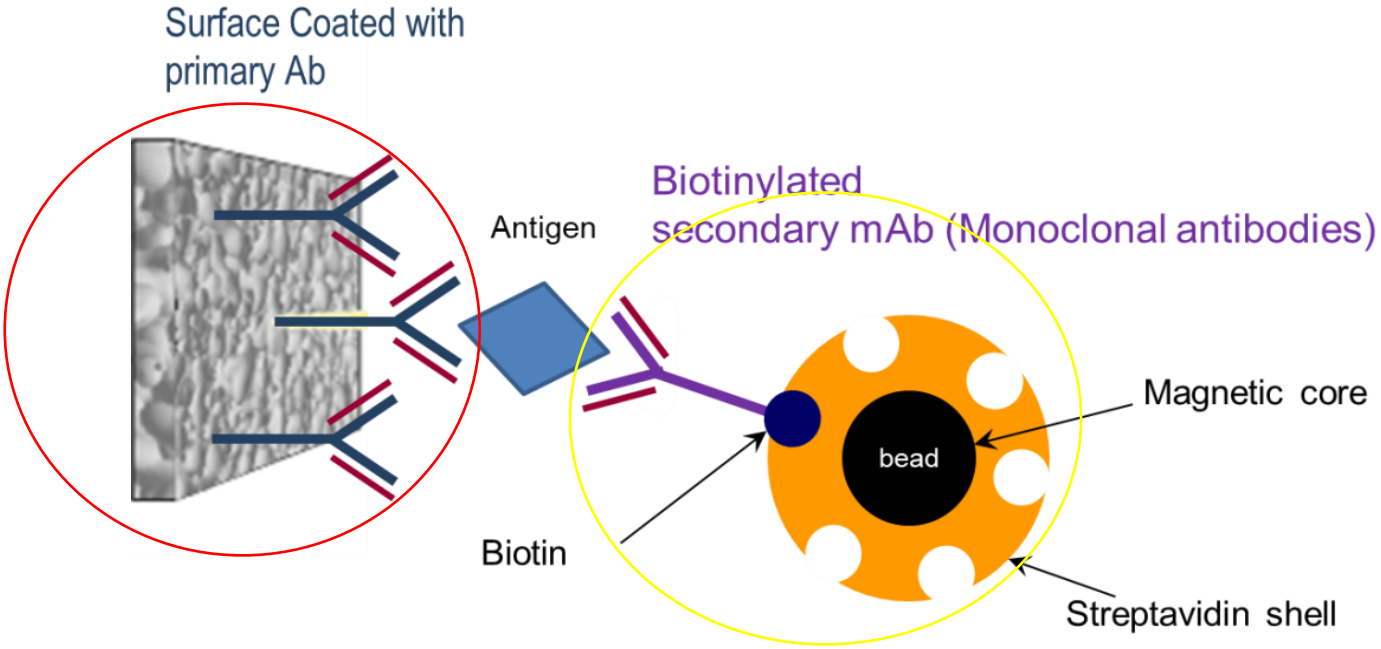

Figure 84: Surface functionalization (red circle) is discussed in 4.2 and nanoparticles functionalization (yellow circle) is discussed in 4.3

To test the device with a sandwich immunoassay, human C-reactive protein (CRP) has been selected to simulate a pathogen we want to detect as proof of concept. CRP is a ring shaped protein produced by the liver that can be found in the blood plasma [153]. Its concentration increases drastically when an inflammation occurs in the body which can indicate an illness including cancer [154]. We chose this protein to test our prototype device because it is a relatively cheap, well known and characterized one that has different corresponding antibodies that can be easily ordered.

After choosing the antigen, a method has to be defined to immobilize the corresponding antibodies to the other parts of the system which are the microchannel surface and the MNP. In order to efficiently perform the bioreceptor function, an antibody immobilization technique should:

- Immobilize as much antibody as possible on the surface to increase the number of pathogen trapped in the system consequently improving the response signal.

- Limit the non-specific binding as much as possible. Non-specific binding is the phenomenon where secondary antibodies bind the surface even in the absence of the analyte (CRP in the proof of concept) in the system thus causing a false positive.

- Be as durable as possible and irreversible so the immunoassay can be performable for as long as possible.

- Be as reproducible as possible so that the results could be similar for two microfluidic reservoirs.

Moreover, the specificity should be as high as possible, namely only the analyte should be bounded by the primary antibody. If other entities take the place of the analyte on the binding site, the detection will not be effective.

The process should not be too expensive. In our case the cost are reduced by the very little amount of antibodies needed to coat the surfaces of a microfluidic channel.

4.2 Surface functionalization with covalent binding

The surface functionalization aims to bind anti-CRP antibodies on the surface of the microfluidic channel inside the detection device so the protein can be specifically bound inside the system and be detected. The reference of primary (or capture) antibody we chose to bind to the surface is MAB17071 from R&D systems (appendix 3). For the final device, this step of surface functionalization should be done in single use microfluidic chips that could be then inserted in the detection device to perform the immunoassay.

4.2.1 Principle and surface functionalization with TESU

The first strategy we performed to graft the primary antibody on the microchannel surface was using 11-triethoxysilyl undecanal 90% (TESU) and was tried on PDMS only. Most used techniques only graft antibodies on the glass or silica substrate of a microfluidic channel and not on the surface of the microfluidic channel material like PDMS. These techniques are easier process but it means that the majority of the surfaces of the channel are not used which decreases a lot the advantages of the detection. Therefore, we decided to test a protocol for binding antibodies on PDMS surface. This polymer is indeed hydrophobic which means that biomolecules can easily adsorb to it and thus create false positive.

We chose to use a covalent binding process which means that the antibody is covalently bound to the surface (they share electrons). Firstly the surface is activated so it can react with the active parts on the sides of the antibody (binding sites). This reaction creates the covalent bond between that antibody and the surface. The remaining activation sites are then blocked with a chemical that does not interact with the bioentities that need to be detected. The covalent immobilization strategy has some advantages [154]:

- A covalent bond is strong and cannot be easily removed by a mechanical strain.

- It shows a high density coating of antibodies in comparison with other methods.
- It is rather cheap.
- The surface activation methods are well known.

The immobilization usually shows also a few drawbacks like the use of toxic reagents, long preparation time with complicated processes. The antibody can lose a part of its activity if its binding site is close to the capture site meaning that its orientation is not optimized (figure 85 [155]). Also, since the covalent bond is strong, it is irreversible unless using strong oxidizers.

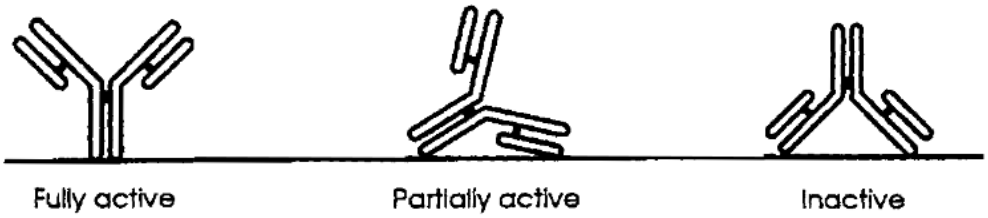

Figure 85: Ideal representation of antibody immobilization orientation [155].

Thus the first thing that has to be done for us to bind the anti-CRP antibody on PDMS is to activate the surface of this material. The activation of PDMS can be done with several techniques but their goals are the same which is to change methyl groups (CH_3) on the surface of the material by hydroxyl groups (OH) (figure 86). These treatments called oxidation also transform the PDMS into a hydrophilic surface and the subsequent steps of functionalization are therefore similar to the ones with glass and silica that are also hydrophilic. With the hydroxyl groups on the surface of the PDMS, it is possible to bind different organosilane molecules that will make the link between this surface and the antibody on it.

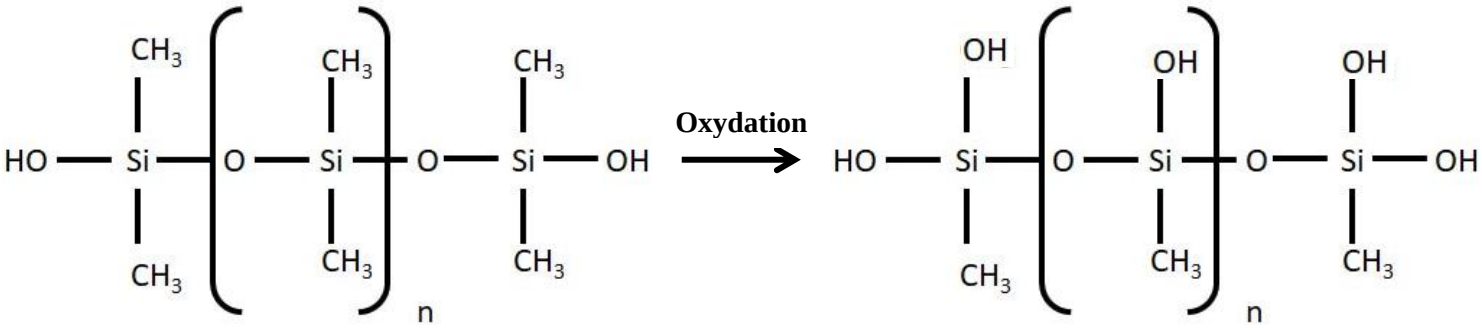

Figure 86: PDMS oxidation creating hydroxyl groups (-OH).

Two main approaches were tried for this oxidation step either using chemicals or plasma O_2. The chemical oxidations were performed using PVA - polyvinyl alcohol ($[CH_2CH(OH)]_n$) or hydrogen peroxide (H_2O_2). To assess and compare the efficacy of these three different approaches, we measured the contact angle formed between a water droplet and the oxidized surface. As mentioned above, PDMS is hydrophobic before treatment which means that the contact angle with a droplet of water is typically way above 90° whereas the contact between a droplet of water and oxidized PDMS is typically about 90° or lower.

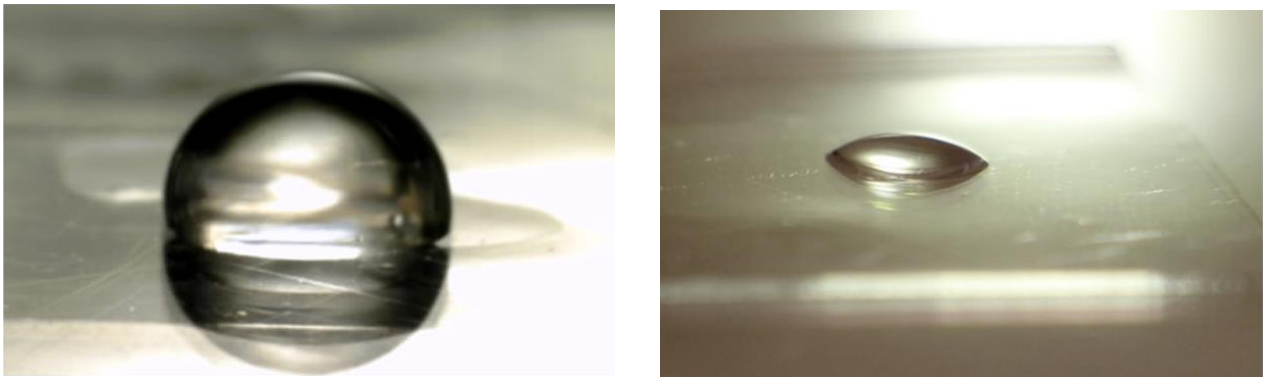

Figure 87: Droplet of water on PDMS before (left) and after oxidation (right).

A droplet of water was put on PDMS flat surfaces at different times after the oxidation using the three different techniques (figure 88).

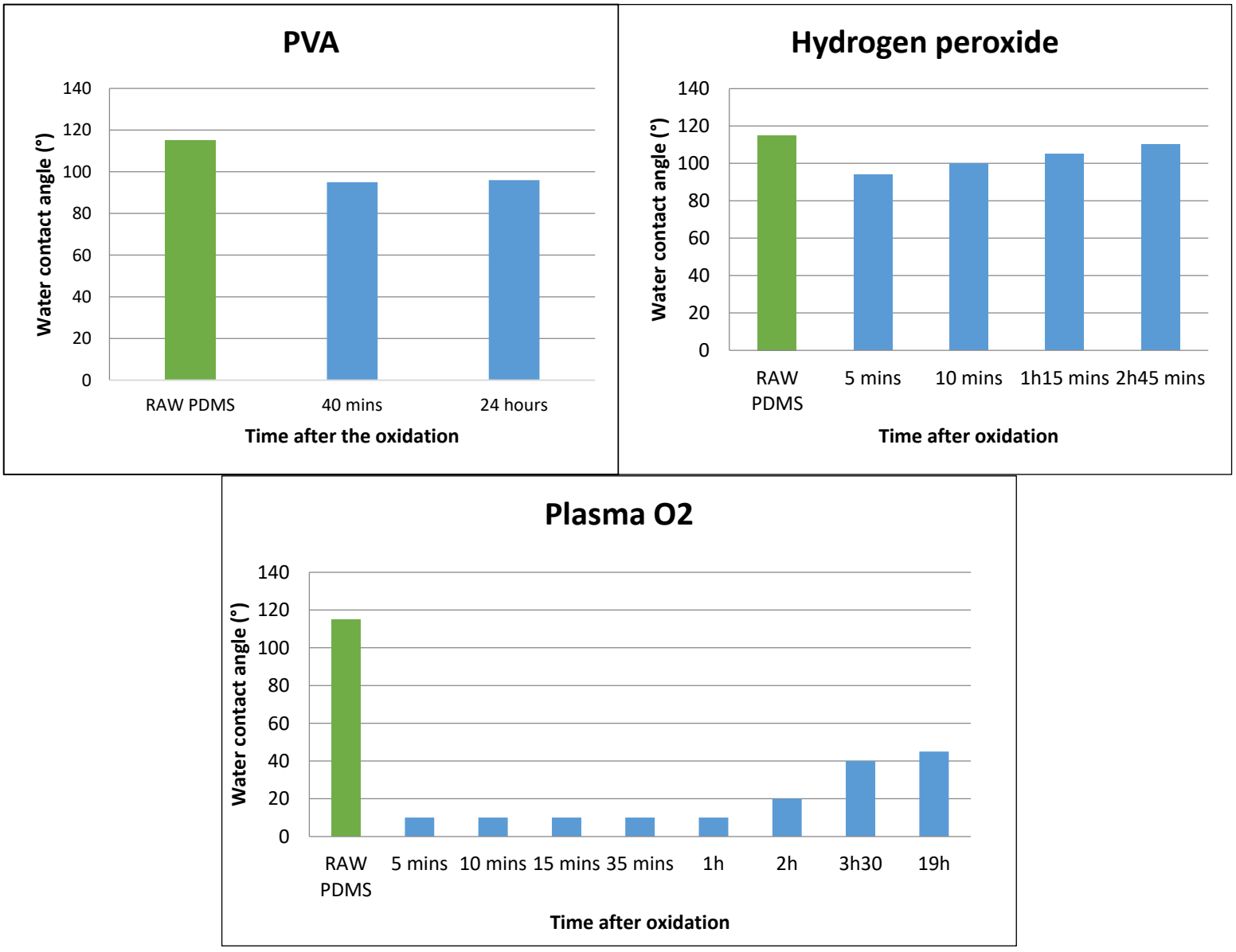

Figure 88: Contact angle for different oxidation techniques and as a function of time.

We can observe that the plasma O_2 has clearly the most important effect on the contact angle and is the most reliable technique as it is also durable in time. Although chemical strategies give poorer performance than plasma O_2, their use can still be interesting. Plasma O_2 cannot indeed oxidize a closed microfluidic channel whereas chemicals can still be injected in it. We can clearly observe on figure 88 that PVA is more effective than hydrogen peroxide which has been consequently abandoned for functionalization.

PDMS surfaces are then put in an ethanol solution containing 2% TESU and 2% trietylamine (TEA) for 1 hour before being dried and heated at 80°C for 2 hours. The silane (TESU) reacts with the hydroxyl group of the activated surface. The primary capture antibodies in carbonate are then dropped on the surface so they can bind with the amino group of the silane. Finally the blocking step is performed to avoid other bioentities to non-covalently attach to the silane. For this step we used bovine serum albumin (BSA) in PBS buffer. The whole structure we tried to obtain is showed on figure 89.

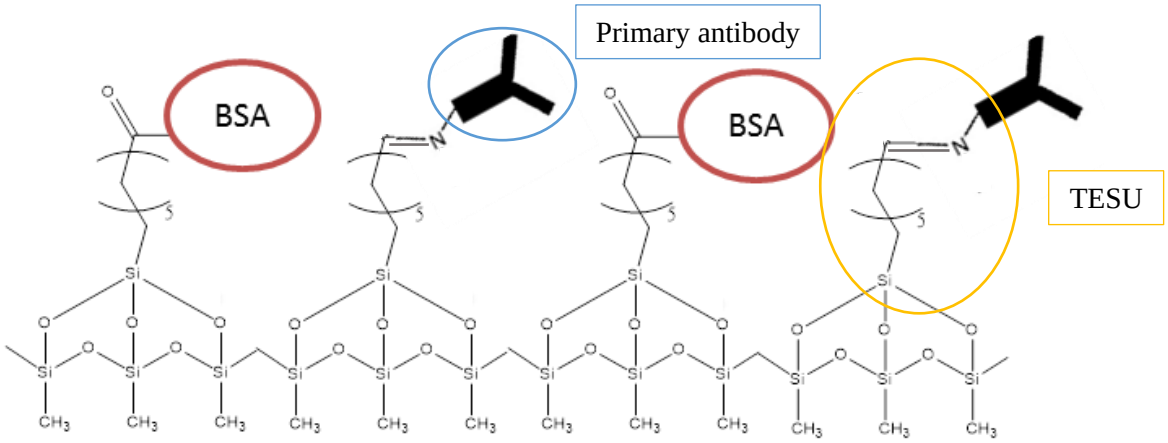

Figure 89: PDMS with MAB17071 antibodies bond by TESU. BSA block the silane active sites not used by the antibodies.

X-ray photoelectron spectroscopy (XPS) was performed at the Laboratoire de Réactivité de Surface (LRS) of Sorbonne Université to verify if the antibodies are indeed bounded to the PDMS surface (figure 90).

Unfortunately, the XPS survey curves did not show definitive results as the nitrogen peak (N1s around 400 eV) is weaker than expected and other peaks that should not appear are visible. For example, a peak that seems to correspond to chlorine appears when Cl should not be present on the surface. We can therefore hypothesis that some antibodies indeed bind to the surface, but only a very small quantity. After these preliminary experiments, we decided to directly work in the LRS laboratory, specialized on surface reactivity treatment, and to change the protocol for the functionalization according to LRS expertise.

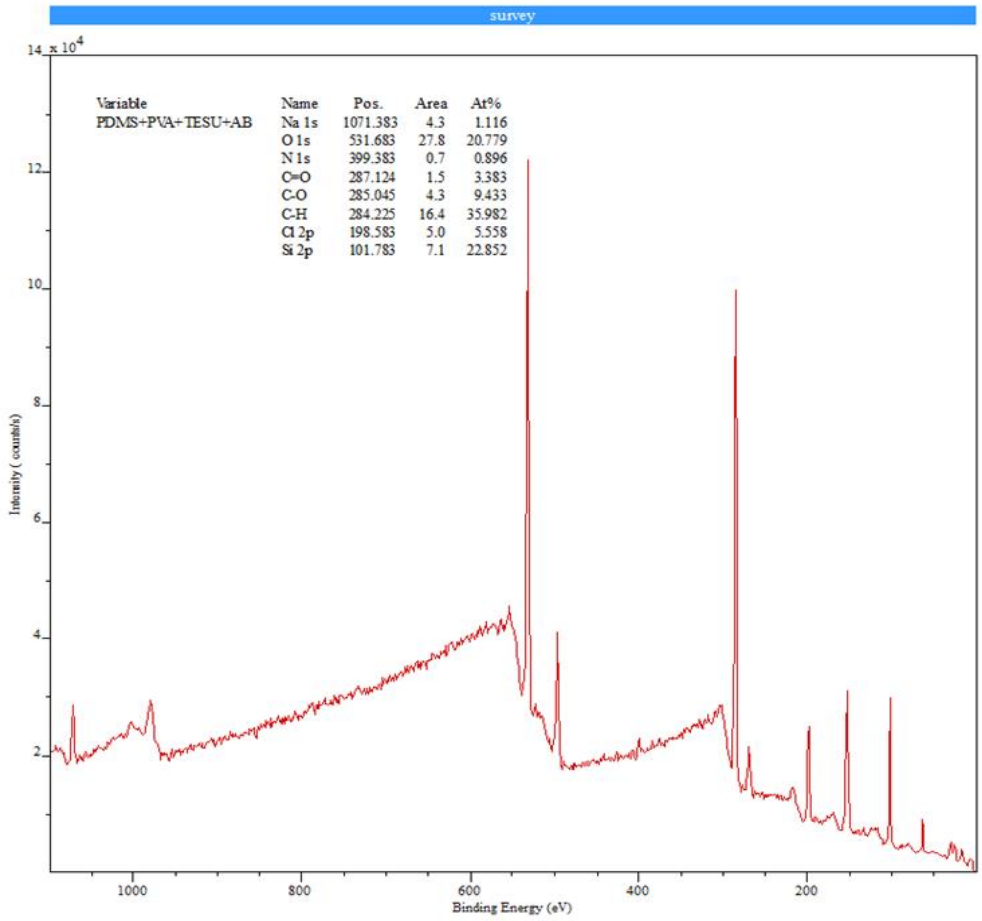

Figure 90: XPS spectra of PDMS surface after the TESU protocol. The nitrogen peak at 400 eV is too small to conclude that we successfully grafted antibodies on the samples.

4.2.2 Surface functionalization with GOPTS and APTES

We tried a second protocol that also uses a covalent bond immobilization strategy developed by Souhir Boujday and Vincent Humblot, researchers at LRS. This time we have been trying to bind the MAB17071 antibody on three different material surfaces PDMS, COC and PMMA. It has been showed that these three materials can be activated via O_2 treatment [156][157][158], therefore we concentrated on this method to oxidize the surface before putting an organosilane.

We first applied a protocol using (3-Glycidyloxypropyl)trimethoxysilane (GOPTS) inspired by a protocol previously used by the LRS [159]. A step where protein G is bounded on top of the silane (GOTPS) is added [160]. This step is necessary to assure that the antibodies bind to the surface with the best orientation to maximize their activity (figure 92). After having problems using GOPTS on PDMS, we switched to protocol using (3-Aminopropyl)triethoxysilane (APTES) (figure 91).

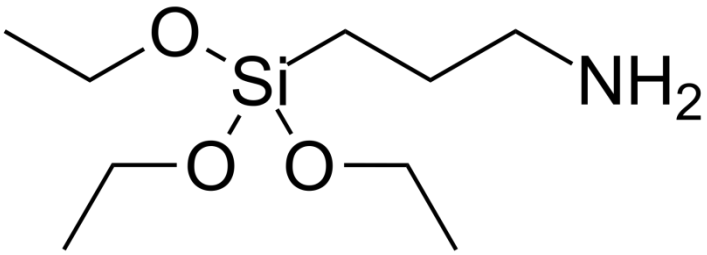

Figure 91: Chemical structure of APTES [161].

APTES was already used for different protocols in LRS laboratory. However we had to change the previously used protocol since toluene was used as the solvent for APTES because toluene is not compatible with COC (see 2.3.2). Therefore we decided to use absolute ethanol as APTES solvent instead. Glutaraldehyde is also added to cross-link the APTES and the protein G. The hydroxyl groups of the surfaces react with the silicon of the silane and thus create a covalent bond whereas the amino groups react with the glutaraldehyde. The protein G then bind to it and finally a bond is created between this protein and the active sites of the anti-CRP capture antibody (figure 92). We made the plasma activation in the cleanroom of the PHENIX laboratory and we made the rest of the chemical reactions in the LRS laboratory.

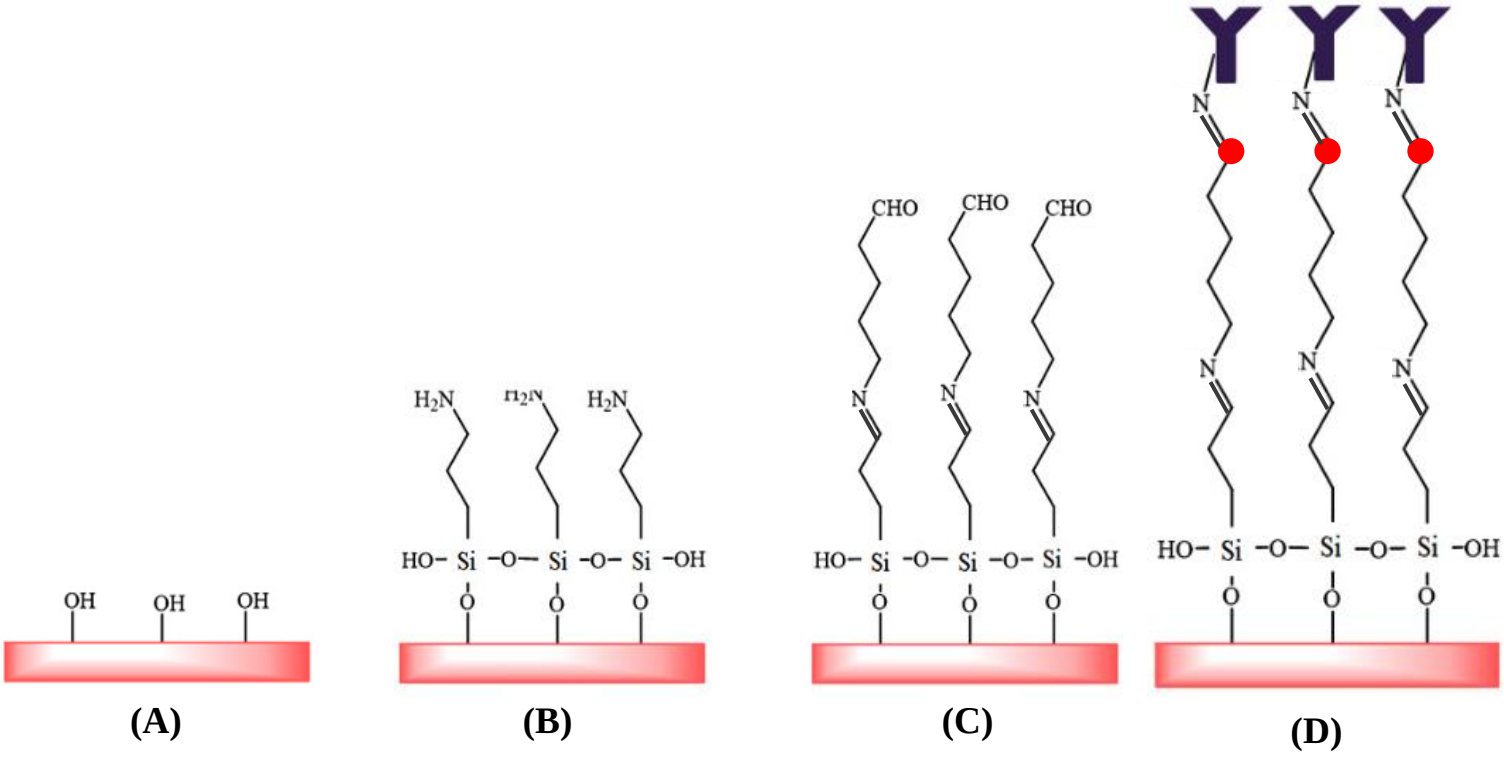

Figure 92: Different steps of the bonding protocol of the antibodies on the surfaces. (A) Activated surface after the plasma treatment. (B) APTES grafted on the surface. (C) Surface chemistry after the glutaraldehyde treatment. (D) Surface with the antibody, in our protocol a protein G is located between the glutaraldehyde and the antibody represented here by the red dot. This schematic is not to scale [162].

The detailed protocol of the grafting protocol of primary antibodies on PDMS, COC and PMMA is presented in appendix 4.

PDMS, COC and PMMA samples are kept after each step and rinsed with Milli-Q (or ultrapure) water for characterization in order to confirm the effectiveness of the protocol.

4.2.3 Surface characterization techniques

We tested our surfaces using three different characterization techniques that complete each other. We used contact angle measurements, attenuated total reflection (ATR) and X-ray photoelectron spectroscopy (XPS). ATR and contact angles were performed under the supervision of Antoine Miche and Vincent Humblot from LRS and XPS were directly done by Antoine Miche as this equipment requires specific training.

Contact angles measurement can assess the hydrophobicity and the surface energy of a sample whereas ATR show the chemistry bonds in the material. Finally XPS analyses the atoms that are present at the surface of the sample and their interactions.

4.2.3.A Contact angle measurement

As discussed in 4.2.1, the basic principle of contact angle measurement consists of assessing the wettability of a surface by measuring the angle formed by the edge of a droplet of a specific liquid and the surface underneath it, this angle being directly influenced by the chemical interactions between the surface and the liquid. There is equilibrium between three phases: the liquid (L), the solid (S) and the gas (G) which is usually the ambient atmosphere. The contact angle depends on the interfacial energies between these three phases. The parameter γ_{SG} is the interfacial energy between the surface and the atmosphere, γ_{LG} is the interfacial energy between the liquid and the atmosphere (also called surface tension of the liquid) and γ_{SL} is the interfacial energy between the liquid and the solid and depends on the chemical interactions between them (figure 93). The equation that links the interfacial energies and the contact angle θ is the Young equation:

$$\gamma_{SG} - \gamma_{SL} - \gamma_{LG} cos\theta = 0$$

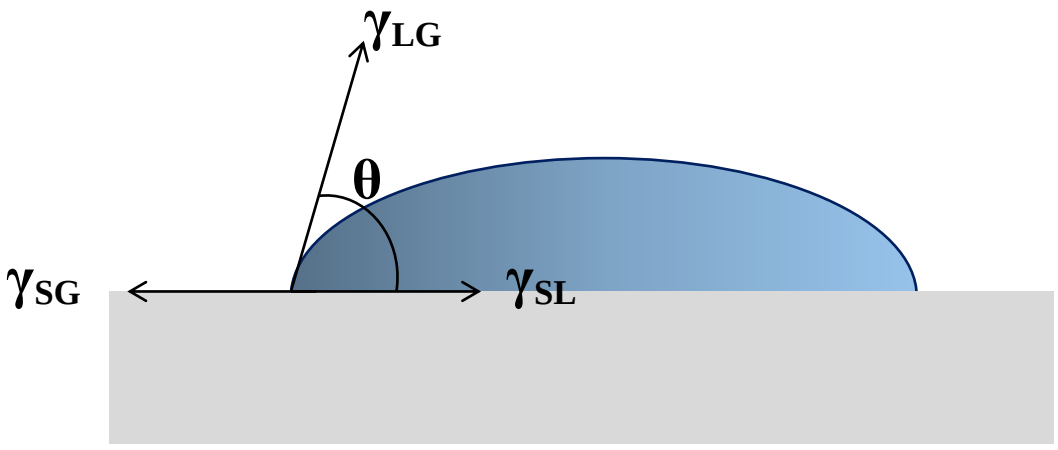

Figure 93: Contact angle depends on the equilibrium between three phases and their interfacial energies γ. (S) is the solid, (L) the liquid and (G) the gas around the droplet.

It should also be noted that surface roughness affect the contact angle, it enhances the wettability.

To make the measurement we used the static sessile drop method with a contact angle goniometer at LRS laboratory [163]. Besides contact angle measurements, this technique allows to determine the surface energy γ_{SG} of the tested material which is also dependent of the surface chemistry. A 1 µL liquid droplet is dropped with a syringe on the sample surface; the droplet has to be small enough so that we can neglect the gravity force. A camera is located at the same level as the droplet and films it with a side view (figure 94). The contact angle is then calculated directly by a software from the images taken by the camera.

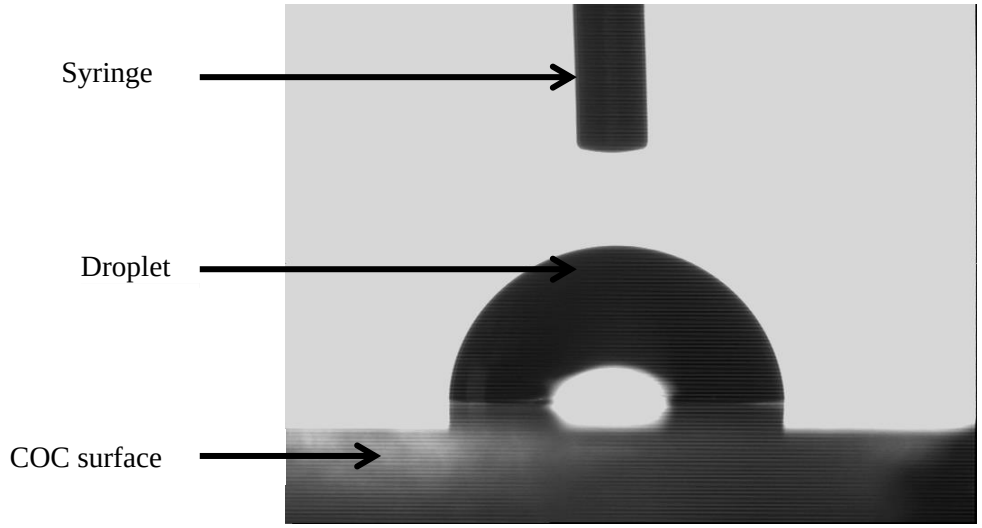

Figure 94: Example of image taken by the side camera of the goniometer. Water droplet on an untreated COC surface.

To determine the surface energy of the material from the contact angle measurement we used the Owens-Wendt model (4.3) which is especially suited for polymers [164]. This method is a derivative of the Young equation and considers that the surface energy of a liquid or a solid can be separated in two parts which depends on its interactions, one dispersive γ^d and the other polar γ^p.

So for the surface energy of the solid material we have: $\gamma_{SG} = \gamma_{SG}^d + \gamma_{SG}^p$ (4.1)

And for the liquid we have: $\gamma_{LG} = \gamma_{LG}^d + \gamma_{LG}^p$ (4.2)

The contact angles are measured for at least two different liquids which dispersive and polar components are known.

The Owens-Wendt model describes the surface energies γ_{LG} and γ_{SG} from the Young equation as following: $\gamma_{LG} \cdot (1 + \cos(\theta)) = 2\sqrt{\gamma_{LG}^d \cdot \gamma_{SG}^d} + 2\sqrt{\gamma_{LG}^p \cdot \gamma_{SG}^p}$ (4.3)

The unknowns are the dispersive and polar components of the solid surface. A curve is created with $x = \sqrt{\frac{\gamma_{LG}^p}{\gamma_{LG}^d}}$ (4.4) and $y = \sqrt{\frac{\gamma_{LG} \cdot (1+\cos(\theta))}{2\sqrt{\gamma_{LG}^d}}}$ (4.5).

We then do linear regression of the ax+b type where $\gamma_{SG}^{p} = a^2$ and $\gamma_{SG}^{d} = b^2$. Finally the surface energy of the material is calculated by doing $\gamma_{SG} = a^2 + b^2$ (4.6).

For our surfaces characterizations, we used three different liquids, Milli-Q water (H_2O), diiodomethane or methylene iodide (CH_2I_2) and ethylene glycol ($C_2H_6O_2$) (table 20).

Table 20: Liquid surface tension of the three liquids used during this project.

Liquid	Liquid surface tension γ_{LG} (10^{-3} N.m^{-1}) at 20 °C
H_2O	72.8
CH_2I_2	50.8
$C_2H_6O_2$	47.7

Contact angles measurements have the advantages to be very cheap and easy to perform. However, the used liquids have to be tested to avoid a chemical degradation of the sample and, unlike attenuated total reflection or X-ray spectroscopy, the results do not precisely describe the molecules present of the surface of the samples. The contact angle measurement is still useful to investigate if the surface hydrophobicity and energy changes between each step of the surface functionalization that can be linked to a change of the surface chemistry. Moreover, the results can be compared to the literature. Three droplets and three measurements were done on every sample surface to increase the precision of the results.

4.2.3.B Attenuated total reflection - Fourier-transform infrared spectroscopy (ATR-FTIR)

Attenuated total reflection (ATR) is an infrared spectroscopy method to observe the chemical bonds of a sample surface. An infrared beam is emitted in a crystal that was previously put in contact to the sample surface to examine. The beam is reflected back to the crystal when it hits the sample but when this reflection is total, it actually penetrates the sample surface to some small depth before being reflected. This makes the chemical bonds vibrate inside the sample creating an evanescent wave, absorbing a part of the infrared spectrum depending on the energy of the chemical bond that attenuated the beam. The absorption spectrum is then recovered by a detector (figure 95). We used a Nicolet 5700 infrared spectrometer for our measurements.

In the case of a Fourier Transform InfraRed spectroscopy (FTIR), the aim is to detect the amount of energy absorbed by the sample for different wavelengths. A Fourier transform is applied by the computer to create the exploitable spectrum from the signal detected at different wavelength. The curves obtained have an x-axis expressed in terms of wavenumber which is $\tilde{\nu} = \frac{1}{\lambda}$ (cm^{-1}) and the y-axis being the absorbance.

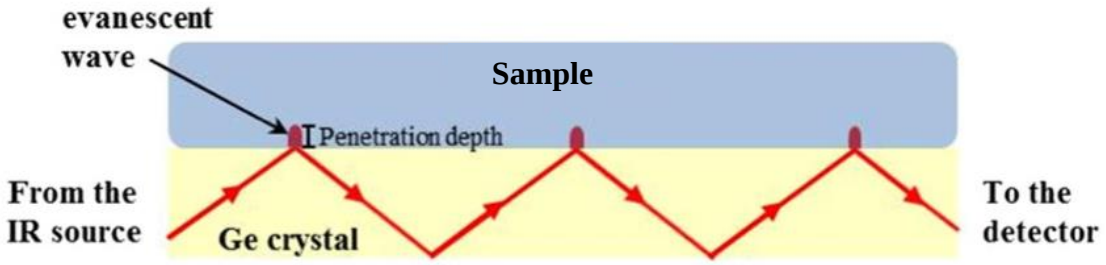

Figure 95: Schematic of the ATR principle [165].

The ATR-FTIR technique does not need sample preparation which is rather sensitive and can work on thick samples. It is also cheaper and easier to operate than X-ray photoelectron spectroscopy. A possible disadvantage is that, for our samples, the mechanical strain of the germanium crystal pressing against the sample can deteriorate chemical chains that are at the surface of the material. Consequently, we did not reuse the samples observed with the ATR-FTIR for other purposes.

ATR-FTIR has been used to observe polymer surfaces [166] and proteins like antibodies for biomedical applications [167][168]. We performed our measurement at LRS laboratory with a germanium crystal to determine if the protocol described in section 4.2.2 worked for each step and on the three different materials: PDMS, COC and PMMA.

4.2.3.C X-ray photoelectron spectroscopy (XPS)

The principle of X-ray photoelectron spectroscopy is to beam X-ray photons (photons that have a wavelength between 10^{-12} m and 10^{-8} m) on the samples that then emit photoelectrons that can be analyzed (figure 96). Each chemical elements emit photoelectrons of a specific energy therefore analyzing them allow us to determine the surface chemistry of a sample.

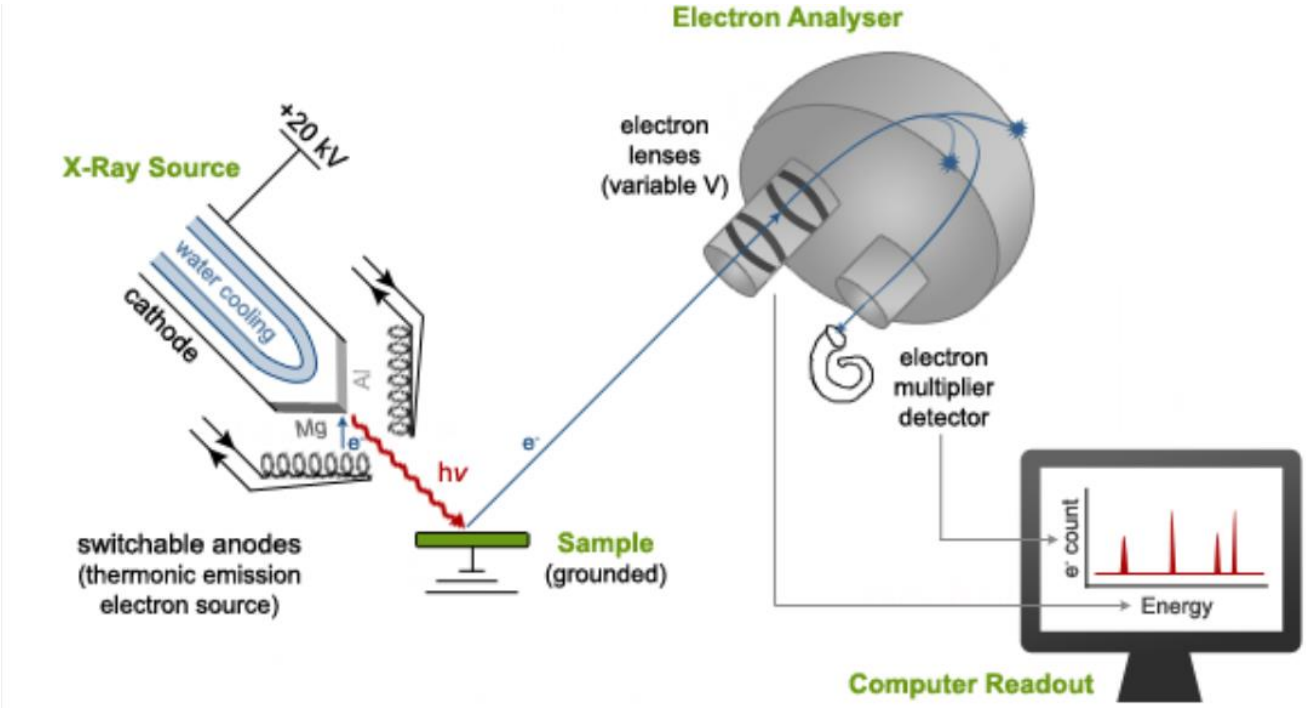

Figure 96: Diagram of an X-ray photoelectron spectrometer [169].

The detected photoelectrons are counted and sorted by their binding energy to create a spectrum. The binding energy of the photoelectron $E_{binding}$ is calculated from the energy of the x-ray photon E_{photon} that created it minus the sum of the kinetic energy $E_{kinetic}$ of the photoelectron and the work function Φ that depends on the spectrometer and the material analyzed: $E_{binding} = E_{photon} - (E_{kinetic} + \Phi)$. The samples analyzed by XPS should not exceed 1 cm² to enter in the vacuum chamber. This method requires a very high vacuum to be applied; the chamber should at least be at a pressure of 10^{-8} millibar or below to avoid any contamination. For our measurements we used an Omicron Argus spectrometer (figure 97).

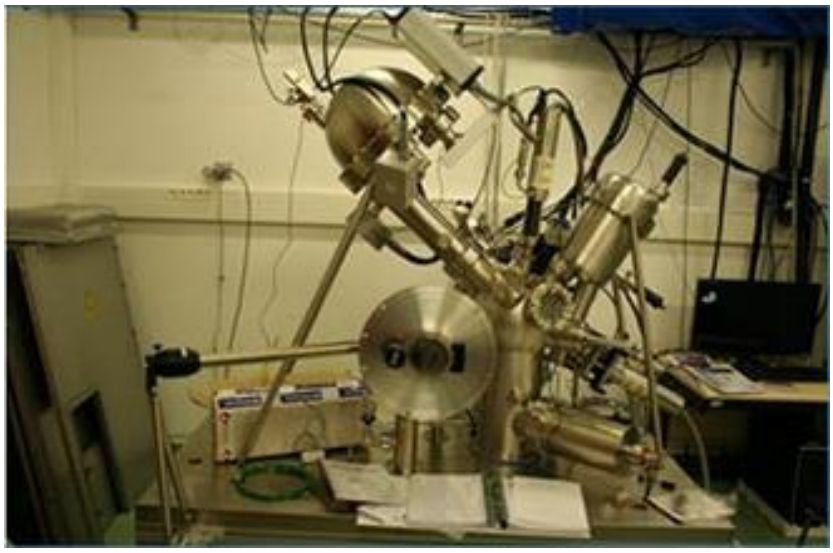

Figure 97: X-ray photoelectron spectroscopy (XPS) setup at LRS laboratory [170].

This technique is very sensitive but only probes between 10 and 12 nm into the sample, depending on the analyzed material, which implies that only the chemical at the top of the chain grafted on the surface can usually be detected. For example if we try to analyze the samples with antibodies bound on top of the APTES, the latter entity will not appear on the obtained spectrum. Its very high sensitivity has also to be carefully considered as any contamination on the analyzed surface will appear on the spectrum. Finally X-ray spectroscopy is more expensive to perform than contact angle measurement or ATR-FTIR. But despite these drawbacks, XPS technique remains one of the best methods to determine the atoms and their chemical bounds found on a sample surface. Unfortunately for us, PDMS is a porous material that releases progressively some gas when it is submitted to a high vacuum; therefore the use of XPS for PDMS surface characterization is difficult but it is well suited for PMMA and COC.

4.2.4 Contact angle and ATR functionalization results

4.2.4.A PDMS

After following the protocol presented in appendix 4, we measured the contact angle between a 1 µL Milli-Q water droplet and the surface of the PDMS sample (figure 98).

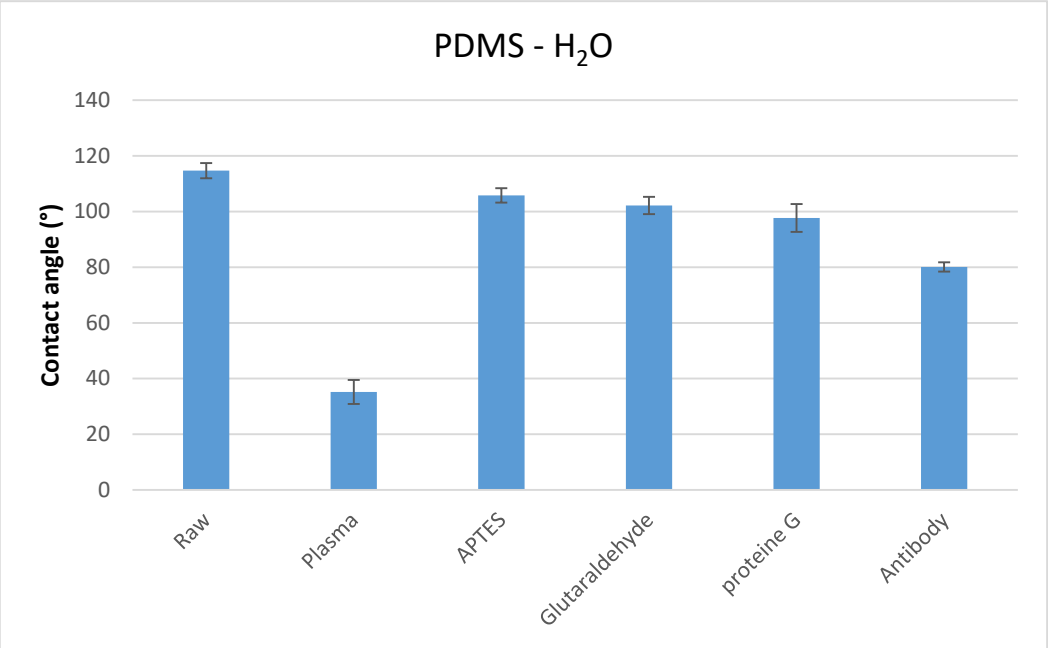

Figure 98: Water contact angle on pristine PDMS, after the plasma O_2 treatment, after APTES grafting, after the glutaraldehyde adding, the protein G and finally after putting the antibodies on top of the formed chemical chain.

The contact angles measured before and after the plasma treatment confirmed that the PDMS surface becomes hydrophilic and they are in agreement with the literature [171]. After the grafting of the APTES the contact angle went back up to above 100°, this is quite above the measurements that can be found in the literature which is closer to 70° [172][173]. The same observation can be made for glutaraldehyde [174]. However there is a significant difference between the pristine PDMS and the PDMS coated with APTES. We could therefore suspect that some APTES and glutaraldehyde were indeed grafted but not in a large enough number to be efficient as bioreceptor. Some effects are nonetheless visible at the antibody binding step which is encouraging. To analyze further these results and calculate the surface energy of the samples, two other liquids were also used to perform the contact angle measurements: diiodomethane and ethylene glycol (figure 99 and 100).

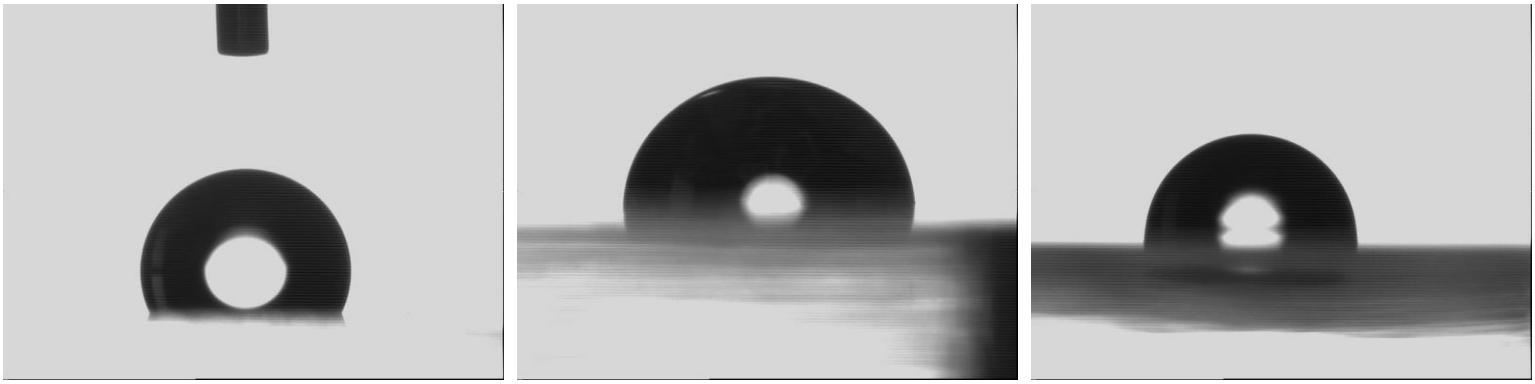

Figure 99: Contact angle photos for the three liquids used on pristine PDMS. (Left) Milli-Q water. (Middle) Diiomethane. (Right) Ethylene glycol.

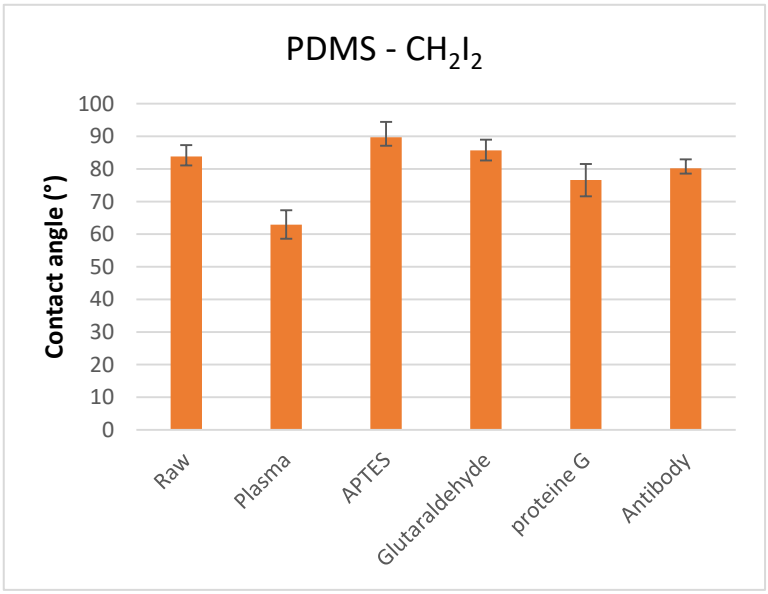

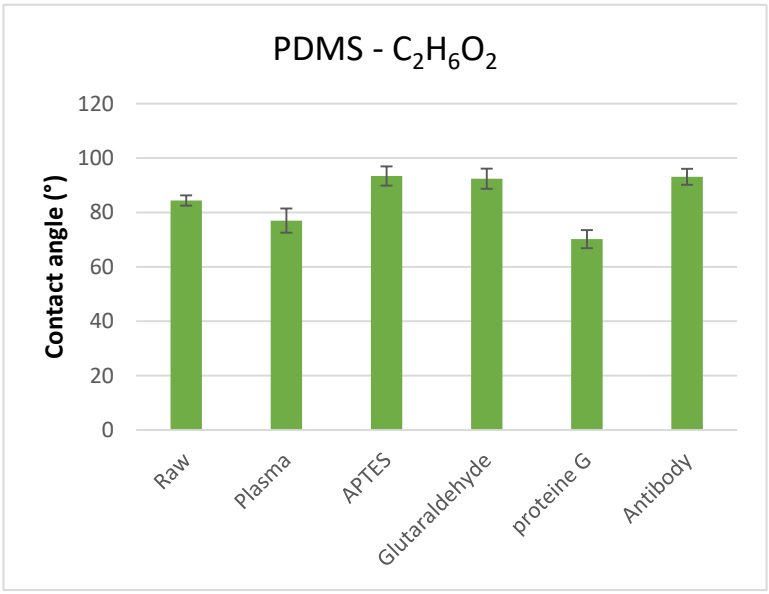

Figure 100: Contact angle measurements for the different steps of the experimental protocol. (Left) With diiodomethane droplets. (Right) With ethylene glycol droplets.

Knowing the dispersive and polar components of the three liquids, it is possible to calculate the surface energy at each steps of the protocol. The [x,y] have been calculated using the previously presented equations (see equation 4.5, section 4.2.3, page 108) (figure 101).

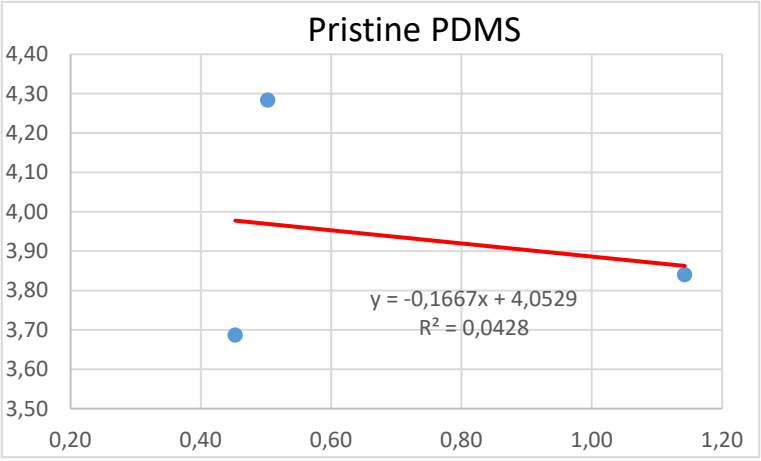

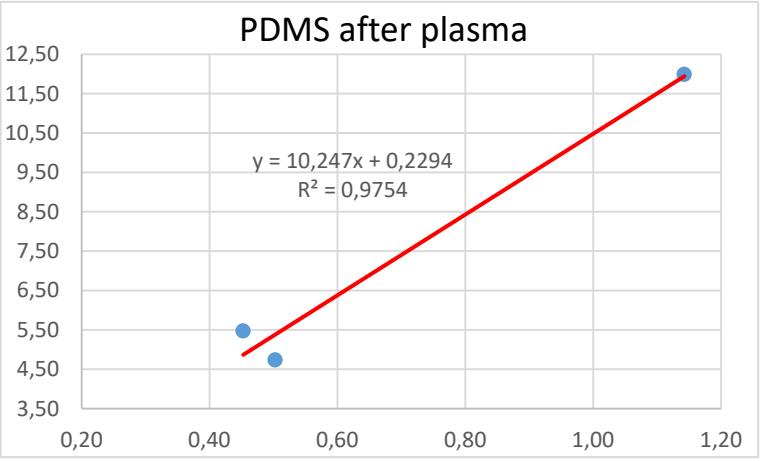

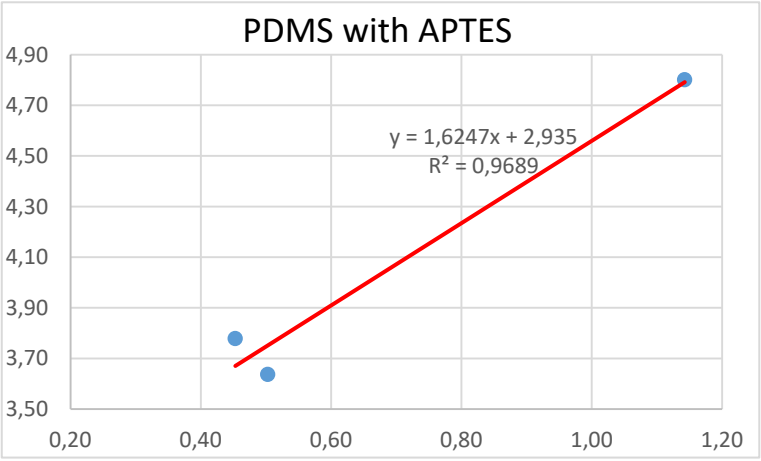

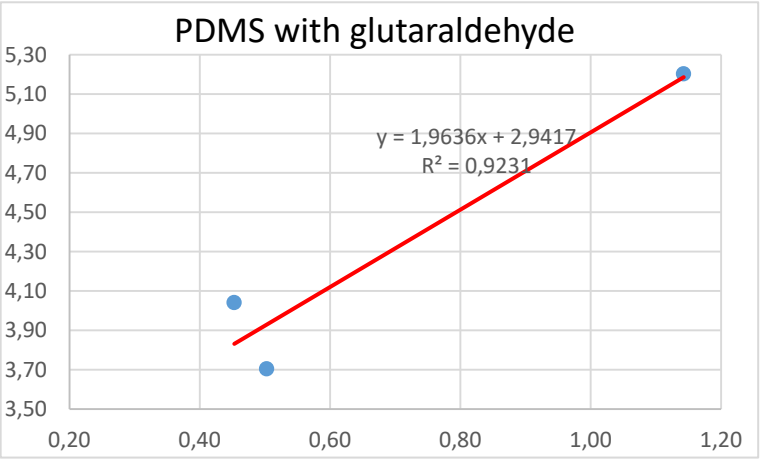

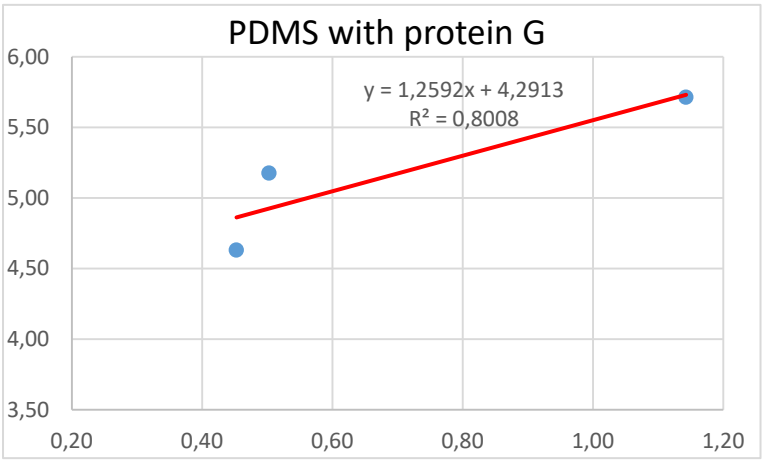

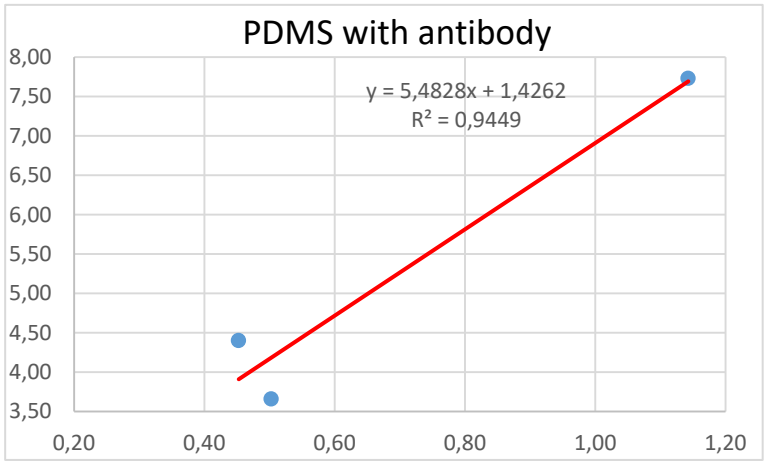

	RAW	PLASMA	APTES	GLUTARALDEHYDE	PROTEIN	ANTIBODY
SUFACE ENERGY (10^{-3}N.M^{-1})		105.1	11.3	12.5	20.0	32.1

Figure 101: Surface energy calculation for each step of the PDMS functionalization protocol.

It seems that the chosen liquids are not very well suited with the PDMS. We can especially make this observation for the untreated PDMS where the linear regression is clearly meaningless ($R^2 < 0.1$) although in the literature it seems that the surface tension is at about 20 10^{-3}N.M^{-1} [175][176]. A fourth solvent should be used to try having more clear results. Despite this it seems that something is happening since the energy varies at each step so we can hypothesis that some antibodies are indeed grafted to the PDMS surface.

We try to further assess this fact with the ATR-FTIR characterization. We used a germanium crystal and we took 512 wavenumber points where we measured the absorbance to create a spectrum that range from 600 cm^{-1} to 4000 cm^{-1}. The signal from air, without any sample against the germanium crystal, is first measured as "background" that is then subtracted from the ATR made on the samples. A baseline correction and a smoothing of 34,713 cm^{-1} were applied on all spectra thanks to the software OMNIC.

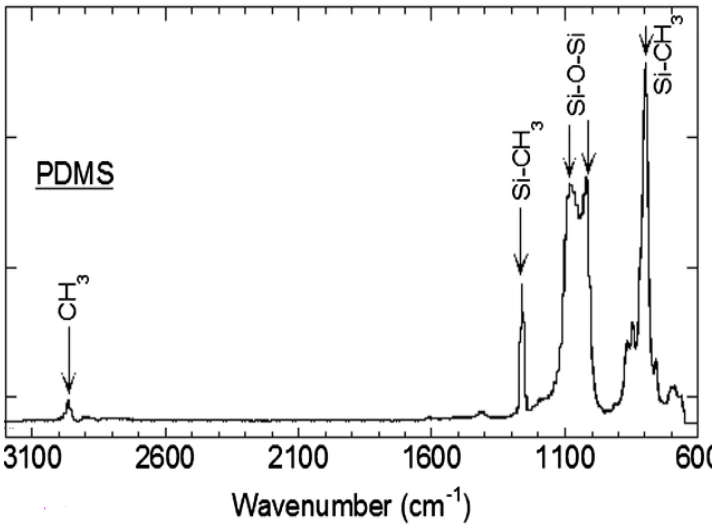

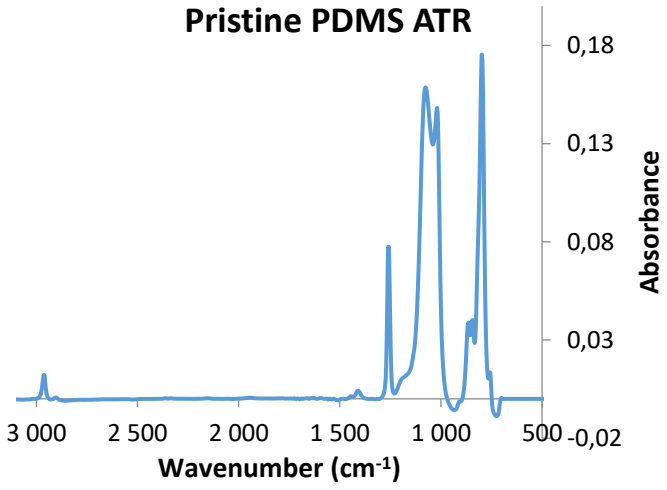

Figure 102: On the left we can see an infrared spectrum (ATR-FTIR) of a PDMS sample found in the literature with chemical bonds description for each peak [177]. On the right is an infrared spectrum that we obtained on our pristine PDMS surface.

We can see on figure 102 that the ATR-FTIR measurement of pristine PDMS is in very good agreement with the literature. For the next steps we should detect the silane of the APTES and the aldehyde group of the glutaraldehyde. The APTES should appear between 1520 and 1640 cm^{-1} approximately while glutaraldehyde should be visible at about 1720-1730 cm^{-1}). For the protein and the antibody we should see a peak that corresponds to amide and amine bonds. They should be visible between 1550 cm^{-1} and 1700 cm^{-1}.

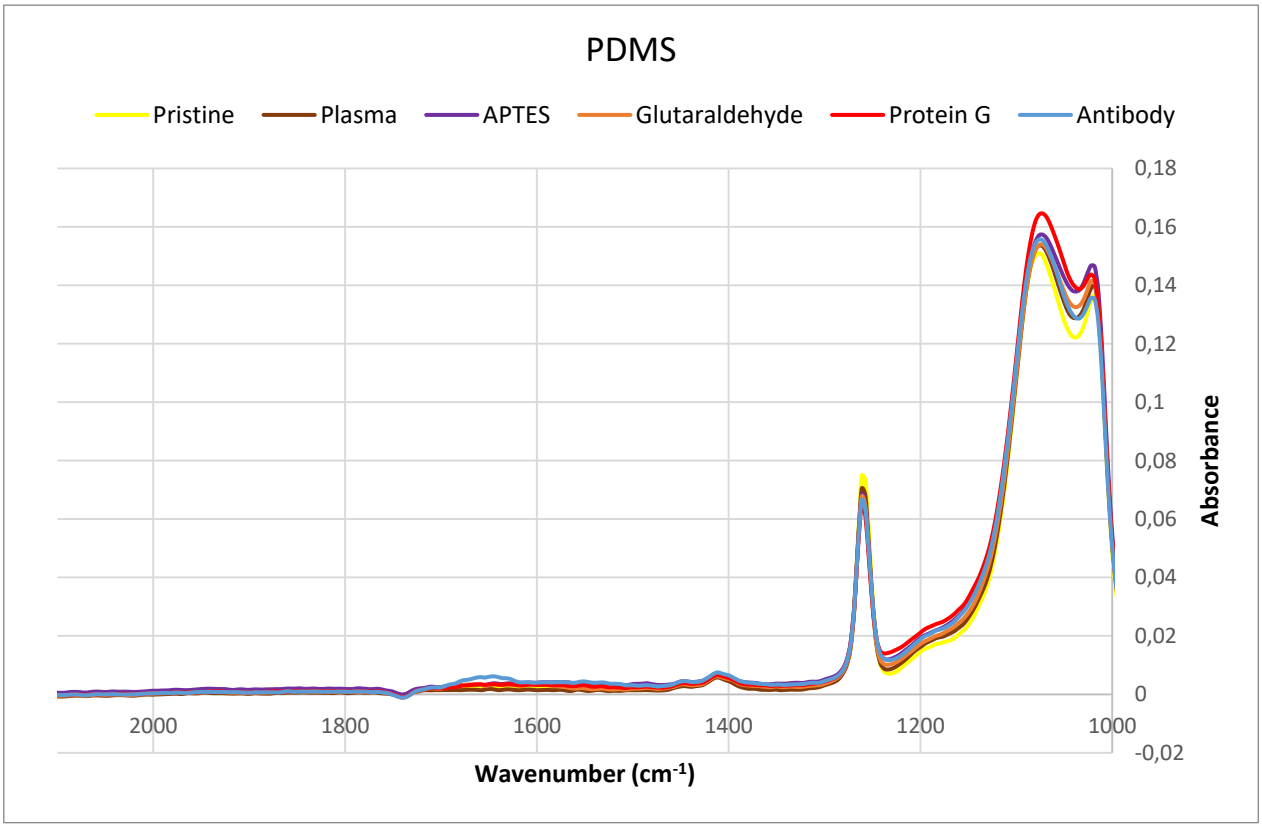

Figure 103: Combined infrared ATR-FTIR spectra of the different steps of antibody bonding on PDMS surfaces

As illustrated on figure 103, the different steps do not show major differences on the ATR. Nevertheless, some batches exhibit some difference for APTES and proteins but the results are not as significant as expected (figure 104).

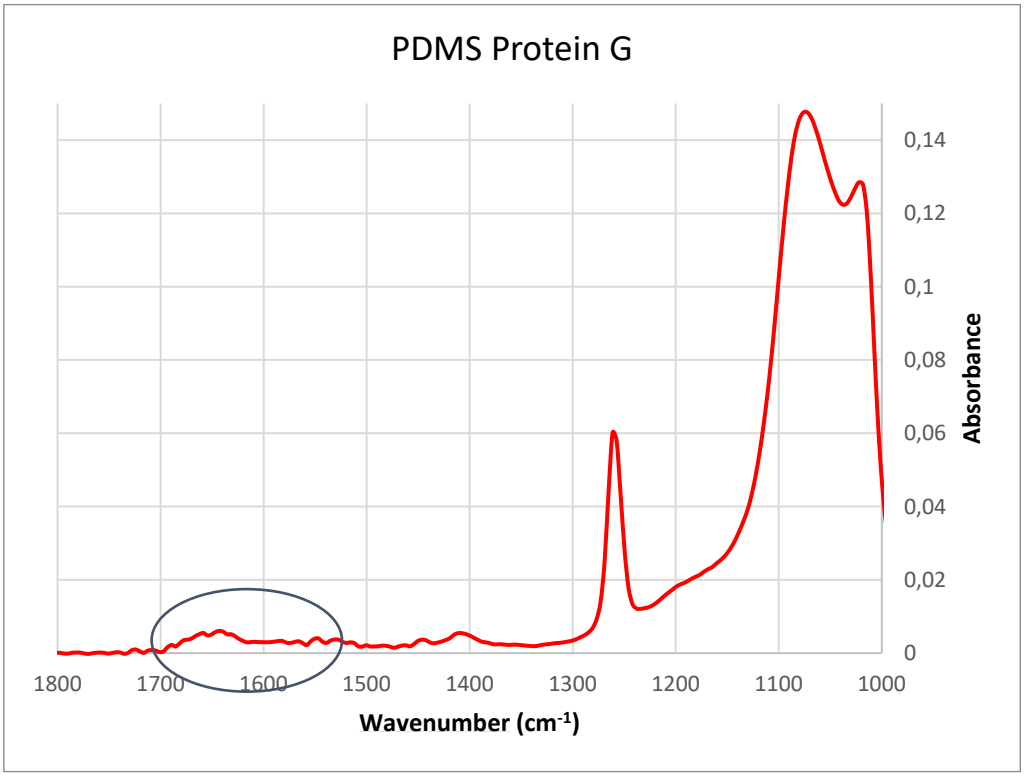

Figure 104: Infrared spectrum for PDMS after protein G grafting. The peak that could correspond to protein chemical bonds are highlighted by the dark blue circle.

We can conclude that, even if it seems that the chemical biofunctionnalization of PDMS happened as we can see some changes on the contact angles and surface tension, the yield seems rather poor for this material. Adding the fact that PDMS is difficult to characterize via XPS because of its degassing and the fact that we try to move away from this material (mainly because PDMS is not well suited for industrialization, see section 2.3.2), we decided to focus only on the COC and PMMA for biofunctionnalization.

4.2.4.B COC

For the COC and PMMA surfaces, the contact angles for the three liquids and the ATR-FTIR spectra are presented step by step as it is easier to compare them two-by-two.

The first figure 105 presented is the effect of O_2 plasma treatment on the COC surface. The contact angle measurements are rather similar with the literature [178].

.

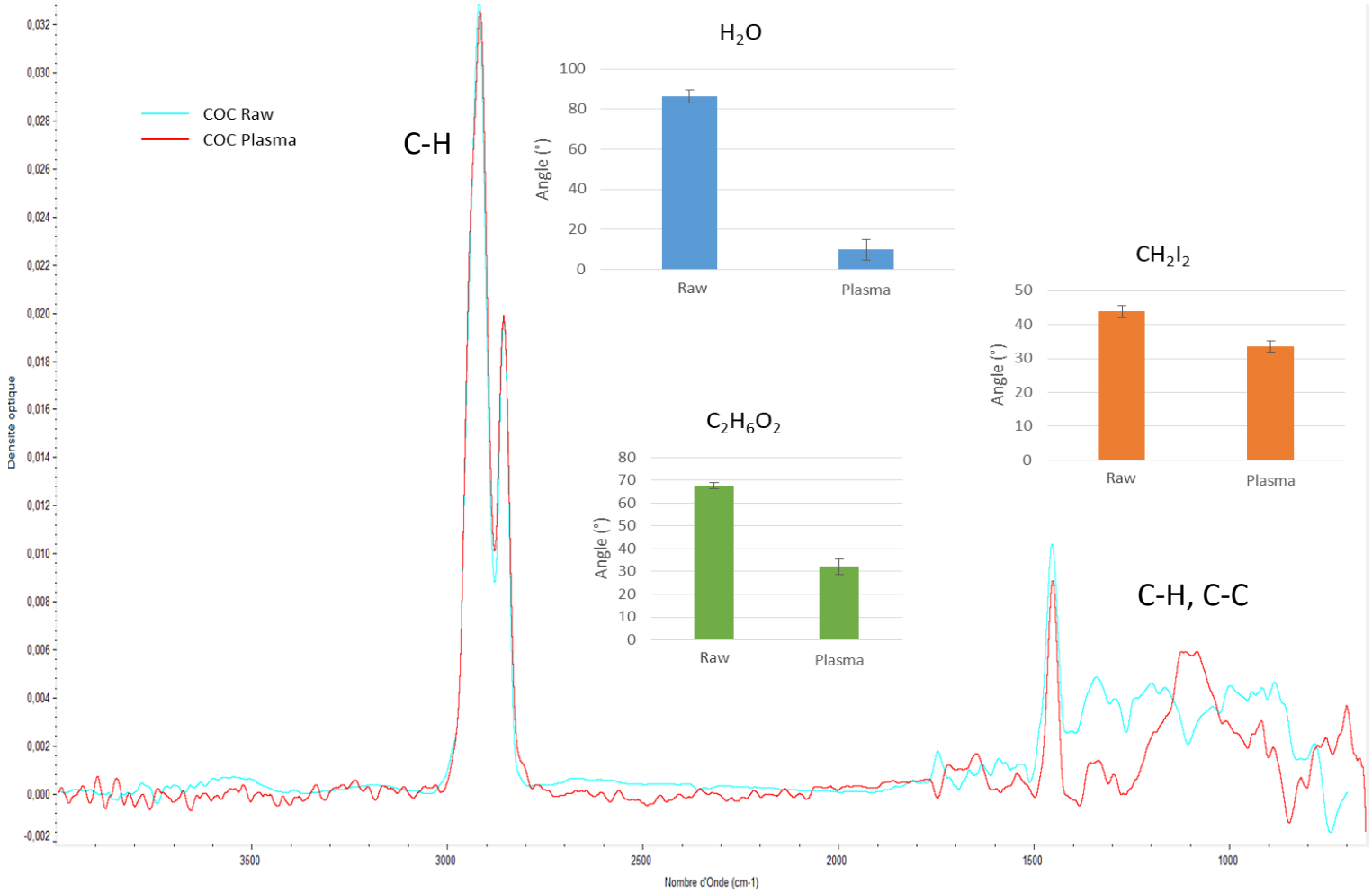

Figure 105: Comparison of infrared ATR-FTIR spectra and contact angles after and before the plasma treatment of COC surfaces.

We observe some differences between the ATR but the effect of the O_2 plasma treatment can be solely confirmed thanks to the contact angle measurements and especially the ultrapure water contact angles. We then assess the APTES grafting.

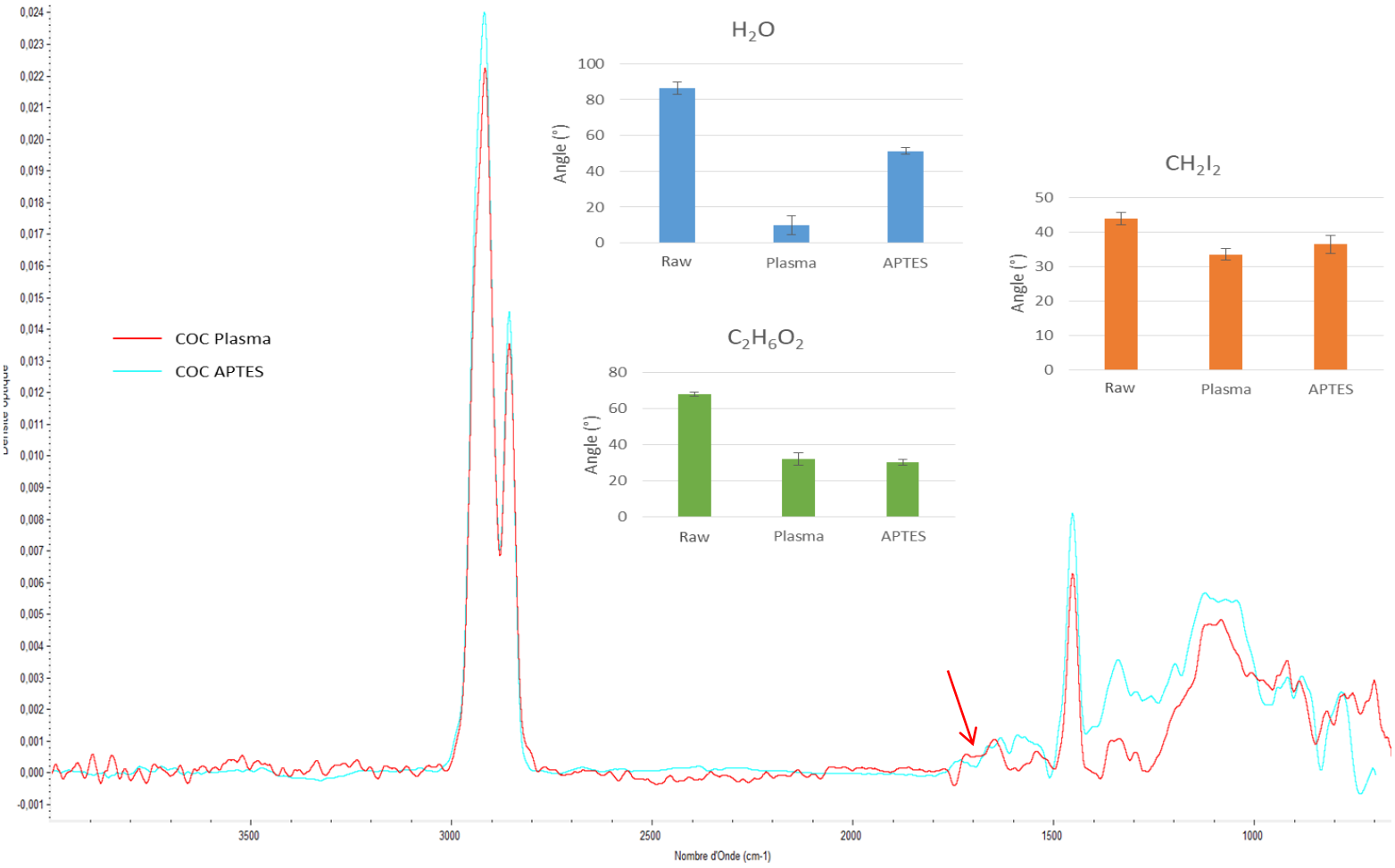

Figure 106: Comparison of infrared ATR-FTIR spectra and contact angle after and before the APTES bonding of COC surfaces.

We can observe a peak at the wavenumber we expected (~1600 cm^{-1}) that could indicate that we have successfully bonded APTES on our surfaces. The clear differences between the untreated surfaces and the ones with APTES in terms of contact angle confirm that assumption.

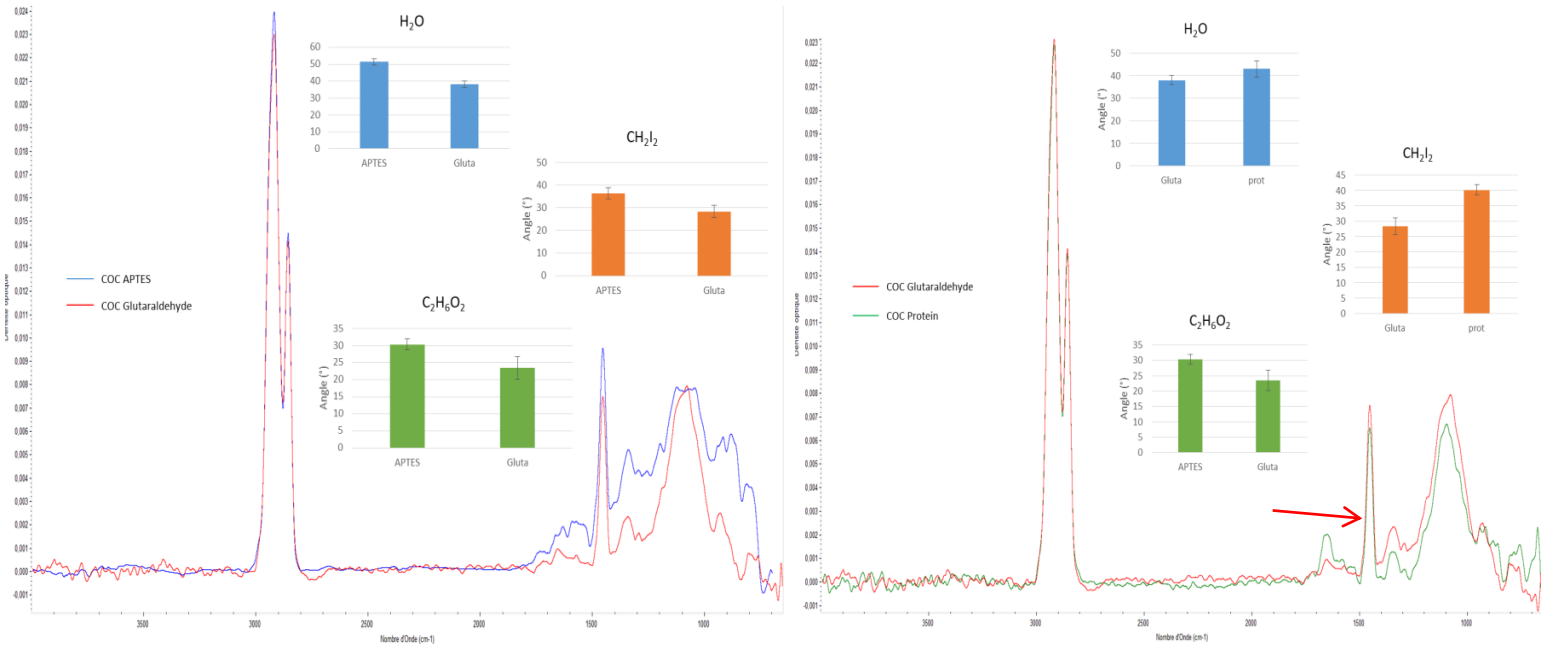

Figure 107: Comparison of infrared ATR-FTIR spectra and contact angle after and before the glutaraldehyde (left) and the protein G (right) bonding of COC surfaces.

Contact angle measurements and ATR seems to show that we successfully grafted proteins on top of the glutaraldehyde on the COC surfaces. However, the ATR does not show coherent results for the glutaraldehyde bonding but the contact angle measurements show some differences.

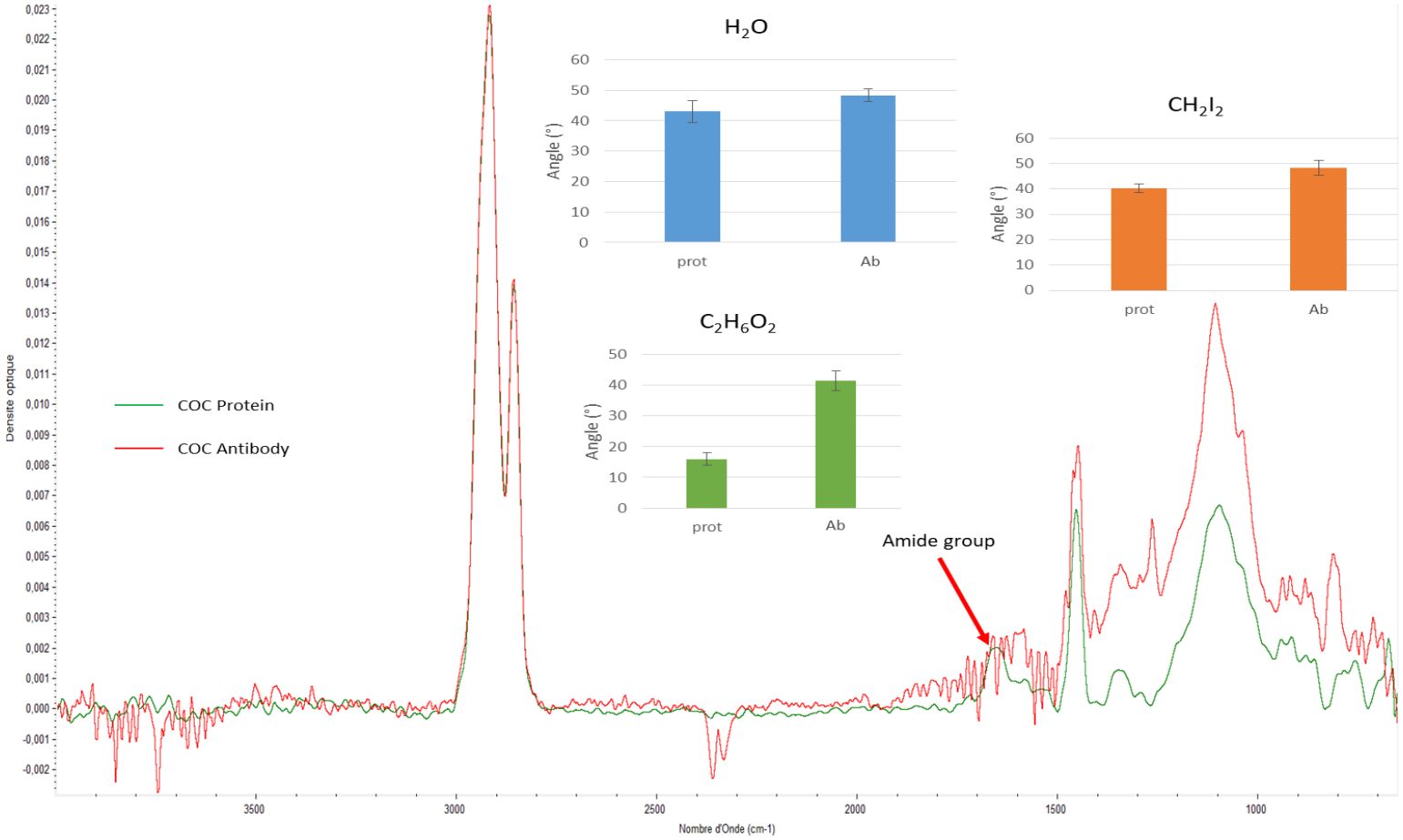

Figure 108: Comparison of infrared ATR-FTIR spectra and contact angle after and before the anti-CRP antibody (Ab) bonding of COC surfaces. The COC antibody infrared spectrum is not smoothed like the other ATR spectra as some information can be lost since the variation are rather small (the smoothed curve is in appendix 5.

The antibody grafting seem to be better on COC than PDMS as we observe a clear difference in ATR spectra that can be linked to the presence of amide groups from the antibody, explaining the variations observed above 3000 cm^{-1}. Moreover, the contact angle measurements on ethylene glycol show a clear change in surface chemistry.

Table 21: Surface energy calculation for each step of the COC protocol.

	RAW	PLASMA	APTES	GLUTARALDEHYDE	PROTEIN G	ANTIBODY
SURFACE ENERGY (10^{-3}N.M^{-1})	29.2	90.3	50.4	62.7	58.6	56.2

The surface energies confirm the APTES and the glutaraldehyde bonding on the surfaces. However the energy is not modified a lot by the protein G and the antibody. The surface energy linear regression can be found in appendix 6.

We can conclude that the protocol is more efficient on COC than PDMS. We tested also PMMA surfaces.

4.2.4.C PMMA

Like with the PDMS and the COC surfaces, the water contact angle is enough to assess the efficiency of the plasma treatment. Our results are comparable to the literature [179][180], the APTES grafting seems to work very well as the difference of contact angle with pristine PMMA is rather high (figure 109).

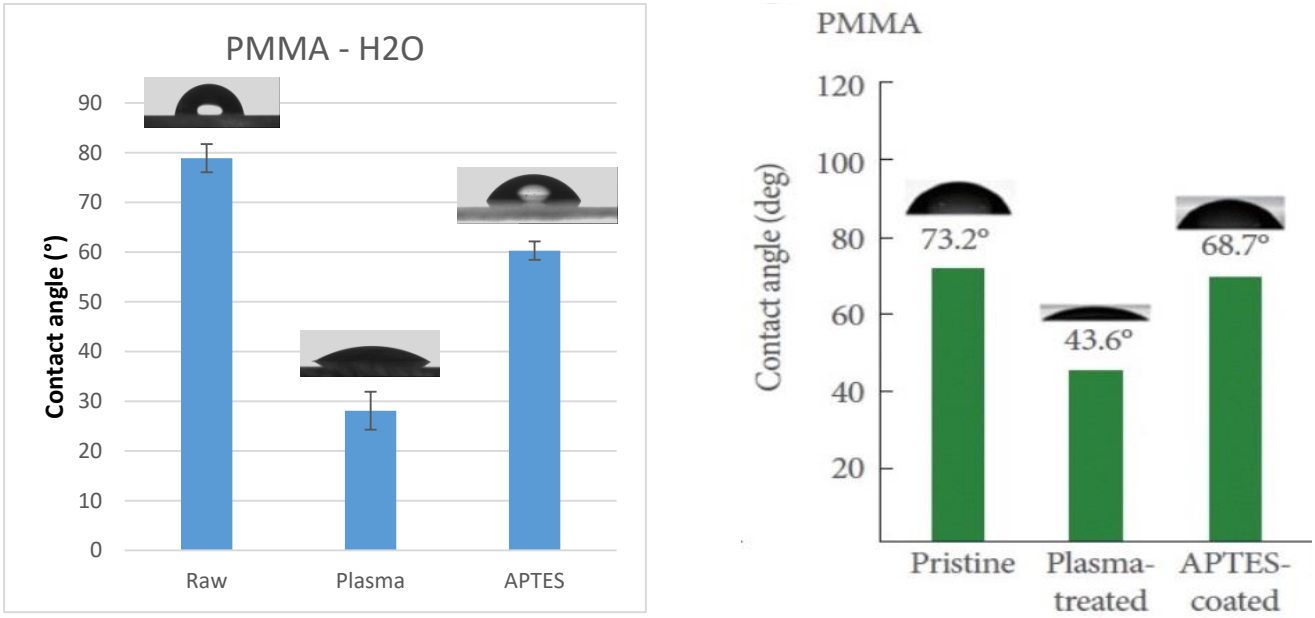

Figure 109: Comparison of water contact angle after plasma and APTES bonding of our samples (left) with the literature (right [180])

Our results with ethylene glycol on pristine PMMA are also comparable with the literature (about 60° [181]). The ethylene contact angle could not be measured after the plasma treatment as it was too close to zero to make a good estimation using the CCD camera. We can see on the figure 110 that a peak appears between 1520 cm^{-1} and 1640 cm^{-1} that should correspond to the amine groups from APTES on the surface of the PMMA. To confirm the difference between the two spectra we subtracted the PMMA ATR after the APTES step with the ATR of the untreated PMMA surface (figure 111).

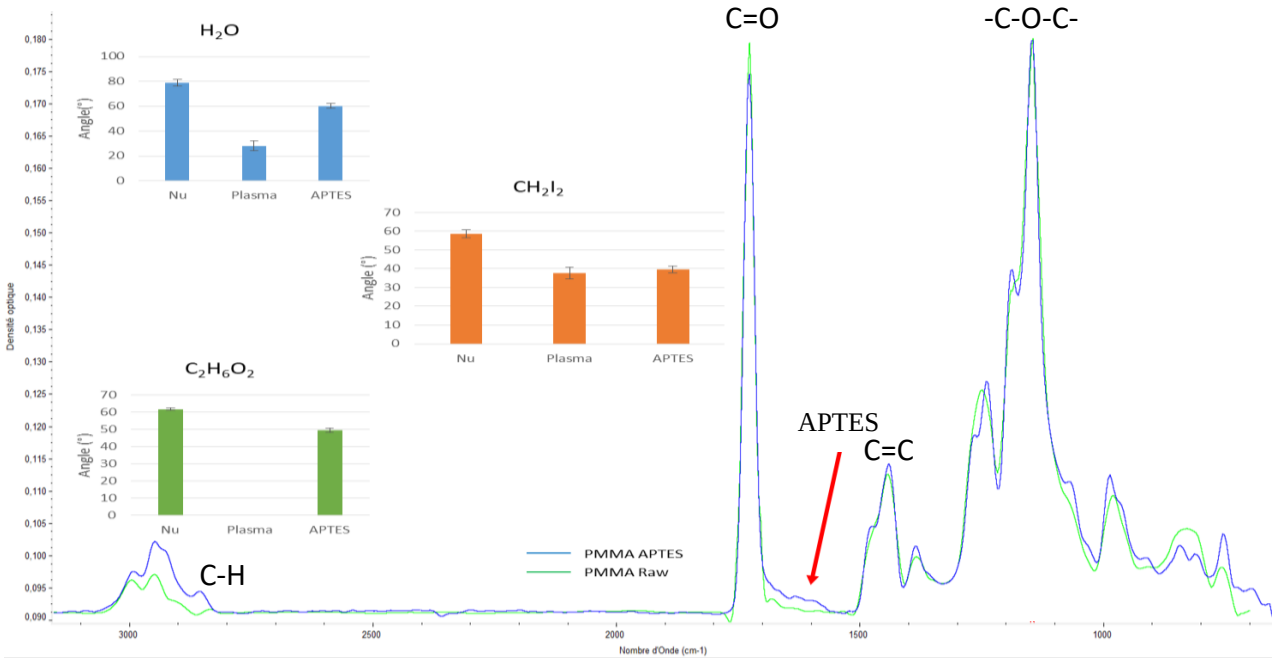

Figure 110: Comparison of infrared ATR-FTIR spectra and contact angle after and before the APTES bonding of PMMA surfaces

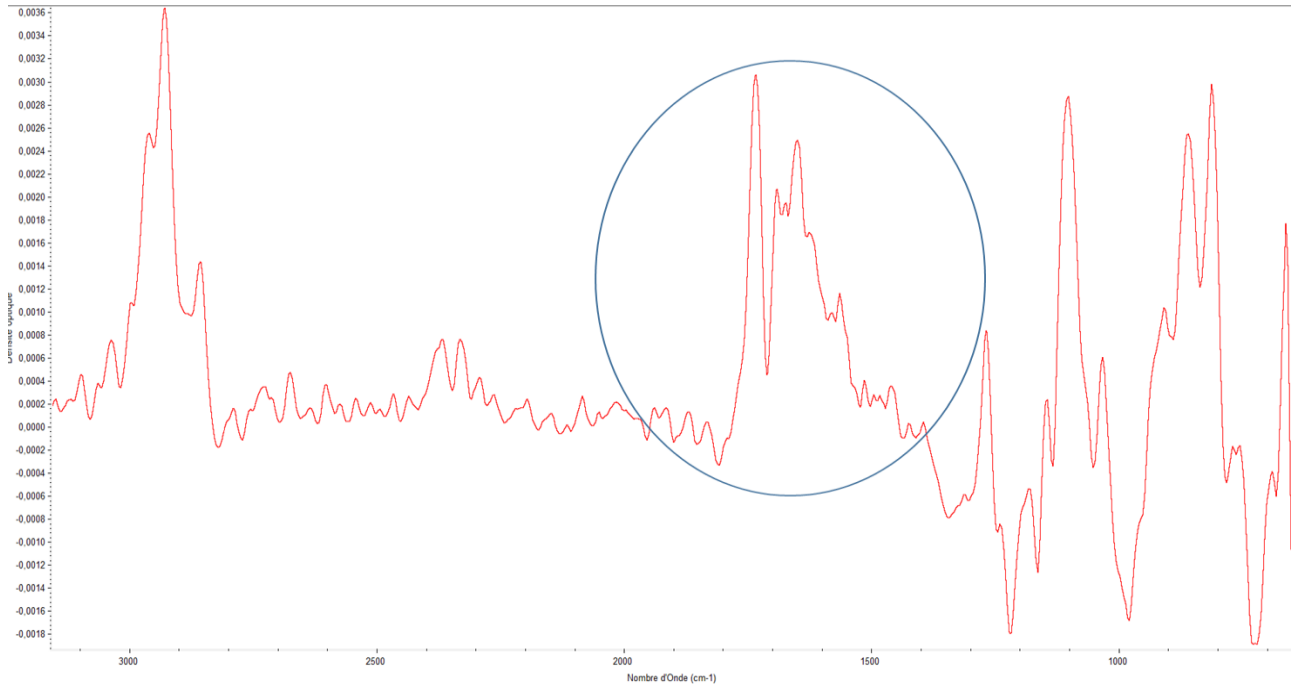

Figure 111: Difference between the ATR spectra after the APTES grafting and the ATR of the raw PMMA. The blue circle underlines the part that probably comes from the amine group of the silane.

For the glutaraldehyde characterization, the ATR is ineffective as the peak of C=O bond at 1720 hide the interval where the glutaraldehyde should be observable (figure 112).

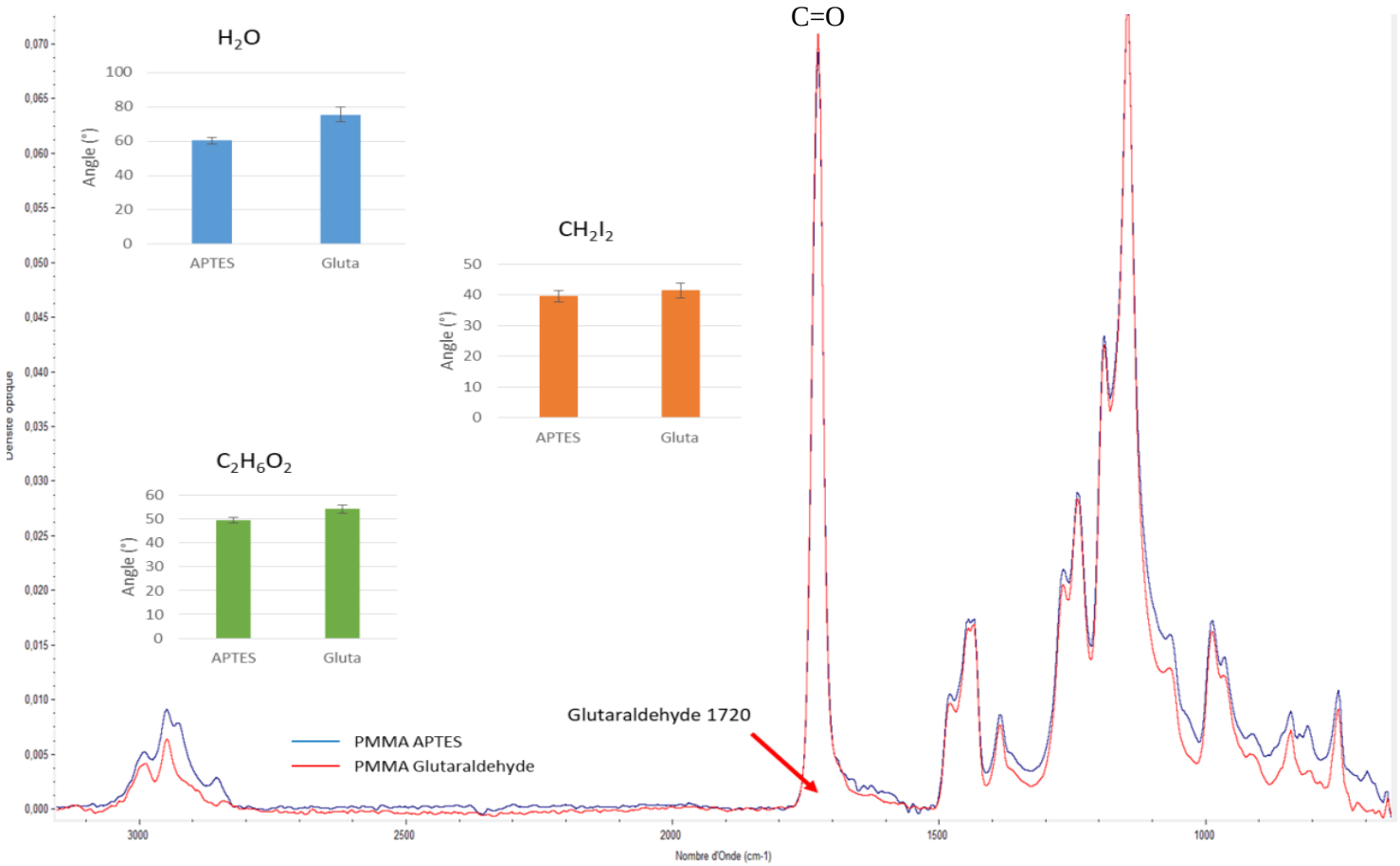

Figure 112: Comparison of infrared ATR-FTIR spectra and contact angle after and before the glutaraldehyde bonding of PMMA surfaces.

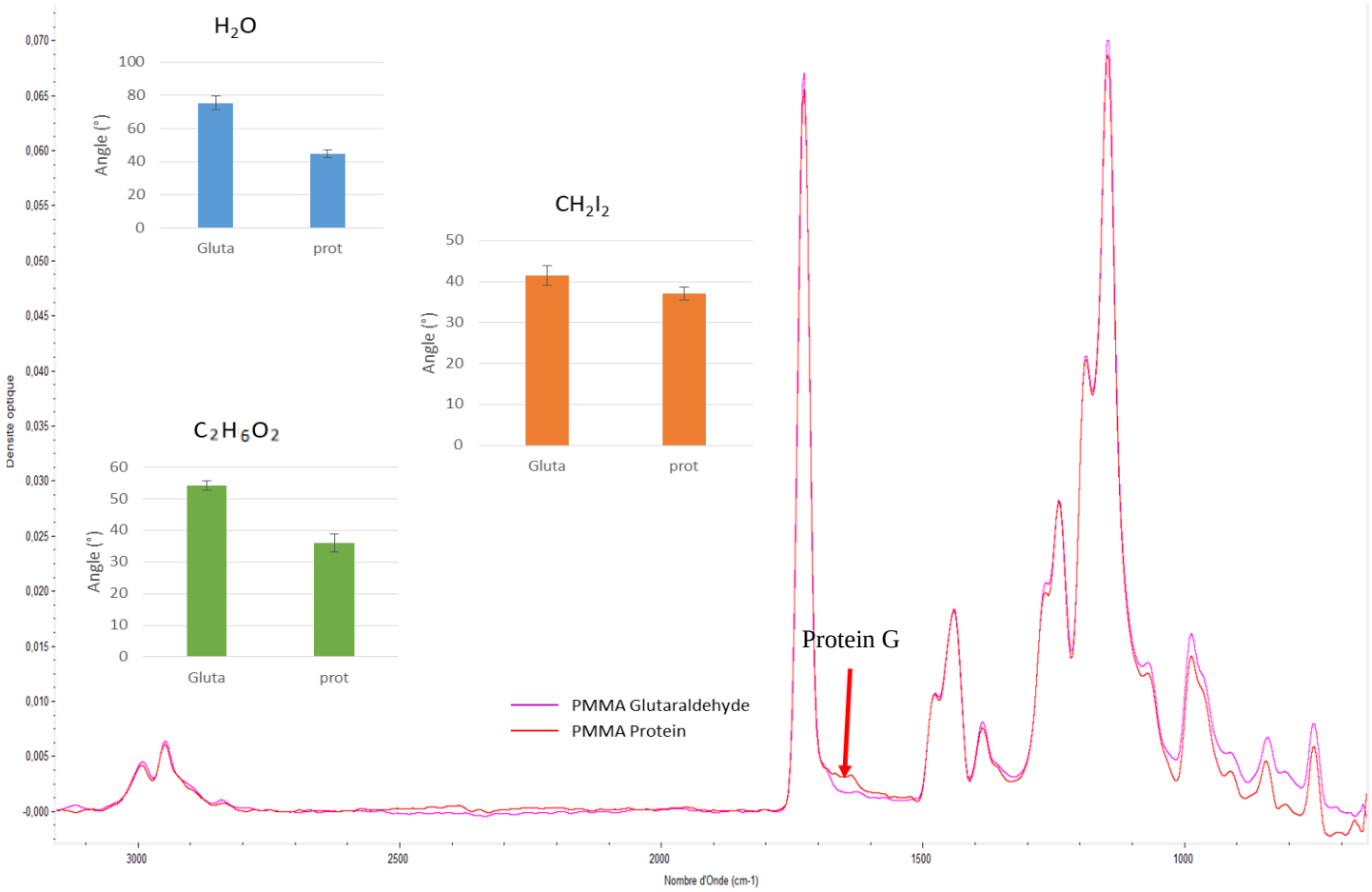

Figure 113: Comparison of infrared ATR-FTIR spectra and contact angle after and before the protein bonding of PMMA surfaces.

The protein G grafting is validated by both measurements. The contact angles are modified by this step. The ATR spectrum displays a clear peak from amine groups contained in the protein (figure 113).

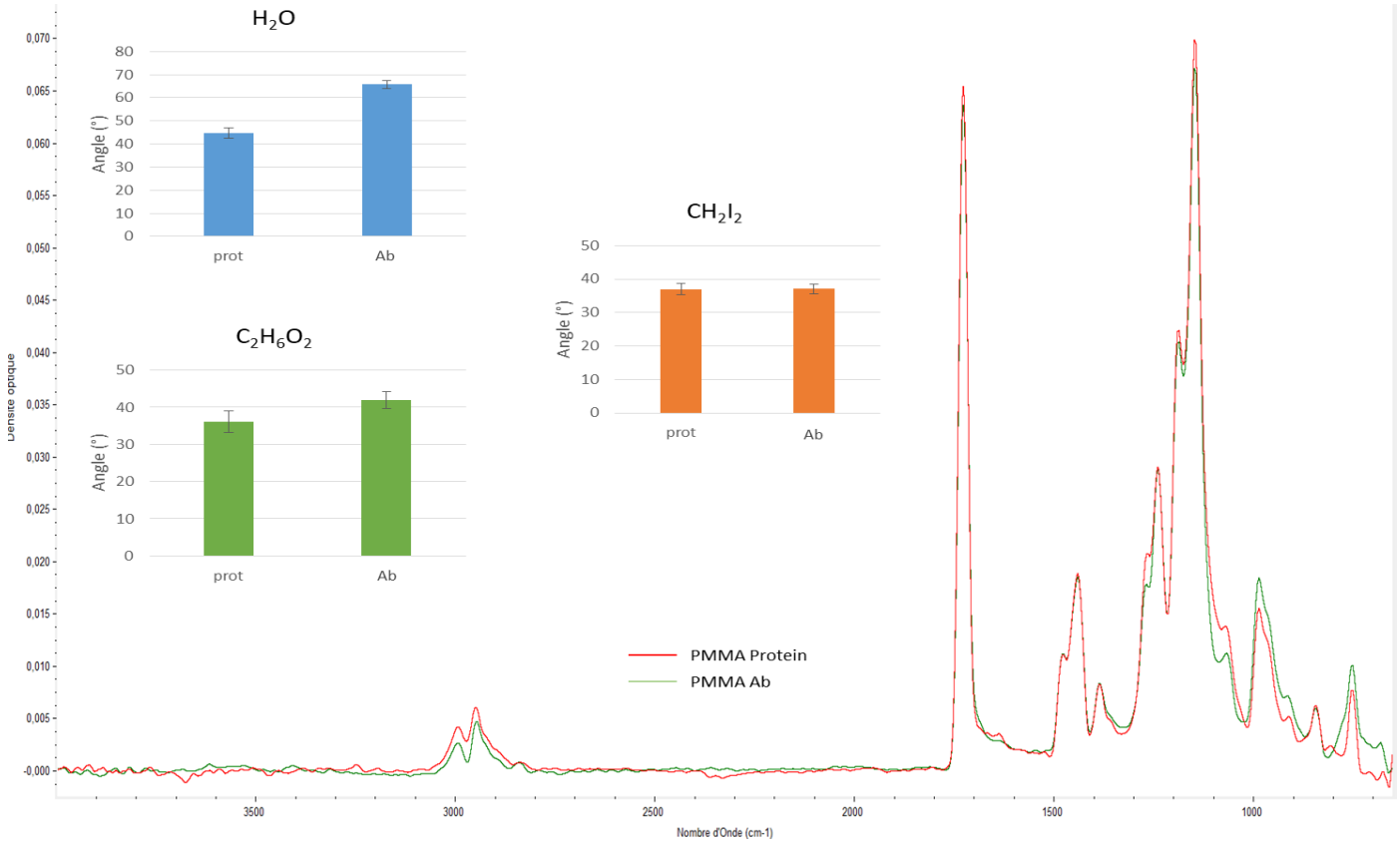

Figure 114: Comparison of infrared ATR-FTIR spectra and contact angle after and before the MAB17071 antibody bonding of PMMA surfaces.

The ATR of the antibody does not show a peak for the antibody. We hypothesize that it is hidden by the C=O peak at 1720 cm^{-1}. However the water contact angle measurements indicates a change in the surface chemistry (figure 114).

Table 22: Surface energy calculation for each step of the PMMA protocol.

	RAW	PLASMA	APTES	GLUTARALDEHYDE	PROTEIN G	ANTIBODY
SURFACE ENERGY (10^{-3}.M^{-1})	27.87	73.6	42.1	33.1	57.6	38.9

There is also a clear difference in surface energy between the PMMA samples with proteins G and the PMMA samples with anti-CRP antibodies that is an indication on the effectiveness of the protocol on the PMMA. We can also observe that the PMMA surface tension calculations are the most accurate as each linear regression have a R^2>0.99. The surface energy linear regression can be found in appendix 6.

4.2.4.D Results discussions

On the three materials that we used for the biofunctionnalization, the PDMS seems to give the worst results and the PMMA the best. We decided to select PMMA to do a XPS characterization to confirm the surface chemistry of the samples for each step of the protocol. Unfortunately the batch made to make this characterization presented very odd patterns at the surface of the samples after the APTES step (figure 115).

Figure 115: PMMA surface after the APTES grafting step. The " P" is a mark we made on the backside of the sample. The horizontal lines pattern appeared for an unknown reason.

The source of these strange lines is unknown (a problem maybe occurred at the sonication cleaning step) but we tried to make the XPS characterizations nonetheless. However, the samples surprisingly degassed inside the vacuum chamber of the XPS equipment. PMMA should not degas like PDMS when it is subject to high vacuum. We could hypothesize that the unknown pattern somewhat trapped some air at the surface of the material which rendered the XPS characterizations impossible. It would be interesting to investigate this unexpected phenomenon to determine its origin and precise nature.

Despite the fact that we could not finalize the XPS characterizations before the end of the PhD, we strongly believe that we managed to bond antibodies on PMMA and maybe also on COC. This affirmation is based on the changes observed on the contact angles, ATR and surface energy of the sample surfaces at each steps. XPS would allow making a semi-quantification of these antibodies bonding.

After successfully grafting anti-CRP antibodies on open surfaces, the future work should focus on developing a method to biofunctionnalize a closed microfluidic channel. Two ways should be possible to do that. Either directly functionalizes the channel by making the chemicals required for the bonding circulates in the channel via the creation of a pressure-controlled flow. The problem of this method is the activation of the surface; it is impossible to do it via plasma O_2 since it cannot penetrate the material very deep. The surface activation can be made by introducing PVA in the channel but it is not as effective as plasma O_2. The second strategy that could work to biofunctionnalize a microfluidic channel is to bond antibodies on two open surfaces that we could close mechanically in a second time to form the microfluidic channel.

After successfully creating the functionalized single-use microfluidic chip, the second step is to have magnetic nanoparticles that are also functionalized with antibodies that are specific to the analyte we want to detect in the tested sample.

4.3 Nanoparticles functionalization

The nanoparticles functionalization aims to bind anti-CRP antibodies to the magnetic nanoparticles so the nanoparticles can be connected to the CRP. This means that the detection of the MNP, via magnetic detection, in the system implies the presence of the analyte. The secondary (or revelation) antibody we chose is biotinylated BAM17072 from R&D systems (see appendix 3)

The strategy to bind antibodies to the MNP is the bioaffinity immobilization technique which is a different strategy in comparison to the covalent immobilization technique used for the surface biofunctionnalization. Bioaffinity is an affinity that two entities already share naturally like antibody with antigen for example or streptavidin with biotin. The latter bioaffinity is widely used in biology because of its strength and high resistance to temperature and pH changes, it is also stable in time. This technique has several other advantages like a good orientation of the proteins grafted by this strategy and good specificity that prevent nonspecific binding (other entities that bind to either the streptavidin or the biotin) [182].

Thus, our strategy is to cover the magnetic nanoparticles with streptavidin where the commercially biotinylated anti-CRP antibodies can bind to by bioaffinity interactions. We selected the FFRS4 iron oxide nanoparticle as they exhibit the best response within our magnetic detection device (see chapter 3).

To coat the nanoparticles with streptavidin, first dibenzocyclooctine N-hydroxysuccinimide is used to stick alkyne on the amine functions that are on the silica shell of the nanoparticules (figure 67). Then we use streptavidin azide to form bonds via click chemistry between the alkynes of the dibenzocyclooctine and the streptavidin [183]. After this step, the biotinylated antibodies can just be put in contact with the streptavidined

nanoparticles so that the bioaffinity immobilization can occur and successfully biofunctionnalize the MNP.

This strategy has been elaborated with the PHENIX laboratory. They will also perform the nanoparticle functionalization as they are specialized in their synthesis and manipulations. A first batch of streptavidin coated FFRS4 has been created. Unfortunately, nanoparticles tended to agglutinate and thus are not detectable with our device prototype. Improvement of the colloidal stability of the suspension is currently undertaken and the next batch should not be subjected to this phenomenon. The coating will be tested by using fluorescent markers coupled with biotin that will bind to the streptavidin. In order to test the bioaffinity immobilization between the biotinylated anti-CRP antibody and the MNP, we will use rat anti-mouse IgG2B fluorescein-conjugated antibody (provided by R&D systems) that will produce a fluorescent signal if the immobilization succeeds.

4.5 Conclusions

Different protocols have been tested to functionalize the open surface of three materials which can be used for microfluidic channels fabrication. Based on the contact angle measurements and ATR characterizations of PDMS, COC and PMMA, we successfully established an experimental protocol to biofunctionnalize the primary antibody onto PMMA surfaces. This protocol should then be adapted for closed microfluidic channels to create biofunctionnalized microfluidic chips.

The functionalization of the magnetic nanoparticles is also on the right track and should be achieved without major difficulties unless the colloidal stability of the MNP with secondary antibodies proves to be an issue that needs to be tackled.

The whole sandwich on an open surface, containing also the CRP, can first be characterized using an enhanced chemiluminescence detection (horseradish peroxidase (HRP)) to validate the chemical bonds (figure 116.A). Then the magnetic detection device can be used to characterize the sandwich structure with the presence of MNP bound to CRP via Streptavidin azide and Biotin. (figure 116.B).

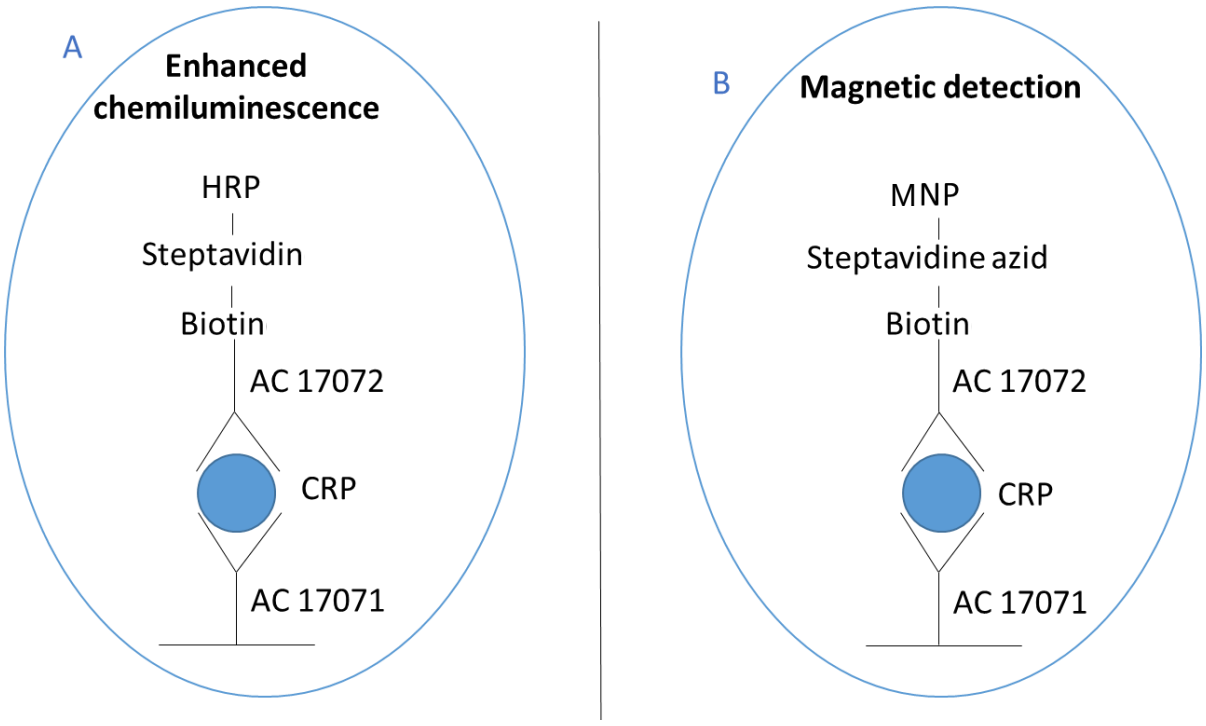

Figure 116: Sandwich immunoassay configuration validation using HRP and magnetic nanoparticles.

After the optimization of the characterizations process on open surfaces, the mechanical assembly of two biofunctionalized open surfaces can be envisaged for the functionalization of a closed microfluidic channel. In the final closed structure, a sample suspension to be tested containing the functionalized nanoparticles can be injected in a prefunctionalized microfluidic reservoir.

General conclusions

In this thesis a miniaturized magnetic nanoparticles detection system prototype for point of care (POC) immunoassays applications has been studied. As the device uses a microfluidic sample holder, the principle of microfluidic and their numerous innovations particularly in lab-on-a-chip for immunoassays have been described. In fact one of the innovations of our prototype in comparison to the previous transportable version using the same frequency mixing detection is the use of microfluidic reservoirs. We presented and discussed how the choice of the material for the microfluidic structure and the microchannel fabrication technology are critical for the properties of the final device.

An overview of the already used technologies for LOC immunoassays have been presented and how the frequency mixing detection technique used for our project positioned itself with different advantages particularly its possibility of integration, in the spectrum of different methods.

The miniaturized prototype device was then described with its magnetic and electronic parts along with the most recent improvements made to optimize the response signal of superparamagnetic nanoparticles. Then the approaches to fabricate the microfluidic channel were detailed before explaining the considerations that leaded to the choice of three polymer materials to create these microchannels: PDMS, COC and PMMA.

To validate and improve the magnetic detection device prototype, we subjected it to a battery of tests to assess its efficiency in various conditions that included different magnetic nanoparticles, different microfluidic channel shapes or in the presence of a static magnetic field. The results are encouraging since we can detect magnetic nanoparticles at low iron oxide concentrations with a dynamic of three orders of magnitude, good linearity and reproducibility. Improvements have been made on every facets of the magnetic detection device to improve its stability and decrease the limit of detection down to 6 ng/μL.

Finally the functionalization strategy for both the microfluidic channel with the primary antibodies and the magnetic nanoparticles with the secondary antibodies have been described. The aim is to create the sandwich configuration needed to perform immunoassays with the magnetic detection device. We tried to bind the primary antibodies on three different surfaces: PDMS, COC and PMMA. The contact angle and ATR characterizations have shown promising results with PMMA but XPS measurements could confirm it in a near future.

The next step for the project is to perform immunoassays with CRP first and then proves that it is robust and can be used for the detection of other pathogens. A fully portable POC device should then be developed by miniaturizing all electronic instrumentation and lock-in amplifiers to perform immunoassays.

A second fully integrated version of the detection device has also been studied during my PhD that would be fabricated using cleanroom process obtain a very miniaturized and integrated second version of the magnetic detection device (see appendix 7 for the design and strategy to produce this second version). The excitation and detection will be fabricated using copper electrodeposition. This will allow to enhance the sensitivity and the limit of detection and to reduce the energy consumption for a miniaturized portable system. The table 23 presents the expected performances of both of the finalized versions of the portable device.

Table 23: Expected performance for the first and second version of the portable magnetic detection device for immunoassay.

Expected results for the first portable device:	**Fully integrated structure specifications:**
• Required biological sample quantity: few µL • Sensitivity of the device: <10 ng/µL • Analysis time: 5 to 10 minutes • Reagent consumption: ~50 µL • Precision: Low intra-assay variability • High specificity, low cross reactivity for two-pathogen detection	• Low power consumption • Small device size: about 3-4 cm • Required biological sample quantity: ~0.5 µL • Sensitivity of the device: <10 ng/µL • Faster analysis time: ~ a minute • Low reagent consumption: ~5 µL • Precision: Low intra-assay variability • High specificity, low cross reactivity for two-pathogen detection

The magnetic detection device presented in this thesis has been patented and a maturation project has been funded by SATT Lutech to develop a portable prototype for rapid and cost-effective pathogen sensing for point of care (POC) testing [184].

List of publications

Journal Publication:

A. RABEHI, **B. GARLAN**, S. ACHTSNICHT, H-J. KRAUSE, A. OFFENHAUSSER, K. NGO, S. NEVEU, S. GRAFF-DUBOIS, H. KOKABI, "Magnetic Detection Structure for Lab-on-Chip Applications Based on the Frequency Mixing Technique", *Sensors*, 18(6), 1747, published: 29 May 2018

International conferences:

A. RABEHI, **B. GARLAN**, F. SHANEHSAZZADEH, H. KOKABI, K. NGO, H.-J. KRAUSE, "Magnetic detection structure for LOC immunoassays, multiphysics simulations and experimental results", *proceedings of EUROSENSORS 2017*, 1(4), 529, 2017, Paris.

National conferences:

A. RABEHI, **B. GARLAN**, H. KOKABI, K. NGO, H.-J. KRAUSE, "Electromagnetic immunoassays using magnetic nanoparticles in a microfluidic structure", JETSAN *(journées d'etude sur la telesante)*, may 2017, Bourges,

B. GARLAN, A. RABEHI, K. NGO, H.-J. KRAUSE H. KOKABI, "Magnetic detection structure for rapid, cheap and nomad immunoassays." JNRDM (Journées Nationales du Réseau Doctoral en Micro-nanoélectronique) November 2017, Strasbourg.

B. GARLAN, A. RABEHI, K. NGO, H.-J. KRAUSE H. KOKABI, "Magnetic nanoparticles detection in a microfluidic chip", Journées Thématiques «Capteurs Magnétiques & Électromagnétiques (EM) et Applications» May 2018, Grenobles.

B. GARLAN, G. PERRY, K. NGO, H.-J. KRAUSE H. KOKABI, "Detection of superparamagnetic nanoparticles for immunoassays", JETSAN *(journées d'etude sur la telesante)*, May 2019, Paris.

Appendix 1: Magnetic measurements step-by-step experimental protocol

This document describes the detailed experimentation steps for magnetic nanoparticles detection using frequency mixing method.

1. Circuit cabling and microfluidic

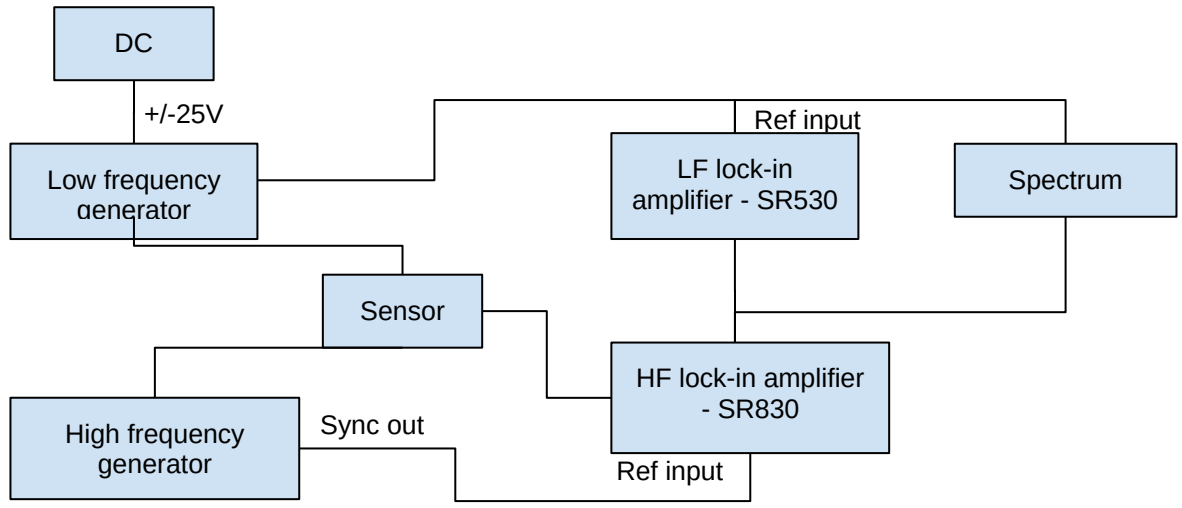

Functional block diagram of the electrical cabling, with real port names of devices. All connections use BNC cables, excepted between the DC supply and the LFG that uses basic jack cable.

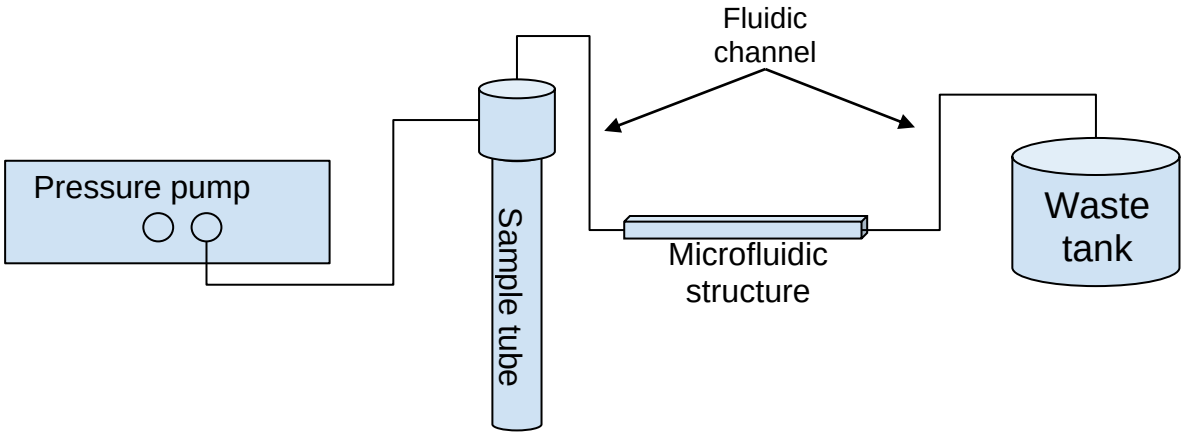

Fluidic schematic for driving nanoparticles into the sensor. The microfluidic structure is inserted between both PCB.

2. Devices activation

Turn on the following instruments:

- DC dual power supply, set the symmetrical voltage on +/- 25V.
- The Stanford Research ultra-low distortion generator DS360, at a frequency of 40 kHz, and 40 V peak to peak voltage
- SR830 lock-in amplifier for high frequency demodulation
- SR530 lock-in amplifier for low frequency demodulation
- Spectrum Analyser
- Microfluidic pressure pump from Fluigent. Then open the corresponding software and enable the heating process that takes 10 minutes.

To avoid the sensor overheating, make sure the DC supply and the high frequency generator are disabled. It is possible to do it with a specific button without shutting down or disconnects the materials.
Electromagnetic devices could be sensitive to their environment, remember to insulate or to turn off some devices around the sensor (especially the extraction hood).

3. Low frequency generator calibration

- With a screwdriver, turn the “Freq” potentiometer on the surface of the corresponding PCB circuit until frequency is equal to 65 Hz. Then adjust the resonance frequency of the bandpass filter with the “Res” potentiometer until you find the maximum amplitude.
- Set the 40 Vpp amplitude to the power output (“Pow out”).
- The “Dist” and “Sym” potentiometers let reduce the harmonic distortion. Using the spectrum analyser and with the low power output (“Sig out”), the best first harmonic rejection (compared to the fundamental) is around 85 / 90 dBV at that amplitude. The second harmonic rejection best setting is about 75 dBV.

This last step usually impact the voltage amplitude, return to the second point if it is necessary

4. Lock-in amplifier setting

- The first lock-in (SR830) let the high frequency demodulation. Ideally, set the time constant to 30 us, and the sensitivity to 100 mV*. Select the first channel X output. You can refer to the datasheet, part “SR830 basics” to understand well these parameters.
- On the second lock-in (SR530), used for low frequency demodulation, set a high time constant (1 second is enough) and 20 mv sensitivity. On the reference bloc, select the 2f mode**.

* The previous setting on sensitivity for both amplifiers can be modified, but it impacts directly the noise level (so the detection limit). Furthermore, there is an optimal value to get the higher signal amplitude level.
** The 2f mode allows to double the reference input frequency, then to have a DC constant output only depending on the first mixing term. Otherwise, you will demodulate the low frequency from excitation signal, which is the wrong value.

5. PCB parallelism adjustment

- Place inside the sensor one or two microfluidic structure
- Connect one of these structures to the fluidic microtubes
- To make sure there are no particles inside the sensor, wash the channels with water or hydrochloric acid (PDMS is proof).
- The non-parallelism between both PCB is part of the offset on the mixed terms when the sensor is empty. By using the spectrum analyser, you have to turn three different adjustment screws to get the correct position of the top PCB. Naturally, that also modifies the gap between them, so try to keep the nearest position *. If the LFG step was well done, you can totally remove the offset **.

* Be careful: if the gap is to short, the top PCB layer is blocked by the microfluidic structure, Although the system is strong, but you may bend the top PCB, so it becomes impossible to make it parallel to the down fixed PCB.
** Sensor mechanical instability can make this step very long and not perfectly concluding.

6. Particles measurement

- When all calibrations are done, keep in mind the setting of all devices, then the actual noise level without any sample in the sensor.
- Connect the test tube that contains diluted nanoparticles to the fluidic circuit (pressure less than 200mBar) and let flow the fluid through the circuit *.
- The DC output is already displayed on the second lock-in amplifier, you do not need anything else to record the measurement result.

* When you see the particles expelled out from the channel, you can stop the pressure pump to avoid waste. It could be useful to make as much measurement as possible.

7. Common problems

Usually, some results look senseless without any voluntary and obvious changes on the setup. For each observation, the main causes are listed by frequency appearance order, with a way to solve them. The most common default are:

- Increasing of the noise level, on empty measurement:
    - Mechanical instability of the sensor
        Return to the fifth step
    - Near electromagnetic perturbation source
        Verify some low frequency working devices, like the extraction hood, or all devices that contains motors
    - particles residues in the channel
        If water is not enough, try with hydrochloric acid.
- No flow in the microfluidic circuit:
    - particles deposit or many air bubbles in the structure
        - Push water with short but strong pressure strokes. Don’t exceed 300 mbar pressure, the PDMS channel could unstick from its glass layer.
        - Otherwise, invert the direction of the flow.
        - Last possibility: wash with hydrochloric acid
- Non detection of the particles but reasonable noise level:
    - Check cables connection and enable buttons of generators
    - Return to the lock-in setting at the fourth step

Appendix 2: COMSOL microfluidic and chemical engineering simulation parameters

Table A1: List of constant parameters used in COMSOL 5.3 Multiphysics simulations

Parameter	Value	Description
Hchannel	0.200 [mm]	"Height of the channel"
Dchannel	0.500 [mm]	"Diameter of channel"
Temp	300 [K]	"System temperature"
Qin	90 [µl/min]	"Inlet flow rate"
D	$10e^{-11}$ [m²/s]	"Analyte diffusion coefficient"
ka	$10e^{6}$ [1/M/s]	"Adsorption rate constant"
kd	$10e^{-3}$ [1/s]	"Desorption rate constant"
Cin	0.1 [nM]	"Inlet analyte concentration"
Cr	$3.3*10e^{-3}$ [nmol/m²]	"Receptor surface concentration"
c0	$1e^{-5}$ [nM]	"Initial concentration"

Table A2: List of parameters used in COMSOL 5.0 Multiphysics simulations

Parameter	Value	Description
Hchannel	0.200 [mm]	"Height of the channel"
Dchannel	0.500 [mm]	"Diameter of channel"
T	300 [K]	"System temperature"
Cin	0.1 [nmol/l]	"Inlet analyte concentration"
Qin	90 [µl/min]	“Inlet flow rate"
Dnp	$1e^{-11}$[m²/s]	"NP/analyte diffusion coefficient"
ka	$1e^{6}$ [l/mol/s]	"Adsorption rate constant"
kd	$1e^{-3}$ [1/s]	"Desorption rate constant"
c0	$1e^{-5}$ [nmol/l]	"Initial conc"
Cr	$3.3e^{-3}$ [nmol/m²]	"Receptor surface concentration"
Av	$6.022e^{23}$ [1/mol]	“Avagadro's number”
Dp	20 [nm]	“Particle diameter”
kB	$1.38065e^{-23}$ [m²*kg/s^2/K]	“Boltzmann constant”

Key assumptions for all simulations:

- Reynolds number was roughly 0.29 – reasonable to assume laminar and not Stokes flow
- No slip at channel walls
- Incompressible fluid (water)
- PDMS walls were rigid (somewhat inaccurate, but likely inconsequential at steady-state)
- No competition in adsorption mechanisms

Appendix 3: Primary and secondary human CRP antibodies purchased for sandwich immunoassay

R&D SYSTEMS
a bio-techne brand

Human C-Reactive Protein/CRP Antibody

Monoclonal Mouse IgG_{2B} Clone # 232007
Catalog Number: MAB17071

DESCRIPTION	
Species Reactivity	Human
Specificity	Detects human CRP in direct ELISAs.
Source	Monoclonal Mouse IgG_{2B} Clone # 232007
Purification	Protein A or G purified from hybridoma culture supernatant
Immunogen	Human plasma-derived CRP Accession # P02741
Formulation	Lyophilized from a 0.2 µm filtered solution in PBS with Trehalose. See Certificate of Analysis for details. *Small pack size (-SP) is supplied as a 0.2 µm filtered solution in PBS.

APPLICATIONS

Please Note: *Optimal dilutions should be determined by each laboratory for each application. General Protocols are available in the Technical Information section on our website.*

Human C-Reactive Protein/CRP Sandwich Immunoassay		**Reagent**
ELISA Capture	2-8 µg/mL	Human C-Reactive Protein/CRP Antibody (Catalog # MAB17071)
ELISA Detection	0.5-2.0 µg/mL	Human C-Reactive Protein/CRP Biotinylated Antibody (Catalog # BAM17072)
Standard		Recombinant Human C-Reactive Protein/CRP (Catalog # 1707-CR)

PREPARATION AND STORAGE

Reconstitution	Reconstitute at 0.5 mg/mL in sterile PBS.
Shipping	The product is shipped at ambient temperature. Upon receipt, store it immediately at the temperature recommended below. *Small pack size (-SP) is shipped with polar packs. Upon receipt, store it immediately at -20 to -70 °C
Stability & Storage	**Use a manual defrost freezer and avoid repeated freeze-thaw cycles.** ● 12 months from date of receipt, -20 to -70 °C as supplied. ● 1 month, 2 to 8 °C under sterile conditions after reconstitution. ● 6 months, -20 to -70 °C under sterile conditions after reconstitution.

BACKGROUND

C-Reactive Protein (CRP) is a secreted protein that belongs to the Pentraxin family. It circulates as a non-covalent homopentamer. The CRP concentration in human plasma is highly increased during acute phase response to tissue injury or infection.

R&D SYSTEMS
a bio-techne brand

Human C–Reactive Protein/CRP Biotinylated Antibody

Monoclonal Mouse IgG_{2B} Clone # 232024
Catalog Number: BAM17072

DESCRIPTION	
Species Reactivity	Human
Specificity	Detects rhCRP in direct ELISAs.
Source	Monoclonal Mouse IgG_{2B} Clone # 232024
Purification	Protein A or G purified from hybridoma culture supernatant
Immunogen	Human plasma-derived CRP
Formulation	Lyophilized from a 0.2 µm filtered solution in PBS with BSA as a carrier protein. See Certificate of Analysis for details.

APPLICATIONS

Please Note: *Optimal dilutions should be determined by each laboratory for each application. General Protocols are available in the Technical Information section on our website.*

Human C-Reactive Protein/CRP Sandwich Immunoassay		**Reagent**
ELISA Capture	2-8 µg/mL	Human C–Reactive Protein/CRP Antibody (Catalog # MAB17071)
ELISA Detection	0.5-2.0 µg/mL	Human C–Reactive Protein/CRP Biotinylated Antibody (Catalog # BAM17072)
Standard		Recombinant Human C–Reactive Protein/CRP (Catalog # 1707-CR)

PREPARATION AND STORAGE

Reconstitution	Reconstitute at 0.5 mg/mL in sterile PBS.
Shipping	The product is shipped at ambient temperature. Upon receipt, store it immediately at the temperature recommended below.
Stability & Storage	**Use a manual defrost freezer and avoid repeated freeze-thaw cycles.** ● 12 months from date of receipt, -20 to -70 °C as supplied. ● 1 month, 2 to 8 °C under sterile conditions after reconstitution. ● 6 months, -20 to -70 °C under sterile conditions after reconstitution.

BACKGROUND

C-Reactive Protein (CRP) is a secreted protein that belongs to the Pentraxin family. It circulates as a non-covalent homopentamer. The CRP concentration in human plasma is highly increased during acute phase response to tissue injury or infection.

bio-techne
bio-techne.com
Global info@bio-techne.com techsupport@bio-techne.com
North America TEL 800 343 7475 Europe | Middle East | Africa TEL +44 (0)1235 529449
China info.cn@bio-techne.com TEL +86 (21) 52380373
Rest of World bio-techne.com/find-us/distributors TEL +1 612 379 2956

Appendix 4: Antibody bonding protocol using APTES on 1 cm² samples of PDMS, PMMA and COC.

1. The three materials are cut into small squares of 1 cm² and cleaned using sonication

2. The APTES:ETOH solution is mixed with a 1:5 ratio and applied to the samples during 2 hours. Afterward, they are cleaned two times by absolute ethanol and then one more time with absolute ethanol with sonication. The samples are heated after at 90°C during 30 minutes.

3. The samples are then immersed in a glutaraldehyde solution at 5% in PBS for 30 minutes. The surfaces are then rinsed with Milli-Q water for 5 minutes.

4. 100 µl of a 20 mg/mL protein G solution in PBS is then dropped on each sample. The droplets should be left on the samples for 2 hours in a close container to avoid evaporation. After that the surfaces are cleaned two times with PBS containing 0.05% TWEEN 20 during 5 minutes then rinsed one time with Milli-Q water for 5 minutes.

5. The MAB17071 antibodies are diluted in PBS to a concentration of 20 mg/L. 100 µL droplets of this solution are put on the samples for 2 hours at room temperature. Like with step 4, the samples are then cleaned two times with PBS-TWEEN 20 and one time with ultrapure water.

6. Finally the blocking step consists of putting the sample into a solution of 1% of BSA in PBS during 30 minutes.

Appendix 5: Smoothed spectra of figure 108

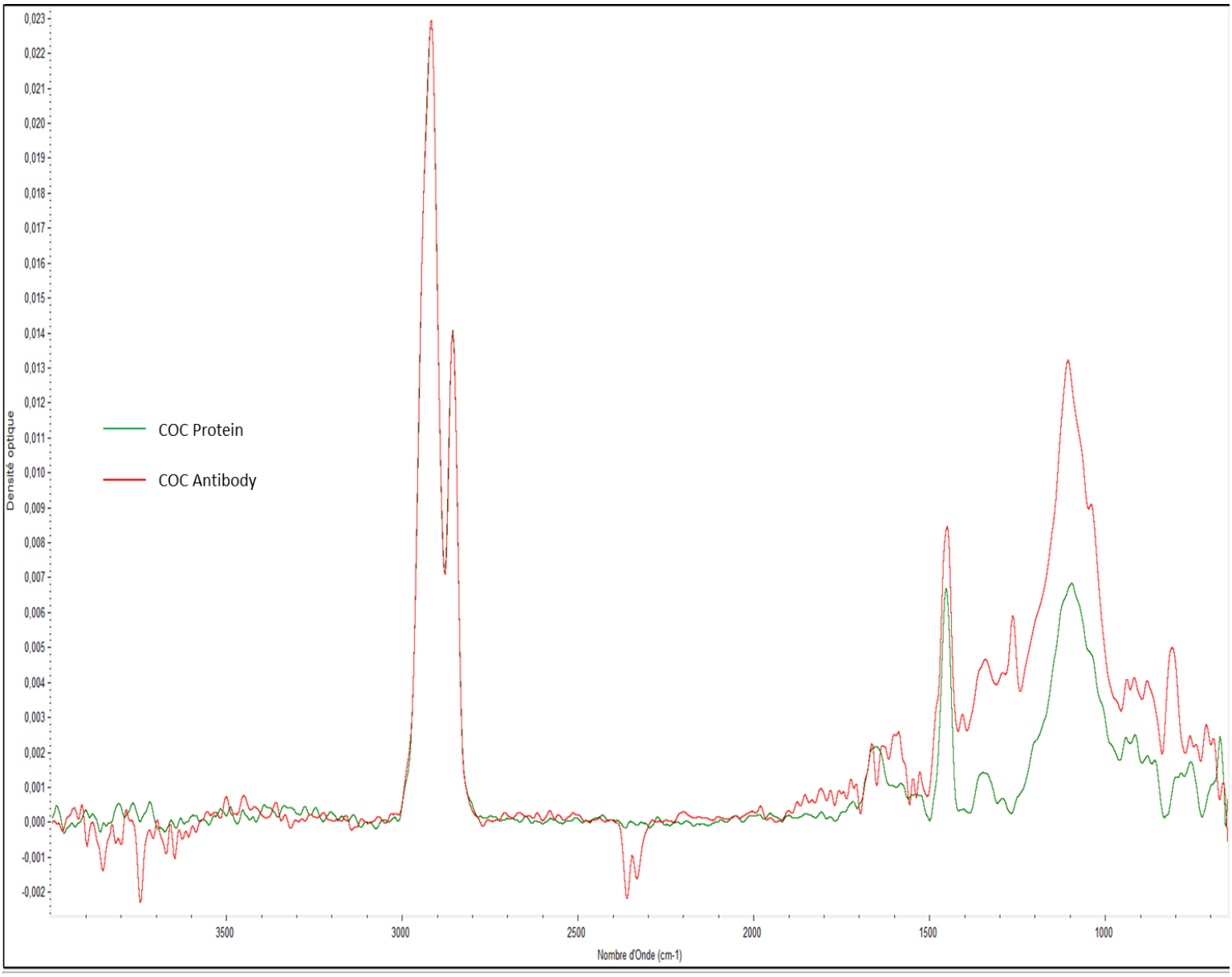

Figure 108[2]: Comparison of ATR and contact angle after and before the anti-CRP antibody (Ab) bonding of COC surfaces. Unlike figure 109, the COC antibody ATR is smoothed like the other ATR spectra.

Appendix 6: Surface energy (10^{-3} $N.M^{-1}$) table and linear regressions

	PRISTINE	PLASMA	APTES	GLUTARALDHEHYDE	PROTEIN G	ANTIBODY
PMMA	27.80	73.62	42.05	33.10	57.53	38.87
COC	29.22	90.31	50.37	62.66	58.54	56.24
PDMS		105.05	11.25	12.51	20.00	32.10

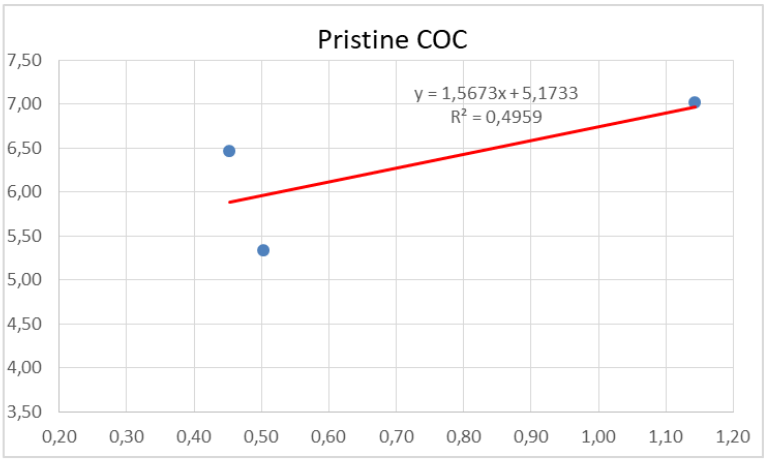

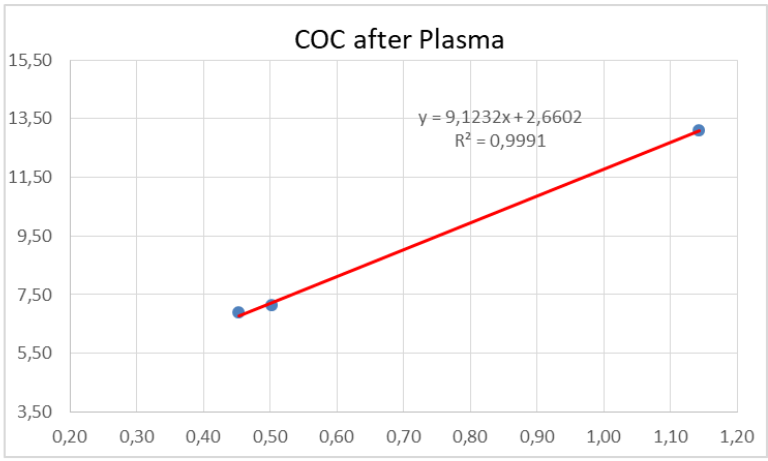

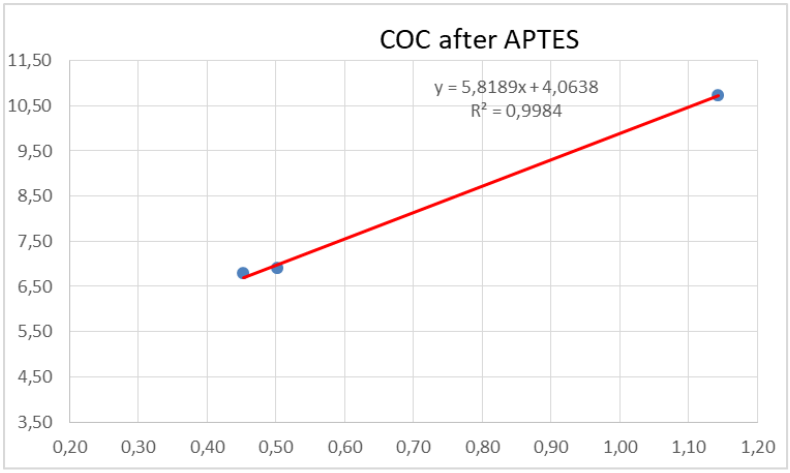

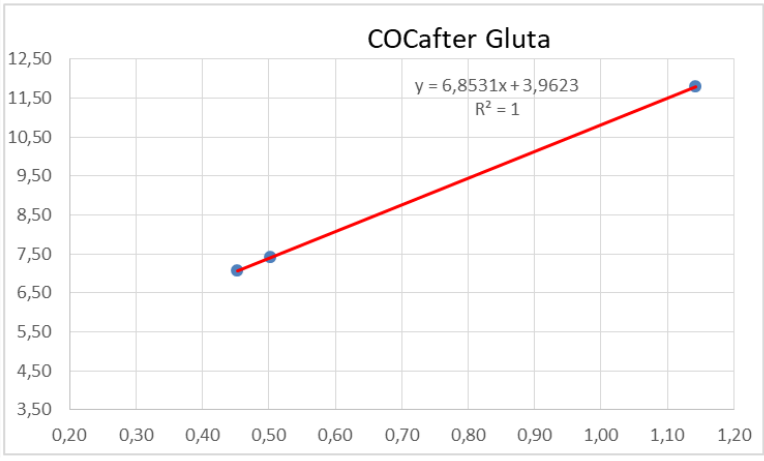

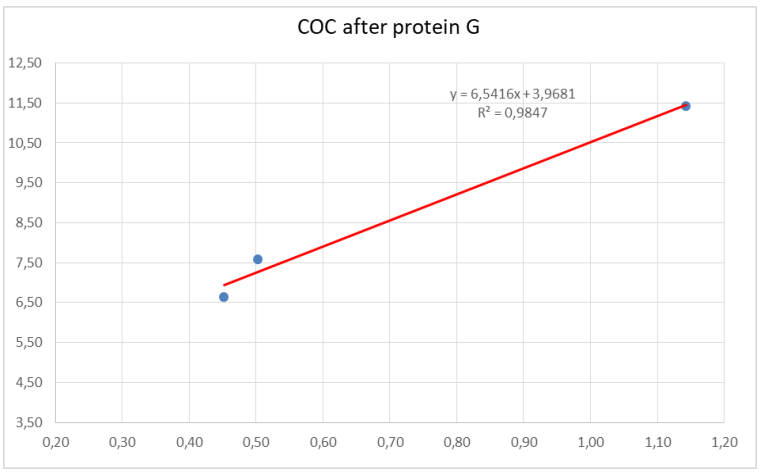

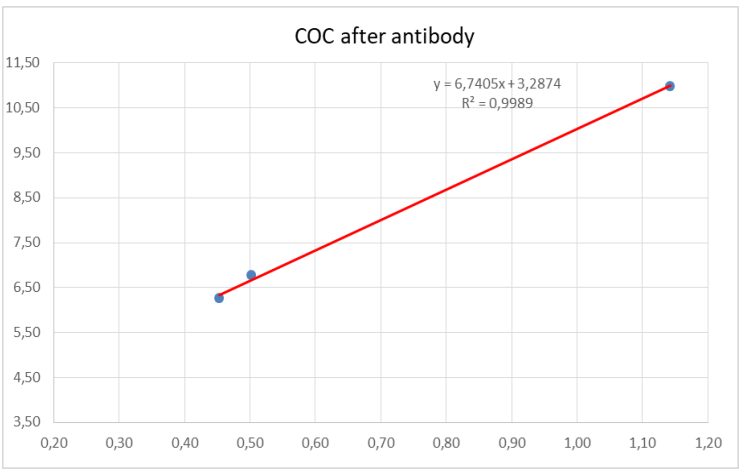

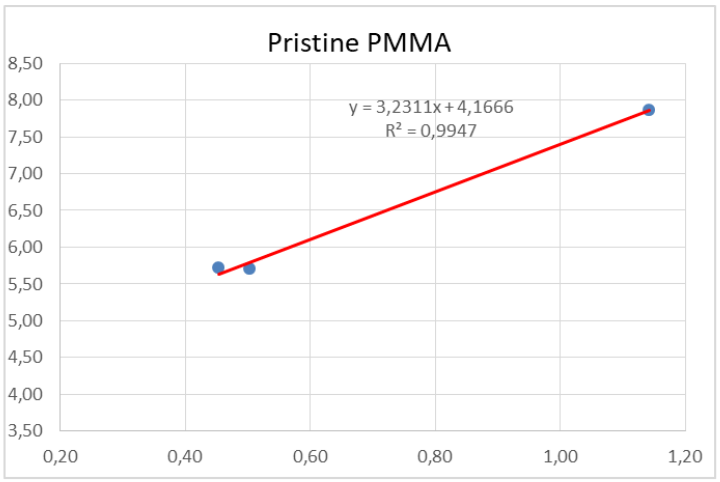

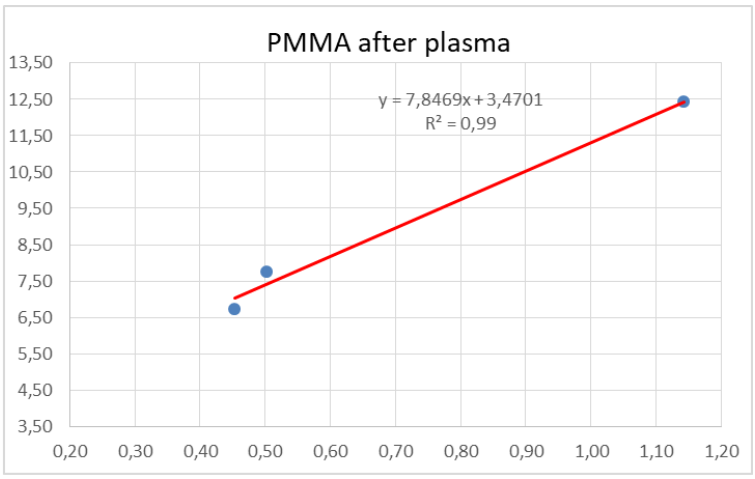

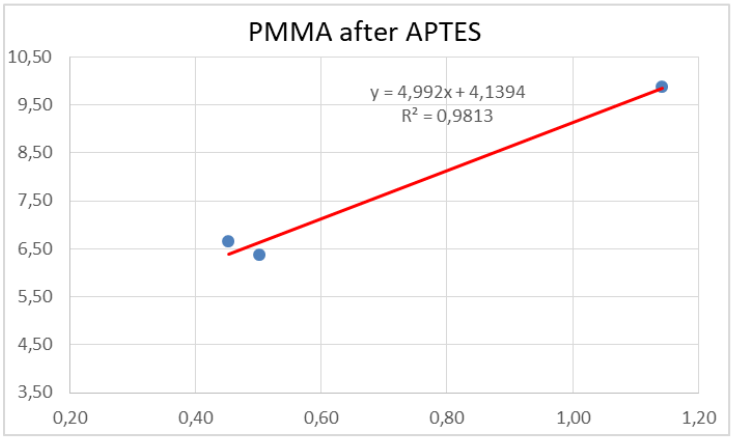

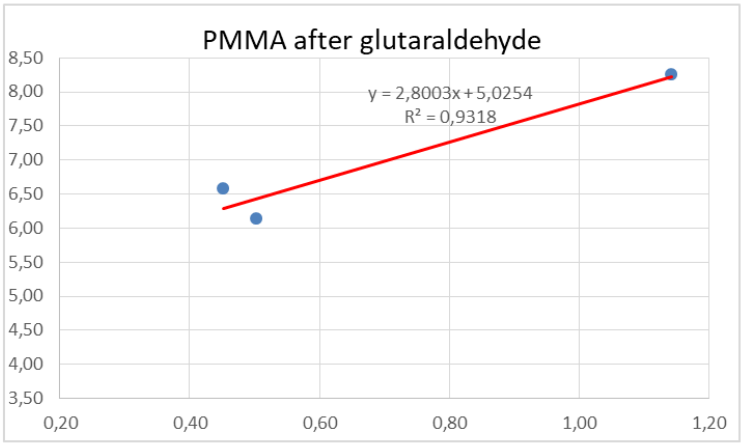

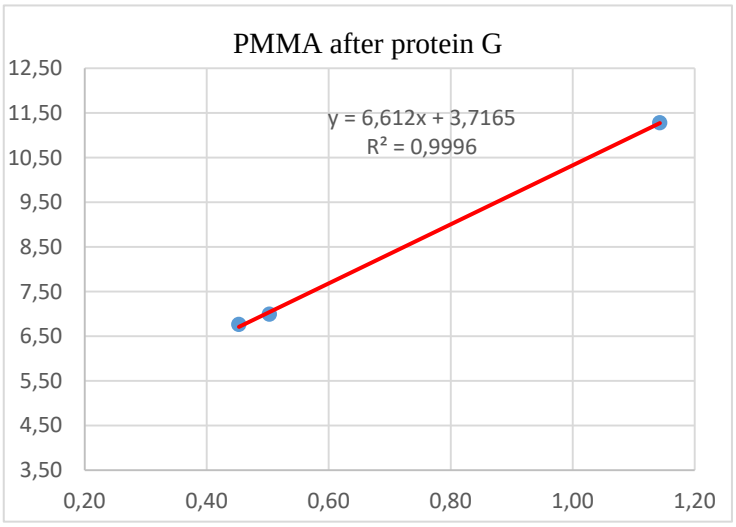

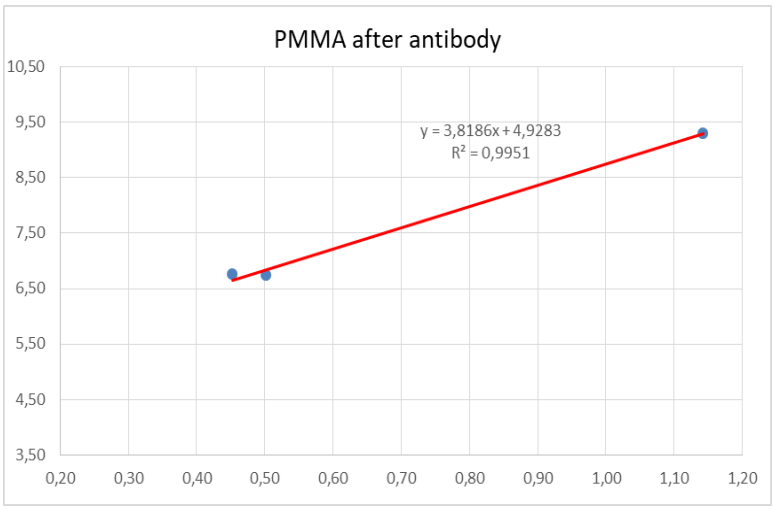

Figure 117: Surface energy calculation for each step of the PMMA and COC functionalization protocol. [x,y] have been calculated using the equation page 108.

Appendix 7: Integrated device

Introduction

The aim of the fully integrated device is to be as small as possible so the coils can be as close as possible to the nanoparticles that are trapped in the microfluidic channel. To obtain the best possible performances, the device will be created in a cleanroom using extremely precise instruments. The principle of this second version of the magnetic detection device is quite similar to the one presented in the rest of this thesis. The main difference is that the coils are mono-layered and not multi-layered, and the microfluidic channel is a part of the device and is not disposable. In fact the coils are thick copper layer fabricated with electrodeposition.

Miniaturization advantages:

- Smaller device
- Less power consumption
- Smaller sample volume needed
- Faster testing

Drawbacks:

- More expensive
- The device has to be single-use as the microfluidic channel can't be changed and its cleaning seems difficult.
- The protocol to create a prototype is complicated

3D models of the prototype:

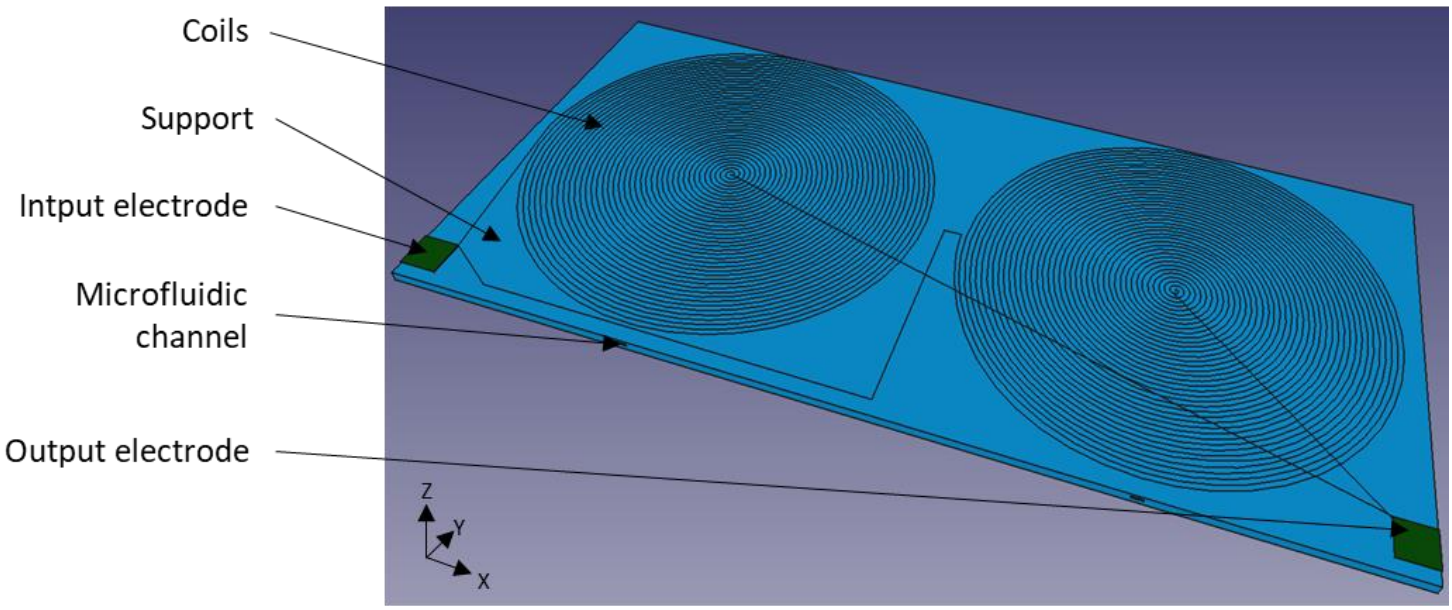

Figure 118: 3D view of the fully integrated device.

Side and above views of the prototype:

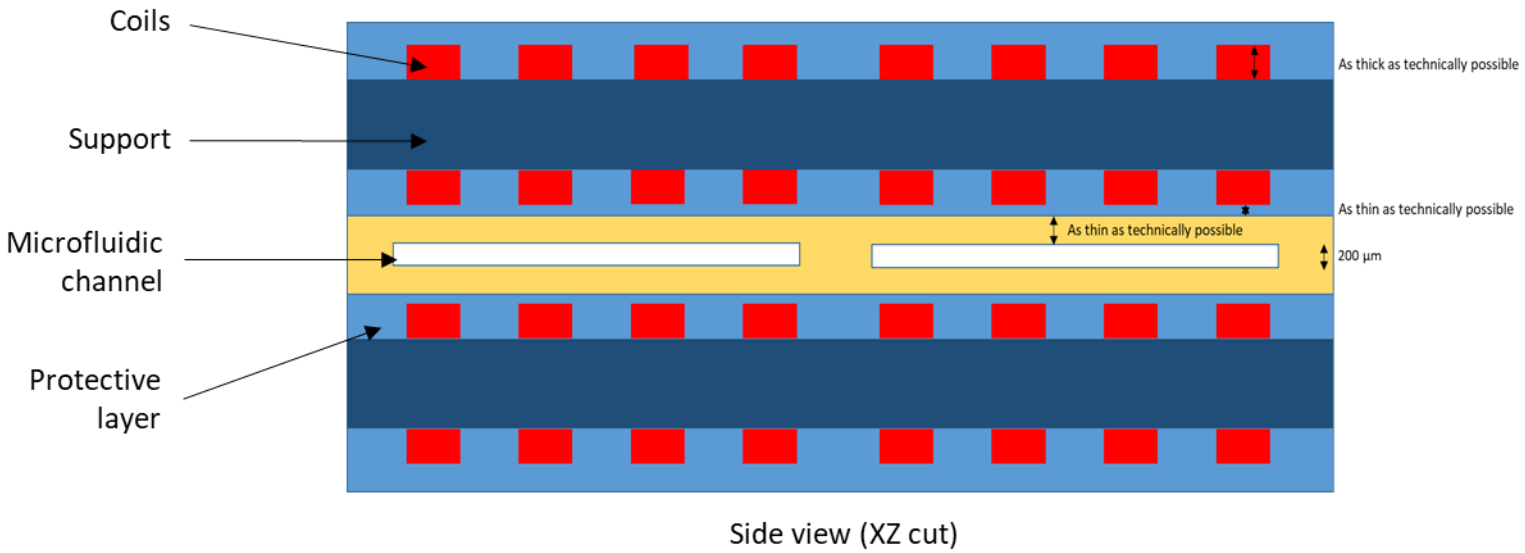

Figure 119: Side view (XZ cut).

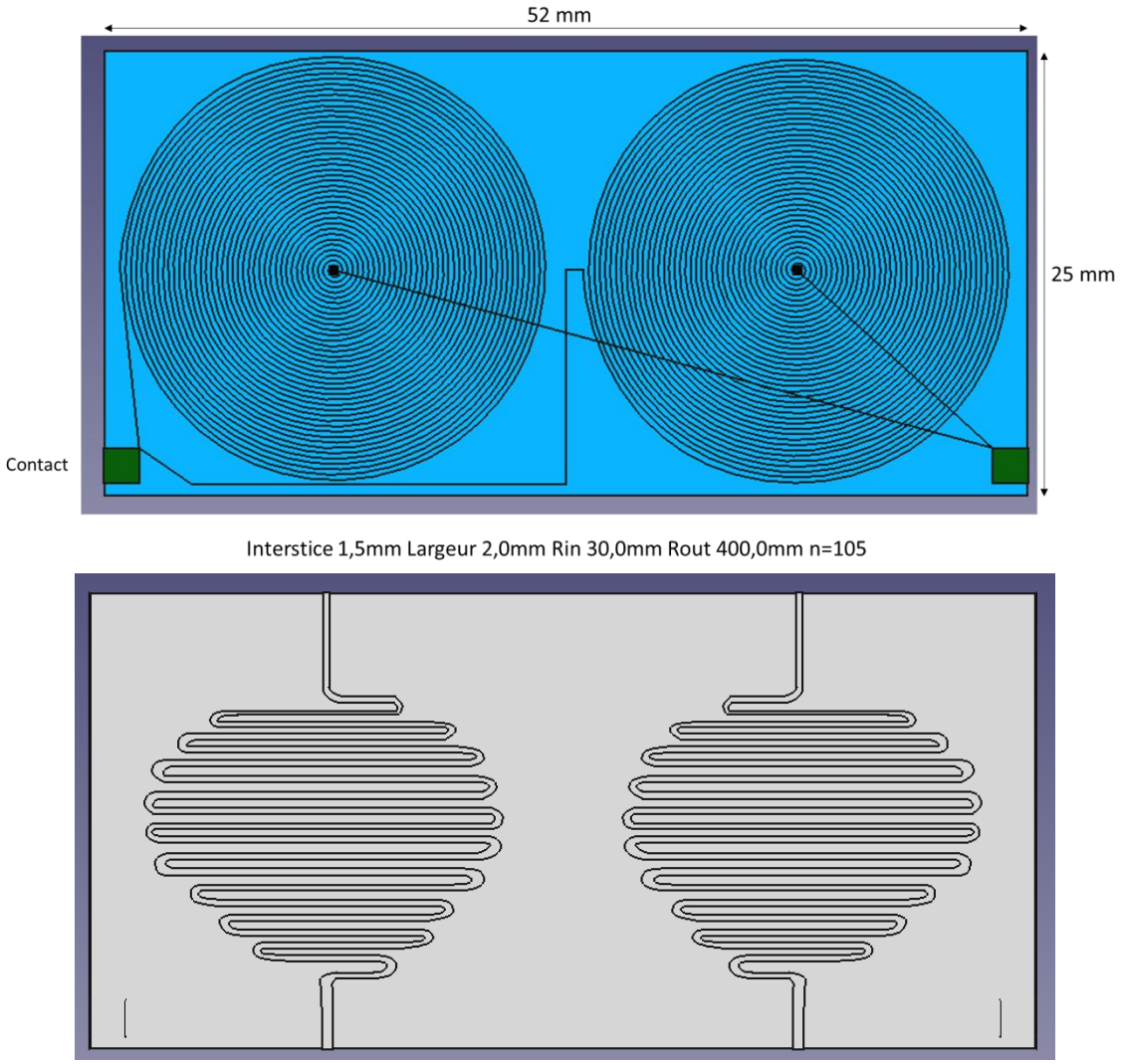

Figure 120: Top view of the microfluidic part without and with a XY cut.

Cleanroom Protocol

A confidential step by step protocol has been established with the help of Mrs. Marion Woytasik from the “Centre de Nanosciences et de Nanotechnologies (C2N)” for the creation of a first prototype.

Detection coil photolithography mask

We made a multi-layered photolithography mask layout using CLEWIN software to test different characteristics for the detection coils like different number of turns and the effect of a gap in the middle of the coils. The goal is to determine if at this size we can have good detection homogeneity and if we can limit the heating created by Joule effect.

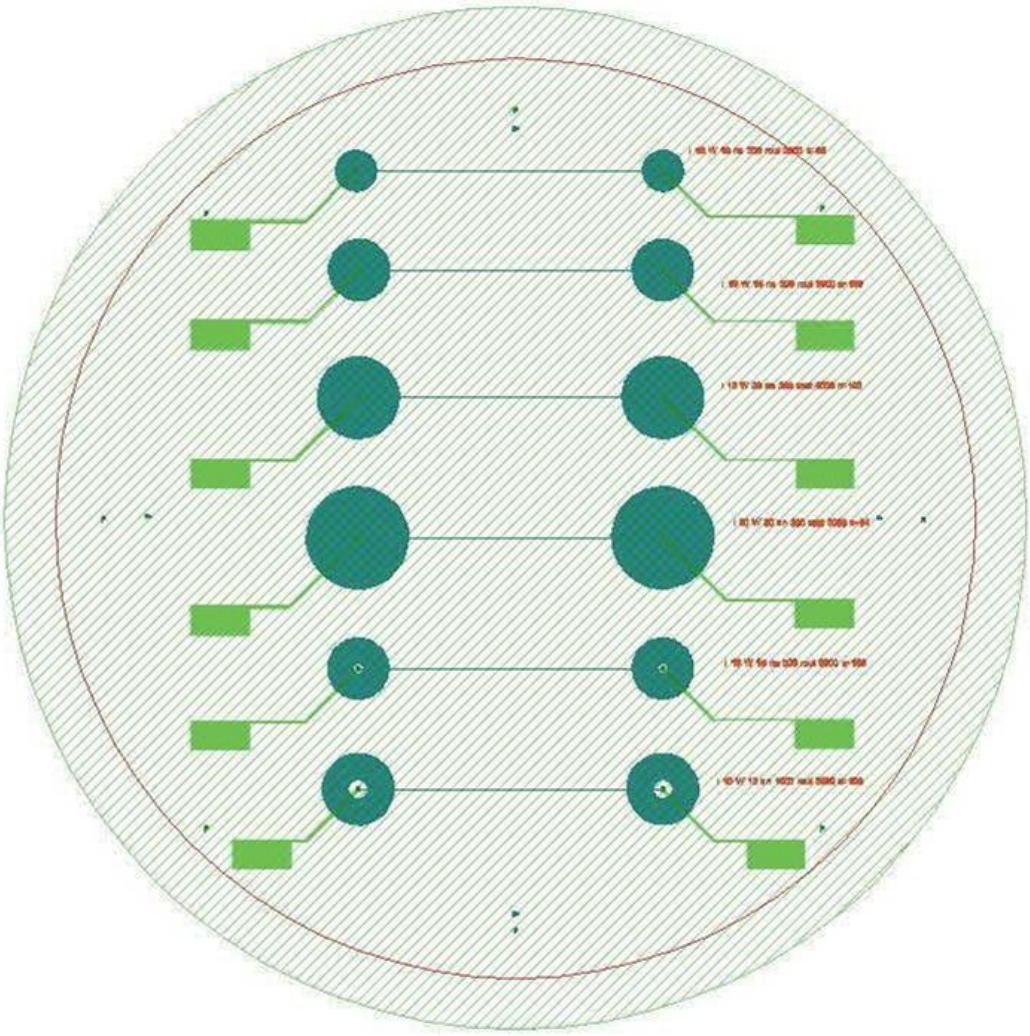

Figure 121: Mask for different detection microcoils on a 4’ wafer

Bibliography

[1]. **Salaam-Blythe, Tiaji.** *U.S. and International Health Responses to the Ebola Outbreak in West Africa.* Congressional Research Service. 2014.

[2]. *The origins and the future of microfluidics.* **Whiteside, Georges M.** July 27, 2006, Nature, Vol. 442, pp. 368-373.

[3]. *Microfluidic immunosensor systems.* **Bange, A., Halsall, H. B., & Heineman, W. R...** 12, 2005, Biosensors and Bioelectronics, Vol. 20, pp. 2488–2503.

[4]. *Comparative Study of Rheological Properties of Ethanol and UDMH based Gel Propellants.* **B.V.S. Jyoti, Mohan Varma and Seung Wook Baek.** 2013. 5th European Conference for Aeronautics and Space Sciences (EUCASS).

[5]. *An Experimental Investigation of the Circumstances Which Determine Whether the Motion of Water Shall Be Direct or Sinuous, and of the Law of Resistance in Parallel Channels.* **Reynolds, Osborne.** 1883, Philosophical Transactions of the Royal Society of London, Vol. 174, pp. 935-982.

[6]. *Design of pressure-driven microfluidic networks using electric circuit analogy.* **Kwang W. Oh, Kangsun Lee, Byungwook Ahna and Edward P. Furlani.** 2012, Lab on a Chip, Vol. 12, pp. 515-545.

[7]. *Chaotic Mixer for Microchannels.* **Abraham D. Stroock, Stephan K. W. Dertinger, Armand Ajdari, Igor Mezić, Howard A. Stone, George M. Whitesides.** 5555, 2002, Science, Vol. 295, pp. 647–651.

[8]. *Experimental and numerical analysis of Y-shaped split and recombination micro-mixer with different mixing units.* **Imran Shaha, Soo Wan Kim, Kyunghwan Kim, Yang Hoi Doh, Kyung HyunChoi.** February 15, 2019, Chemical Engineering Journal, Vol. 358, pp. 691-706.

[9]. *Poly(dimethylsiloxane) thin films as biocompatible coatings for microfluidic devices: Cell culture and flow studies with glial cells.* **Peterson, S. L., McDonald, A., Gourley, P. L., & Sasaki, D. Y.** 1, June 15, 2004, Journal of biomedical materials research, Vol. 72(A), pp. 10-15.

[10]. *Recent developments and applications of protective silicone coatings: Areview of PDMS functional materials.* **Eduok, U., Faye, O., & Szpunar, J.** 2017, Progress in Organic Coatings, Vol. 111, pp. 124-163.

[11]. *Soft Lithography.* **Younan Xia and George M. Whitesides.** 1998, annual reviews, Vol. 37, pp. 550-575.

[12]. *Microfluidics - a review.* **Peter Gravesen, Jens Branebjerg and Ole Ssnderg%rd Jensen.** 1993, Micromech. Microeng., Vol. 3, pp. 168-182.

[13]. *Rapid prototyping polymers for microfluidic devices and high pressure injections.* **Elodie, Sollier, et al., et al.** 2011, Lab Chip, Vol. 11, p. 3752.

[14]. *Siloxane Polymers for High-Resolution, High-Accuracy Soft Lithography.* **Michel, H. Schmid and B.** December 31, 1998, Macromolecules, Vol. 33, pp. 3042-3049.

[15]. *Influence of network structure on glass transition temperature of elastomers.* **Bandzierz, K., Reuvekamp, L., Dryzek, J., Dierkes, W., Blume, A., & Bielinski, D.** 7, June 23, 2016, Materials, Vol. 9.

[16]. *Gas sorption, diffusion, and permeation in poly(dimethylsiloxane).* **Merkel, T. C., et al., et al.** 3, January 04, 2000, Polymer Physics, Vol. 38, pp. 415-434.

[17]. *Intégration de puce à ADN dans un microsystèmefluidique.* **Goulpeau, Jacques.** 2006.

[18]. *A simple method for fabricating multi-layer PDMS structures for 3Dmicrofluidic chips.* **Mengying Zhang, Jinbo Wu, Limu Wang, Kang Xiaoband and Weijia Wen.** November 4, 2009, Lab on a chip, Vol. 10, pp. 1199-1203.

[19]. *A microfluidic colorimetric biosensor for rapid detection of Escherichia coliO157:H7 using gold nanoparticle aggregation and smart phone imaging.* **Zheng, L., Cai, G., Wang, S., Liao, M., Li, Y., & Lin, J.** October 3, 2018, Biosensors and Bioelectronic.

[20]. *PMMA/PDMS valves and pumps for disposable microfluidics.* **Wenhua Zhang, Shuichao Lin, Chunming Wang, Jia Hu,aCong Li, Zhixia Zhuang, Yongliang Zhou, Richard A. Mathies and Chaoyong James Yang.** April 9, 2009, Lab on a chip, Vol. 9, pp. 3088-3094.

[21]. *Recent developments in PDMS surfacemodification for microfluidic devices.* **Zhou, J., Ellis, A. V., & Voelcker, N. H.** 1, 2010, Electrophoresis, Vol. 31, pp. 2-16.

[22]. *When PDMS isn't the best.* **Mukhopadhyay, Rajendrani.** May 1, 2007, American chemical society, pp. 3049-3053.

[23]. *Solvent Compatibility ofPoly(dimethylsiloxane)-Based Microfluidic Devices.* **Lee, J. N., Park, C., & Whitesides, G. M.** 13, 2003, Analytical chemestry, Vol. 75, pp. 6544-6554.

[24]. *Collapse of stamps for soft lithography due to interfacial adhesion.* **K. J. Hsia, Y. Huang, E. Menard, J.-U. Park, W. Zhou, J. Rogers, and J. M. Fulton.** 154106, October 24, 2005, Applied Physics Letters, Vol. 86.

[25]. *Engineers are from PDMS-land, Biologists are from Polystyrenia.* **Berthier, E., Young, E. W. K., & Beebe, D.** 7, January 19, 2012, Lab on a chip, Vol. 12, pp. 1224-1237.

[26]. *Recent Development of Wearable Microfluidics Applied in Body Fluid Testing and Drug Delivery.* **Fan, Yi-Qiang, et al., et al.** 2017, Chinese Journal of Analytical Chemistry, pp. 455-463.

[27]. *Stretchable Microfluidic Radiofrequency Antennas.* **Masahiro, Kubo, et al., et al.** 25, July 6, 2010, Advanced materials, Vol. 22, pp. 2749-2752.

[30]. *Review on microfluidic paper-based analytical devices towards commercialisation.* **Akyazi, T., Basabe-Desmonts, L., & Benito-Lopez, F.** November 3, 2017, Analytica Chimica Acta, Vol. 1001, pp. 1-17.

[31]. *Design for Microfluidic Device ManufactureGuidelines.* **Henne van Heeren, Peter Hewkin.** April 5, 2014, Microfluidics Consortium.

[32]. **Manz A, Becker H (eds).** *Microsystem technology in the life sciences.* s.l. : Springer, 1998.

[33]. *Mail-Order Microfluidics: Evaluation of Stereolithography for the Production of Microfluidic Devices.* **Anthony K. Au, Wonjae Lee and Albert Folch.** 1-3, 2013, The Royal Society of Chemistry, Vol. 00, pp. 1-14.

[34]. *Disposable silicon-glass microfluidic devices:precise, robust and cheap.* **Qi, Z., Xu, L., Xu, Y., Zhong, J., Abedini, A., Cheng, X., & Sinton, D.** Lab on a Chip, Vol. 18, pp. 3872-3880.

[35]. *Thermoplastic microfluidic devices and their applications in protein and DNA analysis.* **Fan, Ke Liua and Z. Hugh.** 2011, Analyst, Vol. 136, p. 1288.

[36]. *Polymer microfabrication technologies for microfluidic systems.* **Becker, H., & Gärtner, C.** 1, 2008, Analytical and bioanalytical Chemestry, Vol. 390, pp. 89-111.

[37]. *Review on micro molding of thermoplastic polymers.* **Heckele, M., & Schomburg, W. K.** December 17, 2003, Micromechanics and Microengineering, Vol. 14, pp. R1-R14.

[38]. *Polymer microfluidic devices.* **Becker, H.** 2, 2002, Talanta, Vol. 56, pp. 267-287.

[39]. **www.chegg.com.** 06/2019

[40]. *Polymer microfluidic chips for electrochemical and biochemical analyses.* **Joël Rossier, Frédéric Reymond, Philippe E. Miche.** 2002, Electrophoresis, Vol. 23, pp. 858-867.

[41]. *Laser processing for bio-microfluidics applications (part I).* **Khan Malek, C. G.** 8, June 14, 2006, Analytical and Bioanalytical Chemistry, Vol. 385, pp. 1351-1361.

[42]. *Excimer laser fabrication of polymer microfluidic devices.* **Xu, Joohan Kim and Xianfan.** 4, NNovember 2003, Journal of laser applications, Vol. 15, pp. 255-260.

[43]. *Polyimide-based microfluidic devices.* **Metz, S., Holzer, R., & Renaud, P.** August 9, 2001, Lab on a Chip, Vol. 1, pp. 29-34.

[44]. *Flexible polyimide probes with microelectrodes and embedded microfluidic channels for simultaneous drug delivery andmulti-channel monitoring of bioelectric activity.* **Metz, S., Bertsch, A., Bertrand, D., & Renaud, P.** 2004, Biosensors and Bioelectronics, Vol. 19, pp. 1309-1318.

[45]. *Photomodification of Polymer MicrochannelsInduced by Static and Dynamic Excimer Ablation:Effect on the Electroosmotic Flow.* **F. Bianchi, Y. Chevolot, H. J. Mathieu and H. H. Girault.** 2001, Analytical Chemistry, Vol. 73, pp. 3845-3853.

[46]. **Jacobs, PF.** *Rapid prototyping & manufacturing: fundamentals of stereolithography.* s.l. : Society of Manufacturing Engineers, 1992.

[47]. *Two-Photon Photopolymerizationand 3D Lithographic Microfabrication.* **Hong-Bo Sun, Satoshi Kawata.** 2004, APS, pp. 169-273.

[48]. *Analytical Performance of Polymer-Based Microfluidic Devices Fabricated By Computer Numerical Controlled Machining.* **Justin S. Mecomber, Apryll M. Stalcup, Doug Hurd, H. Brian Halsall, William R. Heineman, Carl J. Seliskar, Kenneth R. Wehmeyer and Patrick A. Limbach.** 2006, Analytical Chemistry, Vol. 78, pp. 936-941.

[49]. *Rapid prototyping of microfluidic chips in COC.* **Steigert, J., Haeberle, S., Brenner, T., Müller, C., Steinert, C. P., Koltay, P., Ducrée, J.** 2007, Journal of Micromechanics and Microengineering, Vol. 17, pp. 333-341.

[50]. *Microthermoforming of microfluidic substrates by soft lithography (μTSL): optimization using design of experiments.* **Focke, M., Kosse, D., Al-Bamerni, D., Lutz, S., Müller, C., Reinecke, H., … von Stetten, F.** 2011, Journal of Micromechanics and Microengineering, Vol. 21, pp. 1-11.

[51]. *Microthermoforming as a novel technique for manufacturing scaffolds in tissue engineering (CellChips).* **Giselbrecht, S., Gietzelt, T., Gottwald, E., Guber, A. E., Trautmann, C., Truckenmüller, R., & Weibezahn, K. F.** 4, 2004, Vol. 151, pp. 151-1557.

[52]. *Hot embossing - The molding technique for plastic microstructures.* **Heckele, M., Bacher, W., & Müller, K. D.** 1998, Microsystem technologies, Vol. 4, pp. 122-124.

[53]. *Hot embossing as a method for the fabrication of polymer high aspectratio structures.* **Becker, H., & Heim, U.** 2000, Sensors and Actuators, Vol. 83, pp. 130-135.

[54]. *Recent progress in nanoimprint technology and its applications.* **Guo, L Jay.** 2004, Journal of Physics D: Applied Physics, Vol. 37, pp. R123-R141.

[55]. *Fully automated hot embossing processes utilizing high resolution working stamps.* **Glinsner T., Veres T., Kreindl G., Roy E., Morton K., Wieser T., … Lindner P.** 2010, Journal of Vacuum Science & Technology B, Nanotechnology and Microelectronics: Materials, Processing, Measurement, and Phenomena, Vol. 28, pp. 36-41.

[56]. *Roll-to-roll hot embossing of microstructures.* **Velten, T., Bauerfeld, F., Schuck, H., Scherbaum, S., Landesberger, C., & Bock, K.** 2010, Microsystem technologies, Vol. 17, pp. 619-627.

[57]. *REVIEWMicro-injection moulding of polymer microfluidic devices.* **Attia, U. M., Marson, S., & Alcock, J. R.** 2009, Vol. 7, pp. 1-28.

[58]. *Methods and instruments for continuous-flow PCR on a chip.* **Claudia Gärtner, Richard Klemm, Holger Becker.** 2007, Microfluidics, BioMEMS, and Medical Microsystems, Vol. 6465.

[59]. *Injection molded microfluidic chips featuring integrated interconnects.* **Mair, D. A., Geiger, E., Pisano, A. P., Fréchet, J. M. J., & Svec, F.** 2006, Lab Chip, Vol. 6, pp. 1346-1354.

[60]. *Centrifugal microfluidics for biomedical applications.* **Gorkin, R., Park, J., Siegrist, J., Amasia, M., Lee, B. S., Park, J.-M., … Cho, Y.-K.** 2010, Lab on a Chip, Vol. 10, pp. 1758-1773.

[61]. *Centrifugal microfluidics for cell analysis.* **Burger, R., Kirby, D., Glynn, M., Nwankire, C., O'Sullivan, M., Siegrist, J., … Ducrée, J.** 2012, Current Opinion in Chemical Biology, Vol. 16, pp. 409-414.

[62]. *Lab on a CD.* **Madou, M., Zoval, J., Jia, G., Kido, H., Kim, J., & Kim, N.** 2006, Annual Review of Biomedical Engineering, Vol. 8, pp. 601-628.

[63]. *Fabrication of microfluidic systems inpoly(dimethylsiloxane).* **McDonald, J. C., Duffy, D. C., Anderson, J. R., Chiu, D. T., Wu, H., Schueller, O. J. A., & Whitesides, G. M.** 2000, Electrophoresis, Vol. 21, pp. 27-40.

[64]. *Microfabricating high-aspect-ratio structures in polyurethane-methacrylate (PUMA) disposable microfluidic devices.* **Kuo, J. S., Zhao, Y., Ng, L., Yen, G. S., Lorenz, R. M., Lim, D. S. W., & Chiu, D. T.** 2009, Lab on a Chip, Vol. 9, pp. 1951-1956.

[65]. *Microfluidic stickers.* **Bartolo, D., Degré, G., Nghe, P., & Studer, V.** 2008, Lab Chip, Vol. 8, pp. 274-279.

[66]. *Rapid Prototyping of Thermoset Polyester Microfluidic Devices.* **Fiorini, G. S., Lorenz, R. M., Kuo, J. S., & Chiu, D. T.** 2004, Vol. 76, pp. 4697-4704.

[67]. *Rapid prototyping polymers for microfluidic devices and high pressureinjections.* **Sollier, E., Murray, C., Maoddi, P., & Di Carlo, D.** 2011, Lab on a Chip, Vol. 11, pp. 3752-3765.

[68]. *A new USP Class VI-compliant substrate for manufacturing disposablemicrofluidic devices.* **Kuo, J. S., Ng, L., Yen, G. S., Lorenz, R. M., Schiro, P. G., Edgar, J. S., … Chiu, D. T.** 2009, Vol. 9, pp. 870-876.

[69]. *Low-Temperature Thermal Bonding of PMMA MicrofluidicChips.* **Li, J., Chen, D., & Chen, G.** 2005, Analytical Letters, Vol. 38, pp. 1127-1136.

[70]. *Micro ultrasonic welding: joining of chemically inert polymer microparts for single material fluidic components and systems.* **Truckenmüller, R., Cheng, Y., Ahrens, R., Bahrs, H., Fischer, G., & Lehmann, J.** 2006, Microsystem Technologies, Vol. 12, pp. 1027-1029.

[71]. *Integrated polymer chip for two-dimensional capillary gelelectrophoresis.* **Griebel, A., Rund, S., Schönfeld, F., Dörner, W., Konrad, R., & Hardt, S.** 2004, Lab Chip, Vol. 4, pp. 18-23.

[72]. *Replica multichannel polymer chips with a network of sacrificial channels sealed by adhesive printing method.* **Dang, F., Shinohara, S., Tabata, O., Yamaoka, Y., Kurokawa, M., Shinohara, Y., … Baba, Y.** 2005, Lab on a Chip, Vol. 5, pp. 472-478.

[73]. *Microfluidic channel fabrication by PDMS-interface bonding.* **Chow, W. W. Y., Lei, K. F., Shi, G., Li, W. J., & Huang, Q.** 2005, Smart Materials and Structures, Vol. 15, pp. S112-S116.

[74]. *Capillarity Induced Solvent-Actuated Bonding ofPolymeric Microfluidic Devices.* **Shah, J. J., Geist, J., Locascio, L. E., Gaitan, M., Rao, M. V., & Vreeland, W.** 2006, Analytical Chemistry, Vol. 78, pp. 3348-3353.

[75]. *Development of biofactory-on-a-chip technology using excimer laser micromachining.* **Pethig, R., Burt, J. P. H., Parton, A., Rizvi, N., Talary, M. S., & Tame, J. A.** 1998, Journal of Micromechanics and Microengineering, Vol. 8, pp. 57-63.

[76]. *Hydrophilic Surface Modification of PDMS Using Atmospheric RF Plasma.* **Hong, S. M., Kim, S. H., Kim, and J. H., & Hwang, H. I.** 2006, Journal of Physics: Conference Series, Vol. 34, pp. 656-661.

[77]. *A study on photolinkers used for biomolecule attachment to polymer surfaces.* **Dankbar, D. M., & Gauglitz, G.** 2006, Analytical and Bioanalytical Chemistry, Vol. 386, pp. 1967-1974.

[78]. *Two-site, noncompetitive immunoassays usually consist of an analyte "sandwiched" between two antibodies. ELISAs are often run in this format.* **Wikipedia.** Available: https://en.wikipedia.org/wiki/Immunoassay#/media/File:Sandwich_Immunoassay,_ELISA.jpg.

[79]. *Evolution and expectations of enzymatic biosensors for pesticides.* **R. Vargas-Bernal, E. Rodriguez-Miranda and G. Herrera-Perez,.** 2012, Pesticides-Advances in Chemical and Botanical Pesticides.

[80]. *Biosensors and their applications--A review.* **Mehrotra, Parikha.** [ed.] Elsevier. 2, 2016, Journal of oral biology and craniofacial research, Vol. 6, pp. 153-159.

[81]. *Principles of enzyme biosensors.* **Mulchandani, Ashok.** [ed.] Springer. 1998, Enzyme and Microbial Biosensors: Techniques and Protocols, pp. 3-14.

[82]. *Biosensors: A modern day achievement.* **G. Shruthi, C. Amitha and B. B. Mathew.** 1, 2014, Journal of Instrumentation Technology, Vol. 2, pp. 26-39.

[83]. *Enzyme Biosensors for Biomedical Applications: Strategies for Safeguarding Analytical Performancess in Biological Fluids.* **Rocchitta, G., Spanu, A., Babudieri, S., Latte, G., Madeddu, G., Galleri, G., … Serra, P.** 2016, Sensors, Vol. 16, p. 780.

[84]. *Biosensors and their applications – A review.* **Mehrotra, P.** 2016, Journal of Oral Biology and Craniofacial Research, Vol. 6, pp. 153-159.

[85]. *An integrated optical oxygen sensor fabricated using rapid-prototyping techniques.* **Chang-Yen D. A., & Gale B. K.** 2003, Lab on a Chip, Vol. 3, pp. 297-301.

[86]. *Optical Biosensors for theDetection of PathogenicMicroorganisms.* **Yoo, S. M., & Lee, S. Y.** 2016, Trends in Biotechnology, Vol. 34, pp. 7-25.

[87]. *Planar optical waveguide-based biosensor for the quantitative detection of tumor markers.* **Mukundan, H., Kubicek, J. Z., Holt, A., Shively, J. E., Martinez, J. S., Grace, K., … Swanson, B. I.** 2009, Sensors and Actuators B: Chemical, Vol. 138, pp. 453-460.

[88]. *Lateral flow assays: principles, designs and labels.* **Bahadır, E. B., & Sezgintürk, M. K.** 2016, TrAC Trends in Analytical Chemistry, Vol. 82, pp. 286-306.

[89]. *Lab-on-a-Chip Pathogen Sensors for Food Safety.* **Yoon, J.-Y., & Kim, B.** 2012, Sensors, Vol. 12, pp. 10713-10741.

[90]. *Microbial biosensors: A review.* **Su, L., Jia, W., Hou, C., & Lei, Y.** 2011, Biosensors and Bioelectronics, Vol. 26, pp. 1788-1799.

[91]. *Biochip-Based Chemiluminescence Biosensing Method for Detection of Escherichiacoli O157:H7.* **M. Varshney, Y. Li, B. Srinivasan, S. Tung, G. Erf, M. F. Slavik, … W. Fang.** 2006, Transactions of the ASABE, Vol. 49, pp. 2061-2068.

[92]. *Surface plasmon resonance sensors: review.* **Homola, J., Yee, S. S., & Gauglitz, G.** 1999, Sensors and Actuators: B , Vol. 54, pp. 3-15.

[93]. *Microfluidic sensing: state of the artfabrication and detection techniques.* **Wu, J., & Gu, M.** 8, 2011, Journal of Biomedical Optics, Vol. 16.

[94]. *Bead-based immunoassays with microelectrode detection.* **Halsall, H. B., Heineman, W. R., Farrell, S.** 3, 2004, Analytical and Bioanalytical Chemistry, Vol. 379, pp. 358-367.

[95]. *A review on viral biosensors to detect human pathogens.* **Caygill, R. L., Blair, G. E., & Millner, P. A.** 1-2, 2010, Analytica Chimica Acta, Vol. 681, pp. 8-15.

[96]. *On-column conductivity detection incapillary-chip electrophoresis.* **Wu, Z.-Y., Fang, F., Josserand, J., & Girault, H. H.** 24, 2007, Electrophoresis, Vol. 28, pp. 4612-4619.

[97]. *Nucleic Acid-based Detection of Bacterial Pathogens Using Integrated Microfluidic Platform Systems.* **Lui, C., Cady, N., & Batt, C.** 5, 2009, Sensors, Vol. 9, pp. 3713-3744.

[98]. *Surface Plasmon Resonance and Quartz Crystal Microbalance Methods for Detection of Molecular Interactions.* **Liu, Y., Jaiswal, A., Poggi, M. A., & Wilson, W. D.** 2011, Chemosensors, pp. 329-344.

[99]. *Design and Analysis of a High Sensitive Microcantilever Biosensor for Biomedical Applications.* **Ansari, M. Z., & Cho, C.** 2008, 2008 International Conference on BioMedical Engineering and Informatics, pp. 593-597.

[100]. *Comparative advantages of mechanical biosensors.* **Arlett, J. L., Myers, E. B., & Roukes, M. L.** 4, 2011, Nature Nanotechnology, Vol. 6, pp. 203-215.

[101]. *Detection of bacteria in suspension by using a superconducting quantum interference device.* **Grossman, H. L., Myers, W. R., Vreeland, V. J., Bruehl, R., Alper, M. D., Bertozzi, C. R., & Clarke, J.** 1, 2003, Proceedings of the National Academy of Sciences, Vol. 101, pp. 129-134.

[102]. *On the Electrodynamic Qualities of Metals:--Effects of Magnetization on the Electric Conductivity of Nickel and of Iron.* **Thomson, W.** 1856, Proceedings of the Royal Society of London, Vol. 8, pp. 546-550.

[103]. *Advanced ReviewMagnetic nanoparticle biosensors.* **Haun, J. B., Yoon, T.-J., Lee, H., & Weissleder, R.** 3, 2010, Interdisciplinary Reviews: Nanomedicine and Nanobiotechnology, Vol. 2, pp. 291-304.

[104]. *Recent Developments in Magnetic Diagnostic Systems.* **Lee, H., Shin, T.-H., Cheon, J., & Weissleder, R.** 19, 2015, Chemical Reviews, Vol. 115, pp. 10708-10716.

[105]. *Continuous sorting of magnetic cellsviaon-chip free-flowmagnetophoresis.* **Pamme, N., & Wilhelm, C.** 8, 2006, Lab on a Chip, Vol. 6, pp. 974-980.

[106]. *Magnetic Nanoparticles: Design and Characterization, Toxicity andBiocompatibility, Pharmaceutical and Biomedical Applications.* **Reddy, L. H., Arias, J. L., Nicolas, J., & Couvreur, P.** 11, 2012, Chemical Reviews, Vol. 112, pp. 5818-5878.

[107]. **Rabehi, Amine.** *Electromagnetic microsystem for the detection of magnetic nanoparticles in a microfluidic structure for immunoassays.* 2018.

[108]. *CRP determination based on a novel magnetic biosensor.* **Meyer M. H. F., Hartmann M., Krause H.-J., Blankenstein G., Mueller-Chorus B., Oster J., … Keusgen M.** 2007, Biosensors and Bioelectronics, Vol. 22, pp. 973-979.

[109]. *Magnetic particle detection by frequency mixing for immunoassay applications.* **Krause H.-J., Wolters N., Zhang Y., Offenhäusser A., Miethe P., Meyer M. H. F., … Keusgen M.** 2007, Journal of Magnetism and Magnetic Materials, Vol. 311, pp. 436-444.

[110]. *Tunability of Size and Magnetic Moment of Iron Oxide Nanoparticles Synthesized by Forced Hydrolysis.* **Sutens, B., Swusten, T., Zhong, K., Jochum, J., Van Bael, M., Van der Eycken, E., … Verbiest, T.** 7, 2016, Materials, Vol. 9, pp. 554-564.

[111]. *Definition for Polarization P and Magnetization M Fully Consistent with Maxwell's Equations.* **Carlo A. Gonano, Riccardo E. Zich, and Marco Mussetta.** 2015, Progress In Electromagnetics Research B, Vol. 64, pp. 83-101.

[112]. *New type of biosensor based on magnetic nanoparticle detection.* **Nikitin, P. I., Vetoshko, P. M., & Ksenevich, T. I.** 2007, Journal of Magnetism and Magnetic Materials, Vol. 311, pp. 445-449.

[113]. *German Patent Application 10309132.7.* **H.-J. Krause, Y. Zhang, N. Wolters, et al.,.** WO2004/077044 A1, 2004, s.l. : European Patent Application, 2003.

[114]. *A simple and portable magnetic immunoassay for the rapid detection and sensitive quantification of plant viruses.* **Rettcher S., Jungk F., Kühn C., Krause H.-J., Nölke G., Commandeur U., … Schröper F.** 9, 2015, Applied and Environmental Microbiology, Vol. 81, pp. 3039-3048.

[115]. *Francisella tularensis detection using magnetic labels and a magnetic biosensor based on frequency mixing.* **Meyer, Martin HF, et al., et al.** 1, 2007, Journal of magnetism and magnetic materials, Vol. 311. pp. 259-263

[116]. *Magnetic biosensor for the detection of Yersinia pestis.* **Meyer M. H. F., Stehr M., Bhuju S., Krause H.-J., Hartmann M., Miethe P., … Keusgen M.** 2, 2007, Journal of Microbiological Methods, Vol. 68, pp. 218-224.

[117]. *Methods of Increasing Immunity to Interfering Signals.* **Vasilescu, G.** Signals and Communication Technologies, pp. 389-409.

[118]. *Magnetic Field Sensors: Induction Coil (Search Coil) Sensors.* **Dehmel, G.** 2008, Sensors, pp. 205-253.

[119]. *Improved Adhesion/Bonding due to Plasma Treatment of PDMS.* **www.azom.com.** August 14, 2017.

[120]. **www.elveflow.com.** 07/2019

[121]. *Negative Tone Photoresist formulations 50-100.* **Microchem.** 07/2019

[122]. *Plexiglass Data Sheet Lexan 9030 Data Sheet.* **AR, Makrolon.** s.l. : Bayer Sheet Europe, 2004.

[123]. *Adhesion of lens capsule to intraocular lenses of polymethylmethacrylate, silicone, and acrylic foldable materials: an experimental study.* **Oshika, T., Nagata, T., & Ishii, Y.** 5, 1998, British Journal of Ophtamology, Vol. 82, pp. 549-553.

[124]. *The distribution of immune cells in the uveal tract of the normal eye.* **McMenamin, P. G.** 2, 1997, Eye, Vol. 11, pp. 183-193.

[125]. *Microchip-based ELISA strategy for the detection of low-level disease biomarker in serum.* **Liu Y., Wang H., Huang J., Yang J., Liu B., & Yang, P.** 1, 2009, Analytica Chimica Acta, Vol. 650, pp. 77-82.

[126]. *High Glass Transition Temperatures of Poly(methyl methacrylate) Prepared by Free Radical Initiators.* **Hongxiang Tengh, Kotaro Koike, Dingying Zhou, Zen Satoh, Yasuhiro Koike,2,3YOSHIYUKI OKAMOTO.** 2008, Journal of Polymer Science: Part A: Polymer Chemistry, Vol. 47, pp. 315-317.

[127]. *Acrylic aka PMMA Chemical Compatiblity Chart.* **www.industrialspec.com.**

[128]. *Roll manufacturing of flexible microfluidic devices in thin PMMA and COC foils by embossing and lamination.* **Khaled Metwally, Laurent Robert, Samuel Queste, Bernard Gauthier-Manuel, Chantal Khan-Malek.** October 8, 2011, Microsystems technologies.

[129]. *Micro Flow-through PCR in a PMMA Chip Fabricated by KrF Excimer Laser.* **Yao L., Liu B., Chen T., Liu S., & Zuo T.** 3, 2005, Biomedical Microdevices, Vol. 7, pp. 253-257.

[130]. *PMMA, from plexiglass window to a packaging for an implantable glucose sensor.* **Van De Walle, E.** 3, 2015, Chemistry International, Vol. 37.

[131]. *Cyclic Olefin Copolymer.* **https://en.wikipedia.org/wiki/.** 07/2019

[132]. *Immobilization of Biomolecules on CycloolefinPolymer Supports.* **MacCraith, Stephan Laib and Brian D.** 16, 2007, Analytical Chemistry, Vol. 79, pp. 6264-6270.

[133]. *Surface immobilisation of antibody on cyclic olefin copolymer for sandwich immunoassay.* **Raj J., Herzog G., Manning M., Volcke C., MacCraith B. D., Ballantyne S., … Arrigan D. W. M.** 8, 2009, Biosensors and Bioelectronics, Vol. 24, pp. 2654–2658.

[134]. *Nanoimprint lithography in the cyclic olefin copolymer, Topas[sup ®], a highly ultraviolet-transparent and chemically resistant thermoplast.* **Nielsen T., Nilsson D., Bundgaard F., Shi P., Szabo P., Geschke O., & Kristensen A.** 4, 2004, Journal of Vacuum Science & Technology B: Microelectronics and Nanometer Structures, Vol. 22, pp. 1770-1775.

[135]. *TOPAS brochure.* **topas.com.** 2006.

[136]. *Rapid Prototyping of Cyclic Olefin Copolymer (COC) Microfluidic Devices.* **Aghvami S. A., Opathalage A., Zhang Z. K., Ludwig M., Heymann M., Norton M., … Fraden S.** 2017, Sensors and Actuators B: Chemical, Vol. 247, pp. 940-949.

[137]. *An on-chip whole blood/plasma separator with bead-packed microchannel on COC polymer.* **Shim J. S., Browne A. W., & Ahn C. H.** 5, 2010, Biomedical Microdevices, Vol. 12, pp. 949-957.

[138]. *Hemocompatibility of EpoCore/EpoClad photoresists on COC substrate for optofluidic integrated Bragg sensors.* **Hessler S., Rüth M., Sauvan, C., Lemke H.-D., Schmauss B., & Hellmann R.** 2017, Sensors and Actuators B: Chemical, Vol. 239, pp. 916-922.

[139]. *Cyclic olefin polymers: emerging materials for lab-on-a-chip applications.* **Nunes P. S., Ohlsson P. D., Ordeig O., & Kutter J. P.** 2-3, 2010, Microfluidics and Nanofluidics, Vol. 9, pp. 145-161.

[140]. *Poly(dimethylsiloxane).* **Kuo, Alex C. M.** 1999, Polymer Data Handbook.

[141]. *Polydimethylsiloxane thermal degradation Part 1. Kinetic aspects.* **G. Caminoa, S.M. Lomakin, M. Lazzari.** 2001, Polymer, Vol. 42, pp. 2395-3402.

[142]. *Characterization of activated cyclic olefin copolymer: effects of ethylene/norbornene content on the physiochemical properties.* **O'Neil C. E., Taylor S., Ratnayake K., Pullagurla S., Singh V., & Soper S. A.** 24, 2016, The Analyst, Vol. 141, pp. 6521-6532.

[**143]**. *Iron Oxide Monocrystalline Nanoflowers for Highly Efficient Magnetic Hyperthermia.* **Hugounenq P., Levy M., Alloyeau D., Lartigue L., Dubois E., Cabuil V., … Bazzi R.** 29, 2012, The Journal of Physical Chemistry C, Vol. 116, pp. 15702–15712.

[144]. *Magnetic Nanoparticles: Surface Effects and Properties Related to Biomedicine Applications.* **Issa B., Obaidat I., Albiss B., & Haik Y.** 11, 2013, International Journal of Molecular Sciences, Vol. 14, pp. 21266–21305.

[145]. *Superparamagnetic Colloids: Controlled Synthesis and Niche Applications.* **Jeong U., Teng X., Wang Y., Yang H., & Xia Y.** 2007, Advanced Materials, Vol. 19, pp. 33-60.

[146]. *Preparation of spherical silica particles by Stöber process with high concentration of tetra-ethyl-orthosilicate.* **Wang X.-D., Shen Z.-X., Sang T., Cheng X.-B., Li M.-F., Chen L.-Y., & Wang Z.-S.** 2010, Journal of Colloid and Interface Science, Vol. 341, pp. 23-29.

[147]. *PEGylation as a strategy for improving nanoparticle-based drug and gene delivery.* . **Suk J. S., Xu Q., Kim N., Hanes J., & Ensign L. M.** 2016, Advanced Drug Delivery Reviews, Vol. 99, pp. 28-51.

[148]. *Microfluidic pillar array sandwich immunofluorescence assay for ocular diagnostics.* **Green J. V., Sun D., Hafezi-Moghadam A., Lashkari K., & Murthy S. K.** 3, 2011, Biomedical Microdevices, Vol. 13, pp. 573-583.

[149]. *Advances in the preparation of porous polymer monoliths in capillaries and microfluidic chips with focus on morphological aspects.* **Nischang I., Brueggemann O., & Svec F.** 3, 2010, Analytical and Bioanalytical Chemestry, Vol. 397, pp. 953-960.

[150]. *Impedimetric immunosensing in a porous volumetric microfluidic detector.* **Wiederoder M. S., Misri I., & DeVoe D. L.** 2016, Sensors and Actuators B: Chemical, Vol. 234, pp. 493-497.

[151]. *High-field ac susceptometer using Helmholtz coils as a magnetizer.* **Chen, D.-X.** 6, 2004, Measurement Science and Technology, Vol. 15, pp. 1195-1202.

[152]. *Ethnic Differences in C-Reactive Protein Concentrations.* **Kelley-Hedgepeth A., Lloyd-Jones D. M., Colvin A., Matthews K. A., Johnston J., … Sowers M. R.** s.l. : 54, 2008, Clinical Chemistry, Vol. 6, pp. 1027-1037.

[153]. *C-reactive protein: a critical update.* **Pepys M. B., & Hirschfield G. M.** 12, June 2003, The Journal of Clinical Investigation, Vol. 111, pp. 1805-1812.

[154]. *Protein Immobilization Strategies for Protein Biochips.* **Rusmini F., Zhong Z., & Feijen J.** 6, 2007, Biomacromolecules, Vol. 8, pp. 1775-1789.

[155]. *Oriented Immobilization of Antibodies and Its Applications in lmmunoassays and Immunosensors.* **Lu B., Smyth M. R., & O'Kennedy R.** 3, March 1996, The Analyst, Vol. 121, pp. 29R-32R.

[156]. *Microfluidic Bioreactors for Cell Culturing: A Review.* **Godfrey Pasirayi, Vincent Auger, Simon M. Scott, Pattanathu K.S.M. Rahman, Meez Islam, Liam O'Hare and Zulfiqur Ali.** 2, 2011, Micro and Nanosystems, Vol. 3, pp. 137-160.

[157]. *Surface modification-assisted bonding of polymer-based microfluidic devices.* **Tennico Y. H., Koesdjojo M. T., Kondo S., Mandrell D. T., & Remcho V. T.** 2, 2010, Sensors and Actuators B: Chemical, Vol. 143, pp. 799-804.

[158]. *Aqua-Art: A Demonstration of Hydrophilic and Hydrophobic Surfaces Fabricated by Plasma Enhanced Chemical Vapor Deposition.* **Flynn S. P., McKenna M., Monaghan R., Kelleher S. M., Daniels S., & MacCormac A.** 2, 2016, Journal of Chemical Education, Vol. 94, pp. 221-225.

[**159]**. *Layer-by-layer generation of PEG-based regenerable immunosensing surfaces for small-sized analytes.* **Huebner M., Ben Haddada M., Méthivier C., Niessner R., Knopp D., & Boujday S.** 2014, Biosensors and Bioelectronics, Vol. 67, pp. 334-341.

[160]. *Piezoelectric immunosensor for direct and rapid detection of staphylococcal enterotoxin A (SEA) at the ng level.* **Salmain M., Ghasemi M., Boujday S., Spadavecchia J., Técher C., Val F., … Pradier C.-M.** 2011, Vol. 29, pp. 140-144.

[161]. **https://en.wikipedia.org/, Edgar181.** 07/2019

[162]. *Optimization and characterization of biomolecule immobilization on silicon substrates using (3-aminopropyl)triethoxysilane (APTES) and glutaraldehyde linker.* **Gunda N. S. K., Singh M., Norman L., Kaur K., & Mitra S. K.** 2014, Applied Surface Science, Vol. 305, pp. 522-530.

[163]. **Volpe, C. D., et al., et al.** About the possibility of experimentally measuring an equilibrium contact angle and its theoretical and practical consequences. [ed.] K.L. Mittal. *Contact Angle, Wettability and Adhesion.* s.l. : VSP, 2006, Vol. 4, pp. 79-99.

[164]. *Using Attenuated Total Reflection–Fourier Transform Infra-Red (ATR-FTIR) spectroscopy to distinguish between melanoma cells with a different metastatic potential.* **Minnes R., Nissinmann M., Maizels Y., Gerlitz G., Katzir A., & Raichlin Y.** 2017, Scientific Reports, Vol. 7, pp. 4381-4388.

[165]. *Estimation of the surface free energy of polymers.* **Owens D. K., & Wendt R. C.** 8, 1969, Journal of Applied Polymer Science, Vol. 13, pp. 1741-1747.

[166]. *Surfacec modification of commercial polyamide reverse osmosis membranes by radical grafting: An ATR-FTIR study.* **Belfer S., Purinson Y., & Kedem O.** 1998, Acta Polymerica, Vol. 49, pp. 574-582.

[167]. *ATR-FTIR Study of IgG Adsorbed on Different Silica Surfaces.* **Giacomelli C. E., Bremer M. G. E. ., & Norde W.** 1999, Journal of Colloid and Interface Science, Vol. 220, pp. 13-23.

[168]. *FTIR/ATR for protein adsorption to biomaterial surfaces.* **K., Chittur K.** 1998, Biomaterials, Vol. 19, pp. 357-369.

[169]. ***http://www.lrs.upmc.fr/.*** 07/2019

[170]. *X-ray photoelectron spectroscopy.* **Horton, J. Hugh.** 2009, faculty.chem.queensu.ca/people/faculty/horton/research.html.

[171]. *A PDMS/LTCC bonding technique for microfluidic application.* **Malecha K., Gancarz I., & Golonka L. J.** 2009, Journal of Micromechanics and Microengineering, Vol. 19, pp. 105016-105024.

[172]. *A low temperature surface modification assisted method for bonding plastic substrates.* **Vlachopoulou M.-E., Tserepi A., Pavli P., Argitis P., Sanopoulou M., & Misiakos K.** 2008, Journal of Micromechanics and Microengineering, Vol. 19, pp. 015007-6pp.

[173]. *Flow-through functionalized PDMS microfluidic channels with dextran derivative for ELISAs.* **Yu L., Li C. M., Liu Y., Gao J., Wang W., & Gan Y.** 2009, Lab on a Chip, Vol. 9, pp. 1243-1247.

[174]. *The effects of poly(dimethylsiloxane) surface silanization on the mesenchymal stem cell fate.* **Chuah Y. J., Kuddannaya S., Lee M. H. A., Zhang Y., & Kang Y.** 2, 2014, Biomaterials Science, Vol. 3, pp. 383-390.

[175]. **M.J. Owen, W.J. van Ooij and H.R. Anderson.** *First International Congress on Adhesion Science and Technology.* [ed.] VSP. Utrecht : s.n., 1998. p. 258.

[176]. *Polyorganosiloxanes... Surface Active Properties.* **Fox H., Taylor P., & Zisman W.** 11, Industrial & Engineering Chemistry : s.n., 1947, Vol. 39, pp. 1401-1409.

[177]. *Elastomeric microparticles for acoustic mediated bioseparations.* **Johnson L. M., Gao L., Shields IV C., Smith M., Efimenko K., Cushing K., … López G. P.** 2013, Journal of Nanobiotechnology, Vol. 11, p. 22.

[178]. *Characterisation of an irreversible bonding process for COC–COC and COC–PDMS–COC sandwich structures and application to microvalves.* **Cortese B., Mowlem M. C., & Morgan H.** 2011, Sensors and Actuators B: Chemical, Vol. 160, pp. 1473-480.

[179]. *A facile route for irreversible bonding of plastic-PDMS hybrid microdevices at room temperature.* **Tang L., & Lee N. Y.** 2010, Lab on a Chip, Vol. 10, pp. 1274-1280.

[180]. *Fabrication of Polymerase Chain Reaction Plastic Lab-on-a-Chip Device for Rapid Molecular Diagnoses.* **Kieu The Loan Trinh, Hainan Zhang, Dong-Jin Kang, Sung-Hyun Kahng, Ben D. Tall, and Nae Yoon Lee.** May 2016, International Neurology Journal, Vol. 20, pp. S38-48.

[181]. *Low temperature and deformation-free bonding of PMMA microfluidic devices with stable hydrophilicity via oxygen plasma treatment and PVA coating.* **H. Yu, Z. Z. Chong, S. B. Tor, E. Liuaand N. H. Loh.** 2015, Royal Society of Chemistry Advances, Vol. 5, pp. 8377–8388.

[182]. *The avidin-biotin complex in bioanalytical applications.* **Wilchek M., & Bayer E. A.** 1988, Analytical Biochemistry, Vol. 171, pp. 1-32.

[183]. *The growing applications of click chemistry.* **Moses J. E., & Moorhouse A. D.** 2007, Chemical Society Reviews, Vol. 36, pp. 1249-1262.

[184] *Electromagnetic sensing device for detecting magnetic nanoparticles*, **Kokabi H., Krause H.-J., Ngo K.A., Rabehi A.**, European Patent, EP17306381.9, 28466/004EP1, priority: 12.10.2017, issued: 13.06.2019.

List of figures

List of tables

Résumé

L'augmentation continue de la circulation des populations et des biens ces dernières décennies accentue les risques de pandémie due à un mauvais confinement des antigènes dangereux à leur région d'apparition. Il est donc crucial de développer une technique rapide de détection de pathogène pour prévenir ces risques.

Un projet multidisciplinaire a donc était mis en place entre Sorbonne Université à Paris et RWTH University à Jülich pour le développement d'un dispositif laboratoire-sur-puce intégré pour effectuer des tests immunologiques rapides, faciles et abordables.

Ce dispositif de détection de pathogène est composé d'un canal microfluidique entouré de microbobines planaires en circuit imprimé responsables de l'émission et de la détection de champs magnétiques. Ainsi des nanoparticules magnétiques peuvent être détectées et quantifiées puis être corrélées à la présence du pathogène, en tant que marqueurs du test immunologique. Habituellement, l'étape de détection de la présence du pathogène dans un échantillon se fait grâce à un signal fluorescent ou électrochimique qui sont des techniques longues et avec une sensibilité limitée. En conséquence, les tests immunologiques magnétiques semblent être une alternative intéressante. L'utilisation de canaux microfluidiques permet de n'utiliser qu'une très petite quantité d'échantillon pour effectuer un test. Le dispositif a été testé pour la détection de différentes nanoparticules magnétiques avec une limite de détection de 15 ng/µL pour des nanoparticules d'oxyde de fer de diamètre 20 nm et dans un volume de 14 µL correspondant à une petite goutte de sang. Pendant ce doctorat, l'objectif principal a été d'améliorer le prototype du dispositif et la fonctionnalisation de surface du canal microfluidique avec des anticorps.

Mots clés : détection des pathogènes, laboratoire sur puce, détection magnétique, technique de mélange de fréquences, fonctionnalisation de surface

Abstract

The ever-increasing exchange of people and goods these last decades creates pandemic risks that should be prevented by containing the hazardous antigens in the region of the outbreak. Therefore, the rapid detection of a biological entity is critical to tackle this issue and others like environment contamination and bioterrorism.

Consequently, a multidisciplinary project between Sorbonne Université in Paris and RWTH University in Aachen has been conducted to create a completely integrated lab-on-a-chip (LOC) for easy, rapid and cost-effective immunoassays.

The pathogen sensing system is composed of a microfluidic channel surrounded by planar PCB microcoils, which are responsible for the emission and the detection of magnetic fields. This system allows the detection and quantification of magnetic nanoparticles (MNP) used for immunoassays in a "sandwich" antigen-antibody configuration. So far, the final detection step is usually achieved by fluorescence-based or electrochemical techniques, which are time consuming and have limited sensitivity. Therefore, magnetic immunoassays constitute a promising alternative. Using microfluidics allows us to test very small volume samples quickly. We successfully tested this device with different concentrations of nanoparticles, different microfluidic channel layouts, different types of nanoparticles and different materials for the microfluidic channel. Using the frequency mixing magnetic detection technique, a LOD of 15 ng/µL for 20 nm core sized MNP has been achieved with a sample volume of 14 µL corresponding to a drop of blood. Antibody coating was also achieved on a Poly(methyl methacrylate) (PMMA) surface which is a more suitable material than the classically used polydimethylsiloxane (PDMS) for our application. In this thesis, emphasis is put on the improvement of the device prototype and the surface functionalization of the microfluidic channel with antibodies.

Keywords: pathogen sensing, lab-on-a-chip, magnetic detection, frequency mixing technique, surface functionalization.